

①

1990

~~THESIS~~/DISSERTATION

A Laboratory Study of the Effect of Stress State on the  
Elastic Moduli of Sand

Martin David Lewis

AFIT Student Attending: University of Texas - Austin

AFIT/CI/CIA- 90-029D

AFIT/CI  
Wright-Patterson AFB OH 45433-6583

Approved for Public Release IAW 190-1  
Distributed Unlimited  
ERNEST A. HAYGOOD, 1st Lt, USAF  
Executive Officer

DTIC  
ELECTE  
NOV 02 1990  
S B D  
*Co*

AD-A227 973

A LABORATORY STUDY OF THE EFFECT OF STRESS STATE  
ON THE ELASTIC MODULI OF SAND

by

Martin David Lewis, B.S., M.S.

DISSERTATION

Presented to the Faculty of the Graduate School of  
The University of Texas at Austin  
in Partial Fulfillment  
of the Requirements  
for the Degree of

DOCTOR OF PHILOSOPHY

THE UNIVERSITY OF TEXAS AT AUSTIN

December 1990

Copyright  
by  
Martin David Lewis  
1990

Dedicated to

Marcus and Alice

## ABSTRACT

### A LABORATORY STUDY OF THE EFFECT OF STRESS STATE ON THE ELASTIC MODULI OF SAND

Major Martin David Lewis, USAF

Doctor of Philosophy

The University of Texas at Austin, 1990

A study was conducted to determine the effect of stress state on the Young's modulus of an uncemented dry sand. A new laboratory device was built which uses dynamic wave propagation to determine independently the constrained (M), Young's (E), and shear (G) moduli by measuring the dilatational, bar and shear wave velocities, respectively. The device, called the Multi-Moduli Testing Device (MTD), can vary the principal stress, in compression or extension, that is parallel to the longitudinal axis of a cylindrical soil specimen, creating a state of stress in the specimen where  $\bar{\sigma}_1 > \bar{\sigma}_2 = \bar{\sigma}_3$  or  $\bar{\sigma}_1 = \bar{\sigma}_2 > \bar{\sigma}_3$ .

The dilatational and shear wave velocities are determined using pulse test methods. The bar wave velocity is determined using a longitudinal resonant test method in which the first four natural frequencies of the specimen are determined. The bar wave velocity is computed from the natural frequencies using a two-step reduction

process that begins by computing the phase velocity assuming one-dimensional motion. The second step utilizes the three-dimensional solution for longitudinal wave propagation in an infinite rod to adjust the phase velocities. The resulting values for the bar wave velocity are typically within five percent of each other.

Tests were conducted on a dry, uncemented sand subjected to isotropic and biaxial stress conditions. The tests showed that when confined isotropically, all three moduli (M, E and G) could be adequately described by a relationship involving a constant times the mean effective stress raised to a power ranging from 0.45 to 0.51. However, when the sand was subjected to biaxial compression or extension, it was shown that the principal effective stresses influenced each modulus differently. For the constrained modulus, the tests reaffirmed earlier studies which have shown that the principal stress in the direction of wave propagation almost solely controls the modulus. This study has shown the new result that Young's modulus is also dominated by the principal stress in the direction of wave propagation. However, the principal stresses perpendicular to the direction of wave propagation have more influence on Young's modulus than the constrained modulus. (408 pages)

<b>Accession For</b>	
NTIS GRA&I	<input checked="" type="checkbox"/>
DTIC TAB	<input type="checkbox"/>
Unannounced	<input type="checkbox"/>
Justification	
By _____	
Distribution/	
<b>Availability Codes</b>	
Avail and/or	
Special	
A-1	

## **Acknowledgements**

I would like thank my supervising professor, Kenneth H. Stokoe, II, for his guidance, support and confidence throughout the course of this study. His unbounded enthusiasm, and passion for understanding the complexities of the subject of my work, has served as an inspiration during this endeavor.

Thanks are also extended to the remaining members of my committee, Professors José M. Roesset, Stephen G. Wright, Priscilla P. Nelson, and Marc A. Bedford. Particular thanks go to Professors Roesset and Bedford. Professor Roesset's contribution to the finite element modelling was essential to making it such a useful tool for this, and future, research. Professor Bedford was equally instrumental in my understanding the conceptual and theoretical nuances of the wave propagation theory upon which this research is based. Finally, I would like to recognize the other Geotechnical Engineering faculty, Professors Daniel, Olson and Reese, for their contribution and effort to widen my knowledge.

I would like to recognize the contribution made by the administrative and technical support staff of the Department of Civil Engineering to the effort I have just completed. Most notable among these individuals is James Stewart, who was responsible for constructing the test device used in this research and contributed greatly to my practical knowledge. I would also like to express my appreciation to

Teresa Tice-Boggs and Linda Iverson, whose never ending support and good cheer made even the most difficult task seem easy.

I would like to express my thanks to my fellow graduate students at the University of Texas at Austin for their support, education and friendship. I would like to particularly recognize Jerry Eykholt, James Bay, Dong-Soo Kim, Ron Andrus, Marwan Aouad, Mohammed Kayal and James Lee.

I would like to express my appreciation to the U.S. Air Force and the Air Force Institute of Technology whose sponsorship made it possible for me to complete this course of study.

Finally, and most of all, I would like to thank my wife Teresa and my family for their love, patience, help, and support.

## ABSTRACT

### A LABORATORY STUDY OF THE EFFECT OF STRESS STATE ON THE ELASTIC MODULI OF SAND

Publication No. \_\_\_\_\_

Martin David Lewis, Ph.D.  
The University of Texas at Austin, 1990

Supervisor: Kenneth H. Stokoe, II

A study was conducted to determine the effect of stress state on the Young's modulus of an uncemented dry sand. A new laboratory device was built which uses dynamic wave propagation to determine independently the constrained (M), Young's (E), and shear (G) moduli by measuring the dilatational, bar and shear wave velocities, respectively. The device, called the Multi-Moduli Testing Device (MTD), can vary the principal stress, in compression or extension, that is parallel to the longitudinal axis of a cylindrical soil specimen, creating a state of stress in the specimen where  $\bar{\sigma}_1 > \bar{\sigma}_2 = \bar{\sigma}_3$  or  $\bar{\sigma}_1 = \bar{\sigma}_2 > \bar{\sigma}_3$ .

The dilatational and shear wave velocities are determined using pulse test methods. The bar wave velocity is determined using a

longitudinal resonant test method in which the first four natural frequencies of the specimen are determined. The bar wave velocity is computed from the natural frequencies using a two-step reduction process that begins by computing the phase velocity assuming one-dimensional motion. The second step utilizes the three-dimensional solution for longitudinal wave propagation in an infinite rod to adjust the phase velocities. The resulting values for the bar wave velocity are typically within five percent of each other.

Tests were conducted on a dry, uncemented sand subjected to isotropic and biaxial stress conditions. The tests showed that when confined isotropically, all three moduli (M, E and G) could be adequately described by a relationship involving a constant times the mean effective stress raised to a power ranging from 0.45 to 0.51. However, when the sand was subjected to biaxial compression or extension, it was shown that the principal effective stresses influenced each modulus differently. For the constrained modulus, the tests reaffirmed earlier studies which have shown that the principal stress in the direction of wave propagation almost solely controls the modulus. This study has shown the new result that Young's modulus is also dominated by the principal stress in the direction of wave propagation. However, the principal stresses perpendicular to the direction of wave propagation have more influence on Young's modulus than the constrained modulus.

## TABLE OF CONTENTS

Acknowledgements.....	v
Abstract.....	vii
Table of Contents.....	ix
List of Figures.....	xvi
List of Tables.....	xxii
Chapter One - Introduction.....	1
1.1 Background.....	1
1.2 Goal and Objectives.....	5
1.3 Organization.....	7
Chapter Two - Laboratory Testing Devices to Evaluate Dynamic Moduli of Soils.....	11
2.1 Introduction.....	11
2.2 Resonant Testing Devices.....	12
2.3 Pulse Test Devices.....	18
2.4 Other Developments in Dynamic Laboratory Testing.....	21
2.5 Dynamic Properties of Soils Under Different States of Stress.....	23
2.6 Summary.....	35
Chapter Three - Theoretical Background.....	37
3.1 Introduction.....	37
3.2 One-Dimensional Wave Propagation in an Elastic Material.....	38
3.3 One-Dimensional Wave Propagation in a Rod Subjected to a Steady-State End Condition and with an Added Mass.....	44
3.4 Frequency Spectrum of a Solid Cylindrical Rod of Infinite Length.....	52
3.4.1 Torsional Waves in a Solid Cylindrical Rod.....	53
3.4.2 Longitudinal Waves in a Solid Cylindrical Rod.....	57

3.5	Transient Wave Propagation in a Semi-Infinite Solid Cylindrical Rod.....	66
3.6	Summary.....	71
<b>Chapter Four - Modelling a Finite Rod Using Axisymmetric Finite</b>		
	<b>Elements.....</b>	<b>73</b>
4.1	Introduction .....	73
4.2	Development of the Finite Element Program.....	74
	4.2.1 Developing the Axisymmetric Finite Element.....	74
	4.2.2 Constructing the Specimen Stiffness Matrix.....	79
	4.2.3 Specified Boundary and End Conditions.....	83
	4.2.4 Program Input/Output.....	85
4.3	Frequency Responses of Three Model Soils.....	89
	4.3.1 Effect of Stiffness on the Transfer Function of Three Model Soils .....	94
	4.3.2 Effect of Damping Ratio on the Transfer Function of a Loose Sand.....	95
	4.3.3 Effect of Length and Diameter on the Transfer Function of a Loose Sand.....	98
	4.3.4 Effect of Poisson's Ratio on the Transfer Function of a Dense Sand .....	101
4.4	The Effect of End Conditions on the Transfer Function of a Dense Sand .....	105
	4.4.1 Effect of a Rigid Top Mass on the Transfer Function of a Dense Sand .....	106
	4.4.2 Effect of Base Support on the Transfer Function of a Dense Sand .....	109
	4.4.3 Effect of Horizontal Fixity at the Specimen Ends on the Transfer Function of a Dense Sand.....	112
4.5	Summary.....	116

Chapter Five - Test Equipment.....	118
5.1 Introduction .....	118
5.2 The Multi-Moduli Testing Device (MTD).....	119
5.2.1 Specimen Confinement System.....	119
5.2.2 Dynamic Excitation System .....	125
5.2.3 Dynamic Monitoring System.....	129
5.3 Test Specimen Preparation and Set Up .....	136
5.3.1 Preparation of Synthetic Specimens .....	136
5.3.2 Preparation of Compacted Clay Specimens.....	137
5.3.3 Preparation of Uncemented Sand Specimens.....	137
5.4 Summary .....	140
Chapter Six - Measuring Constrained and Shear Moduli Using Pulse Tests.....	143
6.1 Introduction .....	143
6.2 Constrained Modulus from the Axial Pulse Test .....	144
6.2.1 Conducting the Axial Pulse Test.....	144
6.2.2 Justification for Identifying the First Arrival as the Compression Wave Arrival.....	149
6.2.3 Impact of Input Frequency on the Measured Compression Wave Arrival. ....	150
6.2.4 Assumption of Small Strains in the Axial Pulse Test.....	153
6.2.5 Measurement Errors for the Axial Pulse Test and Their Influence on the Constrained Modulus.....	155
6.2.5.1 Errors in Specimen Dimension and Weight.....	155
6.2.5.2 Determining the Error in the Constrained Modulus.....	158
6.3 Determining the Shear Modulus Using an Independent Shear Pulse Test .....	159

6.3.1	Conducting the Shear Pulse Test.....	159
6.3.2	Identifying the Shear Wave Arrival.....	164
6.3.3	Assumption of Small Strains in the Shear Pulse Test.....	166
6.3.4	Determining the Error in the Shear Modulus.....	168
6.4	Summary.....	170
Chapter Seven - Young's Modulus from Longitudinal Resonant Column Testing.....		
7.1	Introduction .....	172
7.2	Determining Young's Modulus of Soil Specimens.....	173
7.2.1	Conducting the Longitudinal Resonant Column Test.....	173
7.2.2	Determining Young's Modulus from Longitudinal Resonant Frequencies.....	179
7.2.3	Computing Poisson's Ratio and the Shear Modulus.....	184
7.2.4	The Assumption of Small Strains in the Longitudinal Resonant Column Test.....	188
7.2.5	Measurement Errors in the Longitudinal Resonant Column Test and Their Influence on the Calculation of Young's Modulus .....	190
7.3	Comparing the Frequency Response Measured in the Laboratory to that Calculated by the Finite Element Model .....	192
7.4	Summary.....	196
Chapter Eight - Test Materials.....		
8.1	Introduction .....	198
8.2.	Synthetic Calibration Specimens.....	199
8.2.1	Polyurethane Specimens.....	199
8.2.2	Polyvinylchloride (PVC) Specimens.....	203

8.2.3	Ultra-High Molecular Weight (UHMW) Polyethylene Specimens .....	206
8.2.4	Portland Cement Concrete (PCC) .....	208
8.3	Soil Specimens .....	211
8.3.1	Compacted Clay .....	211
8.3.2	Washed Mortar Sand .....	217
8.4	Summary .....	223
Chapter Nine	- Stiffness of Sand Under Isotropic Confinement .....	225
9.1	Introduction .....	225
9.2	Testing Sequence and Stress-State .....	226
9.3	Constrained Modulus of Sand Under Isotropic Confinement .....	230
9.4	Young's Modulus of a Sand Under Isotropic Confinement .....	234
9.5	Shear Modulus of a Sand Under Isotropic Confinement .....	239
9.6	The Validity of the Isotropic Linear Elastic Assumption .....	242
9.7	Comparison of Stiffness Equations with Previous Research on Washed Mortar Sand .....	248
9.8	Summary .....	256
Chapter Ten	- Stiffness of Sand Under Biaxial Loading .....	259
10.1	Introduction .....	259
10.2	Biaxial Testing Sequence and Stress State .....	261
10.3	The Constrained Modulus Under a Biaxial State of Stress .....	267
10.4	The Young's Modulus under a Biaxial State of Stress .....	272
10.5	The Shear Modulus Under a Biaxial State of Stress .....	275
10.6	Comparison of Relationships for Sand Under Biaxial States of Stress with Previous Research .....	279

10.7	Summary.....	282
Chapter Eleven - Summary, Conclusions and Recommendations.....		286
11.1	Summary.....	286
11.1.1	Background.....	286
11.1.2	Theoretical and Analytical Studies.....	288
11.1.3	Multi-Moduli Testing Device (MTD).....	290
11.1.4	Tests on Sand and Other Materials.....	293
11.1.5	Effect of Stress State on Elastic Moduli of Sand.....	295
11.2	Conclusions.....	299
11.3	Recommendations for Future Research.....	303
Appendix A - Theoretical Solution of Elasticity for an Isotropic Material.....		307
A.1	Elastic Solution for Isotropic Materials.....	308
A.2	Elastic Solution in Cylindrical Coordinates.....	312
Appendix B - Theoretical Solution for Waves Propagating in a Cylindrical Elastic Rod.....		315
B.1	Equations of Motion for a Linearly Elastic Body.....	316
B.2	The Equations of Motion Expressed in Displacement Potentials.....	318
B.3	The Problem Statement for Waves in a Rod of Circular Cross Section.....	320
B.4	General Solution for Time-Harmonic Motion in a Long Cylindrical Rod with Solid Cross Section.....	323
Appendix C - Theoretical Solution for a Transient Wave Propagating in a Semi-infinite Solid Cylindrical Rod.....		327
Appendix D - Developing an Axisymmetric Finite Element.....		342

Appendix E - Equipment Used in the Multi-Moduli Testing Device.....	352
Appendix F - Sample Preparation and Test Procedures for the Multi-Moduli Testing Device (MTD).....	356
F.1 Preparation of a Sand Sample .....	357
F.2 Assembling the MTD and Preparing a Sample for Testing .....	361
F.3 Beginning a Test Series in the MTD and Conducting Tests at a Single Stress State .....	364
F.3.1 Conducting the Axial Pulse Test.....	364
F.3.2 Conducting the Shear Pulse Test.....	366
F.3.3 Conducting the Longitudinal Resonant Column (LRC) Test.....	367
F.4 Completing Tests at a Single Stress-State.....	368
F.5 Reducing the Lab Data.....	368
F.6 Dismantling the MTD.....	369
Appendix G - Test Data.....	384
References.....	397

## LIST OF FIGURES

Fig. 2.1.	Schematic of Early Resonant Column. (From Drnevich et al, 1978) .....	14
Fig. 2.2.	Cross-sectional View of Anisotropically Loaded Specimens in Torsional Resonant Column Apparatus. (From Ni, 1987) .....	17
Fig. 2.3.	Cut-Away Isometric View of Large-Scale Triaxial Device (LSTD). (From Lee and Stokoe, 1986) .....	20
Fig. 3.1.	Cylindrical Coordinates for Finite Rod.....	39
Fig. 3.2.	Idealized Model for One-Dimensional Wave Motion in a Finite Rod.....	45
Fig. 3.3.	Graphical Solution of $\beta \tan \beta = \frac{M}{m}$ .....	50
Fig. 3.4.	Distribution of Axial Displacements for the First Three Modal Shapes of a Fixed-Free Rod. (From Richart et al, 1970).....	51
Fig. 3.5.	Frequency Spectrum for Torsional Waves in a Cylindrical Rod.....	56
Fig. 3.6.	Frequency Spectrum for Longitudinal Waves in a Cylindrical Rod as a Function of Dimensionless Wave Number.....	62
Fig. 3.7.	Frequency Spectrum for Longitudinal Waves in a Cylindrical Rod as a Function of Frequency.....	64
Fig. 3.8.	Problem Statement for Transient Wave Propagation in a Semi-Infinite Cylindrical Rod.....	67
Fig. 3.9.	Particle Velocity in the Vicinity of the Elementary Wave front Travelling in a Semi-Infinite Rod Due to a Sudden Impact at the End. ....	70
Fig. 4.1.	Axisymmetric Finite Element in Global Cylindrical Coordinates. ....	76
Fig. 4.2.	Finite Element Model Construction. ....	80

Fig. 4.3.	Element and Node Arrangement in a Single Layer of the Finite Element Model.....	81
Fig. 4.4.	Boundary Conditions for Finite Element Model.....	84
Fig. 4.5.	Transfer Function of Model Clay Specimen.....	91
Fig. 4.6.	Transfer Function of Model Loose Sand Specimen.....	92
Fig. 4.7.	Transfer Function of Model Dense Sand Specimen.....	93
Fig. 4.8.	Transfer Functions for Model Dense Sand and Two Model Clays.....	96
Fig. 4.9.	Effect of Damping on the Transfer Function of Model Loose Sand.....	97
Fig. 4.10.	Response Curves for a Visously Damped Single-Degree-of-Freedom System. (From Richart et al, 1970).....	99
Fig. 4.11.	Effect of Specimen Length (L) on the Transfer Function of a Model Loose Sand.....	100
Fig. 4.12.	Effect of Specimen Diameter (2a) on the Transfer Function of a Model Loose Sand.....	102
Fig. 4.13.	Effect of Poisson's Ratio on the Transfer Function of a Model Dense Sand.....	103
Fig. 4.14.	Effect of Added Mass on the Transfer Function of a Model Dense Sand.....	107
Fig. 4.15.	Effect of Base Ratio on the Transfer Function of a Model Dense Sand.....	110
Fig. 4.16.	Effect of Horizontal Fixity at the Base on the Transfer Function of a Model Dense Sand Specimen.....	113
Fig. 4.17.	Effect of Horizontal Fixity of the Base and Top on the Transfer Function of a Model Dense Sand Specimen.....	114
Fig. 5.1.	Schematic Diagram of Multi-Moduli Test Device.....	120
Fig. 5.2.	Multi-Moduli Test Device (MTD) with Outer Cell and Sensor Cables Removed.....	121

Fig. 5.3.	Schematic Diagram of Specimen Confinement System in the MTD. ....	122
Fig. 5.4.	Schematic Diagram of Axial Loading and Longitudinal Vibration Isolation Assembly. ....	124
Fig. 5.5.	Schematic Diagram of Piezoelectric Shaker System in the MTD. ....	126
Fig. 5.6.	Schematic Diagram of Piezoelectric Shaker Mounted Beneath Test Cell of MTD. ....	127
Fig. 5.7.	Schematic Diagram of Shear Wave Generator in the MTD. ....	128
Fig. 5.8.	Connection Diagrams for Piezoelectric Accelerometers Used in the MTD. ....	132
Fig. 5.9.	Diagram of Monitoring Equipment Used for Pulse Tests in the MTD. ....	133
Fig. 5.10.	Diagram of Monitoring Equipment Used for Longitudinal Resonant Column Test in the MTD. ....	135
Fig. 6.1.	Arrangement of MTD for Conducting Axial Pulse Test. ....	145
Fig. 6.2.	Digital Oscilloscope Record of Axial Pulse Test on Loose Sand at 16 psi Confining Pressure (128 Averages). ....	147
Fig. 6.3.	Determining the P-wave Arrival From an Amplified Time Record on the Digital Recording Oscilloscope. ....	148
Fig. 6.4.	Particle Velocity in the Vicinity of the Elementary Wave Front as a Function of Time from Three-Dimensional Theory for Transient Motion in a Rod. ....	151
Fig. 6.5.	Arrangement of MTD for Conducting Shear Pulse Test. ....	160
Fig. 6.6.	Digital Oscilloscope Record of Shear Pulse Test on Loose Sand at 16 psi Confining Pressure (64 Averages). ....	162

Fig. 6.7.	Relative Output for Accelerometer Used in the Shear Pulse Test.....	165
Fig. 6.8.	Determining the Shear Wave Arrival From an Amplified Time Record on the Digital Recording Oscilloscope. ....	167
Fig. 7.1.	Arrangement of MTD for Conducting Longitudinal Resonant Column Test. ....	174
Fig. 7.2.	Dynamic Signal Analyzer Record for Longitudinal Resonant Column Test on a Loose Sand Under 16 psi Confining Pressure (ISO2T7 test).....	178
Fig. 7.3.	Dimensionless Velocity Ratio as a Function of the Dimensionless Wavelength For Various Poisson's Ratios (Fundamental Mode Only).....	183
Fig. 7.4.	Individual Test Printout for ISO2T7 Test on a Loose Sand Under 16 psi Confining Pressure. ....	187
Fig. 7.5.	Transfer Function for Loose Sand Computed Using Finite Element Model and Stiffness Parameters Determined in the Laboratory in the ISO2T7 Test.....	193
Fig. 8.1.	Variations in Young's Modulus with Loading Frequency By Torsional Shear (0.0007%) and Longitudinal Resonant Column Tests at Zero Confining Pressure and Room Temperature (73°F). ....	201
Fig. 8.2.	Dynamic Signal Analyzer Record for Longitudinal Resonant Column Test on a Long PVC Specimen.....	204
Fig. 8.3.	Constrained, Young's and Backcalculated Shear Modulus of PCC as a Function of Curing Time.....	209
Fig. 8.4.	Poisson's Ratio of PCC as a Function of Curing Time (as determined from M and E) .....	210
Fig. 8.5.	Dynamic Signal Analyzer Record for Compacted Clay Specimen #3 at 6.0 psi Confining Pressure at Five Days Following Compaction.....	213

Fig. 8.6.	Comparison of Young's Moduli for Compacted Clay Sample #3 ( $w_c = 39\%$ ) Determined by Cyclic Triaxial, Torsional Shear, and Torsional Resonant Column Tests at Six Days, at 6.0 psi Confining Pressure, and Normalized at 10 Hz. (After Pezo et al, 1990) .....	216
Fig. 8.7.	Average Grain Size Distribution Analyses of Washed Mortar Sand. (From Rix, 1984) .....	219
Fig. 8.8.	Shear Modulus of Dense and Loose Washed Mortar Sand as a Function of Shear Strain Amplitude and Confining Pressure as Determined by Torsional Shear and Torsional Resonant Column Tests. ....	221
Fig. 8.9.	Young's Modulus of Dense and Loose Washed Mortar Sand as a Function of Axial Strain Amplitude and Confining Pressure as Determined by Torsional Shear and Torsional Resonant Column Tests. ....	222
Fig. 9.1.	Assumed Isotropic Stress-State for Tests on Sand Specimens.....	227
Fig. 9.2.	Variation of Constrained Modulus with Mean Effective Stress for ISO1 and ISO2 Test Series on Sand. ....	231
Fig. 9.3.	Variation of Young's Modulus with Mean Effective Stress for ISO1 and ISO2 Test Series on Sand. ....	236
Fig. 9.4.	Variation of Measured Shear Modulus ( $G_m$ ) with Mean Effective Stress for ISO1 and ISO2 Test Series on Sand.....	240
Fig. 9.5.	Variation of Backcalculated Shear Modulus ( $G_b$ ) with Mean Effective Stress for ISO1 and ISO2 Test Series on Sand.....	243
Fig. 9.6.	Comparison of Backcalculated ( $G_b$ ) and Measured ( $G_m$ ) Shear Moduli for ISO1 Test Series on Dense Sand.....	245

Fig. 9.7.	Comparison of Backcalculated ( $G_b$ ) and Measured ( $G_m$ ) Shear Moduli for ISO2 Test Series on Loose Sand.....	246
Fig. 9.8.	Variation of Poisson's Ratio with Mean Effective Stress for ISO1 and ISO2 Test Series on Sand (3rd mode only).....	249
Fig. 9.9.	Comparison of Constrained and Young's (3rd mode) Moduli for ISO2 Test Series on Loose Sand.....	250
Fig. 9.10.	Comparison of Shear Modulus - Mean Effective Stress Relationships from Research Studies on Washed Mortar Sand.....	255
Fig. 10.1.	Directions of Wave Propagation and Particle Motion Assumed for Biaxial Testing with MTD.....	260
Fig. 10.2.	Loading Sequence for BIAx2 and BIAx3 Test Series.....	264
Fig. 10.3.	Loading Sequence for BIAx4 and BIAx5 Test Series on Sand.....	266
Fig. 10.4.	Variation of Constrained Modulus with Mean, Axial and Horizontal Effective Stress for BIAx4 Test Series on Dense Sand.....	268
Fig. 10.5.	Variation of Young's Modulus with Mean, Axial and Horizontal Effective Stress for BIAx4 Test Series on Dense Sand.....	273
Fig. 10.6.	Variation of Measured Shear Modulus with Mean, Axial and Horizontal Effective Stress for BIAx4 Test Series on Dense Sand.....	276

## LIST OF TABLES

Table 2.1.	Summary of Stiffness Coefficients for Shear Modulus Obtained from Various Research Studies. (From Ni, 1987).....	31
Table 2.2.	Summary of Values of the Slope of the Log M - Log $\bar{\sigma}_0$ Relationship* for Dry Sand under Isotropic Confinement. (After Lee and Stokoe, 1986) .....	32
Table 2.3.	Summary of Stiffness Coefficients for Log E - Log $\bar{\sigma}_0$ Relationship* for Soils under Isotropic Confinement from Past Research Studies. ....	34
Table 3.1.	Commonly Used Relationships Between $\mu$ elastic Constants. ....	43
Table 4.1.	Input Variables for Finite Element Model. ....	86
Table 4.2.	Typical Characteristics of Three Model Soils. ....	90
Table 4.3.	Effect of Poisson's Ratio on the Response of a Model Dense Sand* .....	104
Table 4.4.	Effect of Added Mass on the Response of a Model Dense Sand* .....	108
Table 4.5.	Effect of Base Ratio on the Response of a Model Dense Sand* .....	111
Table 4.6.	Effect of Horizontal Fixity on the Response of a Model Dense Sand.....	115
Table 5.1.	Accelerometer Characteristics. ....	130
Table 6.1.	Propagation of Errors in the Axial Pulse Test for a Loose Sand at $\bar{\sigma}_0 = 16.0$ psi (ISO2T7 Test).....	156
Table 6.2.	Propagation of Errors in the Shear Pulse Test for a Loose Sand at $\bar{\sigma}_0 = 16.0$ psi (ISO2T7 Test).....	169
Table 7.1.	Typical Settings for Dynamic Signal Analyzer for Longitudinal Resonant Column Test on Sand.....	175

Table 7.2.	Example of Data Reduction Steps for Longitudinal Resonant Column Test Using Data from ISO2T7 Test on a Loose Sand Confined Isotropically at 16 psi.....	181
Table 7.3.	Summary of Maximum Strains for Example Longitudinal Resonant Column Test.....	189
Table 7.4.	Propagation of Errors in the Longitudinal Resonant Column Test (Values from 1st Mode of ISO2T7 Test).....	191
Table 7.5.	Comparison of Model Bar Velocities to Measured Bar Velocities for Loose Sand (ISO2T7) .....	194
Table 8.1.	Summary of Moduli from Tests on Polyurethanes.....	202
Table 8.2.	Summary of Moduli from Tests on Polyvinylchloride (PVC).....	205
Table 8.3.	Summary of Moduli from Tests on Ultra-High Molecular Weight (UHMW) Polyethylene.....	207
Table 8.4.	Summary of Moduli from Tests on Compacted Clay Specimens.....	214
Table 8.5.	Summary of Soil Characteristics and Properties of Washed Mortar Sand.(From Rix, 1984).....	220
Table 9.1.	Summary of Loading Sequence for Dense Sand Specimen (ISO1 Test Series).....	228
Table 9.2.	Summary of Loading Sequence for Loose Sand Specimen (ISO2 Test Series).....	229
Table 9.3.	Comparison of Stiffness Coefficients for Log M - Log $\bar{\sigma}_o$ Relationship* for Isotropic Confinement.....	233
Table 9.4.	Comparison of Stiffness Coefficients for Log M - Log $\bar{\sigma}_a$ Relationship* for Isotropic Confinement.....	235
Table 9.5.	Comparison of Stiffness Coefficients for Log E - Log $\bar{\sigma}_o$ Relationship* for Isotropic Confinement.....	238

Table 9.6	Comparison of Stiffness Coefficients for Log $G_m$ - Log $\bar{\sigma}_0$ Relationship* Measured by Shear Pulse Test for Isotropic Confinement .....	241
Table 9.7.	Comparison of Stiffness Coefficients for Log $G_b$ - Log $\bar{\sigma}_0$ Relationship* (Backcalculated From the Constrained and Young's Moduli) for Isotropic Confinement .....	244
Table 9.8.	Comparison of Stiffness Coefficients for Log $M$ - Log $\bar{\sigma}_0$ Relationship* from Various Research Studies Using Washed Mortar Sand .....	252
Table 9.9.	Comparison of Stiffness Coefficients for Log $E$ - Log $\bar{\sigma}_0$ Relationship* for Soils under Isotropic Confinement from Various Research Studies.....	253
Table 9.10.	Comparison of Stiffness Coefficients for Log $G$ - Log $\bar{\sigma}_0$ Relationship* from Various Research Studies Using Washed Mortar Sand .....	254
Table 10.1.	Summary of Loading Sequence for Loose Sand Specimen. (BIAX2 Test Series) .....	262
Table 10.2.	Summary of Void Ratios and Densities for Test Series on Sand.....	263
Table 10.3.	Stiffness Coefficients for Log $M$ - Log $\bar{\sigma}_a$ Relationship* for Sand Under Biaxial Loading.....	269
Table 10.4.	Stiffness Coefficients for Constrained Modulus ( $M$ ) of Sand Under Biaxial Loading Using a Two-Stress Model*.....	271
Table 10.5.	Stiffness Coefficients for Young's Modulus of Sand Under Biaxial Loading Using a Two-Stress Model* .....	274

Table 10.6.	Stiffness Coefficients for Independently Measured Shear Modulus of Sand Under Biaxial Loading Using a Two-Stress Model* .....	277
Table 10.7.	Stiffness Coefficients for Backcalculated* Shear Modulus of Sand Under Biaxial Loading Using a Two-Stress Model** .....	278
Table 10.8.	Summary of Stiffness Coefficients for Tests on Washed Mortar Sand Under Biaxial Loading Using a Two-Stress Model** .....	280
Table 10.9.	Comparison of Stiffness Coefficients for Log G - Log $\bar{\sigma}_a$ - Log $\bar{\sigma}_b$ - Log $\bar{\sigma}_c$ Relationship* from Various Research Studies Using Washed Mortar Sand.....	281
Table 11.1.	Summary of Stiffness Coefficients for Tests on Washed Mortar Sand.....	298
Table F.1.	Typical Settings for the Function Generator to Conduct an Axial Pulse Test on Sand.....	365
Table F.2.	Typical Settings for the Function Generator to Conduct a Shear Pulse Test on Sand.....	367

## Chapter One

### Introduction

#### 1.1 Background

Research into the dynamic properties of soils over the past three decades has focused on finding constitutive relationships which best characterize soils subjected to a broad range of strains. It is understood that a soil, either in situ or in the laboratory, exhibits a constitutive relationship more complex than that described by simple linear elasticity. However, research has shown that at shear strains less than 0.001%, most soils behave as a linear elastic continuum. The bulk of this research has been conducted in devices where only an isotropic state of stress could be applied to the soil. Consequently, it was generally believed that the first stress invariant, the mean effective stress [ $\bar{\sigma}_0 = 1/3 (\bar{\sigma}_1 + \bar{\sigma}_2 + \bar{\sigma}_3)$ ], controlled all moduli (Young's, shear, constrained, and bulk) in the same manner. Research during the past decade has shown this was not completely true, at least for shear and constrained moduli.

A fundamental understanding of the relationships between the measured dilatational ( $V_p$ ), shear ( $V_s$ ) and rod ( $V_c$ ) wave velocities, the elastic moduli and the stress conditions under which the velocities are measured is essential to the successful application of seismic testing in the laboratory and the field. As it is commonly believed that a cross-

anisotropic model is conceptually a better representation of natural soil, it is imperative to understand how different states of stress affect the moduli commonly used to characterize soil stiffness. With this knowledge it may be possible to continue to extend the use of seismic testing to include applications such as relating stiffness properties between field and laboratory specimens and the characterization of in situ stress states.

As an additional note, an elastic continuum assumption implies that the soil moduli should be unaffected by the frequency at which a dynamic test is conducted. This was probably a fair assumption when one considers the frequency range over which most dynamic laboratory tests have been conducted (1-300Hz). However, the use of devices such as piezoelectric crystals introduces test methods which are conducted at frequencies at least one order of magnitude greater than used in the past. Many civil engineering materials exhibit different stiffness properties at higher frequencies.

All dynamic laboratory test devices which use methods based on wave propagation theory can be divided into two principal types: resonant devices and pulse devices. Resonant devices measure soil stiffness by first determining a resonant frequency of the soil specimen. One example is the torsional resonant column with which the shear wave velocity, and thus, the shear modulus, is determined by measuring the first-mode resonant frequency in torsion. A second example is the longitudinal resonant column, with which the bar wave velocity is determined by measuring the first-mode resonant frequency in the

longitudinal direction. Although several laboratory devices exist that were designed to resonate both torsionally and longitudinally, the most commonly used devices determine only one soil stiffness.

The second group of dynamic testing devices incorporates pulse methods to measure direct travel times of polarized waves. With the appropriate combination of sources and receivers, it is possible to measure the velocities for dilatational and shear waves, and consequently the constrained and shear moduli can be determined. Most devices in the past have used mechanical or electromagnetic types of vibration sources. However, with the advent of piezoelectric crystal technology, sources capable of operating reliably at higher frequencies are available for use in laboratory and field testing.

Any of these devices, in their simplest form, can measure soil stiffness under isotropic conditions and most torsional resonant column testing is conducted under isotropic states of stress. A limited number of studies have been conducted using the torsional resonant column device where an axial compression load was applied (biaxial compression), and resonant tests on hollow samples has permitted testing under limited triaxial conditions. But the torsional resonant column can only study the anisotropic behavior of the shear modulus. It cannot be used to study the constrained or Young's moduli. Modifications to the longitudinal resonant column to allow study of anisotropic states of stress are inherently more difficult because the device must load the test specimen axially yet still permit it to resonate dynamically. For this reason,

research under true triaxial states of stress have commonly used cubic devices with pulse testing.

Dynamic laboratory testing using pulse methods has been conducted in both small- (4 in) and large- (7 ft) scale cubic laboratory devices which had the ability to vary the stress in all three orthogonal directions. The ability of these test devices to vary the state of stress in the test sample has led to the discovery during the past decade that the mean effective stress does not uniquely control a soil's stiffness. Rather, it has been shown that, for waves polarized along principal stress directions, the dynamic stiffness of a soil skeleton is controlled by the state of stress in the line (dilatational wave), or plane (shear wave), containing the propagating wave and particle motion and was virtually independent of the stress(es) in the other direction(s). However, cubic triaxial testing devices using pulse test methods only measure body wave velocities and cannot measure the bar wave velocity.

In brief summary, the state of the art in laboratory resonant devices typically results in the measurement of shear modulus or Young's modulus under isotropic loading. The torsional resonant column has been modified to conduct tests under biaxial compression or triaxial states of stress but is not commonly used in this manner. State-of-the-art pulse devices can measure either the shear or constrained modulus under isotropic, biaxial and triaxial states of stress. In the writer's knowledge, no device has been developed which would allow the study of the effect of state of stress on the Young's modulus of a soil.

## 1.2 Goal and Objectives

The primary goal of this research was to study the effect of state of stress on Young's modulus of the soil skeleton. To accomplish this goal it was necessary to design and construct a laboratory test device which could measure the bar wave and dilatational wave velocities of a dry cohesionless soil under different states of stress. An additional objective was to measure the shear wave velocity on the same specimen. Therefore, the main goal was broken into several objectives which are enumerated briefly in the following list.

(1) Review recent literature for research on testing of soils under different states of stress, particularly looking for research concerning Young's and constrained moduli in the linear elastic range.

(2) Design a testing device with which small-strain Young's, constrained and shear moduli could be independently determined on the same sand specimen without changing the state of stress. With the testing device one should be able to:

(a) apply, at a minimum, a biaxial state of stress by changing the stress in one direction, both in compression and extension;

(b) determine the state of stress in the specimen and the changes in the shape of the specimen resulting from changes in stress;

(c) excite dynamically the specimen in the small-strain (<0.001%) range and measure its response; and

(d) record and store digitally the dynamic response of the specimen for future analysis.

(3) Develop a method using the device designed in item 2 to determine Young's modulus and develop a data reduction technique that is founded in wave propagation theory.

(4) Study the impact of specimen parameters such as size, shape and stiffness on Young's modulus determined using the test apparatus and test method developed in items 2 and 3.

(5) Develop a method for constructing dry sand specimens which would yield structurally uniform and comparative sand samples.

The research program described in this dissertation explains how each of these five objectives was accomplished.

### 1.3 Organization

The research that is reported in this dissertation describes the theory, modelling, development and construction of a Multi-Moduli Testing Device (MTD). The MTD was designed to measure independently the dilatational, bar, and shear wave velocities from which the constrained, Young's, and shear moduli could be calculated.

A brief description of recent developments in dynamic laboratory testing is presented in Chapter Two. Basic concepts used in current practice are described, with specific emphasis placed on methods to determine constrained and Young's moduli.

The theoretical development used to analyze and reduce the data collected using the tests methods employed in the MTD are presented in Chapter Three and companion Appendices A, B and C. The reader is encouraged to examine the sections developing a specific case for one-dimensional wave propagation in a finite cylindrical rod, three-dimensional wave propagation in an infinite cylindrical rod, and transient motion in a semi-infinite rod resulting from a sudden impact on the end.

The development of a finite element program using axisymmetric, finite elements to model cylindrical test specimens in this study is described in Chapter Four and companion Appendix D. The program was used to model the three representative soil specimens tested in this study, a loose sand, a dense sand, and a moderately stiff clay. In the program the user has the flexibility to specify different specimen

parameters, such as length, diameter and stiffness, and the appropriate end conditions. The output from the program is a transfer function that relates the vertical and horizontal motion at nodes along the top of the specimen to a unit vertical displacement of the nodes at the bottom of the specimen. A qualitative study of the effect of the specimen stiffness, length, diameter, Poisson's ratio and end conditions on the transfer function is included in this chapter.

The design of the MTD and of each of its major systems is described in Chapter Five. The MTD is divided into three main systems which are; (1) Specimen Confinement, (2) Dynamic Excitation, and (3) Dynamic Monitoring. A detailed list of equipment for each system is included in Appendix E. The latter part of Chapter Five describes test specimen preparation and set up. A step by step description for the preparation of a cohesionless sand specimen using a multiple sieve pluviating device that was designed and built for this research is included in Appendix F.

The Axial Pulse and Shear Pulse test methods used to determine the dilatational and shear wave velocities and the respective constrained and shear moduli are described in Chapter Six. A description and justification of the fundamental assumptions in each pulse test is also included in this chapter, along with an assessment of the potential error in each of the computed moduli.

The Longitudinal Resonant Column test, which is used to determine the bar velocity of the test specimen, and thus Young's

modulus, is described in Chapter Seven. The theoretical developments described in Chapter Three are applied in this chapter to the data obtained from the longitudinal resonant column test to yield the bar wave velocity. An assessment of the assumptions made in reducing the data, and an estimate of the error in the computed values of Young's modulus, are also included.

The materials tested, and the results from those tests conducted during the development of the MTD, are described in Chapter Eight. These materials included man-made materials, such as polyurethane, polypropylene, polyvinylchloride and Portland cement concrete, as well as two natural materials, a compacted clay and the dry sand that was the focus of this study.

The two test series conducted on the dry sand confined isotropically at pressures ranging from 4 to 64 psi are described in Chapter Nine. The constrained, Young's, and shear modulus versus mean effective stress relationships are calculated and compared to previous research on the same sand.

Five test series in which the dry sand is subjected to varying biaxial states of stress are described in Chapter Ten. In these test series, both the axial and radial stresses are varied independently up to a maximum effective principal stress ratio of 2.0. The separate influence of each of the axial and radial effective stresses on the constrained, Young's, and shear moduli is presented and compared to results from earlier research on the same sand.

The dissertation is concluded in Chapter Eleven, in which a general summary, fundamental conclusions, and recommendations for further research are presented. This research raised many more interesting questions and identified more potential study areas than were possible to address within its original scope. This, in the writer's opinion, is as valuable a contribution to the profession as the development of the MTD and the understanding of how state of stress affects Young's modulus.

## **Chapter Two**

### **Laboratory Testing Devices to Evaluate Dynamic Moduli of Soils**

#### **2.1 Introduction**

The development of dynamic laboratory testing equipment for determining soil stiffness by measuring velocities of wave propagation has reached a plateau over the past decade. Lately, most advances have been confined to optimization and automation of existing test devices and methods that were initially developed two or more decades ago. There are two basic groups of dynamic laboratory test devices available to the geotechnical researcher, those which are based on resonant methods and those which are based on pulse methods.

This chapter describes the basic concepts associated with each group of dynamic laboratory test devices and briefly discusses their capability and limitations. The discussion will be limited to dynamic laboratory devices which typically test at strains of  $10^{-3}$  percent or less. This precludes discussion of cyclic triaxial and torsional shear testing, a common group of testing devices sometimes considered "dynamic". These devices, whether strain or stress controlled, generally work best when measuring soil stiffness at strains between  $10^{-1}$  and  $10^{-3}$  percent. Ni (1987) and Lee and Stokoe (1986) provide literature summaries of

resonant column testing for the shear moduli and pulse testing for the constrained and shear moduli, respectively. It is not the writer's intention to repeat their work, but to stress the strengths and weaknesses of the devices currently used in practice. Additional reviews of dynamic testing for the laboratory and the field are provided by McSkimin (1961), Richart (1975), and Woods (1978).

This chapter concludes with a brief summary of the relationship between the stress state and the dynamic moduli of soils, as it is currently understood by the soil dynamics community. This relationship is presented in light of the development in the laboratory equipment.

## 2.2 Resonant Testing Devices

The first major group of dynamic laboratory testing devices measure the resonant frequency of a specimen, from which the specimen stiffness is computed using one-dimensional wave propagation theory. These are commonly referred to as resonant column devices, and their first recorded use was by Japanese engineers (Iida, 1938 and Iida, 1940) when wave propagation in a sand column subjected to longitudinal and torsional motion was studied. Their device determined wave velocity from the resonant frequency and height of the sand column and had no provisions to confine the sand other than under its own weight.

The growth of the nuclear power industry in the 1960's revived interest in dynamic soil properties as they pertained to soil-structure

interaction and liquefaction problems. Consequently, the resonant column device reappeared as a tool to study dynamic soil properties. Shannon, et al (1959) and Wilson and Dietrich (1960) designed a new resonant column and data reduction scheme. In their device, the soil specimen was placed on a vibrating base which could be excited longitudinally or torsionally. Most importantly, an isotropic confining pressure could be applied to the specimen.

A schematic of Shannon and Wilson's device is included in Fig. 2.1. Drnevich et al, formalized the resonant column device and data reduction method in 1978. Their proposal was eventually designated a standard (D4015-87) by the American Society for Testing and Materials. Shannon and Wilson's device, also referred to by researchers as the "Drnevich" device, measures the resonant frequency of the soil-device system. The device response has to be determined separately in a calibration test and is then removed from the system response to obtain the soil response. Further, constraints have to be placed on the relative stiffness of the springs attached to the driving base in order to reduce the laboratory data using "free-free" or "fixed-free" one-dimensional wave propagation theory. The process of determining a soil stiffness was relatively complicated and required a computer program and/or the use of several tables.

In the 1960's and through the mid-1970's, researchers developed and used resonant column devices for numerous investigations. These

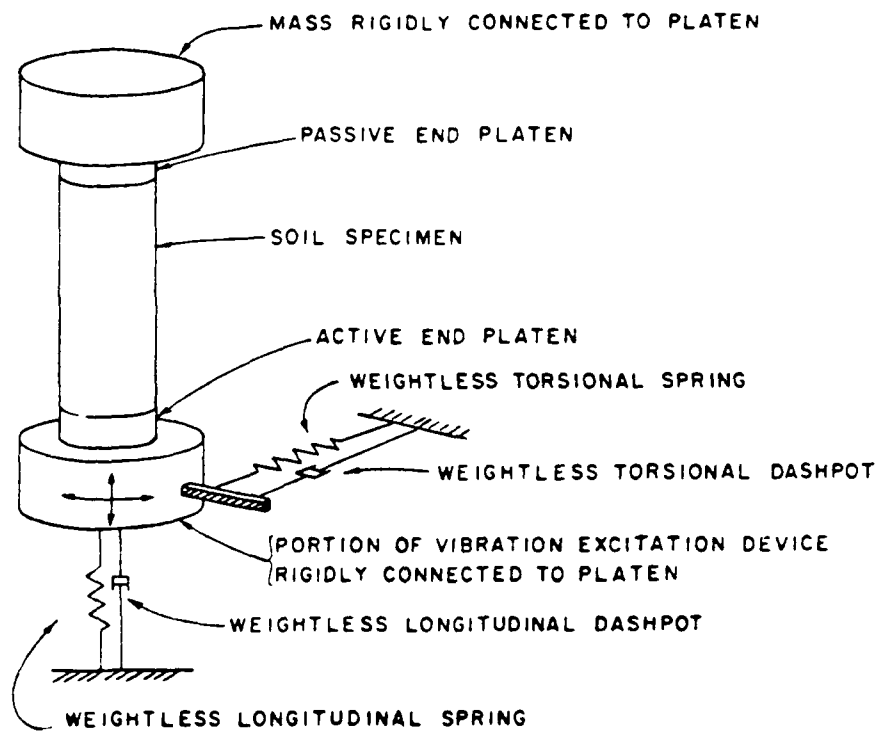


Fig. 2.1. Schematic of Early Resonant Column. (From Drnevich et al, 1978)

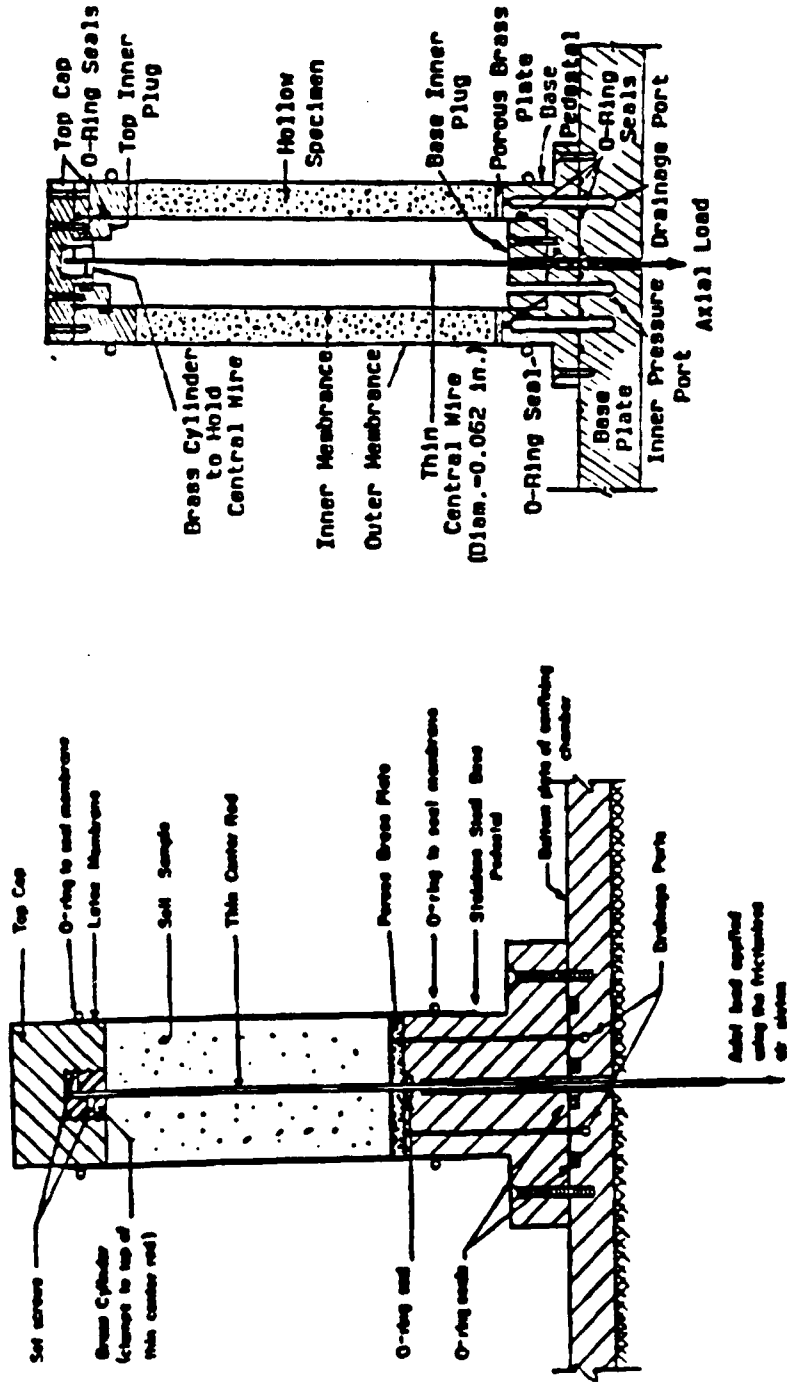
researchers included Hall and Richart (1963), Hardin (1965), Afifi and Richart (1973), and Anderson (1974). In the course of their developments, the driving mechanism was moved to the top of the specimen and the base was rigidly fixed, creating a "fixed-free" device that was easier to use and which had a simpler data reduction process. At the same time, the device became exclusively a torsional resonant column, with research concentrating on determining the factors affecting the shear modulus.

Early versions of the resonant column could only apply an isotropic confining stress. Hardin and Music (1965) modified their device so that it could apply a vertical stress (in addition to the hydrostatic confining stress) to the top of the specimen through a piston bearing directly on the vibration generator. Drnevich et al(1967) modified his device to test hollow cylindrical specimens in order to minimize the variation of shear strain across the specimens. Drnevich also increased the torque capacity of his device so that shearing strains above  $10^{-1}$  percent could be applied to the specimen.

In the late 1970's and early 1980's, a newer version of the torsional resonant column was developed at the University of Texas at Austin (Isenhowar, 1979, Canales, 1980). The driving mechanism was improved to simplify the test set up and to allow significant consolidation in the sample during the course of a test. The torsional resonant column device was further modified to accommodate solid or hollow specimens (Isenhowar, 1979). Allen and Stokoe (1982) modified the torsional

resonant column to apply an anisotropic loading to solid samples ( $\bar{\sigma}_1 > \bar{\sigma}_2 = \bar{\sigma}_3$ ) by pulling down on a thin wire that ran through the center of the specimen and was connected to the top cap. Stokoe and Ni (1985) further modified the apparatus to test hollow specimens, which allowed testing under true triaxial conditions. In 1987, Ni connected the resonant column testing devices at the University of Texas to a microcomputer and all aspects of the test and data reduction were fully automated. Figure 2.2 is a schematic of the anisotropic torsional resonant column device set up with a hollow specimen that was used by Ni (1987).

One of the important aspects of the development of resonant column devices is that the majority are now constructed to measure only one elastic moduli under one state of stress, specifically, the shear modulus under isotropic confining pressures. A second point is that only one-dimensional wave propagation theory is applied in the data reduction. It will be shown in Chapter 3 that this is appropriate for torsional resonant column testing because the fundamental mode in the three-dimensional problem is independent of frequency. However, that is not the case for longitudinal motion. It will be shown that the fundamental longitudinal mode is a function of frequency and one-dimensional approximations quickly become inadequate as the frequency increases. One final point, only torsional resonant column devices have been modified to allow testing under anisotropic states of



a. Solid Specimen (from Allen, 1982)

b. Hollow Specimen

Fig. 2.2. Cross-sectional View of Anisotropically Loaded Specimens in Torsional Resonant Column Apparatus. (From Ni, 1987)

stress, specifically biaxial compression ( $\bar{\sigma}_1 > \bar{\sigma}_2 = \bar{\sigma}_3$ ) and triaxial ( $\bar{\sigma}_1 > \bar{\sigma}_2 = \bar{\sigma}_3$ ) states of stress. To the knowledge of this writer, no resonant device has been constructed with the specific intent of measuring Young's modulus under anisotropic states of stress.

### 2.3 Pulse Test Devices

In laboratory pulse tests, the time for an induced disturbance to travel from its point of origin to a detecting sensor (or between two detecting sensors) is measured. The distance travelled by the disturbance, divided by the travel time corrected for any instrument delays is the pulse velocity. The specimen stiffness is then calculated from the velocity in accordance with wave propagation theory in an elastic whole space. The disturbance can be generated by any number of devices, i.e. mechanical, electro-mechanical, or piezoelectric. Typically, the detecting sensors are velocity (geophones) or acceleration transducers which convert physical motion into electrical signals that can be amplified and recorded.

Pulse tests can be used to measure two body wave velocities, the dilatational and shear wave velocities. For both waves propagating between source and receiver locations, the respective particle motion for the dilatational wave will be parallel to the direction of wave propagation whereas it is perpendicular for the shear wave. Consequently, it is

possible to design a pulse generator intended to generate predominantly one or the other of the two wave types and orient the receiver with the corresponding direction of particle motion. This use of "polarized" waves is the basis of all pulse testing.

The devices constructed for pulse testing are either right circular cylinder or cubic in nature. Cubic devices have the advantage to vary the three orthogonal stresses independently, whereas cylindrical devices can only load specimens biaxially. Lawrence (1963) used piezoelectric crystals or ceramics to generate and detect disturbances in a traditional triaxial test cell. Schmertmann (1978) generated pulsed dilatational and shear waves in cylindrical samples by striking a rod with a ball and scissor-type mechanical generator within a test chamber. Roesler (1979) buried a DC motor exciter in a 30 cm cubical sample in order to generate shear waves. Knox, et al, (1982) constructed a large-scale triaxial device (LSTD) at the University of Texas (UT) in which 7 ft cubical samples were loaded in true triaxial states of stress. Accelerometers were buried at different locations and elevations inside the sample. The LSTD was used subsequently by Chu et al (1984) and Lee and Stokoe (1986) to study: (1) the effect of stress state on dilatational and shear wave velocities (and hence, constrained and shear moduli), (2) the influence of structural anisotropy on dilatational and shear wave velocities, and (3) the importance of (1) and (2) on in situ testing. These goals dictated the use of such a large device versus the relatively small laboratory devices

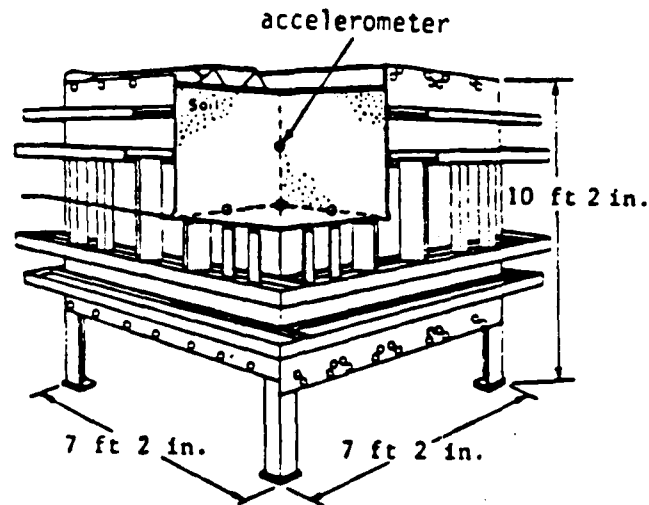


Fig. 2.3. Cut-Away Isometric View of Large-Scale Triaxial Device (LSTD). (From Lee and Stokoe, 1986)

used by earlier researchers. Figure 2.3 is an illustration of the LSTD used at the University of Texas over the past decade.

Pulse testing in cubic devices has the advantage of measuring dilatational and shear body waves under triaxial stress conditions with relative ease. Through the use of "polarized" waves it is possible to investigate the effects of structural anisotropy (in large samples) and stress-induced anisotropy. However, pulse methods in cubical devices

cannot measure the bar wave velocity (and Young's modulus) directly; rather it has to be calculated from other moduli assuming isotropic linear elastic properties in the specimen. Until recently, pulse methods have not been used to find the bar wave velocity in normal laboratory-sized soil samples.

#### 2.4 Other Developments in Dynamic Laboratory Testing

One of the most significant developments over the past quarter of a century is the routine use of piezoelectric crystals and ceramics for a variety of applications. There are signs that such use is slowly making its way into the realms of geotechnical laboratory testing. For years, the use of piezoelectric technology in resonant column devices has been limited to the accelerometers used to measure the motion of the drive plate and/or the free end.

Piezoelectric technology can be applied in both resonant and pulse devices currently used in dynamic laboratory testing. First, the advent of piezoelectric vibration generators, made by stacking piezoelectric ceramic disks and connecting them in series, has made it possible to replace the cumbersome electromagnetic or electro-mechanical vibration mechanisms used in resonant column devices. The piezoelectric shaker has a greater frequency range than the current driving mechanisms which are generally limited to less than 1000 Hertz.

However, piezoelectric shakers also can not operate well at very low frequencies (<300 Hz) and a trade off has to be considered.

Piezoelectric technology can also be applied in pulse tests, particularly with the customization and miniturization allowed by the technology. Strassburger (1982) and Dyvik and Madshus (1986) have measured small-strain shear moduli using piezoelectric bender elements embedded in soil samples to generate and detect shear waves.

Strachan (1985) proposed an alternative test method for ensuring full saturation in triaxial test samples by measuring the dilatational wave velocity generated and detected by piezoelectric crystals mounted in the center of the base and top cap of the sample. Strachan demonstrated that the well-known sensitivity of the dilatational wave velocity to small quantities of air in the pore fluid can be correlated to the wave propagation velocity and the B-value coefficient (change in pore pressure over change in isotropic stress).

There is a second area of dynamic laboratory testing where advances in technology are having an impact. That area involves the control and recording of dynamic laboratory testing and its subsequent data reduction. As mentioned earlier, Ni (1987) has fully automated the torsional shear and resonant column test devices. It is the writer's observation that this is the state of the art, however, even now electronic laboratory equipment is available that has many times more the capability of the equipment assembled by Ni. Perhaps the most significant development is the use of dynamic signal analyzers which

allow, through the use of Fast Fourier Transforms (FFT), real time analysis of laboratory measurements in the frequency domain. Just one example is provided by Tawfiq, et al (1988) who used random noise to conduct pulse testing of cohesive soils and then analyzed the response in the frequency domain. It is the writer's opinion that frequency domain analysis will become more common in dynamic laboratory testing in the future.

## 2.5 Dynamic Properties of Soils Under Different States of Stress

The study of the effects of stress state on dynamic material properties was initiated by Duffy and Mindlin (1957), who derived a longitudinal wave equation for a material composed of elastic, perfectly rounded particles arranged in a face-centered cubic array. Their equation, in terms of Young's modulus,  $E$ , is

$$E = \frac{2(8 - \nu_p)}{8 - 5\nu_p} \left[ \frac{3G_p^2 \bar{\sigma}_0}{2(1 - \nu_p)} \right] \quad (2.1)$$

where  $\nu_p$  and  $G_p$  are Poisson's ratio and shear modulus of the material particles and  $\bar{\sigma}_0$  is the effective isotropic confining stress. Duffy and Mindlin's experiments with steel spheres, arranged in the shape of a bar, showed this cubic root relation between Young's modulus and confining

stress was likely a lower bound, as they actually measured a higher root for confining pressures below 5 psi.

Hardin and Richart (1963) used a "Shannon-Wilson" free-free type of resonant column device to evaluate both longitudinal and shear wave velocities in granular material. They found that the shear modulus of sand varied with approximately the square root of the isotropic confining pressure. They also showed that the void ratio was one of the most significant variables affecting shear modulus, with other factors such as moisture content, grain characteristics, and gradation influencing the modulus mainly by how they affect void ratios.

Hardin (1965) used a Kelvin-Voigt model to analyze the response of a cylindrical column with different boundary conditions and concluded that it would be suitable for representing the resonant column system. He also concluded that damping measurements in the resonant column were hysteretic in nature, i.e. independent of frequency.

Drnevich (1967) investigated the effect of strain history on the dynamic properties of a dry Ottawa sand. One finding of his work was that the low-amplitude (<0.001%) shear modulus of undisturbed sand varied with the square root of confining pressure.

Hardin and Black (1966) published an extensive study of the effect of isotropic confining pressure on the stiffness of sand. They also concluded that shear modulus was proportional to the square root of the confining pressure, and in 1968 extended those conclusions to include normally consolidated clay. Hardin and Black concluded that the

functional relationship for shear modulus would include many factors, the most likely being:

$$G = f(\bar{\sigma}_o, e, H, S_r, \tau_o, C_g, A_p, f, t, OCR, T, O, K_T) \quad (2.2)$$

in which

$\bar{\sigma}_o$	=	effective octahedral normal stress,
$e$	=	void ratio,
$H$	=	ambient stress and vibration history,
$S_r$	=	degree of saturation,
$\tau_o$	=	octahedral shear stress,
$C_g$	=	grain characteristics, grain shape, grain size, grading, and mineralogy,
$A_p$	=	amplitude of vibration,
$F$	=	frequency of vibration,
$T$	=	secondary effects that are a function of time,
$O$	=	soil structure, and
$K_T$	=	temperature, including freezing.

Based on numerous tests on different soils, they suggested an empirical equation for clay and clean sands when  $e \leq 2.972$  (Hardin and Black, 1968). This equation can be written as:

$$G_{\max} = 1230 F(e) \text{OCR}^K \bar{\sigma}_0^{0.5} \quad (2.3)$$

where

$$F(e) = (2.973 - e)^2 / (1 + e),$$

OCR = overconsolidation ratio, and

K = overconsolidation adjustment factor.

The value of K varies between 0 and 0.5, depending on the plasticity index PI and equals zero for a PI equal to zero. The units for both  $G_{\max}$  and  $\bar{\sigma}_0$  are psi. This equation is known as the "Hardin - Black" equation.

This early work by Hardin and Black was enlarged by a series of tests on clean sands and cohesive soils by Hardin and Drnevich (1972). They identified strain amplitude, mean effective stress and void ratio as the three most important factors affecting shear modulus. Degree of saturation and overconsolidation ratio were also important for cohesive soils, but appeared less so for sands. It should be noted that their test program, which utilized resonant column and cyclic torsional shear devices, utilized a frequency range between 1 and about 300 Hz, and was conducted under isotropic states of stress.

Although the Hardin - Black equation can be applied to predict the low-amplitude shear modulus for many types of soil, Hardin (1978)

proposed a modification of this equation in an attempt to extend its range to higher void ratios and to make the equation dimensionally correct.

That equation, referred to as the "Hardin" equation, is

$$G_{\max} = A (\text{OCR})^K Pa^{1-n} \bar{\sigma}_o^n / F(e) \quad (2.4)$$

where

$$\begin{aligned} A, n &= \text{dimensionless coefficients (called stiffness} \\ &\quad \text{coefficients in this study),} \\ Pa &= \text{atmospheric pressure (in same units as } G_{\max} \\ &\quad \text{and } \bar{\sigma}_o \text{),} \\ F(e) &= 0.3 + 0.7e^2. \end{aligned}$$

For most practical applications, Hardin suggested the use of  $A = 625$  and  $n = 0.5$ .

Research in the 1970's concentrated on refining the laboratory testing methods and improving the empirical relationships put forth by Hardin and Black in the late 1960's. One of the most notable developments was the discovery in the early 1980's of how stress state impacts the magnitude of the shear modulus. In particular, it was determined that shear wave velocity, and consequently the shear modulus, was dependent on the effective stress in the plane containing the direction of wave propagation and direction of particle motion and

was nearly independent of the anti-plane stress (Roesler, 1979; Knox, et al, 1982; Allen & Stokoe, 1982; and Lee, 1985). In 1986, Lee and Stokoe published the results of a comprehensive set of seismic tests on sand in a large scale triaxial device (LSTD) where the sand was subjected to both isotropic and anisotropic stress conditions. They found for waves propagating along principal stress directions:

$$G_{\max} = C \bar{\sigma}_a^{na} \bar{\sigma}_b^{nb} \bar{\sigma}_c^{nc} \quad (2.5)$$

where

- $G_{\max}$  = shear modulus at small strains ( $<10^{-4}\%$ ),
- $\bar{\sigma}_a$  = principal stress in the direction of wave propagation,
- $\bar{\sigma}_b$  = principal stress in the direction of particle motion, and
- $\bar{\sigma}_c$  = principal stress in the out-of-plane direction (i.e. the third principal stress).

The factor C is simply a coefficient. Parameters na, nb, and nc are stiffness coefficients. For practical purposes,  $nc = 0$  and Eq. 2.5 can be rewritten as

$$G_{\max} = C \bar{\sigma}_a^{na} \bar{\sigma}_b^{nb} \quad (2.6)$$

This approach for representing modulus has been referred to in the literature as the "individual stress approach" or "three-stress approach" in the case of Eq. 2.5 and the "two-stress approach" in the case of Eq. 2.6.

Lee (1985) performed extensive wave propagation tests on a dry sand sample confined under isotropic, biaxial, and triaxial states of stress in the cubical LSTD at UT. Shear wave velocities were measured along all principal stress directions. Lee's results also showed that shear wave velocities depend about equally on  $\bar{\sigma}_a$  and  $\bar{\sigma}_b$ , with  $\bar{\sigma}_c$  having a negligible effect. In his studies, Lee expressed shear modulus as

$$G = S \bar{\sigma}_0^{na} \bar{\sigma}_0^{nb} P_a^{1-na-nb} / F(e) \quad (2.7)$$

where S, na, and nb are the stiffness coefficients and F(e) is defined as in Eq. 2.4. Ni (1987) has tabulated the results obtained by other studies for the stiffness parameters that define the small-strain shear modulus. His summary is included in Table 2.1.

It is noted that the foregoing discussion has concentrated on the stress-state affecting the shear modulus. It has illustrated how, for shear waves propagating along principal stress directions, the principal stresses in the plane containing the direction of wave propagation and particle motion control the value of shear modulus. However, pulse tests in the LSTD at UT conducted during the same period of time has lead to an equally important discovery. It was found that for dilatational waves

travelling along principal stress directions, the principal stress parallel to the line of wave propagation and particle motion almost solely controls the constrained modulus.

In pulse tests on small- and large-scale laboratory sized specimens, Schmetmann (1978), Kopperman, et al (1982) and Chu, et al, (1984), have shown the dilatational wave velocity is proportional to the mean effective stress raised to a power between 0.14 and 0.24. Tests by some researchers make a distinction between stiffness coefficients for dilatational waves travelling in a vertical (anisotropic) plane of the specimen versus waves propagating in the horizontal (isotropic) plane of a structurally anisotropic specimen. The values are typically different. Lee and Stokoe (1986) tabulated the results of other studies for the dilatational velocity as defined by the mean effective stress. Their table is recreated in Table 2.2.

An examination of Table 2.2 shows that if the constrained modulus is derived from the dilatational wave velocity, it will typically vary as a function of mean effective stress raised to a power between 0.34 and 0.48. It was shown by Kopperman et al (1982) and Chu et al (1984) that, for waves travelling along principal stress directions, the constrained modulus is controlled almost solely by the effective principal stress in the direction of wave propagation (and particle motion). This distinction is only important for specimens loaded anisotropically.

Table 2.1. Summary of Stiffness Coefficients for Shear Modulus  
Obtained from Various Research Studies. (From Ni, 1987)

Author	Void Ratio	F(e)	S	n	na	ab	nc	Range of Stress, psi	Remarks
Hardin and Richart (1963)	0.53 - 0.63	-	-	0.46 - 0.50 0.54 - 0.62	-	-	-	2.1 - 13.9 13.9 - 69.4	Ottawa sand, a <sup>***</sup>
Lawrence (1965)	0.56 - 1.48	I <sup>*</sup>	681(350) <sup>**</sup>	0.50 - 0.66	-	-	-	20 - 100	Kaolinite and Boston blue clay, b
Hardin and Black (1966)	0.64 - 0.65	-	-	0.50 0.60	-	-	-	2.1 - 13.9 13.9 - 69.4	Ottawa sand, a
Hardin and Drnevich (1972)	< 0.80	II	724(686)	0.50	-	-	-	-	Round Ottawa sand, a
Black (1968)	0.77 - 0.88	I I	625(321) 830(425) to 625(321)	0.50 0.50	-	-	-	- 27.8 - 55.6	Angular crushed sand, a Edgar plastic clay, a
Hardin and Iwasaki, et al (1977)	< 2.0 0.61 - 0.86	I II	625(321) 724(882)	0.50 0.40	-	-	-	- 2.8 - 83	Soils Toyoura sand, a
Hardin (1978)	0.4 - 1.2	III	625	0.50	-	-	-	-	Soils, a
Roesler (1979)	-	-	-	-	0.298	0.214	0.00	7.25 - 25	Fine round grain sand, c
Kokusho (1980)	0.64 - 0.79	II	678(826)	0.50	-	-	-	13.9 - 27.8	Toyoura sand, d
Allen and Stokoe (1982)	0.67 - 0.70	III	720	0.48	0.24	0.22	-	4.0 - 64.0	Washed mortar sand, a
Knowlton et al (1982)	-	-	-	0.40	0.24	0.18	0.02	10 - 40	Washed mortar sand, c
Yu and Richart (1983)	0.52 - 0.62	-	-	-	0.24	0.28	-	3 - 28.4	Ottawa sand and Brazil sand, a
Chung, et al (1984)	0.68	III	523	0.48	-	-	-	1.45 - 44	Monterey No. 0 sand, a
Heiniger and Studer (1985)	0.62 - 0.70	II	563(686)	0.50	-	-	-	14.5 - 87	Coarse-grain sand, a
Stokoe, et al (1985)	0.62 - 0.70	-	-	0.40	0.18	0.18	-	10 - 40	Washed mortar sand, c
Stokoe and Ni (1985)	0.69	III	721	0.44	0.22	0.22	-	3.0 - 55.0	Washed mortar sand, a
Lee and Stokoe (1985)	0.62 - 0.70	-	-	0.40	0.20	0.20	0.00	10 - 40	Washed mortar sand, c
This research	0.64 - 0.72	III III III	687	0.44	0.22 0.23 0.24	0.23 0.20 0.23	0.02	2 - 55 12 - 24 12 - 24	Washed mortar sand, a Ticino sand, a Reil-Bedford sand, a

\* -  $F(e) = 1 - (2.97 - e)^2 / (1 + e)$ , II =  $(2.17 - e)^2 / (1 + e)$ , III =  $0.3 + 0.7 e^2$

\*\* - Number in the bracket is the original value which is referred to F(e) shown, while the number not in the bracket is the value of S which is referred to the III of F(e).

\*\*\* - Remarks: a = resonant column test, b = supersonic pulse test, c = pulse test (cubic sample), d = cyclic triaxial test

Table 2.2. Summary of Values of the Slope of the Log M - Log  $\bar{\sigma}_0$  Relationship\* for Dry Sand under Isotropic Confinement. (After Lee and Stokoe, 1986)

Reference	nm	Confining Pressure	Remark
Matsukawa and Hunter (1956)	0.40	0.3 - 3.0 psi	a
Schmertmann (1978)	0.40 - 0.46	5 - 20 psi	a1
	0.28 - 0.36	5 - 20 psi	a2
Kopperman, et al (1982)	0.40	10 - 40 psi	b1
	0.46 - 0.48	10 - 40 psi	b2
Chu, et al (1984)	0.34	10 - 40 psi	b1
	0.44 - 0.46	10 - 40 psi	b2
Lee and Stokoe (1986)	0.42	15 - 30 psi	b1
	0.44	15 - 30 psi	b2

\*  $M = C \bar{\sigma}_0^{nm}$

- a. Pulse Test in Cylindrical Chamber
- b. Pulse Test in Large-Scale Triaxial Device (LSTD)
  - 1. M from  $V_p$  in vertical plane of sample, i.e.  $V_{pa}$
  - 2. M from  $V_p$  in horizontal plane of sample, i.e.  $V_{pi}$

At first perusal, very little can be found in geotechnical literature specifically addressing the measurement of Young's modulus using dynamic wave propagation. Actual published results are less common today because of the recent emphasis on studying the shear modulus. The writer has discovered what appears to be some confusion on the part of recent researchers when reviewing past literature. What early researchers mistakenly called the dilatational or compressive wave velocity was, by the very nature of the test in which they were measured

(in resonant column tests), the bar wave velocity. This has caused recent reviewers to group what were tests measuring the bar wave velocity with those which measured the dilatational velocity. The only way the writer knows to measure the dilatational velocity is through the use of pulse tests.

Reexamining the literature, and retabulating the results of various researchers in light of this discovery, it can be seen in Table 2.3 that Young's modulus (as determined from the square of the bar wave velocity) is a function of the mean effective stress raised to a power which typically ranges between 0.45 and 0.55 with some values as high as 0.70.

Only two recent references were found by the writer where Young's modulus values were reported, and both of these involved longitudinal resonant column tests. Heiniger and Struder (1985) built a resonant column device to test coarse granular materials and reported Young's and shear moduli values for gravel and Monterey O sand. Unfortunately, their tests were done only at two confining pressures. The writer does note that they measured multiple longitudinal and torsional resonant frequencies but still used only the first resonant frequency to compute the respective moduli. Saxena, et al, (1988) reported longitudinal and torsional resonant tests on uncemented and partially cemented Monterey O sand. Their relationship for Young's modulus of

Table 2.3. Summary of Stiffness Coefficients for Log E - Log  $\bar{\sigma}_0$  Relationship\* for Soils under Isotropic Confinement from Past Research Studies.

Reference	nm	Confining Pressure	Remark
Duffy and Mindlin (1957)	0.50 0.34	< 5 psi > 5 psi	a
Shannon, et al (1959)	0.50	> 4 psi	a
Hardin (1961)	0.46 - 0.62	3 - 55 psi	a
Smoots and Stickel (1962)	0.32 - 0.56	> 4 psi	a
Wilson and Miller (1962)	0.40 - 0.50	> 4 psi	a
Hardin and Richart (1963)	0.54 - 0.70 0.46 - 0.50	< 14 psi > 14 psi	a

\*  $E = C \bar{\sigma}_0^{nm}$

a. Longitudinal Resonant Column Tests

the uncemented sand involved the mean effective stress raised to a power of 0.39. It appears not much work is been done measuring the Young's modulus of soil materials.

## 2.6 Summary

Dynamic laboratory testing devices can be divided into two general groups: those which use pulse methods, and those which use resonant methods. The pulse devices measure stiffness by determining the time for a polarized body wave (dilatational or shear) to travel through the material between a dynamic source and receiver. The distance divided by the corrected travel time yields the body wave velocity which is then used to calculate stiffness. Pulse test devices are either cylindrical or cubic in nature, allowing testing under biaxial ( $\bar{\sigma}_1 > \bar{\sigma}_2 = \bar{\sigma}_3$  or  $\bar{\sigma}_1 = \bar{\sigma}_2 > \bar{\sigma}_3$ ) or true triaxial ( $\bar{\sigma}_1 > \bar{\sigma}_2 > \bar{\sigma}_3$ ) loadings, respectively. However, they can only measure the constrained and shear moduli and are not able to measure Young's modulus.

Resonant method devices measure stiffness by finding a characteristic resonant frequency of the specimen. A wave velocity is computed from the resonant frequency by applying one-dimensional wave propagation theory. Typically, resonant devices only find the first resonant frequency, either torsional or longitudinal, and no use is made of the multiple resonant frequencies which are sometimes observed.

Torsional resonant devices can, with modification, apply biaxial (compression only) and triaxial loadings to specimens. However, all longitudinal resonant devices are used only under isotropic loading because of the difficulty associated with making measurements under biaxial or triaxial loadings. Although first introduced in the 1930's,

resonant column devices have only been used extensively to study dynamic soil properties since the 1960's. The bulk of those studies have concentrated on the parameters affecting the shear modulus with the implied assumption that the parameters would affect the other elastic moduli in the same manner. In particular it was commonly accepted that the shear modulus, and the other elastic moduli as well, were a function of the mean effective stress raised to a power between 0.30 and 0.50. This is true only for specimens under isotropic confinement.

Research over the past decade, in which pulse and resonant devices were used to study soils under biaxial and triaxial loading conditions have shown that the elastic moduli are affected differently by the different principal stresses. That research, which was confined primarily to dry sands, has shown that for waves propagating along principal stress directions, the constrained modulus is controlled almost solely by the principal stress in the direction of wave propagation and particle motion. It was also found that the shear modulus is controlled about equally by the principal stresses in the direction of wave propagation and particle motion, and is virtually unaffected by the third principal stress. No research studies have been found which described how the state of stress influences Young's modulus.

## **Chapter Three**

### **Theoretical Background**

#### **3.1 Introduction**

Inherent in this research is the assumption of small strains, hence the test materials are assumed to behave linearly elastically. There are many well developed wave propagation problems that are founded in linear elastic theory. Comprehensive discussions of many problems are given by Rayleigh (1945) and Love (1944). Theoretical and experimental developments for wave propagation in waveguides are relatively more recent, dating to the mid-1900's. The advent of high speed computing using numerical methods has broadened the capability of the mechanics researcher to study more complex and arbitrary problems. However, the theory applied in this research is founded in fundamental solutions developed long before the computer.

This chapter, along with the detailed developments contained in Appendices A, B and C, presents the theoretical foundation used for the reduction of the measurements made in the laboratory. General solutions of the equations of motion in cylindrical coordinates are contained in Appendices A and B. A particular solution for one-dimensional wave propagation in a finite rod is presented in this chapter because of its specific application to the developed test. Similarly, the

three-dimensional solution for waves propagating in the axial direction of an infinite bar is also presented in detail. Finally, a brief summary of the theoretical solution for transient waves propagating in a semi-infinite rod due to an impact on the end is included. A detailed development for the transient case is included in Appendix C.

### 3.2 One-Dimensional Wave Propagation in an Elastic Material

If the body forces and the stress tensor depend only on one spatial variable the stress equations of motion, expressed in indicial notation, become

$$\tau_{11,1} + \rho f_i = \rho \ddot{u}_i \quad (3.1)$$

where  $\tau_{ij}$  is the stress tensor,  $\rho$  is the mass density,  $f_i$  is the vector describing the external forces, and  $\ddot{u}_i$  is the vector describing the acceleration. The displacement equations of motion become

$$\mu u_{i,11} + (\lambda + \mu) u_{1,1i} + \rho f_i = \rho \ddot{u}_i \quad (3.2)$$

where  $u_i$  is the vector describing the displacements and  $\mu$  and  $\lambda$  are material constants. These equations, here expressed in Cartesian coordinates ( $x_1$ ,  $x_2$  and  $x_3$ ), can also be expressed in cylindrical

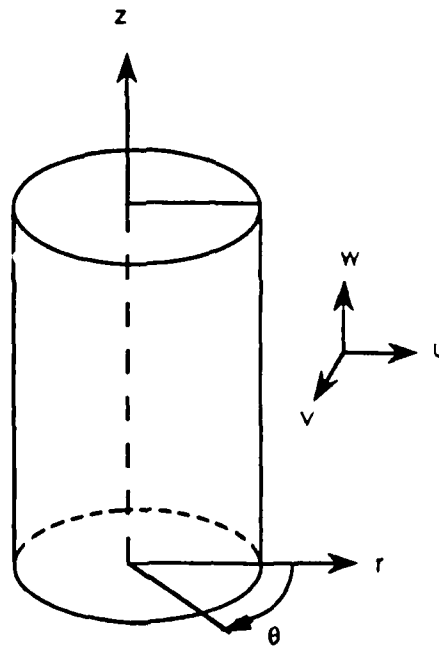


Fig. 3.1. Cylindrical Coordinates for Finite Rod.

coordinates ( $r$ ,  $\theta$ , and  $z$ ) as illustrated in Figure 3.1. The strain-displacement and stress-strain relationships expressed in cylindrical coordinates are given in Appendix A.2 and the displacement equations of motion are given in Appendix B. In cylindrical coordinates,  $z$ , with its corresponding displacement,  $w$ , will be chosen as the dependent spatial variable for the purposes of the following discussion.

Now consider the case where  $w$  is the one non-vanishing displacement, which assumes  $u$ ,  $v$ ,  $\frac{\partial v}{\partial r}$  and  $\frac{\partial u}{\partial \theta}$  equal zero. As a result

Eqs. A.18-A.24 reduce to

$$\tau_z = (\lambda + 2\mu) \frac{\partial w}{\partial z}, \quad \tau_r = \tau_\theta = \lambda \frac{\partial w}{\partial z} \quad (3.3a,b)$$

and the only displacement equation of motion that is not trivial is

$$\frac{\partial^2 w}{\partial z^2} + \frac{1}{1-2\nu} \frac{\partial}{\partial z} \left( \frac{\partial w}{\partial z} \right) = \frac{1}{C_T^2} \frac{\partial^2 w}{\partial t^2}, \quad (3.4)$$

where  $\nu$  is the Poisson's ratio and  $C_T$  is the shear wave velocity.

Rearranging Eq. 3.4 yields the familiar equation for a one-dimensional dilatational wave travelling in a half-space

$$(\lambda + 2\mu) \frac{\partial^2 w}{\partial z^2} = \rho \frac{\partial^2 w}{\partial t^2} \quad (3.5)$$

or

$$\frac{\partial^2 w}{\partial z^2} = \frac{1}{C_L^2} \frac{\partial^2 w}{\partial t^2} \quad (3.6)$$

$C_L$  is referred to alternatively as the compressional, dilatational, P-wave, or constrained wave velocity and is also represented using the symbol,  $V_p$ . The constrained modulus,  $M$ , is defined as

$$M = \lambda + 2\mu = \rho C_L^2 = \rho V_p^2 \quad (3.7)$$

Now consider a second case where  $\tau_z$  is the one non-vanishing stress, which assumes  $\tau_r = \tau_\theta = \tau_{rz} = \tau_{r\theta} = \tau_{\theta z} = 0$ . Then Eqs. A.14 through A.24 yield

$$\epsilon_r = \epsilon_\theta = -\frac{\lambda}{2(\lambda+2\mu)} \epsilon_z = -v\epsilon_z \quad (3.8)$$

where  $v$  is the Poisson's ratio. Substituting Eqs. 3.8, A.14 and A.24 into Eq. A.20 yields

$$\tau_z = \frac{\mu(3\lambda+2\mu)}{(\lambda+\mu)} \epsilon_z \quad (3.9)$$

If the expression for  $\tau_z$  in its displacement form is substituted into Eq. 3.1 in the absence of external forces, it yields the well known equation of motion for a plane wave travelling along a rod in the absence of external forces, thus

$$\frac{\mu(3\lambda+2\mu)}{(\lambda+\mu)} \frac{\partial^2 w}{\partial z^2} = \rho \frac{\partial^2 w}{\partial t^2} \quad (3.10)$$

or

$$\frac{\partial^2 w}{\partial z^2} = \frac{1}{C_B^2} \frac{\partial^2 w}{\partial t^2} \quad (3.11)$$

$C_B$  is referred to as the bar or rod wave velocity and is also often represented by the symbol,  $V_c$ . The Young's modulus,  $E$ , is defined as

$$E = \frac{\mu(3\lambda+2\mu)}{(\lambda+\mu)} = \rho C_B^2 = \rho V_c^2 \quad (3.12)$$

Now consider one final case, that where the displacement is confined to the plane normal to the z-axis, which is equivalent to assuming  $w$  and any derivatives with respect to  $r$  and  $\theta$  are equal to zero. Then the only stresses that are non-zero are given by

$$\tau_{rz} = \mu \frac{\partial u}{\partial z}, \quad \tau_{\theta z} = \mu \frac{\partial v}{\partial z}. \quad (3.13a,b)$$

and the displacement equations of motion then reduce to the two uncoupled equations given by

$$\frac{\partial^2 u}{\partial z^2} = \frac{1}{C_T^2} \frac{\partial^2 u}{\partial t^2}, \quad \frac{\partial^2 v}{\partial z^2} = \frac{1}{C_T^2} \frac{\partial^2 v}{\partial t^2} \quad (3.14a,b)$$

$C_T$  is referred to as the shear, distortional or S-wave velocity and is also often represented by the symbol,  $V_s$ . The shear modulus is defined as

$$G = \mu = \rho C_T^2 = \rho V_s^2 \quad (3.15)$$

The deformational behavior of an isotropic, linear elastic material can be defined by any two of the elastic constants, or any two of the velocities  $V_s$ ,  $V_c$  or  $V_p$ . Table 3.1 lists some of the more commonly used relationships.

Table 3.1. Commonly Used Relationships Between Elastic Constants.

	$E, \nu$	$E, \mu$	$\lambda, \mu$
$\lambda$	$\frac{E\nu}{(1+\nu)(1-2\nu)}$	$\frac{\mu(E-2\mu)}{3\mu-E}$	$\lambda$
$\mu$	$\frac{E}{2(1+\nu)}$	$\mu$	$\mu$
$E$	$E$	$E$	$\frac{\mu(3\lambda+2\mu)}{\lambda+\mu}$
$B$	$\frac{E}{3(1-2\nu)}$	$\frac{\mu E}{3(3\mu-E)}$	$\lambda + \frac{2}{3}\mu$
$\nu$	$\nu$	$\frac{E-2\mu}{2\mu}$	$\frac{\lambda}{2(\lambda+\mu)}$

- $\lambda$  = Lamé's constant  
 $\mu$  = Shear modulus  
 $E$  = Young's modulus  
 $B$  = Bulk modulus  
 $\nu$  = Poisson's ratio

### 3.3 One-Dimensional Wave Propagation in a Rod Subjected to a Steady-State End Condition and with an Added Mass

The development of the closed form solution for one-dimensional motion in a finite rod is well known. See, for example, Richart et al (1970) and more recently, Norman-Gregory and Selig (1989). As defined in the previous section, one-dimensional motion assumes the wave propagates with a plane front without dispersion and is dependent only on the axial spatial variable and time. The governing equation of motion is given by Eq. 3.11. The axial displacement,  $w(z,t)$  can be assumed to take the following steady-state form:

$$w(z,t) = Ce^{i(kz-\omega t)} + De^{-i(kz+\omega t)} \quad (3.16)$$

where  $k$  is the wave number and equals  $\omega/C_B$ , and  $C, D$ , are constants to be determined from the boundary conditions.

The boundary conditions considered for this solution are those anticipated to best represent the conditions in the test apparatus. In the test apparatus developed in this research, the rigid base is subjected to a steady-state sinusoidal vibration and the top is capped by a rigid mass. The conceptual problem is illustrated in Fig. 3.2.

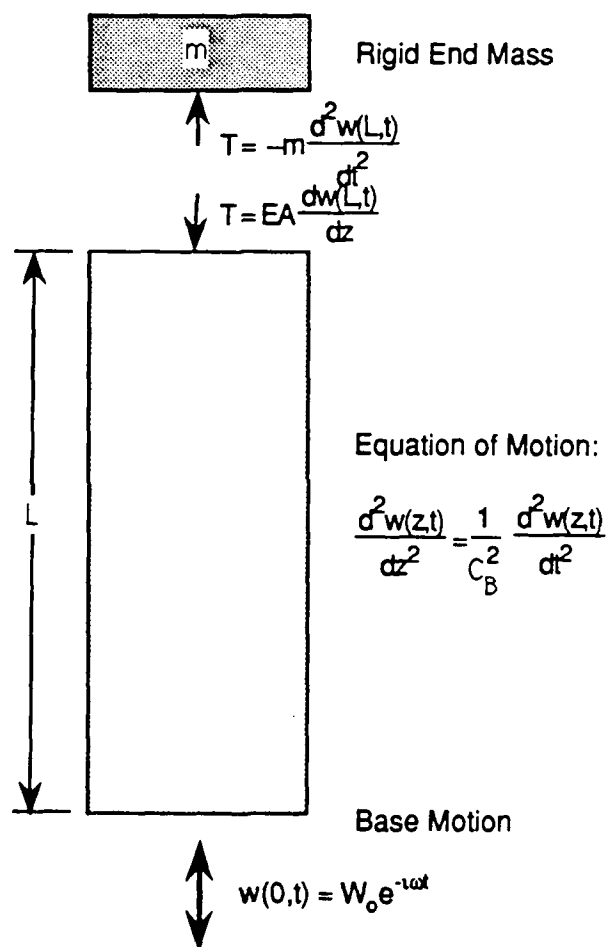


Fig. 3.2. Idealized Model for One-Dimensional Wave Motion in a Finite Rod.

The boundary conditions are;

$$\text{at } z = 0, \quad w(0,t) = W_0 e^{-i\omega t} \quad (3.17a)$$

$$\text{at } z = L, \quad EA \frac{dw(L,t)}{dz} = -m \frac{d^2w(L,t)}{dt^2} \quad (3.17b)$$

Substituting Eq. 3.16 into the first boundary condition at  $z = 0$  yields

$$C + D = W_0 \quad (3.18)$$

Differentiating (3.16) with respect to  $z$  and  $t$  yields

$$\frac{d^2w(z,t)}{dt^2} = -\omega^2 [C e^{i(kz-\omega t)} + D e^{-i(kz+\omega t)}] \quad (3.19)$$

and

$$\frac{dw(z,t)}{dz} = ik [C e^{i(kz-\omega t)} - D e^{-i(kz+\omega t)}] \quad (3.20)$$

Substituting Eqs. 3.19 and 3.20 into the second boundary condition at  $z = L$  yields

$$ikEA [C e^{i(kL-\omega t)} - D e^{-i(kL+\omega t)}] = -m\omega^2 [C e^{i(kL-\omega t)} + D e^{-i(kL+\omega t)}] \quad (3.21)$$

Collecting coefficients and eliminating  $e^{-i\omega t}$ , two equations for C and D are determined. Cast in matrix form, these equations are

$$\begin{bmatrix} 1 & 1 \\ (m\omega^2 - ikEA)e^{ikL} & (m\omega^2 + ikEA)e^{-ikL} \end{bmatrix} \begin{Bmatrix} C \\ D \end{Bmatrix} = \begin{Bmatrix} W_0 \\ 0 \end{Bmatrix} \quad (3.22)$$

Equations 3.22 can be solved for C and D which gives the solution for  $w(z,t)$ . The denominator of the solution is the determinant of the coefficients. If the determinant vanishes,  $w(z,t)$  goes to infinity, a condition analogous to "resonance." If the determinant is set equal to zero, it yields the following equation,

$$(m\omega^2 + ikEA)e^{ikL} - (m\omega^2 - ikEA)e^{-ikL} = 0 \quad (3.23)$$

Collecting real and imaginary terms yields

$$-m\omega^2(e^{ikL} - e^{-ikL}) + ikEA(e^{ikL} + e^{-ikL}) = 0 \quad (3.24)$$

and noting Euler's identities

$$2i \sin kL = (e^{ikL} - e^{-ikL}), \quad (3.25a)$$

$$2 \cos kL = (e^{ikL} + e^{-ikL}), \quad (3.25b)$$

Eq. 3.24 reduces to

$$ikEA(2\cos kL) = m\omega^2(2i \sin kL) \quad (3.26)$$

Cancelling  $i$ , multiplying by  $L$  and recalling the relations  $k = \omega/C_B$ ,  $E = \rho C_B^2$  and  $\rho = \gamma/g$ , yields with development

$$Lm\omega^2 \sin \frac{\omega L}{C_B} = \omega \rho C_B A L \cos \frac{\omega L}{C_B} \quad (3.27)$$

$$\frac{\omega L}{C_B} \frac{\sin \frac{\omega L}{C_B}}{\cos \frac{\omega L}{C_B}} = \frac{A\gamma L}{mg} \quad (3.28)$$

$$\beta \tan \beta = \frac{W_s}{W_m} = \frac{M}{m} \quad (3.29)$$

where

- $M$  = mass of the sample,
- $m$  = added mass,
- $W_s$  = weight of the sample,
- $W_m$  = weight of the added mass, and
- $\beta$  =  $\frac{\omega L}{C_B}$ .

Equation 3.29 is the same result obtained for one-dimensional wave propagation in a finite rod where one end is fixed,  $w(0,t) = 0$ , and

the other end has an added mass. Richart et al (1970) developed this solution for one-dimensional torsional motion. Similarly, Norman-Gregory and Selig (1989) recently rederived this equation for one-dimensional longitudinal motion with a fixed end and added mass at the other end.

Equation 3.29 is a transcendental equation with an infinite number of roots for any given ratio of sample and added mass. This is illustrated in Fig. 3.3, where values for  $\beta$  are given for  $M/m = 2.0$ . It is therefore possible to compute the frequency for any given weight ratio, sample length and bar velocity. These frequencies correspond to the resonant frequencies of the system. Thus it can be shown that

$$\omega_n = \frac{\beta_n C_B}{L}, \quad n=1,2,3\dots \quad (3.30)$$

where  $\beta_n$  are the solutions to Eq. 3.29 for a given mass ratio and  $n$  corresponds to the distribution of strain or displacement in the rod. These distributions are also referred to as modes of vibration, i.e.  $n = 1$  is the first mode,  $n = 2$  the second mode, etc. These values of  $n$  refer to the distribution of longitudinal displacements with respect to  $z$ , which assumes a plane wave front, or that the longitudinal displacement is equal in the plane perpendicular to the axis of the rod at any particular point.

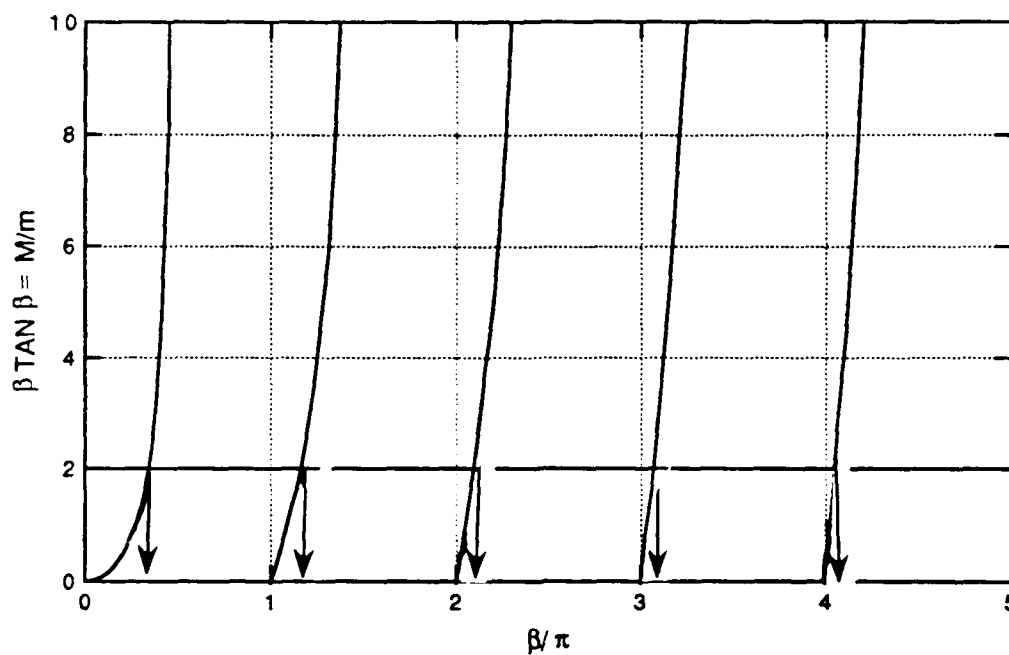


Fig. 3.3. Graphical Solution of  $\beta \tan \beta = \frac{M}{m}$ .

It is relatively simple to solve in a similar manner the corresponding case of one-dimensional motion for a rod with one end fixed,  $w(0,t) = 0$ , and the other end free,  $dw(L,t)/dz = 0$ . This has been done by Richart et al (1970) and others. The relative shapes of the first three modes are illustrated in Fig. 3.4. It can easily be concluded that the corresponding wave lengths for each mode,  $\lambda_n$ , are given by

$$\lambda_n = \frac{4L}{(2n-1)}, \quad n = 1, 2, 3, \dots \quad (3.31)$$

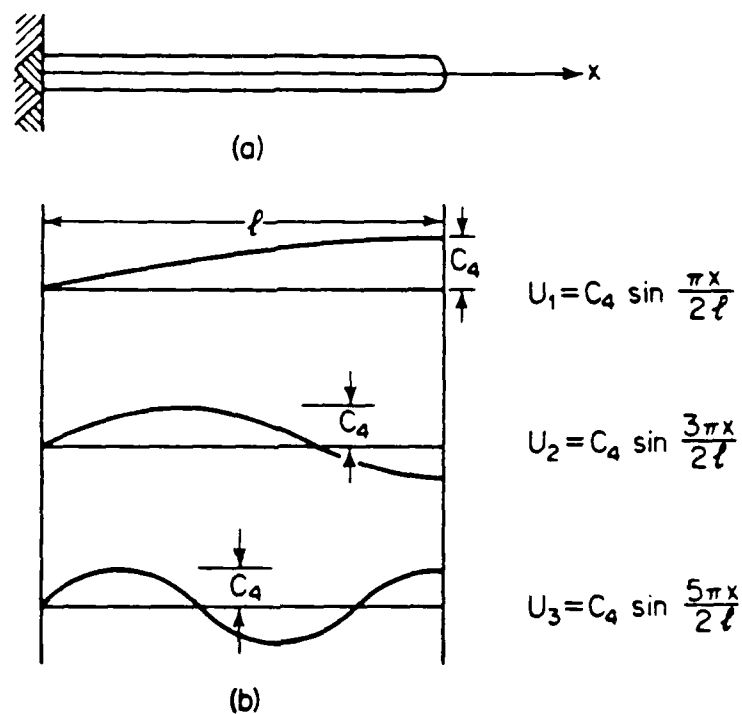


Fig. 3.4. Distribution of Axial Displacements for the First Three Modal Shapes of a Fixed-Free Rod. (From Richart et al, 1970)

The resonant frequencies of each mode for the fixed-free case also follow directly from the solution. These are

$$\omega_n = \frac{(2n-1)\pi C_B}{2L}, \quad n = 1, 2, 3, \dots \quad (3.32)$$

The presence of a mass at the free end serves to reduce the resonant frequency or alternatively, increase the modal wavelengths.

This is easily seen in Fig. 3.3 where, as the mass ratio increases to infinity, the values of  $\beta_n$  approach  $(2n-1)\pi/2$ , and the natural frequencies approach those for the fixed-free case (zero mass at the free end).

### 3.4 Frequency Spectrum of a Solid Cylindrical Rod of Infinite Length

The general solution for time-harmonic motion in an infinite cylindrical rod with solid cross section is developed in Appendix B. The frequency spectrum of an infinite rod is frequently considered for three separate types of motions; torsional, longitudinal, and flexural. The assumptions associated with each of these types of waves greatly simplifies the frequency equation derived for the general case. In the general problem, every choice of integer  $n$  and real valued wave number  $k$  yields an infinite number of roots corresponding to an infinite number of modes of wave propagation in the rod. The general problem is further complicated when imaginary and complex-valued wave numbers are considered. The simplest case of torsional waves is described here first in order to lay the ground work for the more complicated case of longitudinal waves. Flexural waves will not be discussed as they were not the focus of this study. However, any text on motions in waveguides includes an analogous discussion of flexural modes.

### 3.4.1 Torsional Waves in a Solid Cylindrical Rod

Torsional waves assume that only the circumferential displacement is non-zero and that it is independent of  $\theta$ . Stated differently, it assumes that the displacements in the axial and radial directions and any derivatives with respect to the circumferential direction equal zero. The only displacement equation of motion which applies is Eq. B.25, the others being trivial. Reducing Eq. B.25 using Eq. B.27 yields

$$\frac{\partial^2 v}{\partial r^2} + \frac{1}{r} \frac{\partial v}{\partial r} - \frac{v}{r^2} + \frac{\partial v}{\partial z} = \frac{1}{C_T^2} \frac{\partial^2 v}{\partial t^2} \quad (3.33)$$

Similarly, the only non-trivial boundary condition is

$$\text{at } r = a, \quad \tau_{r\theta} = \frac{\partial v}{\partial r} - \frac{v}{r} = 0 \quad (3.34)$$

If the displacement  $v$  is of the form

$$v(r,z,t) = \frac{1}{q} B_2 J_1(qr) e^{i(kz - \omega t)} \quad (3.35)$$

where  $J_1(qr)$  is a Bessel function of the first kind and order one and  $B_2$  is a constant. When Eq. 3.35 is substituted into Eq. 3.34, it yields the frequency equation for  $r = a$  in the form

$$(qa)J_0(qa) - 2J_1(qa) = 0 \quad . \quad (3.36)$$

$J_0(qa)$  is a Bessel function of the first kind and order zero and  $q$  is defined by

$$q^2 = \frac{\omega^2}{C_T^2} - k^2 \quad (3.37)$$

This is a transcendental equation whose roots have been tabulated by Abramowitz and Stegun (1964), or they can be computed numerically.

Rewriting Eq. 3.37 to allow examination yields

$$\left(\frac{\omega a}{C_T}\right)^2 = (q_n a)^2 + (ka)^2 \quad (3.38)$$

where

- $a$  = radius of rod,
- $\omega$  = circular frequency,
- $k$  = wave number,
- $C_T$  = distortional wave velocity, and
- $q_n$  = roots to Eq. 3.37.

Recalling that  $\omega = kC$ , where  $C$  is the phase (or apparent) velocity, Eq. 3.38 can also be written as

$$\left(\frac{C}{C_T}\right)^2 + \left(\frac{q_n a}{ka}\right)^2 = 1 \quad (3.39)$$

A special solution to Eq. 3.36 is when  $q = 0$ . In this case, Eq. 3.39 shows that  $C = C_T$ , or the phase velocity equals the distortional wave velocity and does not change with frequency. This means that the lowest torsional mode is not dispersive. Further, if one takes the limit as  $q \rightarrow 0$  in Eq. 3.35, it assumes the form

$$v(r,z,t) = \frac{1}{2} B_2 r e^{i(kz - \omega t)} \quad (3.40)$$

which shows that the displacement is proportional to the radius for the lowest torsional mode.

An examination of the higher modes can now be made. In general, one mode of propagation corresponds to each root of Eq. 3.36. The solution to Eq. 3.38 is plotted in Fig. 3.5 for the first four modes corresponding to  $q_0 a = 0$ ,  $q_1 a = 5.136$ ,  $q_2 a = 8.417$ , and  $q_3 a = 11.62$ . It is noted that  $ka$  can be real or imaginary for real values of  $q_n a$ . Thus, the mode branches are hyperbolic for real values and circular for imaginary values of  $k$ . The implication of this graph in practice is that, below a certain frequency known as the cutoff frequency, a torsional mode will

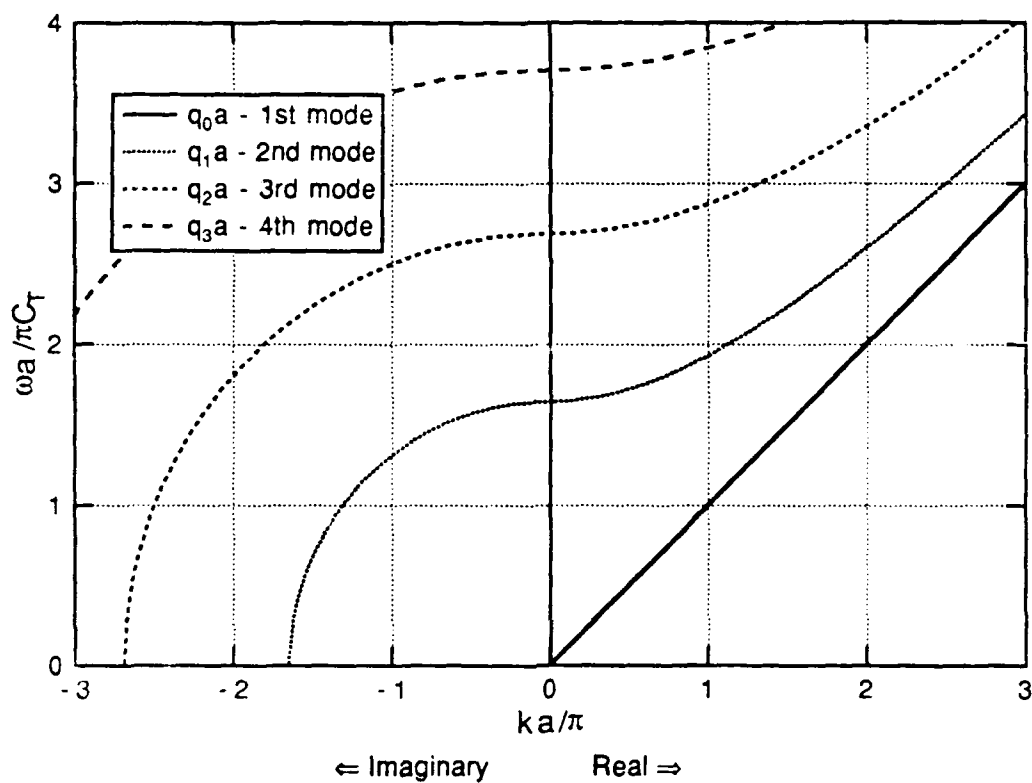


Fig. 3.5. Frequency Spectrum for Torsional Waves in a Cylindrical Rod.

not propagate along a given rod of known radius and stiffness. Even if the initial excitation at the rod end contains higher frequencies, the higher modes will be evanescent and decay quickly.

### 3.4.2 Longitudinal Waves in a Solid Cylindrical Rod

Waves travelling longitudinally, i.e. parallel to the axis of the rod, are assumed to be axially symmetric, and contain displacements in the axial and radial dimensions only. Axisymmetry assumes that the circumferential displacement, and any derivatives with respect to it, equal zero. Thus, the displacement equations of motion follow from Eqs. B.24 and B.26 as.

$$\nabla^2 u - \frac{u}{r^2} + \frac{1}{1-2\nu} \frac{\partial \Delta}{\partial r} = \frac{1}{C_T^2} \frac{\partial^2 u}{\partial t^2} \quad (3.41)$$

and

$$\nabla^2 w + \frac{1}{1-2\nu} \frac{\partial \Delta}{\partial z} = \frac{1}{C_T^2} \frac{\partial^2 w}{\partial t^2} \quad (3.42)$$

The Laplacian in radially symmetric coordinates is

$$\nabla^2 = \frac{\partial^2}{\partial r^2} + \frac{1}{r} \frac{\partial}{\partial r} + \frac{\partial^2}{\partial z^2} \quad (3.43)$$

and the dilatation is

$$\Delta = \frac{\partial u}{\partial r} + \frac{u}{r} + \frac{\partial w}{\partial z} \quad (3.44)$$

It is possible, with extensive calculation, to manipulate and solve these equations for the displacements. However, it is simpler to cast the

problem in terms of displacement potentials. The pertinent definitions follow from Eqs. B.17, B.18 and B.19, which reduce to the following for the axisymmetric case;

$$u = \frac{\partial \phi}{\partial r} - \frac{\partial \psi_{\theta}}{\partial z} \quad (3.45)$$

$$\frac{\partial \psi_r}{\partial z} = \frac{\partial \psi_z}{\partial r} \quad (3.46)$$

$$w = \frac{\partial \phi}{\partial z} + \frac{1}{r} \frac{\partial (\psi_{\theta} r)}{\partial r} \quad (3.47)$$

where  $\phi$  is a scalar potential and  $\psi_{\theta}$ ,  $\psi_r$  and  $\psi_z$  are the three components of,  $\psi$ , the vector potential. Noting Eqs. B.39 to B.42, it is convenient to use potentials of the following form

$$\phi = A J_0(pr) e^{i(kz - \omega t)} \quad (3.48)$$

$$\psi_{\theta} = C J_1(qr) e^{i(kz - \omega t)} \quad (3.49)$$

and substituting these into Eqs. 3.45 and 3.47, yields for the displacements

$$u = \{-pA J_1(pr) - ikC J_1(qr)\} e^{i(kz - \omega t)} \quad (3.50)$$

$$w = \{ikAJ_0(pr) + qCJ_0(qr)\} e^{i(kz-\omega t)} \quad (3.51)$$

Here  $p$  and  $q$  are as defined by Eqs. B.34 and B.36, respectively. The two non-trivial boundary conditions which follow from Eqs. B.31a,b and c are

$$\text{at } r = a, \quad \tau_r = (\lambda+2\mu)\frac{\partial u}{\partial r} + \lambda\frac{u}{r} + \lambda\frac{\partial w}{\partial z} = 0 \quad (3.52)$$

$$\text{at } r = a, \quad \tau_{rz} = \mu\left(\frac{\partial u}{\partial z} + \frac{\partial w}{\partial r}\right) = 0 \quad (3.53)$$

If one writes  $(\lambda+2\mu)$  and  $\lambda$  in terms of  $p^2$  and  $q^2$  by manipulating Eqs. B.34 and B.36, and then substitutes Eqs. 3.50 and 3.51 into Eqs. 3.52 and 3.53, two homogeneous equations in terms of the constant coefficients  $A$  and  $C$  are obtained. These are, in matrix form,

$$\begin{bmatrix} \left(-\frac{1}{2}(q^2-k^2)J_0(pa) + \frac{p}{a}J_1(pa)\right) & \left(-ikqJ_0(qa) + \frac{ik}{a}J_1(qa)\right) \\ -2ikpJ_1(pa) & (q^2-k^2)J_1(qa) \end{bmatrix} \begin{Bmatrix} A \\ C \end{Bmatrix} = 0 \quad (3.54)$$

The requirement that the determinant of the coefficients must vanish yields the frequency equation for the longitudinal modes as

$$\frac{2p}{a} (q^2+k^2)J_1(pa)J_1(qa) - (q^2-k^2)^2J_0(pa)J_1(qa)$$

$$- 4k^2pqJ_1(pa)J_0(qa) = 0 \quad (3.55)$$

This equation is known as the Pochhammer-Chree frequency equation, and was first published by Pochhammer (1876). The five variables in Eq. 3.55,  $\omega$ ,  $k$ ,  $a$ ,  $C$ , and  $C_T$  can be reduced to three independent dimensionless variables; the dimensionless velocity,  $C/C_T$ , the dimensionless wave number  $ka$ , and Poisson's ratio,  $\nu$ .

If Eq. 3.55 is multiplied by  $a^4$  and divided by  $J_1(pa)$  and  $J_1(qa)$ , it can be recast in the form

$$2pa[(qa)^2+(ka)^2] - [(qa)^2-(ka)^2]2\frac{J_0(pa)}{J_1(pa)} - 4(ka)^2(pa)(qa)\frac{J_0(qa)}{J_1(qa)} = 0 \quad (3.56)$$

Here it is convenient to redefine  $pa$  and  $qa$  by noting that  $\omega = kc$  and  $k = 2\pi/\lambda$ . Thus,

$$(pa)^2 = \left(\frac{2a}{\lambda}\right)^2\pi^2\left[\left(\frac{C}{\alpha C_B}\right)^2-1\right] \quad (3.57)$$

and

$$(qa)^2 = \left(\frac{2a}{\lambda}\right)^2\pi^2\left[\left(\frac{C}{\gamma C_B}\right)^2-1\right] \quad (3.58)$$

where  $\alpha$  and  $\gamma$  are defined by Poisson's ratio,  $\nu$ , as

$$\alpha^2 = \left(\frac{C_L}{C_B}\right)^2 = \frac{(1-\nu)}{(1+\nu)(1-2\nu)} \quad (3.59)$$

and

$$\gamma^2 = \left(\frac{C_T}{C_B}\right)^2 = \frac{1}{2(1+\nu)} \quad (3.60)$$

It is now possible to solve the frequency equation numerically, by first assuming  $a = 1$ , and choosing a value for  $\nu$ . Then by iterating  $C/C_B$  for a given value of  $2a/\lambda$ , it is possible to find values of  $C/C_B$  which satisfy the frequency equation. This has been done for the first three modes which are illustrated in Fig. 3.6 for Poisson's ratios of 0.30 and 0.49.

This iterative solution technique assumes real values for  $2a/\lambda$ . It is also conceivable that either one or both of the values for  $(pa)^2$  and  $(qa)^2$  could be negative, making them purely imaginary. If this occurs, the corresponding Bessel functions in Eq. 3.56 are replaced with modified Bessel functions.

The vertical axis in Fig. 3.6 is the ratio of the phase velocity to the bar velocity,  $C/C_B$ , known as the dimensionless velocity. The horizontal axis is the dimensionless wave number  $ka/\pi$ . The dimensionless wave number can be written in several different forms, such as:

$$\frac{ka}{\pi} = \frac{\omega a}{\pi C} = \frac{2fa}{C} = \frac{2a}{\lambda} \quad (3.61)$$

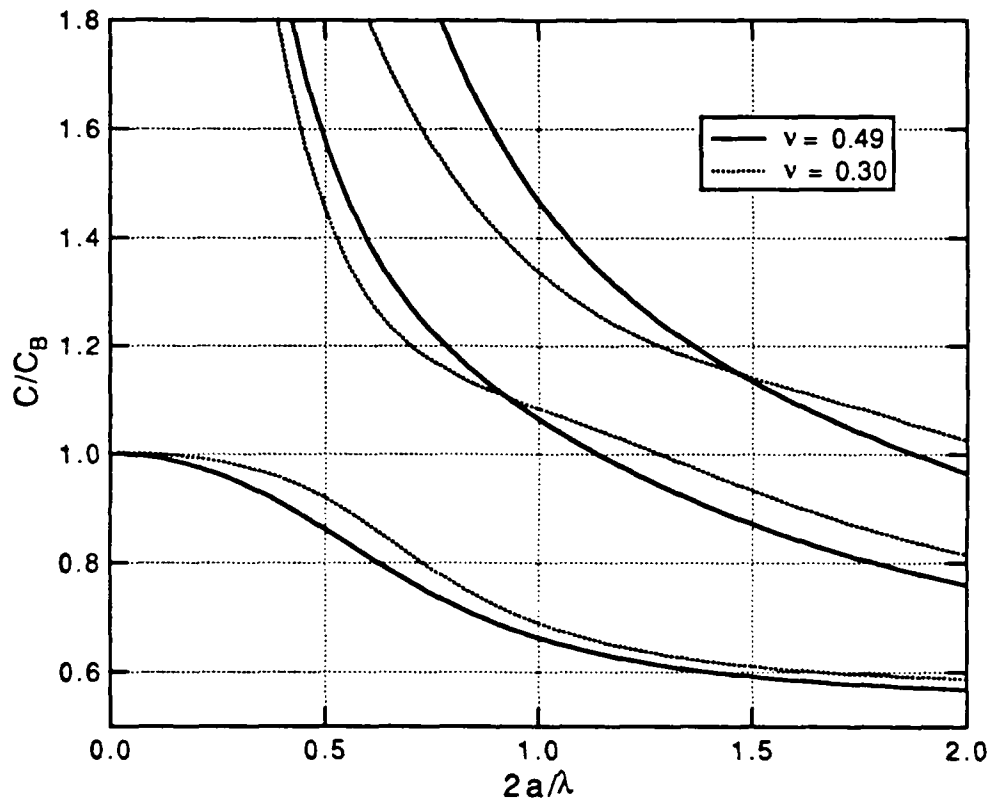


Fig. 3.6. Frequency Spectrum for Longitudinal Waves in a Cylindrical Rod as a Function of Dimensionless Wave Number.

An examination of the lowest longitudinal mode in Fig. 3.6 shows that, as the dimensionless wave number goes to zero, the phase velocity approaches the value of the theoretical bar velocity. Stated in other terms, as the wavelength becomes long with respect to the diameter of the rod,  $2a/\lambda \rightarrow 0$ , the apparent phase velocity approaches the theoretical bar velocity. Conversely, as the wave length becomes short with respect to the diameter of the rod,  $2a/\lambda \rightarrow \infty$ , the phase velocity approaches the Rayleigh wave velocity. Recall that the Rayleigh wave is a surface wave that has a velocity that is on the order of 85-95 percent of the shear wave velocity and whose amplitude decays exponentially with depth from the surface, becoming insignificant at depths greater than about one wavelength below the surface.

The higher longitudinal modes in Fig. 3.6 become asymptotic to the vertical axis as the dimensionless wave number approaches zero, whereas they become asymptotic to the shear wave velocity as the dimensionless wave number becomes infinite. The three modes have been replotted in Fig. 3.7 as functions of frequency by rewriting the frequency equation in terms of  $\omega a/\pi C_B$ . It can be seen there are specific frequencies at which the dimensionless velocity goes to infinity. These frequencies are known as the cutoff frequencies and are easily determined.

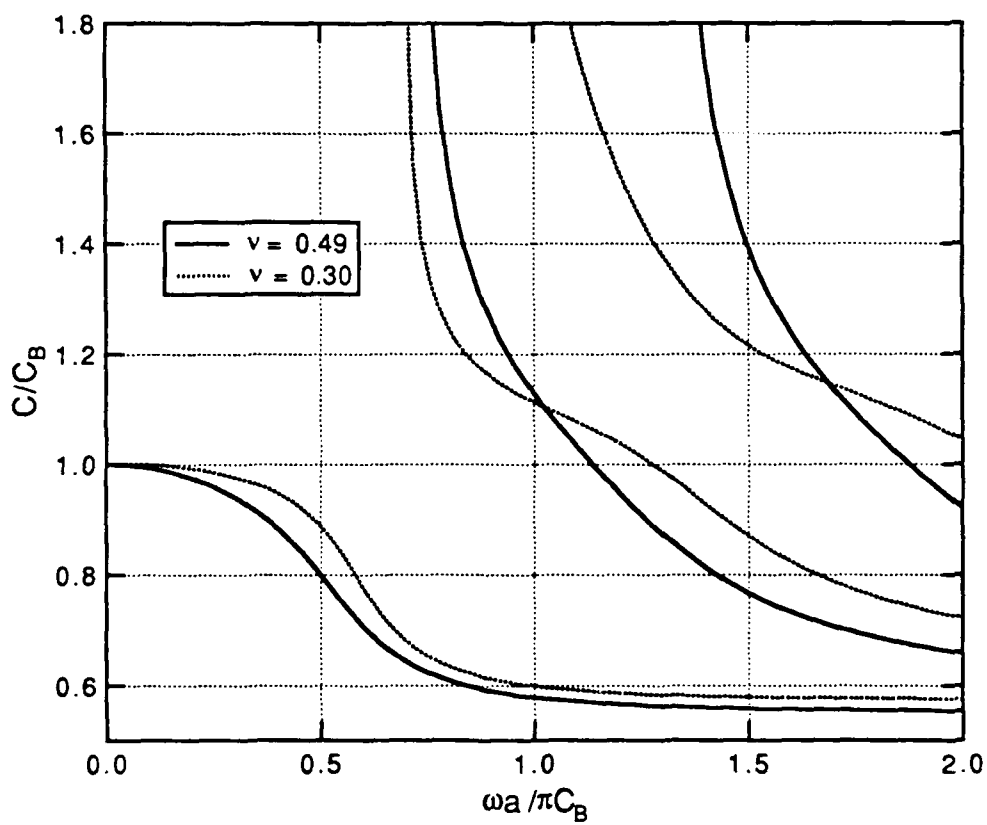


Fig. 3.7. Frequency Spectrum for Longitudinal Waves in a Cylindrical Rod as a Function of Frequency.

As  $k \rightarrow 0$ , Eqs. 3.56, 3.57 and 3.58 become respectively

$$2p'a(q'a)^2 - [(q'a)^2]^2 \frac{J_0(p'a)}{J_1(p'a)} = 0 \quad (3.62)$$

$$(p'a)^2 = \left( \frac{\omega_{co}a}{\alpha C_B} \right)^2 \quad (3.63)$$

$$(q'a)^2 = \left( \frac{\omega_{co}a}{\gamma C_B} \right)^2 \quad (3.64)$$

Substituting Eqs. 3.63 and 3.64 into Eq. 3.62 gives

$$\frac{2\gamma^2}{\alpha^2} - (p'a) \frac{J_0(p'a)}{J_1(p'a)} = 0 \quad (3.65)$$

and values of  $p'a$  which satisfy this transcendental equation yield the cutoff frequencies

$$\frac{\omega_{co}a}{\pi C_B} = \frac{(p'a)\alpha}{\pi} \quad (3.66)$$

### 3.5 Transient Wave Propagation in a Semi-Infinite Solid Cylindrical Rod

The simplest solution for transient waves in a rod assumes a one-dimensional state of stress and the applicable equation of motion, derived in Section 3.2 was

$$\frac{\partial^2 w}{\partial z^2} = \frac{1}{C_B^2} \frac{\partial^2 w}{\partial t^2} \quad (3.67)$$

where  $w$  is the displacement parallel to the longitudinal axis of the rod and  $C_B$  is the theoretical bar velocity defined by (3.12). This wave equation predicts that a pulse will not change shape as it propagates along a rod, however researchers have shown, (Bancroft, 1941, Hudson, 1943 and Davies, 1948), that this is typically not the case. If the pulse is applied rapidly the resulting wave form shows dispersion as it travels along the rod.

The problem considered in this section is illustrated in Fig. 3.8. General methods of solution have been investigated by researchers such as Rosenfeld and Miklowitz (1965) and others. A solution for the axisymmetric case can be obtained using integral transform methods if mixed boundary conditions are specified at  $z = 0$ . Such a solution was presented by Folk et al (1958) and is reproduced in the manner of Achenbach(1973) in Appendix C.

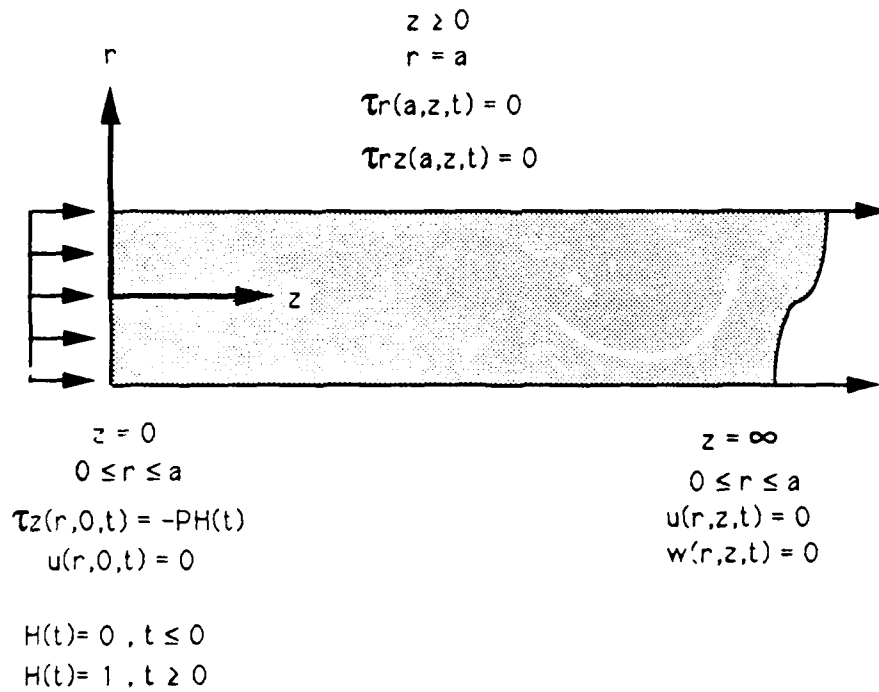


Fig. 3.8. Problem Statement for Transient Wave Propagation in a Semi-Infinite Cylindrical Rod.

The solution presented in Appendix C solves for the particle velocity in the axial direction in the vicinity of the elementary wave front that is travelling at the theoretical bar velocity. That solution is of the form

$$\dot{w}(z, t) = \frac{-P}{\rho c_b} [F_1 + F_2] \quad (3.68)$$

where  $F_1$  and  $F_2$  are given by

$$F_n = \frac{1}{\pi} \int_0^{\infty} \frac{\sin(q_n \eta + \frac{\eta^3}{3})}{\eta} d\eta \quad (3.69)$$

and where

$$q_1 = \frac{z - C_B t}{(3\zeta t)^{1/3}}, \quad q_2 = -\frac{z + C_B t}{(3\zeta t)^{1/3}} \quad (3.70a,b)$$

and

$$\zeta = \frac{1}{4} v^2 C_B a^2 \quad (3.71)$$

In this form  $F_1$  and  $F_2$  can be recognized as integrals of Airy's integral

$$Ai(q_n) = \frac{1}{\pi} \int_0^{\infty} \cos(q_n \eta + \frac{\eta^3}{3}) d\eta \quad (3.72)$$

Thus we can rewrite the expressions for  $F_1$  and  $F_2$  as

$$F_1 = \int_0^{q_1} Ai(s) ds + \frac{1}{6} \quad (3.73)$$

$$F_2 = \int_0^{q_2} Ai(s) ds + \frac{1}{6} \quad (3.74)$$

where the  $1/6$  terms enter as the values for  $F_1$  and  $F_2$  for  $q_1 = 0$  and  $q_2 = 0$ , respectively.

The solution for Eq. 3.68 was determined numerically and plotted in Fig. 3.9 as a function of  $q_1$ . The two solutions shown in Fig. 3.9 are for a rod with a bar wave velocity of 1000 fps, a length of 0.96 ft, a diameter of 0.24 ft and Poisson's ratios of 0.25 and 0.49, respectively. The elementary solution is shown as a solid line in the figure. The integrals in Eqs. 3.73 and 3.74 approach  $-2/3$  for large values of time,  $t$ , and the solution agrees with the elementary solution,  $V = P/\rho C_B$ . Alternatively, for small values of time, the integrals vanish, thus showing that at some distance ahead of and behind the wave front,  $z = C_B t$ , the approximation agrees with elementary theory.

It is important to remember that this approximate solution for transient waves in a cylindrical rod is appropriate at some distance from the end of impact. The evanescent waves produced by the nature of the applied force, an instantaneous step function, may still exist at points close to the end of the rod. The point at which it is safe to use this approximation is a subject of detailed study and not a part of this dissertation. However, it is assumed the solution will at least provide

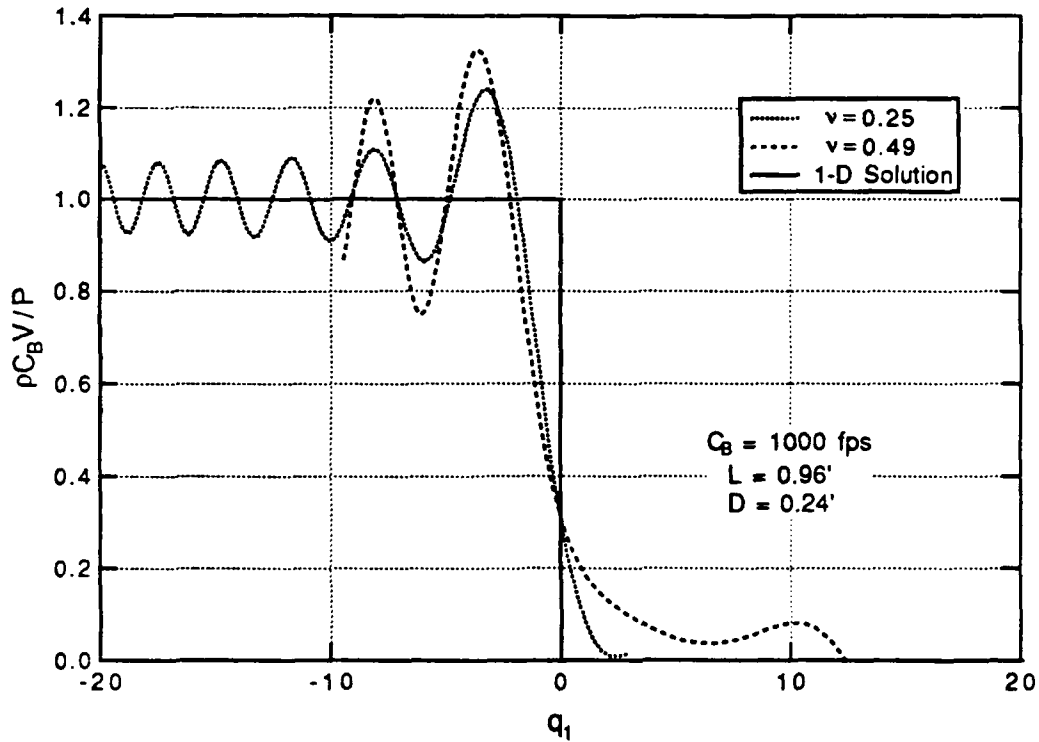


Fig. 3.9. Particle Velocity in the Vicinity of the Elementary Wave front Travelling in a Semi-Infinite Rod Due to a Sudden Impact at the End.

some insight into the behavior of the transient waves in rods with large enough length-to-diameter ratios. In Fig. 3.9, the solution appears to be appropriate for length-to-diameter ratios of at least four.

This approximate solution for transient waves in a rod due to an impact at one end has significant implications for this research. As will be shown in Chapter 6, the fact that theory suggests some energy precedes the arrival of the elementary wave front (travelling at the bar wave velocity) establishes a premise for identifying the first arrivals at a point as those corresponding to a wave travelling at the dilatational velocity.

### 3.6 Summary

The theoretical solution for one-dimensional wave propagation in a finite cylindrical rod is well known. An examination of a particular case, where one end is subjected to a steady-state longitudinal vibration and the other is capped by a rigid mass, shows that resonant frequencies occur at relative phase angles of approximately plus and minus 90 degrees. It was shown that at resonance, the solution for this case is identical to that for a fixed-free rod with an added mass at the free end. The solution relates known sample and added masses to the natural frequencies, sample length and bar wave velocity. Consequently, the bar wave velocity can be computed using one-dimensional theory if the natural frequencies of the specimen can be determined.

Research has shown that the phase velocity,  $C$ , for longitudinal waves in a long cylindrical bar are frequency dependent and are typically less than the theoretical bar wave velocity,  $C_B$ . The three-dimensional

solution for the longitudinal waves travelling in a cylindrical rod applies the assumption of axisymmetry to the general problem statement. The derived frequency equation relates three dimensionless variables: the dimensionless velocity ratio,  $C/C_B$ , the dimensionless wave number,  $ka/\pi$ , and Poisson's ratio. The fundamental mode of this equation shows that for small wave numbers, i.e. long wavelengths with respect to the bar radius, the phase velocity approaches the bar wave velocity. Further, as the wave number becomes very large, i.e. short wavelengths with respect to the bar radius, the phase velocity approaches the value of the Rayleigh wave velocity. Therefore, if the wave number, the phase velocity, and Poisson's ratio are known, it is possible to calculate the theoretical bar wave velocity.

An approximate solution for transient longitudinal waves in a semi-infinite bar, due to a sudden impact on the free end, shows that some wave motion will precede the square wave front which propagates at the bar wave velocity. The solution suggests that some energy may travel at a velocity that approaches that of the dilatational wave velocity.

This brief overview of each of these theoretical solutions is supplemented by detailed developments in Appendices A, B, and C. The particular case for one-dimensional wave propagation in a finite rod, three-dimensional wave propagation in a long cylindrical rod, and transient longitudinal motion in a semi-infinite rod are of specific interest because they provide the basis for the development of the test apparatus and data reduction methods used in this research.

## **Chapter Four**

### **Modelling a Finite Rod Using Axisymmetric Finite Elements**

#### **4.1 Introduction**

A computer program was developed using axisymmetric finite elements to model the response at the top of a finite, isotropic, linearly elastic rod subjected to a steady-state vertical motion at the base. The program was developed to study the impact of various parameters on the response of model test specimens. These parameters include, but are not limited to, specimen stiffness, length, diameter, Poisson's ratio, damping and theoretical end conditions. The program was developed for use on a microcomputer and, in its present form, is limited to solutions of the response at nodes along the top surface of the specimen.

The program outputs a transfer function which relates the motion of points on the top surface to that of the bottom surface as a function of frequency. With this transfer function it is also possible, through the use of Fourier transforms, to predict the time-displacement motion of the top of the model specimen in response to a specified time-displacement motion at the base. Such a program was developed to study briefly the first wave arrivals for several transient input motions.

Three model soils were defined for the study. The first typifies a moderately stiff clay with high material damping, the second typifies a loose sand under low confining pressure with moderate material damping, and the third typifies a dense sand under moderate confining pressure with low material damping. The following sections describe the development of the finite element program and observations concerning changes in the frequency spectrum of the model specimen caused by varying different specimen parameters and boundary conditions.

## 4.2 Development of the Finite Element Program

### 4.2.1 Developing the Axisymmetric Finite Element

The key to the success of the finite element modelling was the use of axisymmetric elements. This allowed modelling a three-dimensional problem as a two-dimensional problem, greatly reducing the computer processing requirements. A complete description of the development of the axisymmetric elements used in this program is contained in Appendix D. A condensation of Appendix D is included in this section for the benefit of the reader.

The equations for the strain displacement  $(u,v,w)$ , and stress-strain relationships expressed in cylindrical coordinates  $(r,\theta,z)$  were

developed and are presented in Appendix A. These relationships can be derived for the axisymmetric case by setting  $v$  and any derivatives with respect to  $\theta$  equal to zero. The strain-displacement equations then become

$$\epsilon_r = \frac{\partial u}{\partial r}, \quad \epsilon_\theta = \frac{u}{r}, \quad \epsilon_z = \frac{\partial w}{\partial z}, \quad (4.1a,b,c)$$

and

$$\gamma_{rz} = 2\epsilon_{rz} = \frac{\partial u}{\partial z} + \frac{\partial w}{\partial r}. \quad (4.2)$$

The stress-strain relationships are derived from Eqs. A.18-A.24, and are given in matrix notation by

$$\tau = \mathbf{D} \epsilon \quad (4.3)$$

where  $\tau$  and  $\epsilon$  are column matrices containing the pertinent stresses and strains, respectively, and  $\mathbf{D}$  is the matrix containing the stiffness parameters that relate them.

Defining a two-dimensional 4-node, linear, finite element as shown in Fig. 4.1, where the  $z$ -axis corresponds to the central axis of

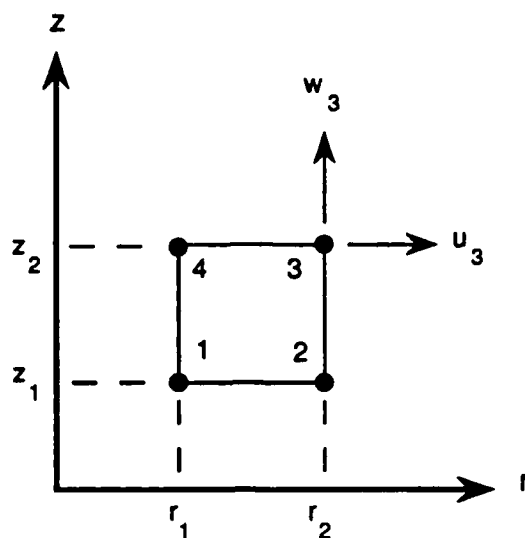


Fig. 4.1. Axisymmetric Finite Element in Global Cylindrical Coordinates.

the cylindrical specimen and the  $r$ -axis is perpendicular to it, and if  $u$  is the displacement in the  $r$ -direction and  $w$  is the displacement in the  $z$  direction, then

$$u = f_n u_n \quad \text{and} \quad w = f_n w_n \quad (4.4a,b)$$

where  $f_n$  are prescribed interpolation functions and  $u_n$  and  $w_n$  are the respective nodal displacements. In matrix notation

$$\begin{Bmatrix} u \\ w \end{Bmatrix} = \mathbf{N}^T \mathbf{U} \quad (4.5)$$

where  $\mathbf{N}^T$  is the matrix of interpolation functions,  $f_n$ , and  $\mathbf{U}$  is a column matrix of the nodal displacements,  $u_n$  and  $w_n$ . It is possible to write the strain-displacement relationships given in Eqs. 4.1 and 4.2 using the interpolation functions and their partial derivatives with respect to  $r$  and  $z$ ,  $f_{nr}$  and  $f_{nz}$ , respectively. These are then

$$\epsilon_r = f_{nr}u_n, \quad \epsilon_\theta = \frac{1}{r}f_nu_n, \quad \epsilon_z = f_{nz}w_n, \quad \text{and}$$

$$\gamma_{rz} = f_{nz}u_n + f_{nr}w_n. \quad (4.6)$$

These can be written in matrix notation as

$$\boldsymbol{\epsilon} = \mathbf{B} \mathbf{U} \quad (4.7)$$

where  $\mathbf{B}$  is the matrix containing the interpolation functions and their derivatives. To form the element stiffness matrix it is first noted that

$$\boldsymbol{\tau} = \mathbf{D} \boldsymbol{\epsilon} = \mathbf{D} \mathbf{B} \mathbf{U} \quad (4.8)$$

and

$$\boldsymbol{\epsilon}^T = \mathbf{U}^T \mathbf{B}^T. \quad (4.9)$$

If the equations of motions for this element are stated in matrix form they would be

$$\mathbf{M} \ddot{\mathbf{U}} + \mathbf{K} \mathbf{U} = \mathbf{P} \quad (4.10)$$

where

- $\mathbf{M}$  = element mass matrix,
- $\mathbf{K}$  = element stiffness matrix,
- $\mathbf{U}$  = nodal displacement matrix,
- $\ddot{\mathbf{U}}$  = nodal acceleration matrix, and
- $\mathbf{P}$  = external forcing functions.

By assuming steady-state motions, and by the virtue of the conservation of work and the definition of internal work, it is possible to show that the element stiffness matrix is given by

$$\mathbf{K} = \int_V \mathbf{B}^T \mathbf{D} \mathbf{B} dV \quad (4.11)$$

Written in global cylindrical coordinates  $\mathbf{K}$  is given by

$$\mathbf{K} = \int_0^{2\pi} \int_{z_1}^{z_2} \int_{r_1}^{r_2} \mathbf{B}^T \mathbf{D} \mathbf{B} r dr dz d\theta . \quad (4.12)$$

It can be shown similarly that the element mass matrix is given in global coordinates as

$$M = \int_0^{2\pi} \int_{z_1}^{z_2} \int_{r_1}^{r_2} \rho \mathbf{N} \mathbf{N}^T r \, dr dz d\theta \quad (4.13)$$

where  $\rho$  is the mass density of the element. The resulting element matrices are 8x8, which corresponds to four nodes multiplied by the two degrees of freedom at each node.

#### 4.2.2 Constructing the Specimen Stiffness Matrix

The finite element model is constructed in layers of elements as is illustrated in Fig. 4.2. Only half of the cylinder needs to be discretized because of the axisymmetry of the problem. Each layer is composed of 1 to 20 elements, and the layer stiffness and mass matrices are constructed using the individual element stiffness and mass matrices developed in the previous section. The arrangement of elements in a layer is illustrated in Fig. 4.3. There can be a maximum of 42 nodes in a layer, and with two degrees of freedom at each node, the resulting layer stiffness and mass matrices have a maximum size of 84x84. The number of layers and number of elements are specified initially. All layers have the same height,  $dz$ , and the same number of elements in the radial direction.

The solver for the finite element model takes advantage of the fact that the combined stiffness matrix for all layers will contain only

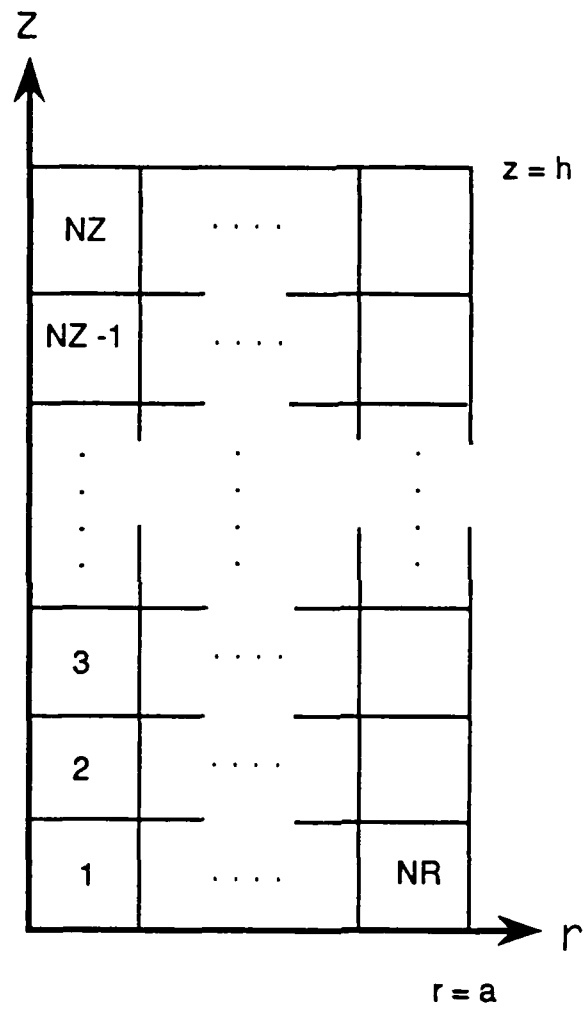


Fig. 4.2. Finite Element Model Construction.

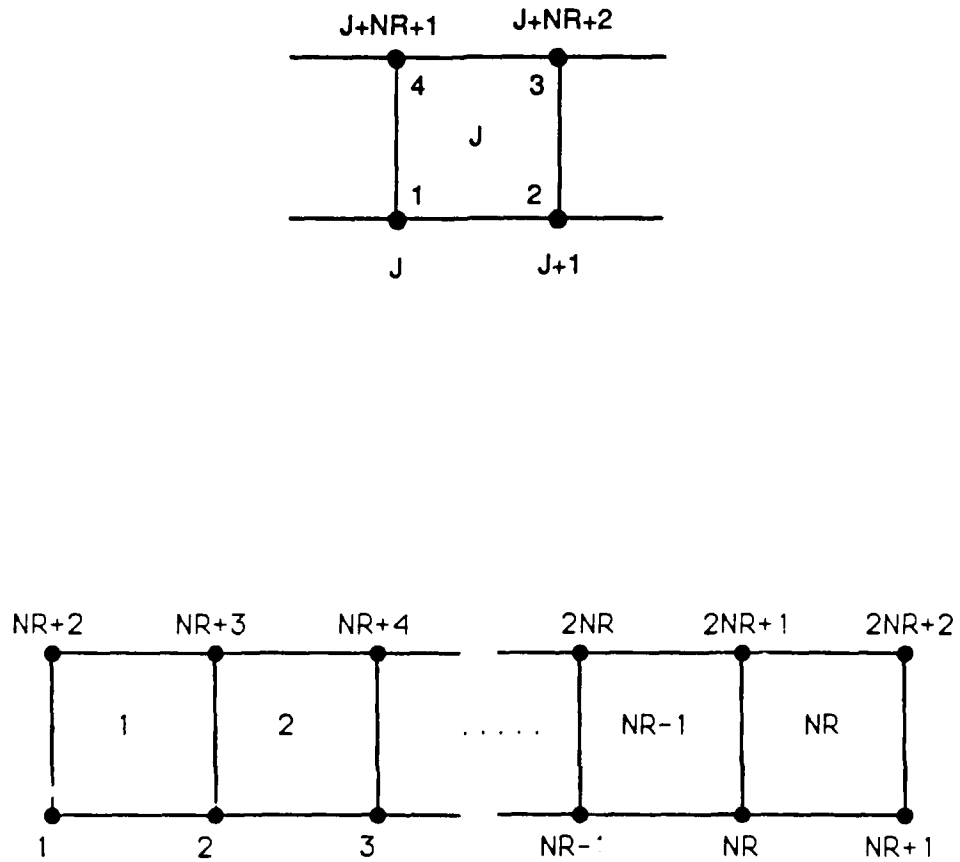


Fig. 4.3. Element and Node Arrangement in a Single Layer of the Finite Element Model.

non-zero values that are confined to a band not greater than 168 (2x84) values on each side of the diagonal. If we call  $\mathbf{S}$  the dynamic stiffness matrix for a layer and partition it as

$$\mathbf{S} = \begin{bmatrix} \mathbf{S}_{11} & \mathbf{S}_{12} \\ \mathbf{S}_{21} & \mathbf{S}_{22} \end{bmatrix} \quad (4.14)$$

where the subscript 1 refers to the degrees of freedom at the bottom face of a layer and the subscript 2 to those of the top face, the equations of motion are of the form

$$\begin{bmatrix} \mathbf{S}_{11} & \mathbf{S}_{12} & & & \\ \mathbf{S}_{21} & \mathbf{S}_{22} + \mathbf{S}_{11} & \mathbf{S}_{12} & & \\ & \dots & \dots & \dots & \\ & \mathbf{S}_{21} & \mathbf{S}_{22} + \mathbf{S}_{11} & \mathbf{S}_{12} & \\ & & \mathbf{S}_{21} & \mathbf{S}_{22} & \end{bmatrix} \begin{Bmatrix} \mathbf{U}_1 \\ \mathbf{U}_2 \\ \vdots \\ \mathbf{U}_{n+1} \end{Bmatrix} = \begin{Bmatrix} \mathbf{P}_1 \\ \mathbf{P}_2 \\ \vdots \\ \mathbf{P}_{n+1} \end{Bmatrix} \quad (4.15)$$

If all the layers have the same properties, then the matrix  $\mathbf{S}$  needs only be formed once. The solution is then obtained by initially letting

$$\mathbf{S}'_{11} = \mathbf{S}_{11} ,$$

$$\mathbf{P}'_1 = \mathbf{P}_1 ,$$

$$\mathbf{S}'_{22} = \mathbf{S}_{22} - \mathbf{S}_{21}(\mathbf{S}'_{11})^{-1}\mathbf{S}_{12} , \text{ and}$$

$$\mathbf{P}'_2 = \mathbf{P}_2 - \mathbf{S}_{21}(\mathbf{S}'_{11})^{-1}\mathbf{P}_1 .$$

Then repeating  $n$  times,

$$\mathbf{S}'_{11} = \mathbf{S}_{11} + \mathbf{S}'_{22} ,$$

$$\begin{aligned}
 P'_1 &= P'_2 , \\
 S'_{22} &= S_{22} - S_{21}(S'_{11})^{-1}S_{12}, \text{ and} \\
 P'_2 &= - S_{21}(S'_{11})^{-1}P'_1 .
 \end{aligned}$$

Finally, the desired displacements at the top are given by

$$U = (S'_{22})^{-1}P'_2 . \quad (4.16)$$

#### 4.2.3 Specified Boundary and End Conditions

The boundary and optional end conditions are illustrated in Fig. 4.4. The radial displacement is fixed on the centerline due to the axisymmetric assumption, but the axial displacement is not. The radial and axial displacements are free on the outer surface of the rod, except as prescribed at the ends. Also, it is assumed that the outer surface remains free of external stresses.

The program has more flexibility in prescribing the end condition along the base,  $z = 0$ . The number of nodes subjected to a unit vertical displacement can be specifically identified and can be less than the total along the base, allowing modelling of cases where only part of the

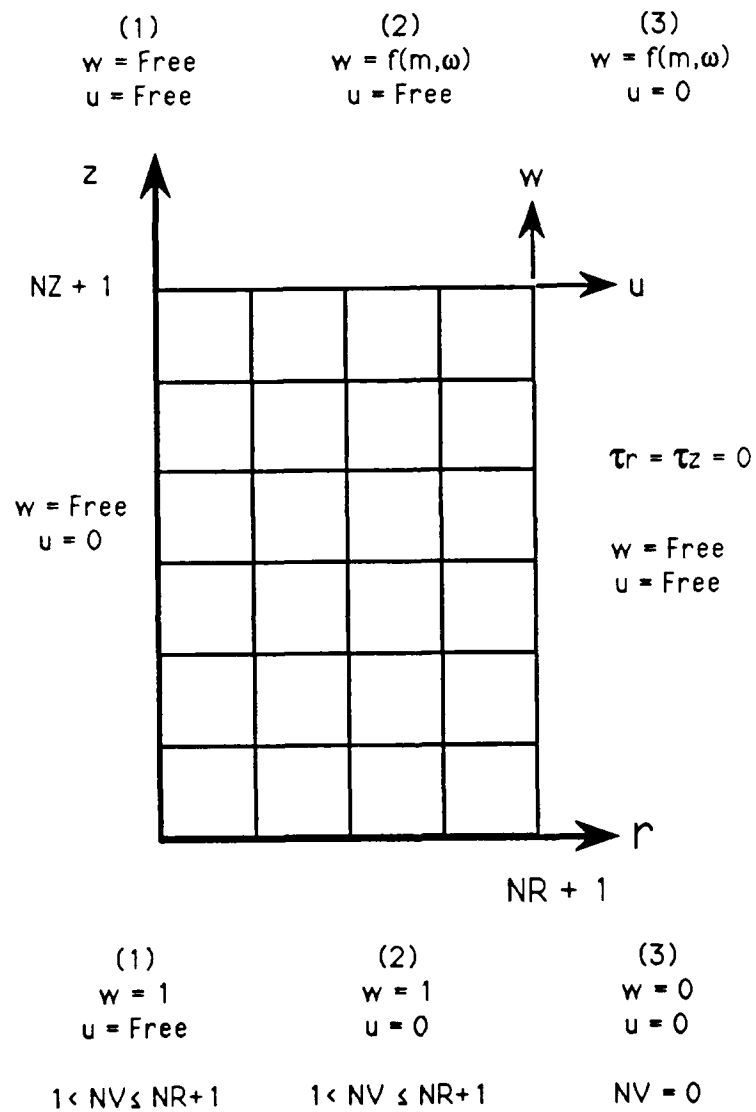


Fig. 4.4. Boundary Conditions for Finite Element Model.

base is supported. A second special base condition fixes the vertical displacements and subjects the single center node to a vertical unit force. The radial displacement can be specified as fixed or free in either case.

There are two choices for the end condition at the top,  $z = h$ . First, the top surface can be specified free, not limiting either the axial or radial displacements. Secondly, it can be specified as having a rigid, distributed mass creating an end condition in which all the vertical displacements are forced to be equal. Consequently, a vertical stress is applied due to the inertia of the mass. The radial displacement can also be specified as fixed or free when the rigid mass is present, and will be the same as is specified for the bottom.

A qualitative study of the impact that each of these end conditions has on the model's response is included in Section 4.4. A comparison of the model response and a response measured in an actual laboratory test is discussed in Chapter 7.3.

#### 4.2.4 Program Input/Output

The finite element program was written with two input versions; one uses screen and keyboard interaction and the second reads input directly from a file. The input information required is listed in Table 4.1 and is briefly described below.

Table 4.1. Input Variables for Finite Element Model.

Input Parameter	Units	Program Variable
<b>A. <u>Element Description</u></b>		
No. of Layers	Each	NZ
No. of Elements	Each	NR
Total Height	inches	H
Element Thickness	inches	$T_i, i = 1 \Rightarrow NR$
<b>B. <u>Material Properties</u></b>		
Young's Modulus	psi	E
Shear Modulus	psi	G
Poisson's Ratio		PR
Unit Weight	pcf	GAM
Damping Ratio		DAMP
<b>C. <u>Boundary Conditions</u></b>		
No. of Displaced Nodes at Base	Each	NV
Weight of Added Mass, Horizontal Fixity (Top & Bottom)	lbs	AMASS IHOR
<b>D. <u>Frequency Range</u></b>		
Starting Frequency	Hz	BFR
Ending Frequency,	Hz	EFR
Initial Frequency Increment	Hz	DF

**Element Size/Dimension:** The operator provides the number of vertical layers and the total height, in inches, of the model specimen. The program divides the total height by the number of layers so that each layer has the same height. The total number of radial elements

and their individual thicknesses in inches are input by the operator starting with the inner element first. The radial dimensions of the respective elements are the same for each layer.

Material Properties: Two of the following three material properties must be entered: Young's Modulus, shear modulus, and Poisson's ratio. The missing property is entered as zero and determined from the other two by assuming isotropic properties. The total unit weight is entered in pounds per cubic foot and the damping is entered as a decimal, for example,  $D = 0.05$  for 5 percent material damping. The model uses hysteretic damping so the material constants are converted to complex form using the input value for damping ( $G^* = G[1+iD]$ ).

Boundary Conditions: The number of displaced nodes at the base is entered. This is equal to the number of fully supported elements plus one. If a point load at the center of the base is desired, a zero is entered. If there is an added mass at the top, its weight is entered in pounds. If a zero is entered for the added mass, the top boundary is free. Lastly, the horizontal displacement condition at the top and bottom is specified as fixed or free.

Frequency Range: The starting and ending frequency of the desired frequency range are entered along with the initial frequency increment. The program will automatically increment at 1X, 0.1X, or 0.01X the specified increment depending on the change in magnitude

of the transfer function, as determined by the two previous frequency increments.

The output from the program is the response of the nodes along the top surface for each steady state frequency. Only the response of the node on the centerline was of interest in this study, although the program could output both the horizontal and vertical displacements for each top node. The response for a specific node is in the form of a complex transfer function. (The transfer function in this form can be read by another program to estimate the response, in the time domain, to a transient input motion at the base). However, it is difficult to interpret a transfer function in its complex form so it is converted and displayed using amplification ratios and phase differences.

The amplification ratio at a particular frequency is the magnitude of the complex value of the transfer function, and the phase difference is the arctangent of the ratio of the imaginary and real part of the complex value. A simple conversion program reads the complex value of the transfer function at each frequency and produces a second output file which lists the amplification and phase at each corresponding frequency. The transfer function in this form can then be graphed in a manner which is identical to that produced by the dynamic signal analyzer (DSA) used for the longitudinal resonant column test described in Chapter 7. This provides tremendous utility in comparing the effect of different parameters on the response of a specimen and permits a direct comparison with measurements made in the laboratory.

### 4.3 Frequency Responses of Three Model Soils

Three model soils were chosen to study the effect of several test parameters on the predicted response. These soils represent a moderately stiff clay, a loose sand under low confining pressure and a dense sand under moderate confining pressure. Their baseline properties and dimensions are summarized in Table 4.2. The material parameters have been related assuming the model soils are linearly elastic, isotropic materials with hysteretic damping. The minimum element size was selected as one-tenth of the minimum wavelength that was computed by dividing the shear wave velocity by the highest desired frequency. The shear wave velocity was chosen because it is the lowest of the three velocities ( $V_s < V_c < V_p$ ), and thus, it is the most conservative.

The frequency response (transfer function) for each model soil is illustrated in Figs. 4.5, 4.6, and 4.7, where both the relative amplification and phase are shown for each soil. These response curves are for the top node on the centerline of the mesh, a point which corresponds to the location of the top vertical accelerometer in the test apparatus. Each case here assumes a free surface (no added mass) at the top and unrestrained horizontal motions at the base.

The one qualitative observation which is common to all response curves, regardless of the input parameters, is that the peak amplitudes essentially correspond to phase angles of plus or minus 90 degrees.

Table 4.2. Typical Characteristics of Three Model Soils.

<u>Parameter</u>			<u>Stiff Clay</u>	<u>Loose Sand</u>	<u>Dense Sand</u>
Shear Wave Velocity	fps	$C_T$	650	350	800
Bar Wave Velocity,	fps	$C_B$	1115	564	1239
Compressive Wave Velocity	fps	$C_L$	2732	655	1306
Poisson's Ratio		$\nu$	0.47	0.30	0.20
Unit Weight	pcf	$\gamma$	95	95	105
Damping Ratio		D	0.05	0.02	0.002
Length	in	L	5.6	6.3	6.3
Radius	in	a	1.4	1.4	1.4
Length-Diameter Ratio		$\frac{L}{2a}$	2.0	2.25	2.25
Shear Modulus	psi	G	8664	2512	14506
Young's Modulus	psi	E	25472	6531	34815
Constrained Modulus	psi	M	153070	8793	38683
Maximum Frequency	Hz	F	5000	2500	5000
Minimum Element Size ( $C_T/10F$ )	in	dr	0.156	0.168	0.192
Element Mesh Size			9 x 36	9 x 38	8 x 33

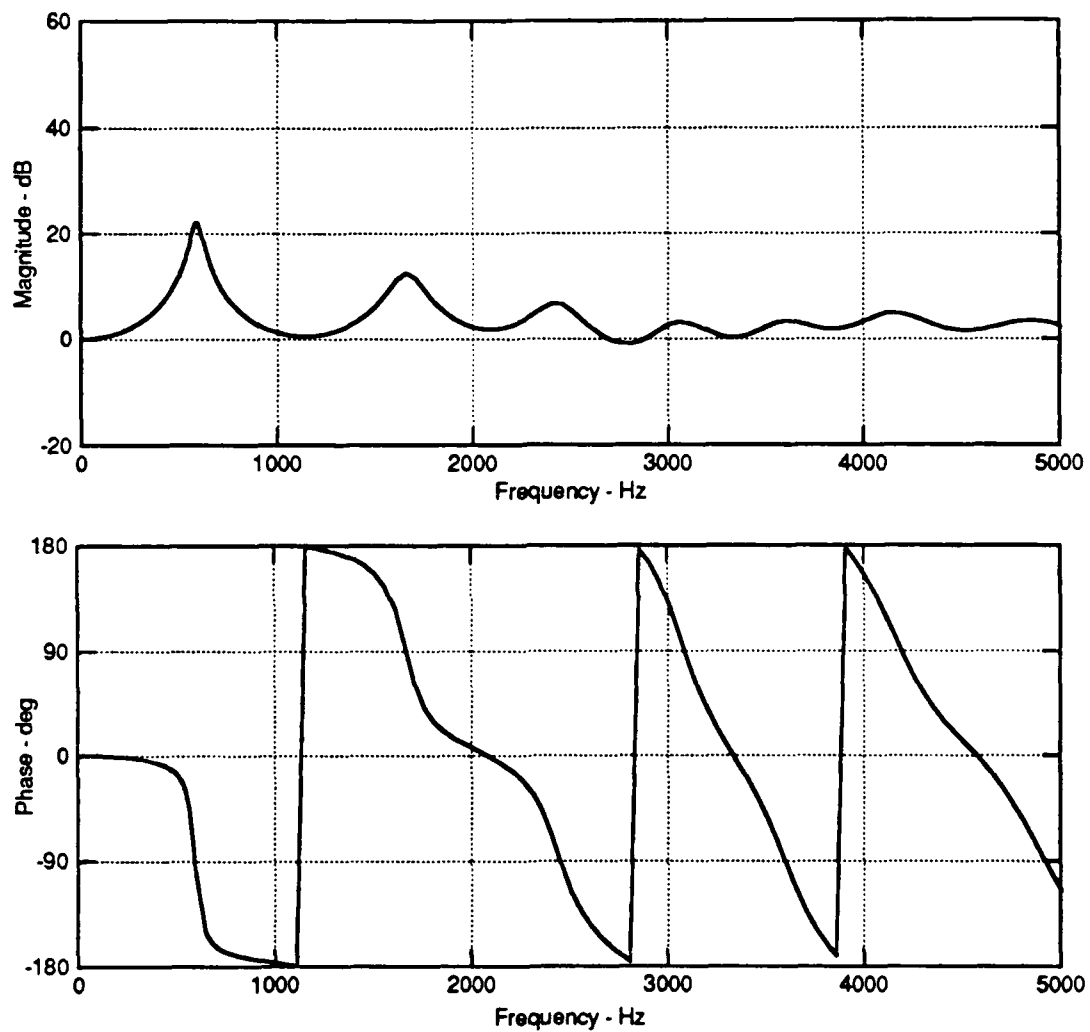


Fig. 4.5. Transfer Function of Model Clay Specimen;  $L = 5.6$  in,  $2a = 2.8$  in,  $V_s = 650$  fps, and no added mass.

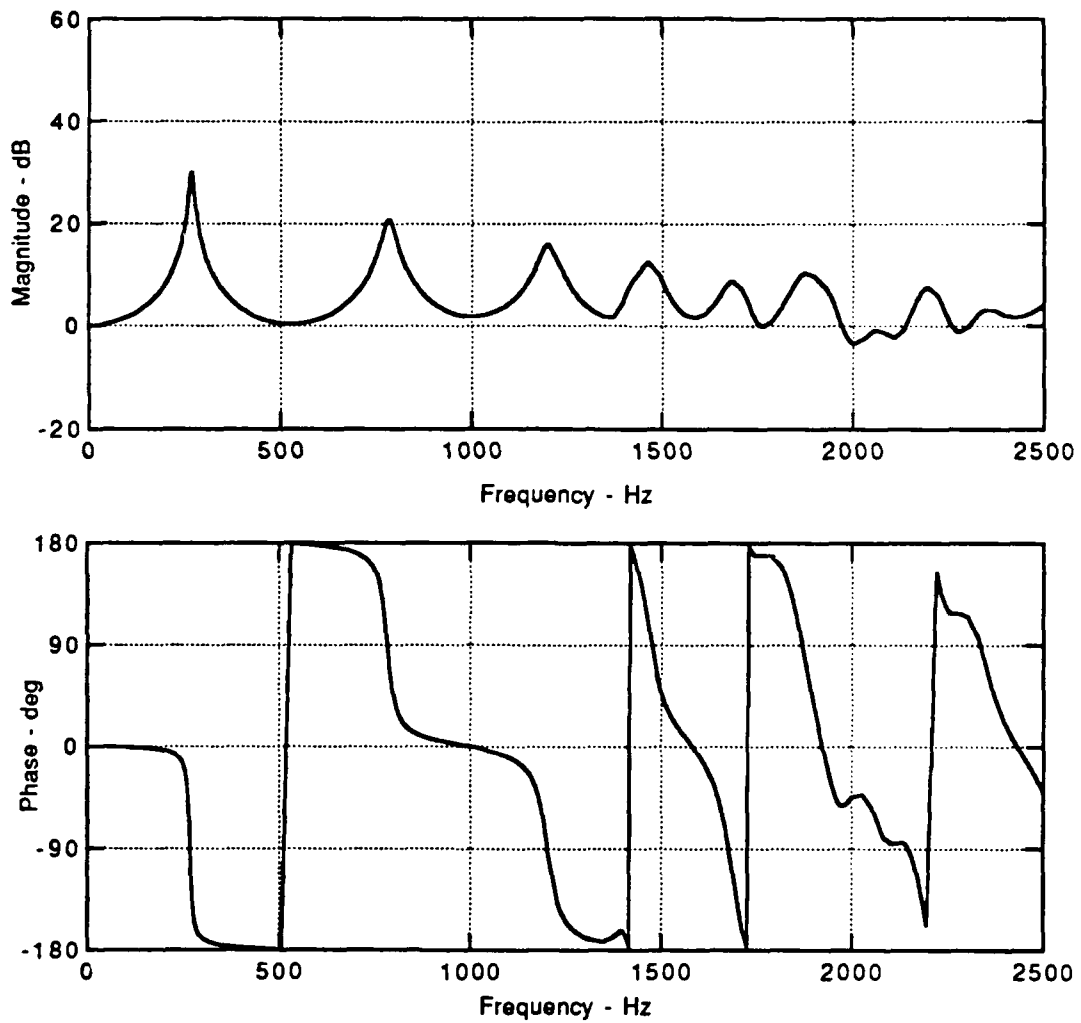


Fig. 4.6. Transfer Function of Model Loose Sand Specimen;  $L = 6.3$  in,  $2a = 2.8$  in,  $V_s = 350$  fps, and no added mass.

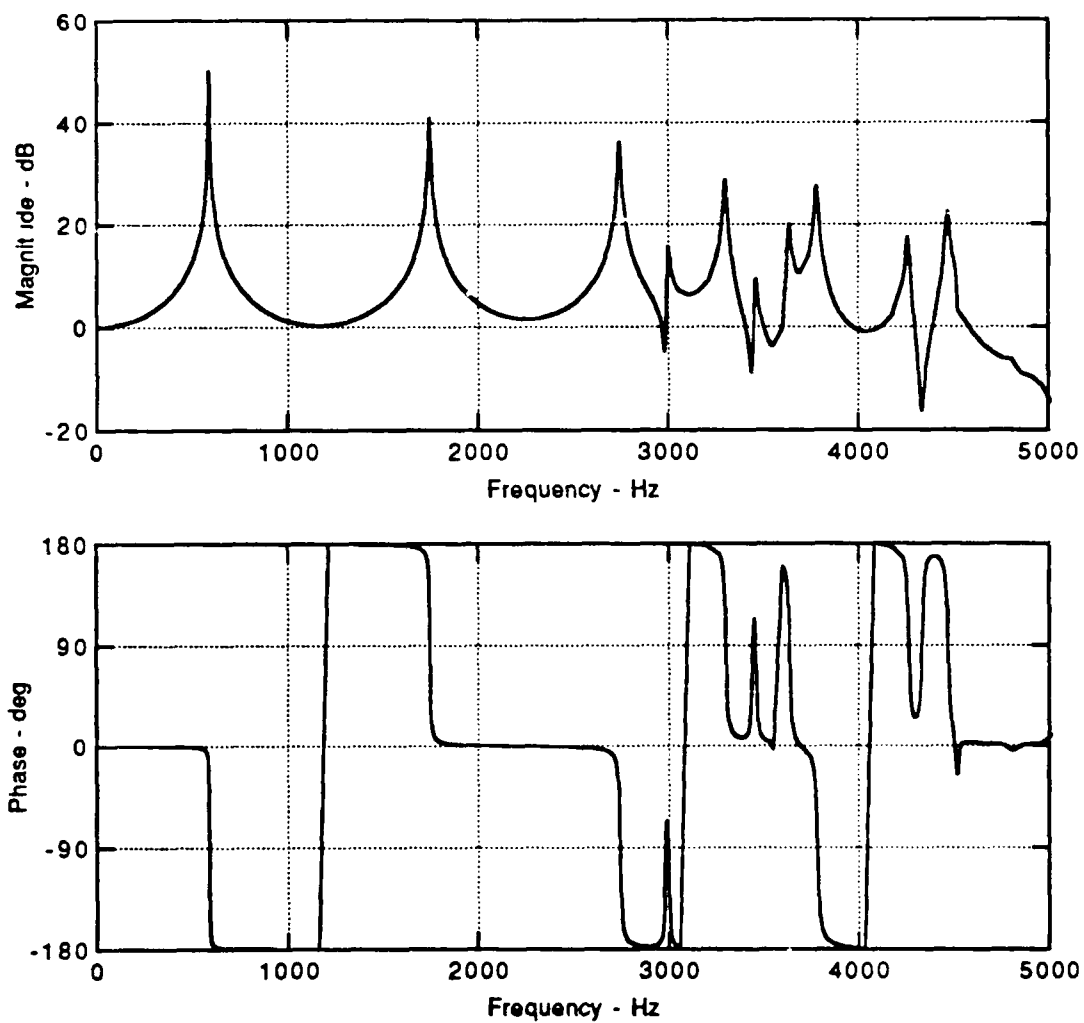


Fig. 4.7. Transfer Function of Model Dense Sand Specimen;  $L = 6.3$  in,  $2a = 2.8$  in,  $V_s = 800$  fps, and no added mass.

at  $\pm 90$  degrees,  $f_n$ , which is the natural frequency of the undamped specimen. This correspondence at  $\pm 90$  degrees phase is in accordance with the solution for one-dimensional wave propagation in a finite rod subject to steady-state displacement and inertial mass end conditions as is discussed in Section 3.3.

A number of qualitative observations can be drawn by varying the specimen input parameters and comparing the resulting transfer functions. This has been done and is described in the following section. The effect of changes in the specified end conditions is a more complex subject and will be addressed in Section 4.4.

#### 4.3.1 Effect of Stiffness on the Transfer Function of Three Model Soils

The qualitative effect of stiffness on the frequency response of a specimen can be deduced by comparing the amplification curves of each of the three model soils. It is easily noted by examining Figs. 4.6 and 4.7 that, as soil stiffness increases, the magnitude of the natural frequency corresponding to each relative mode increases. For example, the frequencies of the first peak amplitude for the loose and dense sand are approximately 275 and 600 Hz for Young's moduli of 6,531 and 34,815 psi, respectively. This is consistent with one-dimensional theory which suggests that frequency is proportional to the square root of the stiffness. An exact correlation is not possible here

because the other parameters such as damping and Poisson's ratio are also varying. Their relative effects on specimen response are discussed in the following sections.

#### 4.3.2 Effect of Damping Ratio on the Transfer Function of a Loose Sand

The transfer functions of the dense sand,  $D = 0.2\%$ , and two model clays,  $D = 5.0\%$  and  $D = 20\%$ , are shown together in Fig. 4.8. Although a material damping value of 20% is high for a typical clay, some of the polyurethane specimens that were tested (see Chapter 8) had damping values nearly this high. Figure 4.9 shows the frequency responses of the model loose sand at three damping ratios,  $D = 5.0\%$ ,  $D = 2.0\%$  and  $D = 0.5\%$ , which correspond to typical values for material damping in most soils.

Several qualitative observations are immediately apparent. As the damping ratio increases, the magnitudes of the corresponding peaks in the amplification curve decrease. It also can be shown that the frequency corresponding to the peak at each mode,  $f_r$ , decreases slightly with increasing damping. It can be further noted that the decrease in magnitude of successive amplitude peaks becomes greater as the damping ratio increases. Lastly, the peaks are not only lower but broader for successively higher modes.

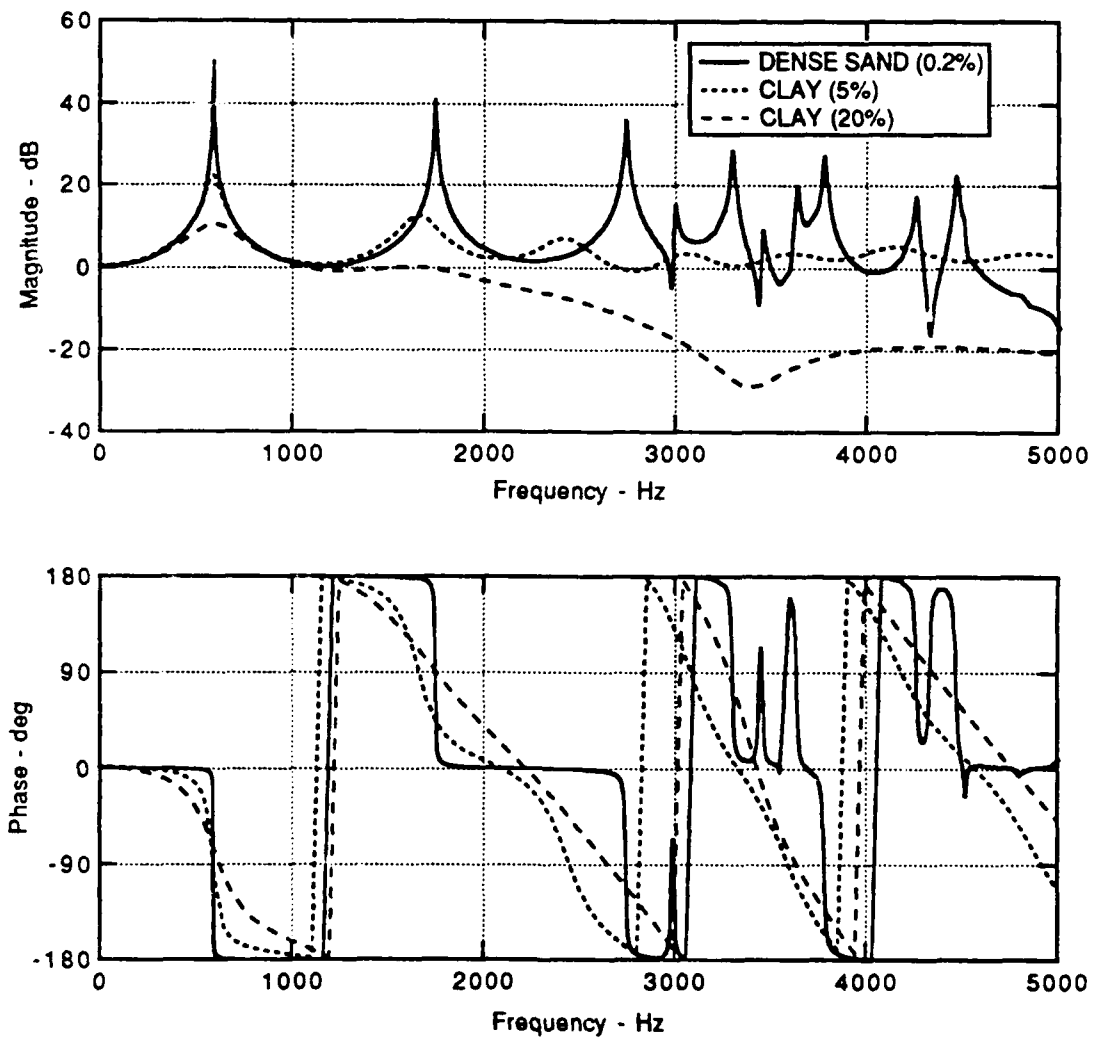


Fig. 4.8. Transfer Functions for Model Dense Sand and Two Model Clays.

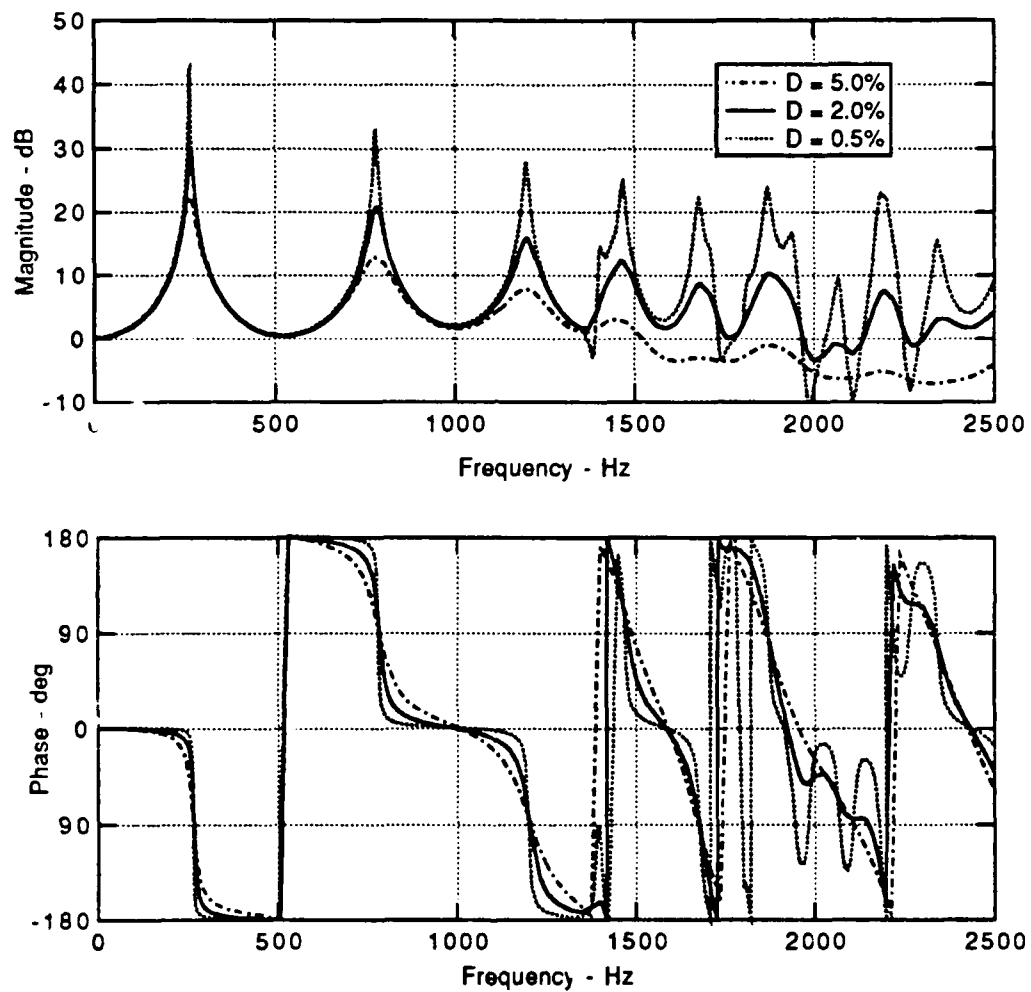


Fig. 4.9. Effect of Damping on the Transfer Function of Model Loose Sand;  $L = 6.3$  in,  $2a = 2.8$  in,  $V_s = 350$  fps, and no added mass.

Additional observations can be made by examining the phase diagrams in Figs. 4.8 and 4.9. The slope of the phase diagram in the vicinity of the natural frequency (at  $\pm 90^\circ$ ) is steeper for lower values of damping, and the slope subsequently decreases for consecutively higher modes. Further, the values of the natural frequencies increase for very high damping values, most likely reflecting the increase of damping in the stiffness value. However, it appears that small changes in damping do not affect the value of the natural frequency when damping is confined to a range between 0.5 and 5.0 percent.

This behavior in both the amplitude and phase response curves can be compared to the single-degree-of-freedom system such as that illustrated in Fig. 4.10 from Richart et al (1970). Similar behavior is noted for  $f_r$  and  $f_n$  as was seen for the range of damping values (0.2% - 5.0%) and frequencies (0-5000 Hz) used for this study.

#### 4.3.3 Effect of Length and Diameter on the Transfer Function of a Loose Sand

In order to examine the impact of changes in the length or the diameter on the response of a specimen, five differently sized specimens were chosen for the model loose sand. Three of the specimens had the same radius and different lengths and three had the same length and different diameters.

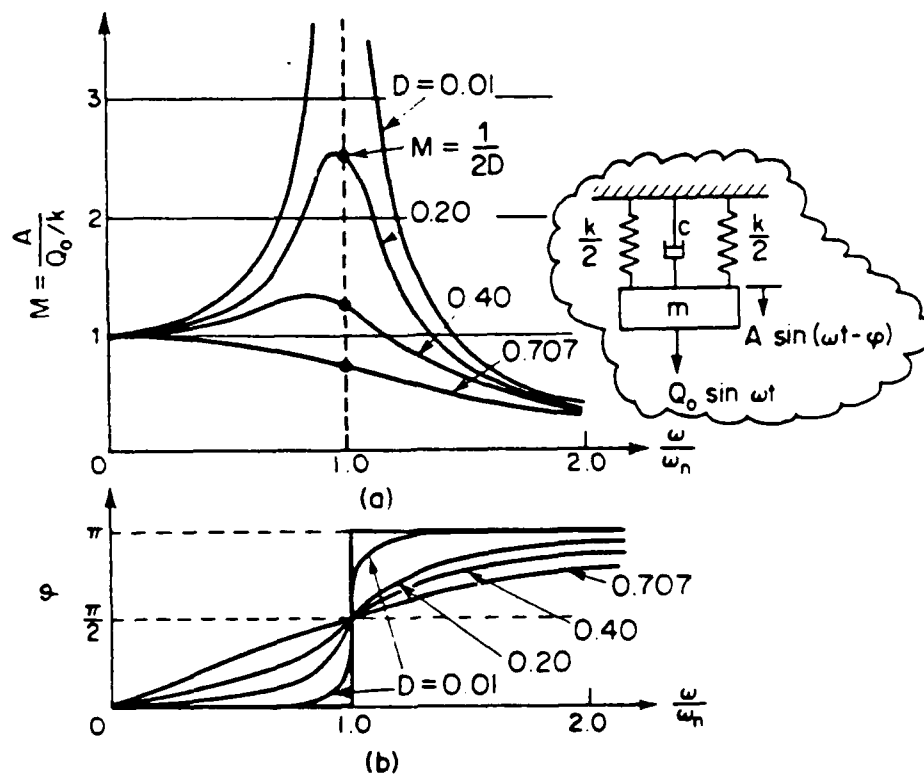


Fig. 4.10. Response Curves for a Viscously Damped Single-Degree-of-Freedom System. (From Richart et al, 1970)

The effect of length on the transfer function is illustrated in Fig. 4.11. It is apparent that the natural frequency of each respective mode decreases as the sample length increases. This follows directly from the one-dimensional solution which shows for the fixed-free case,

$$\omega_n = \frac{(2n-1)}{2L} \quad (4.30)$$

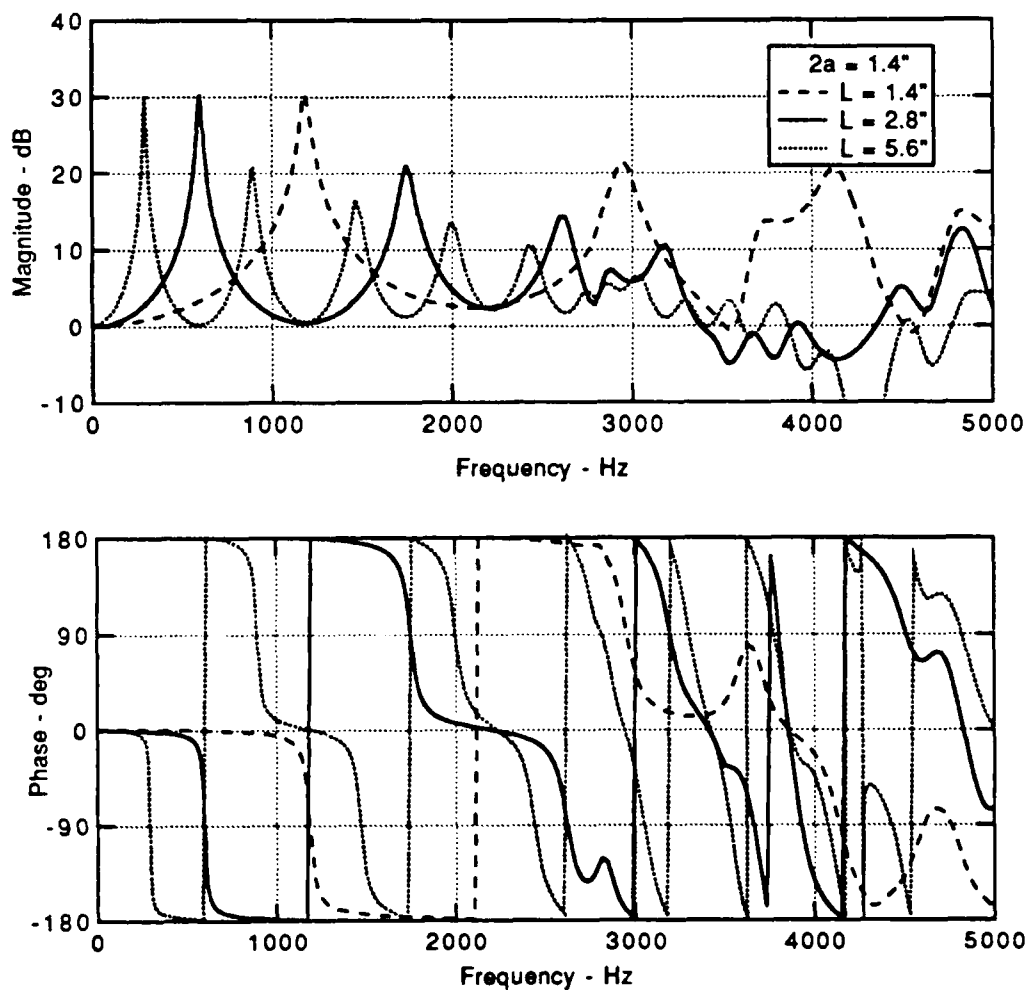


Fig. 4.11. Effect of Specimen Length ( $L$ ) on the Transfer Function of a Model Loose Sand;  $2a = 1.4$  in,  $D = 2.0\%$ ,  $V_s = 350$  fps, and no added mass.

or that the natural frequency is simply inversely proportional to the sample length.

The effect of diameter (2a) is illustrated in Fig. 4.12. It can be seen that the number of modes clearly visible without interference from higher frequency motions decreases as the diameter increases, or as the length-to-diameter ratio decreases. These high frequency motions could be due to the higher propagating modes described in the three-dimensional solution for waves propagating in an infinite rod (discussed in Chapter 3). Without specifically explaining their cause, it is obvious that the presence of these high frequency motions prohibits the clear identification of the natural frequencies which are required to compute the Young's modulus. Specimens tested in this research normally had length-to-diameter ratios of 2.0 to 2.5, and were primarily limited to this size because of the test apparatus. Nevertheless, it was normal to clearly observe three or four natural frequencies.

#### 4.3.4 Effect of Poisson's Ratio on the Transfer Function of a Dense Sand

The transfer functions of the model dense sand at three different values of Poisson's ratio are shown in Fig. 4.13. In this exercise, the value of the Young's modulus was held constant and the shear

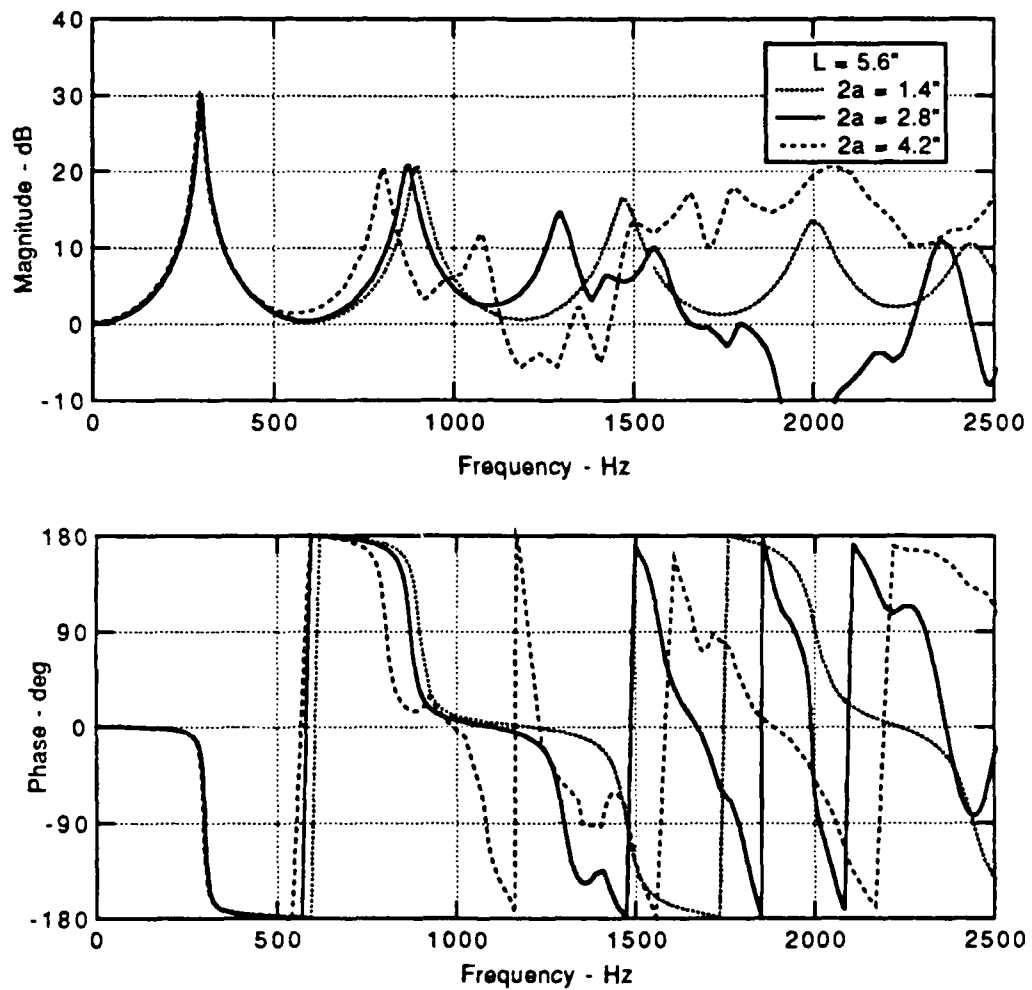


Fig. 4.12. Effect of Specimen Diameter ( $2a$ ) on the Transfer Function of a Model Loose Sand;  $L = 5.6$  in,  $D = 2.0\%$ ,  $V_s = 350$  fps, and no added mass.

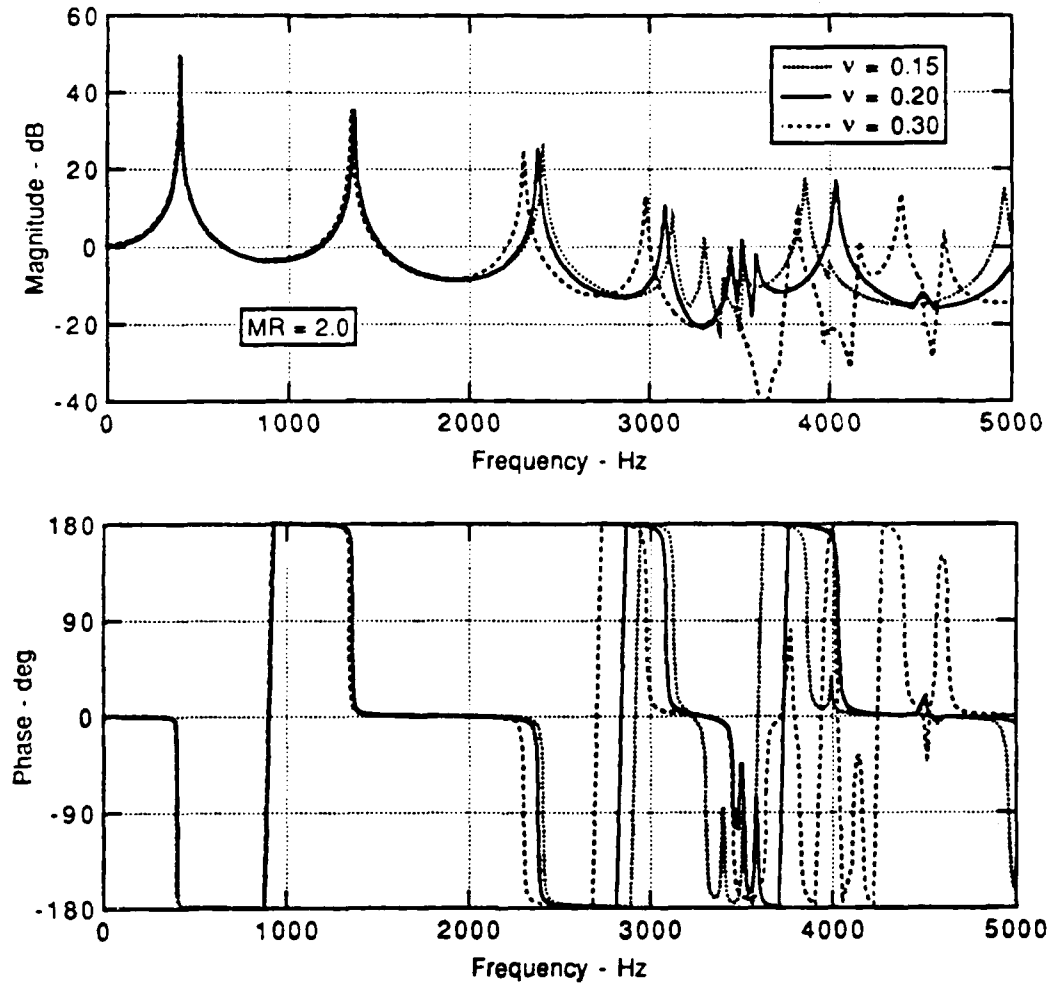


Fig. 4.13. Effect of Poisson's Ratio on the Transfer Function of a Model Dense Sand;  $L = 6.3$  in,  $2a = 2.8$  in,  $D = 0.2\%$ ,  $V_s = 800$  fps, and  $MR = 2.0$ .

Table 4.3. Effect of Poisson's Ratio on the Response of a Model Dense Sand\*.

a. Comparison of Natural Frequencies

Poisson's Ratio	Natural Frequency**, $f_n$ , Hz			
	Mode 1	Mode 2	Mode 3	Mode 4
0.15	405.3	1364.7	2415.3	3137.2
0.20	405.8	1360.2	2380.8	3088.9
0.30	404.9	1348.3	2308.2	2988.3

b. Comparison of Computed Velocities

Poisson's Ratio	Bar Wave Velocity+, $V_c$ , fps			
	Mode 1	Mode 2	Mode 3	Mode 4
0.15	1240.8	1241.4	1241.5	---
	0.10%++	0.15%	0.15%	---
0.20	1242.6	1241.4	1241.7	1240.9
	0.24%	0.15%	0.17%	0.10%
0.30	1240.8	1241.7	1242.4	1242.8
	0.10%	0.17%	0.23%	0.26%

\*  $L = 6.3$  in,  $2a = 2.81$  in,  $C_B = 1239.6$  fps,  $D = 0.2\%$ ,  $MR = 2.0$

\*\* Natural Frequencies determined at  $\phi = \pm 90^\circ$ .

+ Computed using reduction program described in Chapter 7.

++ Percent change from input value of bar wave velocity.

modulus was varied to obtain the appropriate values of Poisson's ratio.

The responses were compared for a model specimen with an added mass that was half of the mass of the specimen (resulting in a mass ratio, MR, of 2.0). Table 4.3 compares the natural frequencies and the

bar wave velocities (computed in a manner described in Chapter 7) for each value of Poisson's ratio.

It appears Poisson's ratio has little effect on the computed natural frequencies or on the value of the bar wave velocity computed from them. It has no discernable effect on the frequency of the first mode and causes less than one quarter of a percent error in the computed velocities for any mode. It is reasonable to expect that any significant variations in Poisson's ratio will probably be accompanied by significant changes in other properties such as stiffness, the effect of which will likely overshadow any effects attributable to changes in Poisson's ratio.

#### 4.4 The Effect of End Conditions on the Transfer Function of a Dense Sand

The finite element program was especially written with the ability to change the end conditions in order to examine their effect on the transfer functions of the model specimens. Of particular concern is the effect of a rigid mass at the top, the amount of base support and the horizontal fixity at the ends. Each of these points is addressed separately in the following paragraphs.

#### 4.4.1 Effect of a Rigid Top Mass on the Transfer Function of a Dense Sand

Almost all dynamic laboratory tests involving soil have an added mass at the top of the specimen because of the presence of a top cap and accelerometers for dynamic measurements. Only in the case of synthetic or pavement materials can an accelerometer be glued directly to the test specimen and its presence be neglected, providing its weight is small compared to that of the specimen's. Further, in the case of a soil specimen using a top cap, the relative stiffness between the material of the top cap (in this case stainless steel) and the soil is quite large. Therefore, the top cap is presumed rigid with respect to the soil, and it is assumed that the vertical displacements along the top of the specimen are forced to be equal.

To examine the effect of a rigid mass at the top of a specimen two more transfer functions were computed for the dense sand assuming added masses weighing 1.179 and 4.714 pounds, corresponding to mass ratios of 2.0 and 0.5, respectively. (Recall the mass ratio was defined in Chapter 3 as the mass of the sample divided by the added mass at the top.) The resulting transfer functions are plotted along with the free surface transfer function in Fig. 4.14. The natural frequencies and computed bar wave velocities for each of the first four modes are summarized in Table 4.4.

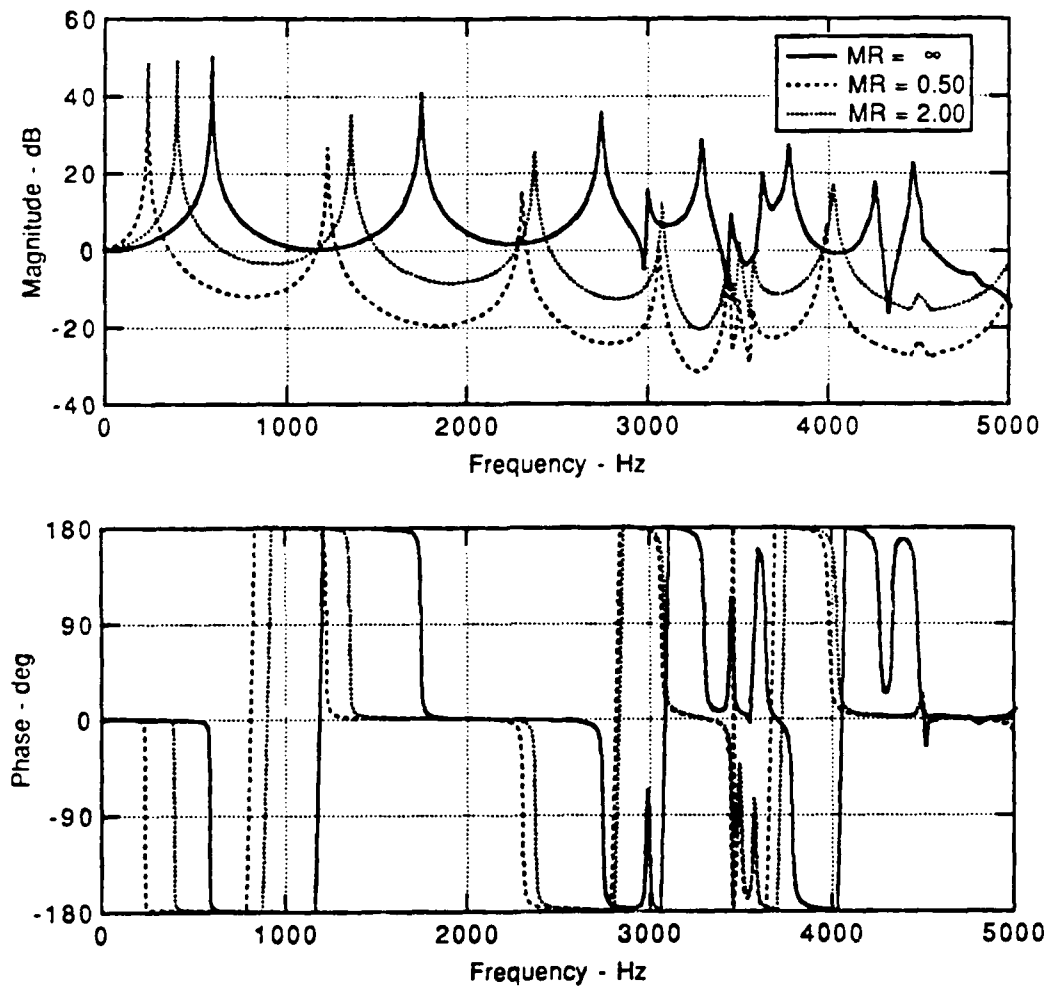


Fig. 4.14. Effect of Added Mass on the Transfer Function of a Model Dense Sand;  $L = 6.3$  in,  $2a = 2.8$  in,  $V_s = 800$  fps and  $D = 0.2\%$ .

Table 4.4. Effect of Added Mass on the Response of a Model Dense Sand\*

a. Comparison of Natural Frequencies

Mass <sup>Δ</sup> Ratio	Natural Frequency**, $f_n$ , Hz			
	Mode 1	Mode 2	Mode 3	Mode 4
∞	589.6	1746.7	2745.3	---
2.0	405.8	1360.2	2380.8	3088.9
0.5	246.2	1230.5	2312.0	3072.0

b. Comparison of Computed Velocities

Mass <sup>Δ</sup> Ratio	Bar Wave Velocity <sup>+</sup> , $V_c$ , fps			
	Mode 1	Mode 2	Mode 3	Mode 4
∞	1256.6 1.37% <sup>++</sup>	1254.1 1.17%	1249.0 0.76%	--- ---
2.0	1242.6 0.24%	1241.4 0.15%	1241.7 0.17%	1240.9 0.10%
0.5	1240.8 0.10%	1241.5 0.16%	1242.0 0.19%	1242.8 0.26%

<sup>Δ</sup> Mass Ratio = Mass of Specimen/Added Mass.

\*  $L = 6.3$  in,  $2a = 2.81$  in,  $C_B = 1239.6$  fps,  $D = 0.2\%$ ,  $MR = 2.0$

\*\* Natural Frequencies determined at  $\phi = \pm 90^\circ$ .

+ Computed using reduction program described in Chapter 7.

++ Percent change from input value of bar wave velocity.

The most obvious observation is the reduction in natural frequency of each of the respective modes with the increase in the added mass. The added mass also reduces the amplification slightly at each resonant peak, having a greater impact on the higher modes.

Probably most important is how the presence of the added mass appears to improve the agreement of the computed bar wave velocity with the input value. This implies that having the added mass may improve the accuracy of the measured values for the bar wave velocity.

#### 4.4.2 Effect of Base Support on the Transfer Function of a Dense Sand

Any laboratory testing involving a natural soil necessitates a condition where the base is completely supported. However, some synthetic and pavement materials were larger than the available sample base, and consequently were not fully supported. For the purposes of comparison, the base ratio is defined as the ratio of the area of the base to the sample cross-sectional area. Thus a base ratio of 1.00 is a fully supported base. Two additional transfer functions were determined for the dense sand assuming a free surface at the top and assuming base ratios of 0.766 and 0.563, corresponding to a 2.81 in. diameter sample supported on 2.46 in. and 1.56 in. bases, respectively. The transfer functions for the three cases are shown together in Fig. 4.15, and the natural frequencies and computed bar wave velocities for each of the first four modes are summarized in Table 4.5.

Two observations can be made by examining Fig. 4.15. First, the natural frequencies decrease markedly when the base diameters are less than 87.5 percent of the sample diameter. Consequently, the

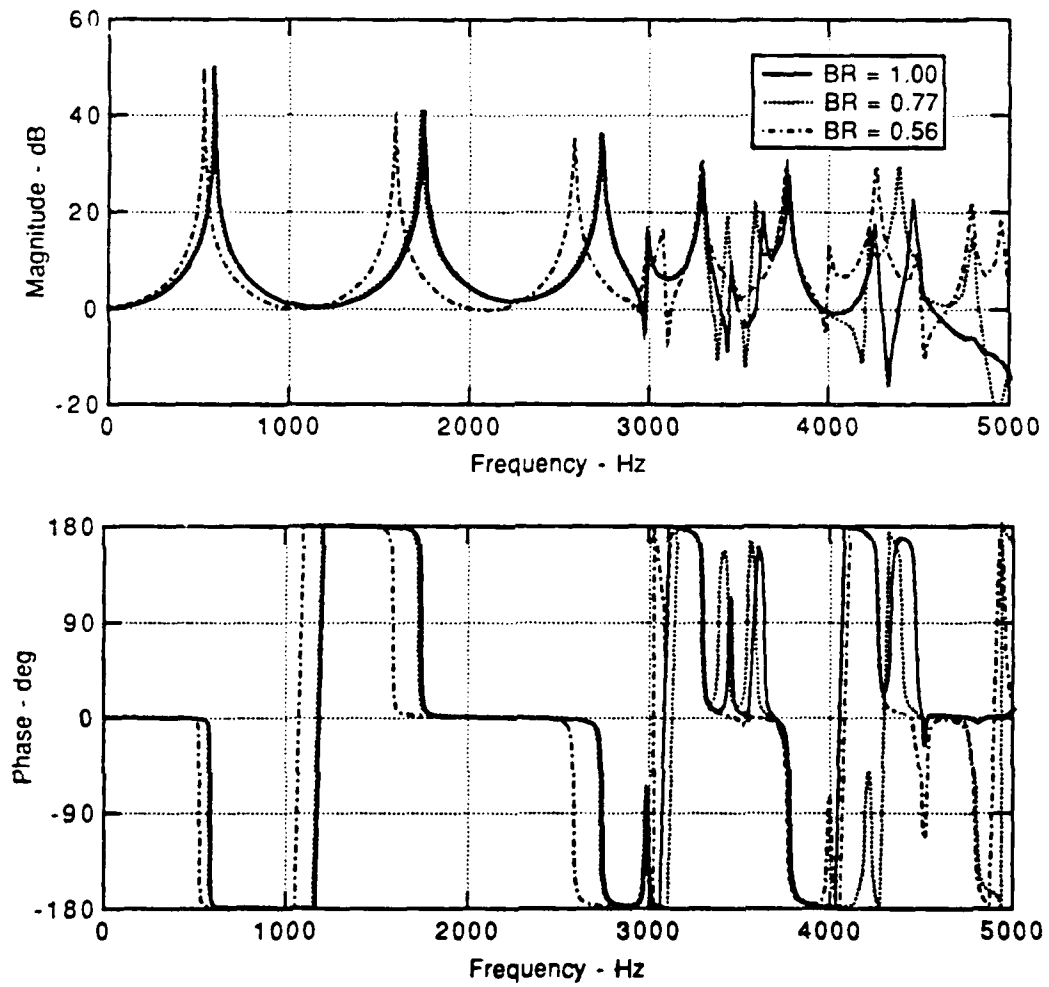


Fig. 4.15. Effect of Base Ratio on the Transfer Function of a Model Dense Sand;  $L = 6.3$  in,  $2a = 2.81$  in,  $V_s = 800$  fps,  $D = 0.2\%$  and no added mass.

Table 4.5. Effect of Base Ratio on the Response of a Model Dense Sand\*

a. Comparison of Natural Frequencies

Base <sup>Δ</sup> Ratio	Natural Frequency**, $f_n$ , Hz		
	Mode 1	Mode 2	Mode 3
1.00	589.6	1746.7	2745.3
0.77	584.9	1734.6	2739.1
0.56	533.7	1593.9	2591.6

b. Comparison of Computed Velocities

Base <sup>Δ</sup> Ratio	Bar Wave Velocity+, $V_c$ , fps		
	Mode 1	Mode 2	Mode 3
1.00	1256.6 1.37% <sup>++</sup>	1254.1 1.17%	1249.0 0.76%
0.77	1246.8 0.58%	1247.0 0.15%	1247.3 0.17%
0.56	1139.3 -8.09%	1160.3 -6.40%	1203.9 -2.88%

<sup>Δ</sup> Base Ratio = Area of base pedestal/area of sample.

\*  $L = 6.3$  in,  $2a = 2.81$  in,  $C_B = 1239.6$  fps,  $D = 0.2\%$ , Free Top.

\*\* Natural Frequencies determined at  $\phi = \pm 90^\circ$ .

+ Computed using reduction program described in Chapter 7.

++ Percent change from input value of bar wave velocity.

computed value of the bar wave velocity can be five to ten percent below the input value, underestimating the Young's modulus by up to 20 percent. Second, the influence of the base ratio tends to increase for the higher modes. Nevertheless, for materials similar to dense

sand, it can be concluded that, if the base diameter is greater than 90 percent of the sample diameter, the computed bar wave velocity from the first few modes will be within two percent of the theoretical input value.

#### 4.4.3 Effect of Horizontal Fixity at the Specimen Ends on the Transfer Function of a Dense Sand

The effect of a fixed or free horizontal displacement condition at the specimen ends is illustrated in Figs. 4.16 and 4.17. Figure 4.16 is the response of a dense sand with a free surface at the top, i.e. only the horizontal displacements at the base are fixed. Figure 4.17 is the transfer function of the dense sand with an added mass at the top, i.e. the horizontal displacements are fixed at the bottom and the top. The natural frequencies and computed velocities are summarized for each case in Table 4.6.

The fixity of the horizontal displacements at the bottom appears to have little impact on the frequency response, with only a minor effect appearing in the third mode. The fixity of displacements at both the bottom and the top appears to have little effect on the first two modes, while there is a minor increase in the natural frequency of the third mode. A similar trend appears in the computed bar wave velocities, where the fixed end conditions increase the error in the computed

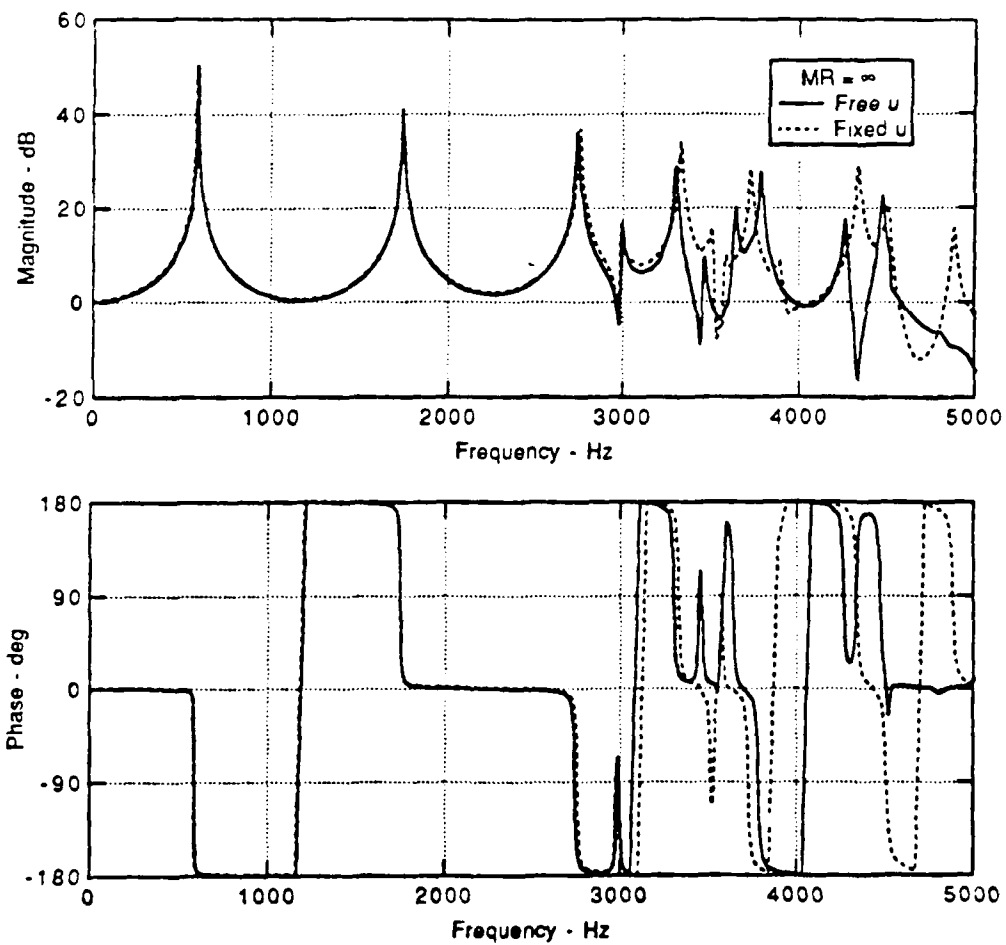


Fig. 4.16. Effect of Horizontal Fixity at the Base on the Transfer Function of a Model Dense Sand Specimen;  $L = 6.3$  in,  $2a = 2.81$  in,  $V_s = 800$  fps,  $D = 0.2\%$  and no added mass.

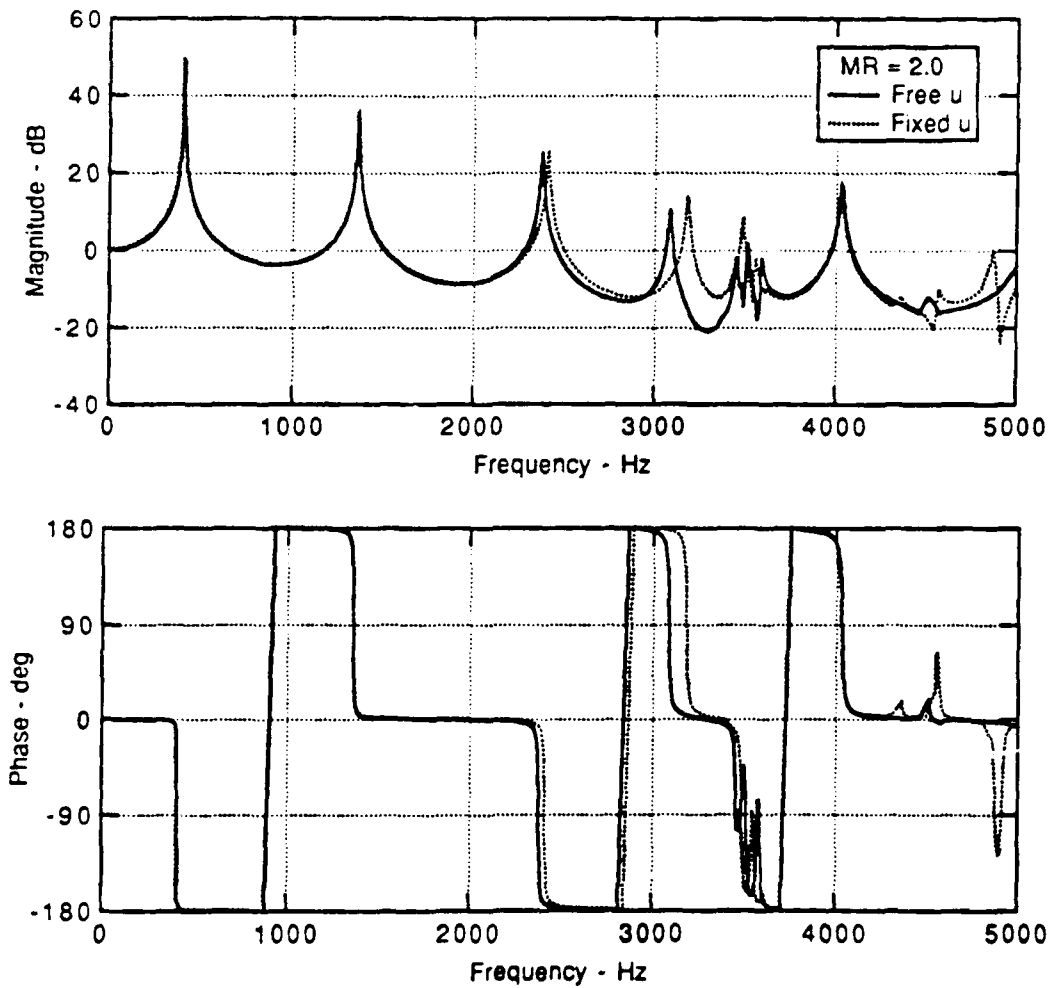


Fig. 4.17. Effect of Horizontal Fixity of the Base and Top on the Transfer Function of a Model Dense Sand Specimen;  $L = 6.3$  in,  $2a = 2.81$  in,  $V_s = 800$  fps,  $D = 0.2\%$  and  $MR = 2.0$ .

Table 4.6. Effect of Horizontal Fixity on the Response of a Model Dense Sand.

a. Comparison of Natural Frequencies

MR = $\infty$	Natural Frequency**, $f_n$ , Hz			
	Mode 1	Mode 2	Mode 3	Mode 4
u - Free	589.6	1746.7	2745.3	---
u - Fixed	590.4	1751.0	2765.9	---
MR = 2.0				
u - Free	405.8	1360.2	2380.8	3088.9
u - Fixed	406.0	1369.4	2419.9	---

b. Comparison of Computed Velocities

MR = $\infty$	Bar Wave Velocity+, $V_c$ , fps			
	Mode 1	Mode 2	Mode 3	Mode 4
u - Free	1256.6 1.37% <sup>++</sup>	1254.1 1.17%	1249.0 0.76%	--- ---
u - Fixed	1258.2 1.50%	1256.6 1.37%	1254.3 1.19%	--- ---
MR = 2.0				
u - Free	1242.6 0.24%	1241.4 0.15%	1241.7 0.17%	1240.9 0.10%
u - Fixed	1243.2 0.29%	1248.9 0.75%	1255.1 1.25%	--- ---

\*  $L = 6.3$  in,  $2a = 2.81$  in,  $C_B = 1239.6$  fps,  $D = 0.2\%$ .

\*\* Natural Frequencies determined at  $\phi = \pm 90^\circ$ .

+ Computed using reduction program described in Chapter 7.

++ Percent change from input value of bar wave velocity.

velocity. Nevertheless, the total error still does not exceed two percent, so it is possible to conclude that the horizontal fixity will have little effect on the value of the bar velocity measured in the laboratory.

#### 4.5 Summary

A finite element program was developed to study the relative influence of a number of material properties and boundary conditions on the frequency response of three model soils. The program utilized two-dimensional, four-node, axisymmetric, linear elements assembled in layers to model solid cylindrical specimens. The program output is the transfer function for the relative motion of points at the top of the model specimen resulting from a unit vertical displacement at the bottom. The three model soils represented a stiff clay, a loose sand under a low confining pressure and a dense sand under a moderate confining pressures.

As was expected, specimen stiffness and length have a direct impact on the natural frequencies of the model specimens. The natural frequencies of the specimen are roughly proportional to the square root of the specimen stiffness and inversely proportional to the specimen length. Also, greater length-to-diameter ratios (from smaller relative diameters) provide a larger number of observable natural frequencies before they are obscured by higher frequency motions. It is further

shown that there is little impact on the natural frequencies for model specimens with damping less than five percent. However, increases in damping decrease the peak magnitudes of the transfer function, and that decrease becomes more pronounced for successively higher modes. Lastly, moderate differences in the Poisson's ratio of the material appear to have little effect on the natural frequency or the computed bar wave velocity of a specimen.

A qualitative examination of the effect of various end conditions was also conducted. The presence of a rigid mass at the top significantly reduces the natural frequencies of the specimen. However, it is shown that the specimen with the added mass predicts the bar wave velocity much better than if the specimen top is free. The natural frequencies of the model specimens are also reduced if the base diameter is less than 90 percent of the sample diameter. Lastly, the horizontal displacement condition at the ends has little effect on the natural frequencies of the specimen, only increasing the error in the computed bar wave velocity from less than one to between one and two percent.

## **Chapter Five**

### **Test Equipment**

#### **5.1 Introduction**

The equipment used to construct the Multi-Moduli Testing Device (MTD) was selected using several criteria, specifically: cost, commercial availability, versatility, potential for automation and ability to meet the goals of the research study. It is important to remember that the MTD was designed to study the impact of stress state on the behavior of a cohesionless sand and, therefore, is necessarily more complicated than if it were designed to study intact, self-supporting materials such as plastics or Portland cement concrete. Necessarily then, the discussion in this section addresses testing cohesionless samples.

The MTD was designed to independently measure three different wave velocities in a sand specimen subjected to biaxial states of stress. Consequently, it has the ability to determine three different moduli, specifically; the constrained, Young's, and shear moduli. Most importantly, these measurements can be conducted without changing the stress state on the sample. The MTD has the capability to vary the stress in the axial direction, either in compression or extension. As a result, a wide variety of test series can be designed to test the impact of stress path on the stiffness of sands and other soils.

This chapter describes the equipment assembled to construct the MTD and to perform the three principal tests it was designed to conduct. A detailed list of the equipment components and their manufacturers is included in Appendix E. A description of the sample preparation procedures, and associated equipment, is also included in this chapter.

## 5.2 The Multi-Moduli Testing Device (MTD)

The MTD can be divided into three major subsystems which roughly correspond to their three principal functions. The functions of the three major subsystems are: 1) apply and measure the state of stress in the test specimen, 2) provide dynamic excitation, and 3) sense and record the specimen's response to the dynamic excitation. These three subsystems will be referred to as the Confinement, Excitation, and Monitoring systems, respectively. Figure 5.1 is a schematic diagram of the MTD. Figure 5.2 is a photograph of the MTD (with the containment cell and sensor cables removed).

### 5.2.1 Specimen Confinement System

Figure 5.3 is a schematic drawing of the confinement system of the MTD. The containment cell is a 10-inch diameter (ID), stainless steel cylinder approximately 18-inches high. The top and bottom plates are

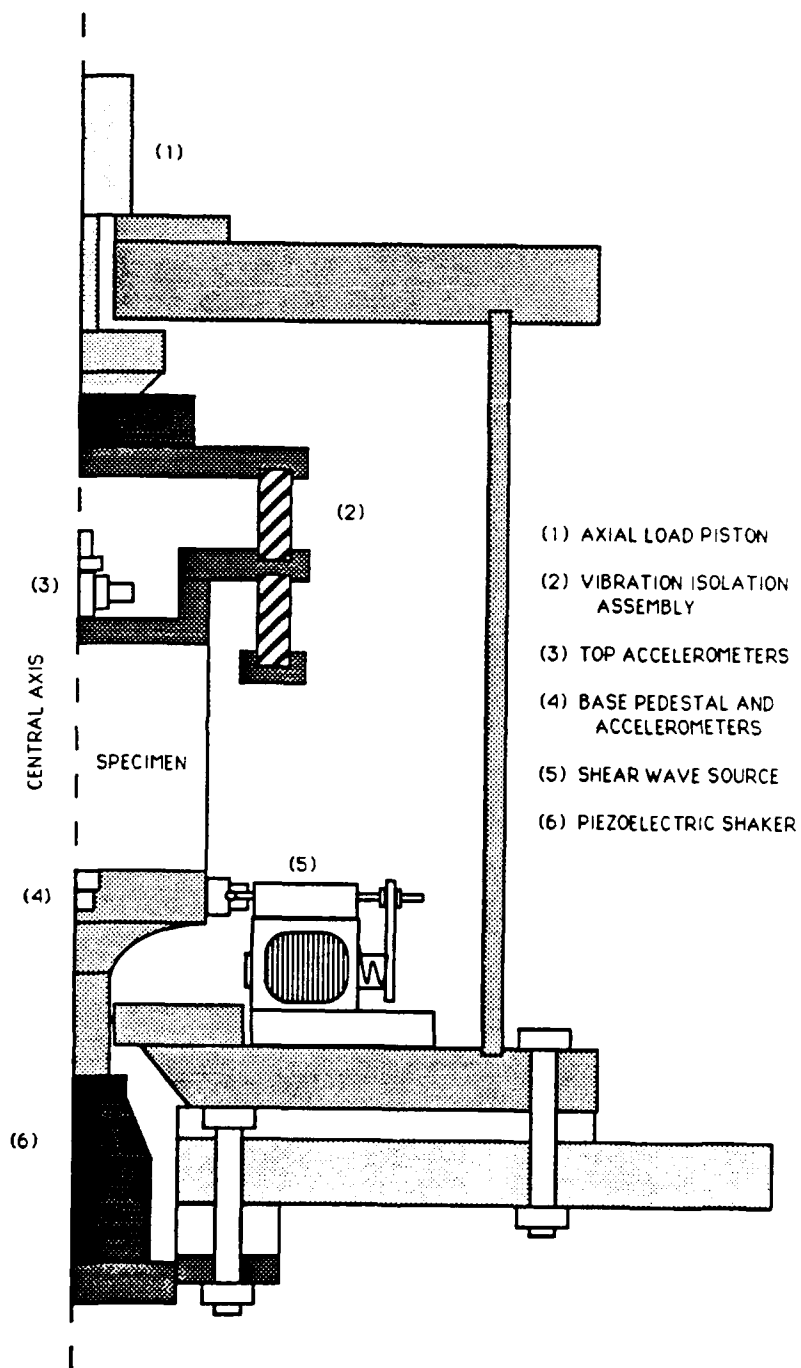


Fig. 5.1. Schematic Diagram Multi-Moduli Test Device (MTD).

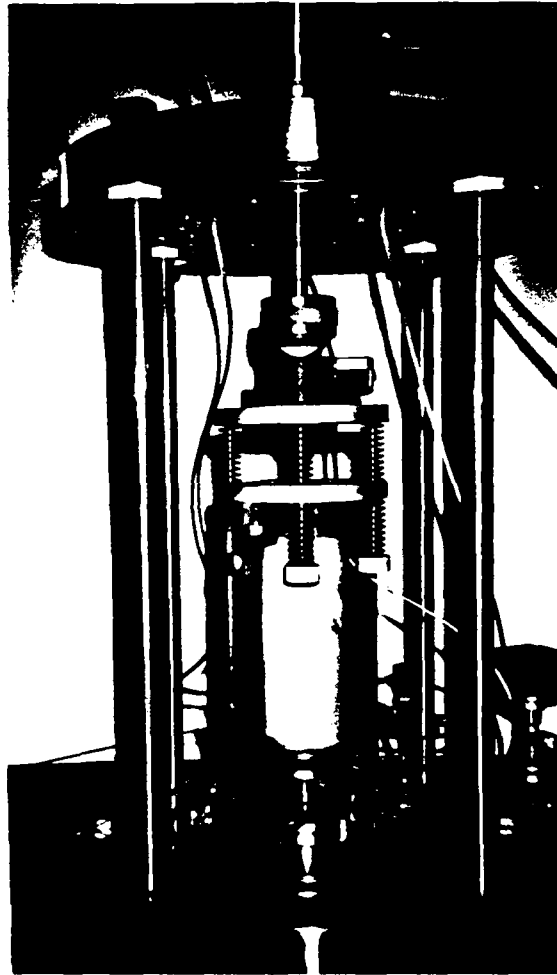


Fig. 5.2. Multi-Moduli Test Device (MTD) with Outer Cell and Sensor Cables Removed.

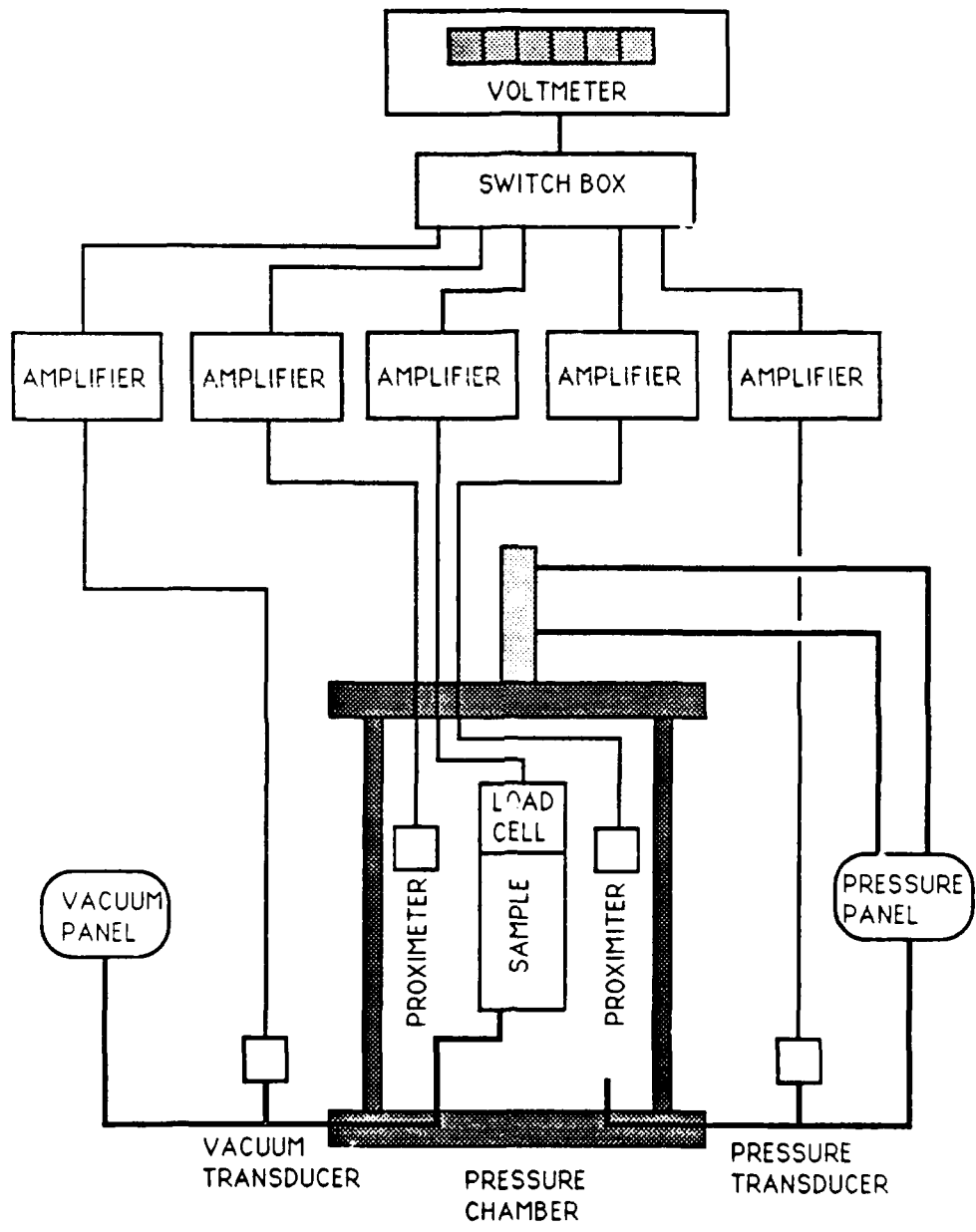


Fig. 5.3. Schematic Diagram of Specimen Confinement System in the MTD.

1.4 inch thick stainless steel pieces which are 14-inches in diameter and are connected by four, 0.75-inch (OD) stainless steel rods. The containment cell is sealed using standard butile rubber O-rings in face seal glands cut in the top and bottom plates.

Cell pressure is controlled by a pressure regulator (0-150 psi range) and monitored using a pressure transducer, calibrated using a standardized Heise pressure gage ( $\pm 0.2$  psi). Internal specimen pressure is controlled by a vacuum regulator (0-30 psi) and monitored by a vacuum transducer (0-48 w/linearity of  $\pm 0.5\%$ ), calibrated using a standardized Heise vacuum gage ( $\pm 0.5$  psi). Axial pressure is varied using a double acting air piston and monitored using a standard static load cell (50 lb, 100 lb or 300 lb capacity). The axial load is transferred to the sample through a specially designed vibration isolation assembly. This assembly is illustrated in Fig. 5.4 and is designed so the static load is transferred to the top cap ring through springs in compression, while allowing the sample top to move dynamically. Changes in sample height are measured using 11-mm (diameter) proximeters with a sensitivity range between 0.04 and 0.16 inches with a linearity of  $\pm 0.004$  inches. A complete list of the equipment model numbers and manufacturers is included in Appendix E.

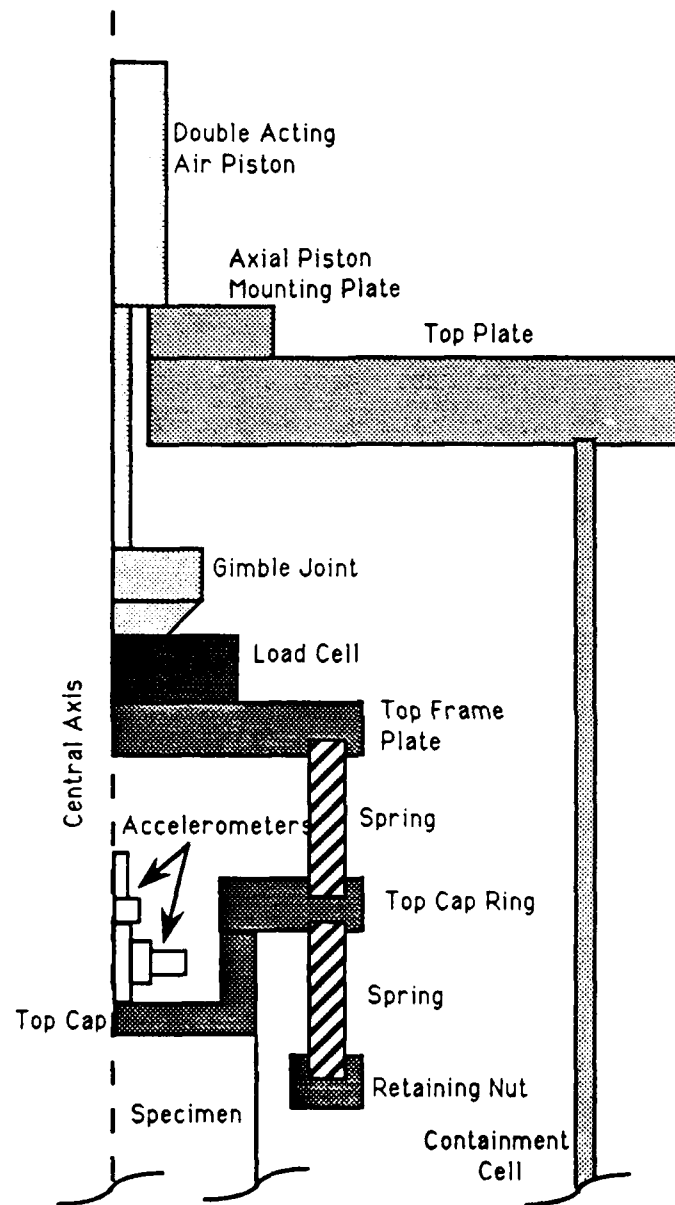


Fig. 5.4. Schematic Diagram of Axial Loading and Longitudinal Vibration Isolation Assembly.

their opposing faces. To make a vibration generator, the disks are stacked and their faces connected in series. This crystal stack is then sandwiched between a reaction mass and an attachment fixture. When a voltage is applied across the crystals they expand, reacting against the inertia of the backing mass and apply a force to the test structure through the attachment fixture. Some shakers contain an accelerometer and/or force transducer in the attachment fixture which allows accurate monitoring of the input vibration to the test structure. The shaker is powered by an amplifier connected through an impedance matching network. A schematic of the piezoelectric shaker system is shown in Fig. 5.5.

A schematic of the shaker mounted in the MTD is shown in the Fig. 5.6. The shaker is mounted vertically beneath the test table and connected to a stainless steel piston which passes through an O-ring seal in the base plate. The specimen base attaches directly to the top of this piston allowing the flexibility of changing bases without disassembling the shaker or base seal plate. The shaker is mounted on a threaded circular plate which allows minor adjustments in the height of the shaker and subsequently the specimen base.

The tapping device used as a source for the shear pulse test is made of a 0.125-inch diameter stainless steel rod mounted on a solenoid that was salvaged from an 8-track tape player. The function generator is connected through a rectifier circuit to a variable amplifier/power supply and is connected via an off-on switch to the tapping device. The function

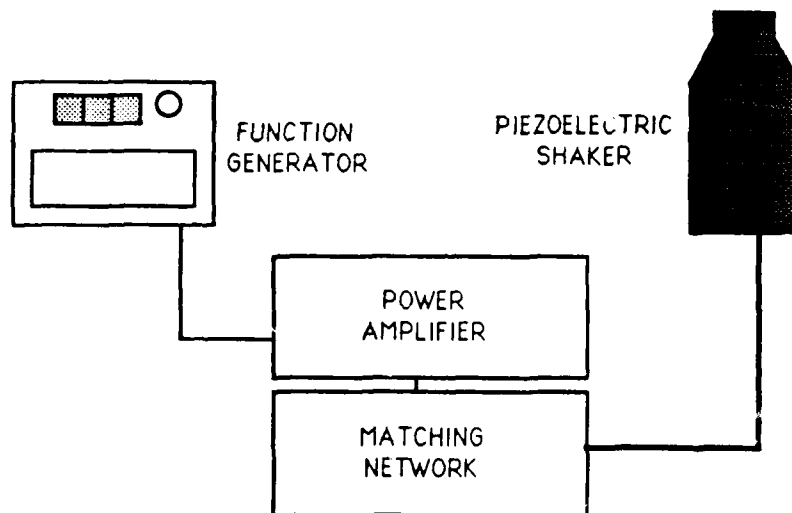


Fig. 5.5. Schematic Diagram of Piezoelectric Shaker System in the MTD.

generator provides a square wave signal which the rectifier chops so only the positive voltage steps of the square wave reach the amplifier. When the switch is closed, the positive voltage signal activates the solenoid and drives the rod against the side of the base pedestal. A small piece of steel is glued to the side of the base to protect its surface. A schematic of the shear wave source is included in Fig. 5.7.

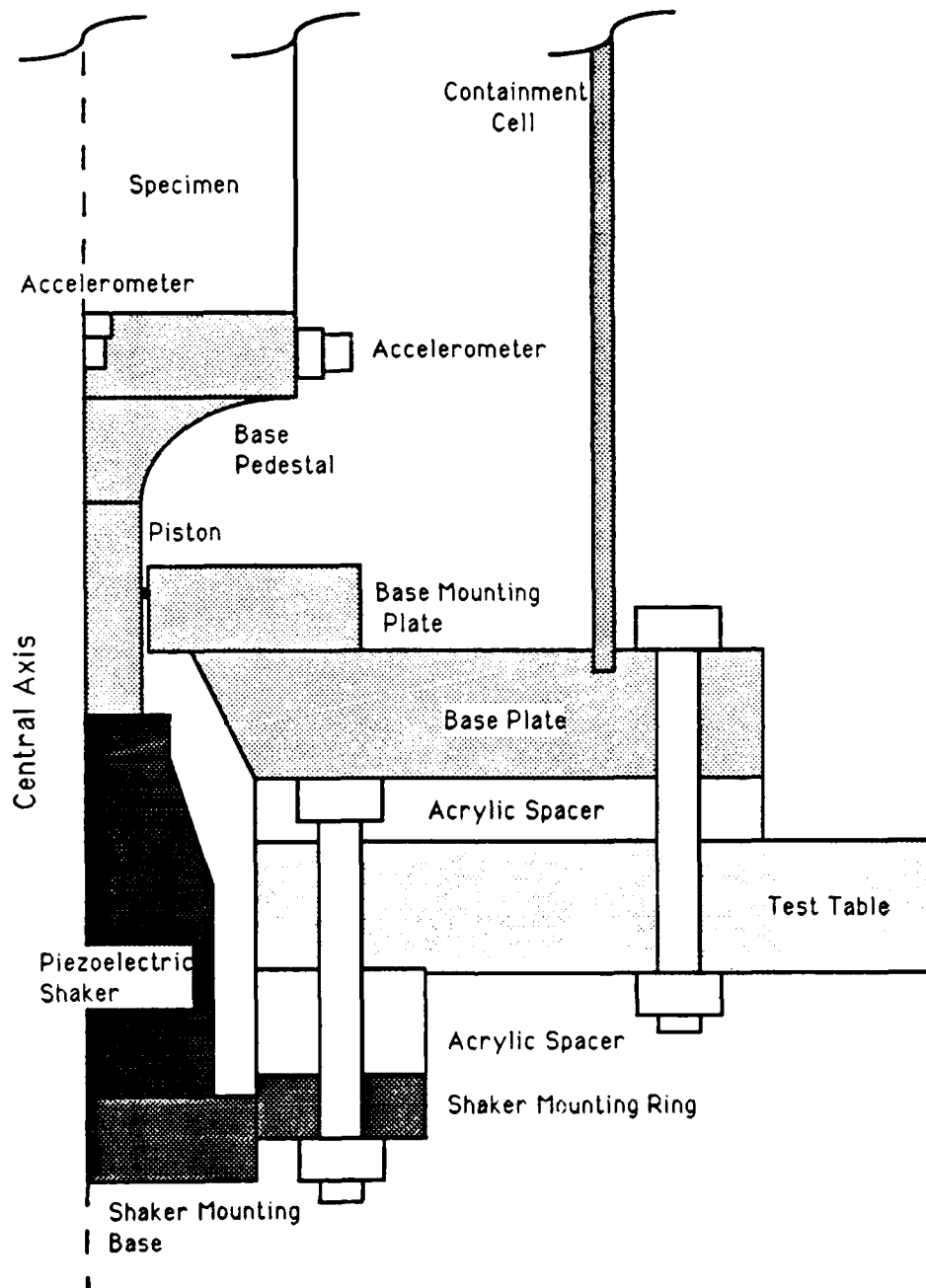


Fig. 5.6. Schematic Diagram of Piezoelectric Shaker Mounted Beneath Test Cell of MTD.

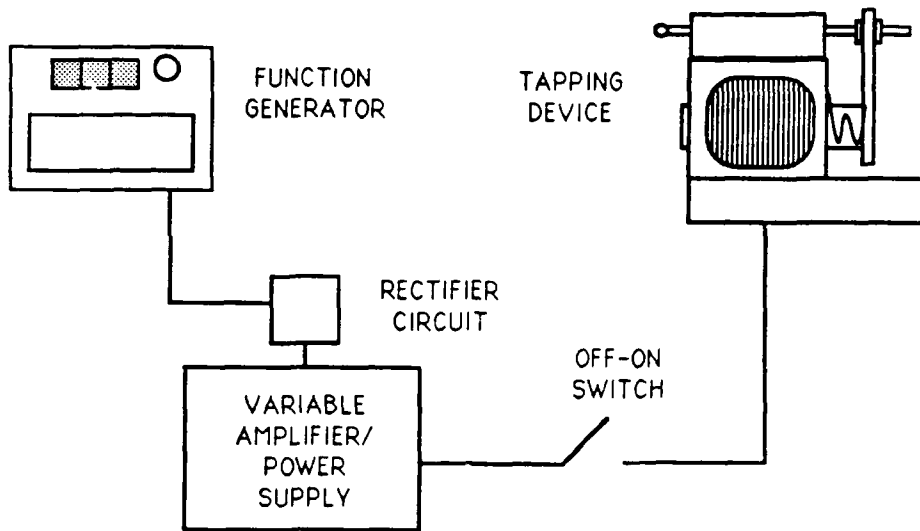


Fig. 5.7. Schematic Diagram of Shear Wave Generator in the MTD.

A function generator provided the source signal for both pulse tests. For the longitudinal resonant column test, the source signal was internally generated and controlled by the dynamic signal analyzer that was also used for measuring and recording the specimen response. A complete list of the equipment model numbers and manufacturers is included in Appendix E.

### 5.2.3 Dynamic Monitoring System

The third principal subsystem senses the dynamic response of the specimen and records that response for future analysis. The two main components of this system are the sensing devices and the recording devices.

Piezoelectric accelerometers were used exclusively to sense the input motion and response of the specimen. Two types of accelerometers were used. The first is an internally amplified, high sensitivity, high frequency accelerometer. An internal hybrid charge amplifier converts the high impedance charge signal of the piezoelectric crystal to a strong, low impedance voltage output signal. These accelerometers have a voltage sensitivity of approximately 100 mV/g, a frequency range ( $\pm 5\%$ ) of 3-15,000 Hz and a mounted resonance greater than 50,000 Hz. The second type of accelerometer was a miniature charge output accelerometer. These lightweight accelerometers have a charge sensitivity of approximately 1.5 pC/g, a frequency range ( $\pm 1\text{dB}$ ) range of 1-18000 Hz, and a mounted resonance greater than 55,000 Hz. The charge accelerometer requires an in-line charge converter to convert the high impedance charge output to a low impedance voltage output. A summary of the characteristics of both types of accelerometer is given in Table 5.1.

The internally amplified accelerometers and the in-line charge converters used for the charge output accelerometer require +18 VDC

Table 5.1. Accelerometer Characteristics.

	(a)	(b)
Voltage Sensitivity, mV/g	100	1.3
Transverse Sensitivity, %	5	5
Acceleration Range, g	60	1000
Resonant Frequency, kHz	>50	55
Frequency Response ( $\pm 3$ dB), Hz	2-25,000	0.6-30,000
Power Requirements, +VDC	18	18
Weight, grams	15	1.3

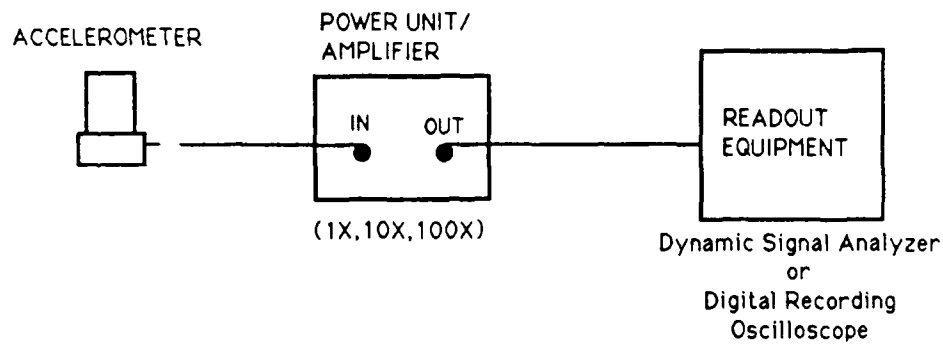
(a) Internally amplified, low impedance accelerometer.

(b) Charge output, high impedance accelerometer w/in-line charge converter.

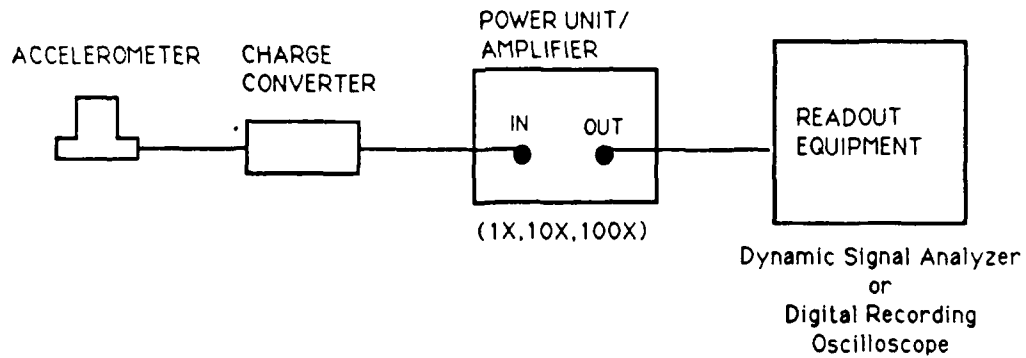
power to operate. In addition, signal amplification is sometimes required to boost the magnitude of the output signals to enable accurate recording by the readout equipment. A general purpose combined power unit and amplifier with selectable gains of 1X, 10X, and 100X provides both the DC power required and permitted matching output signal levels to the recording equipment. A conceptual diagram of the connections for both types of accelerometers is given in Fig. 5.8.

Two recording devices were used; one for the axial and shear pulse tests and one for the longitudinal resonant column test. A 6-channel digital recording oscilloscope is used to record, temporarily store, and transfer time domain signals from the pulse tests. The oscilloscope has a sampling rate which ranges from 20 MHz to 1 MHz depending on the number of channels being utilized. Each channel has a 10-bit vertical resolution, which increases to 14-bit with averaging. The amplitude range is 1 mV/div to 10 V/div (10 divisions) with an accuracy of  $\pm 1\% + 0.01 \text{ div}$ . The oscilloscope also has a versatile menu of wave form and measurement functions. The oscilloscope triggers on the source signal provided by the function generator, or on one of the accelerometers. The signals recorded in this research were typically the average of 64 or 128 repeated inputs. Figure 5.9 illustrates the equipment set up for the pulse tests using the digital recording oscilloscope.

A digital dynamic signal analyzer is used to control and record the frequency response of the specimen for the longitudinal resonant column test. The signal analyzer has two channels and an internal function generator. As used in this test, the analyzer outputs a steady-state sinusoidal source signal to the vibration generator and then measures the relative amplitude and phase between the signals received at the two input channels. The analyzer can perform user-programmed frequency sweeps, recording and displaying the frequency response spectra in



a) Low Impedance, Internally Amplified Accelerometer



b) High Impedance, Charge Output Accelerometer

Fig. 5.8. Connection Diagrams for Piezoelectric Accelerometers Used in the MTD.

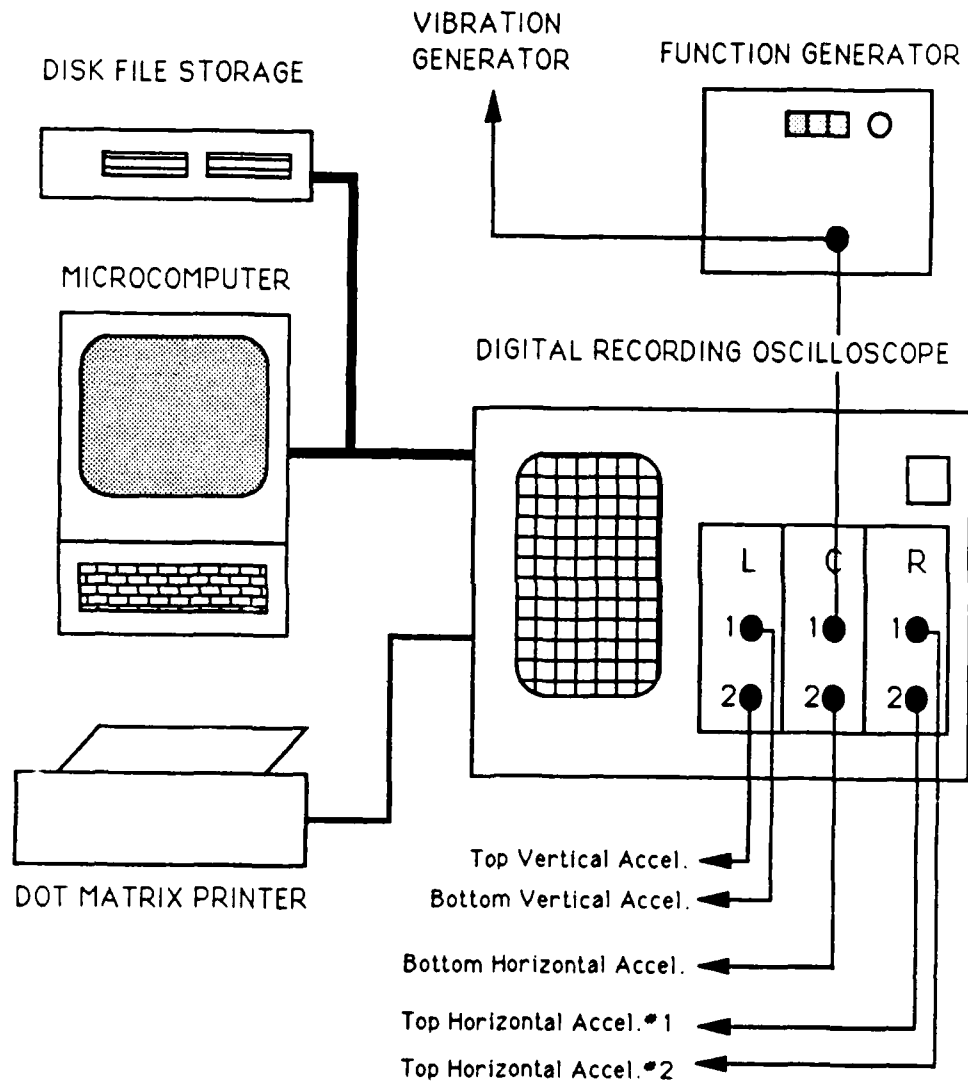


Fig. 5.9. Diagram of Monitoring Equipment Used for Pulse Tests in the MTD.

relative amplitude and phase. Figure 5.10 illustrates the equipment set up for the longitudinal resonant column test using the dynamic signal analyzer.

Neither the digital recording oscilloscope, nor the dynamic signal analyzer, has permanent file storage capability so they have to be augmented with disk file storage. Both have IEEE 488 interfaces and can transfer files, as well as be controlled remotely. The digital recording oscilloscope requires another instrument, such as a computer to act as the controller, directing the transfer of the recorded wave form from the oscilloscope to disk file storage. The dynamic signal analyzer can act as a controller itself and thus only requires an external file storage device. Data files were recorded in binary form on 3.5-inch diskettes.

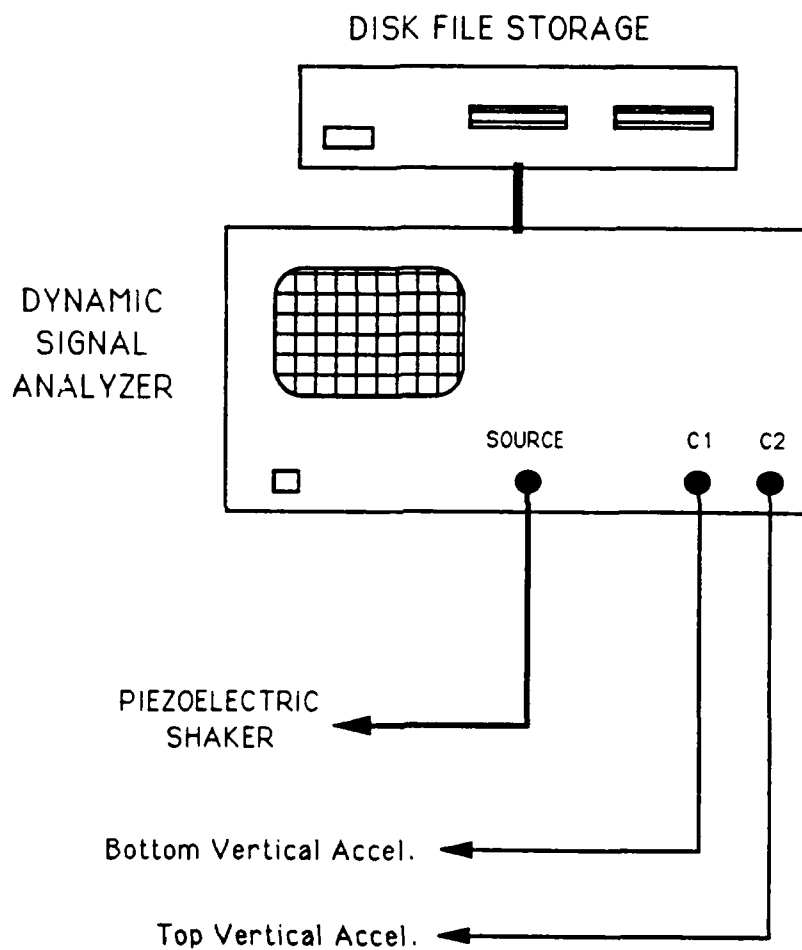


Fig. 5.10. Diagram of Monitoring Equipment Used for Longitudinal Resonant Column Test in the MTD.

### 5.3 Test Specimen Preparation and Set Up

This section briefly describes how each test material was installed in the MTD. The bulk of the discussion in this section is directed toward the preparation of uncemented sand specimens for which a special mold and pluviation device were constructed.

#### 5.3.1 Preparation of Synthetic Specimens

Synthetic specimens were epoxied to the sample base using a rapid-setting (5 minute) two-part epoxy. When a top cap was used, it too was epoxied to the top of the specimen. In those tests in which a top cap was not used, the accelerometers were glued directly to the center of the top of the specimen using quick setting (1 minute) superglue. In all cases, sufficient epoxy or glue was used to insure an even continuous bond between the test specimen and the base and top cap surfaces.

Each synthetic specimen was machined to a right circular cylinder with their ends smooth to  $\pm 0.001$  inches across the diameter. Their diameters ranged from 1.4 to 4.0 inches and never varied over the length by more than  $\pm 1\%$  of the diameter.

### 5.3.2 Preparation of Compacted Clay Specimens

Compacted clay specimens were not glued at the ends, but a moderate amount of vacuum grease was applied to improve contact at the ends. The clay specimens were encased in a latex membrane that was secured at the base and top cap with butile rubber O-rings. A minor amount of vacuum grease was applied to the base and top cap sides to improve the seal. Vacuum grease was also used for some tests to improve the contact between the specimen and the base and top cap. Three evenly spaced strips of filter paper less than 0.5-inches wide ran the length of the specimens between the clay surface and the membrane. All clay specimens were about 2.8 inches in diameter and 5.6 inches in length.

### 5.3.3 Preparation of Uncemented Sand Specimens

Preparation of sand specimens is made difficult by the fact sand has no strength unless confined. For this reason a special sample mold was constructed to prepare sand samples. In addition, a new pluviating apparatus was constructed which allowed the preparation of test specimens with consistent densities. A step by step description for the preparation of a sand is included in Appendix F.

Miura and Shosuke (1982) demonstrated a sample preparation technique using a multiple sieving pluviation (MSP) apparatus and

determined, with extensive testing, its effect on the static and cyclic deformation and strength properties of sand. Their apparatus was composed of a hopper with a variable nozzle diameter, and a stack of six, 8-inch diameter sieves through which the sand fell into the sample mold. They demonstrated the MSP gave a wide range of reproducible specimen densities by controlling the height of fall and the nozzle diameter. Their results showed that the nozzle diameter was the predominate factor controlling specimen density. LoPresti and Pedroni (1989) have also shown, using a similar apparatus, that the resulting specimen density was mainly a function of deposition intensity (weight/time/area). In both cases, the controlling factor was the rate at which the sand was allowed to fall.

The sample mold is made of two halves which bolt tightly together, forming a cylindrical shell which has a diameter equal to the base plus twice the membrane thickness. The membrane is precut to a specific length, installed on the base and held with one O-ring. The mold is carefully fitted together around the base with the O-ring fitting in the slot provided for it in the mold. After bolting the two halves together and levelling the mold, the membrane is stretched over the mold's top edge, and an aluminum restraining ring is slipped on. A 1.0 to 1.5 psi vacuum is applied at the ports in each mold half to hold the membrane against the inside surface of the mold. The membrane is then adjusted so there are no folds or creases in it. The sample mold is now ready to permit pluviation of the sand.

The MSP apparatus developed for this research has a large funnel at the top to hold the sand. Various sized nozzles can be inserted in the funnel which control the rate of sand fall. A short 6-inch section separates the funnel from the top-most sieve which is typically sized 5 to 15 times the  $D_{50}$  grain size. The column contains six sieves, spaced two inches apart and oriented at 45 degrees to one another. The sieve openings increase in size from top to bottom, with the bottom four being the largest and the same. Below the bottom sieve is a 12-inch long section through which the sand falls freely into the mold. The MSP is constructed of cast acrylic tubing with an inside diameter just less than the mold diameter. The MSP column rests directly on the top of the mold and is held in place by an acrylic retaining ring. Enough sand to fill the mold and 2 to 3 inches of the bottom of the MSP column is preweighed, poured in the funnel, and then released.

After the sand has pluviated, the column is disassembled one section at a time and all loose sand "vacuumed" into a preweighed flask. The excess sand in the base of the column is "vacuumed" and the top of the mold is struck off using a steel straight edge taking care to capture all excess sand and not disturb the sand in the mold. The difference between the weight of the sand used and the weight recaptured is the specimen weight.

Finally, the top cap is placed carefully on the top of the specimen, the membrane folded up its sides and an O-ring installed. The vacuum in the mold is released and applied to the specimen itself. Now the mold is

removed, the vacuum on the specimen increased to a predetermined level, and the initial diameter and height are measured using a Pi tape and digital calipers, respectively. The remaining steps in assembling the MTD for a test series are listed in Appendix F.

#### 5.4 Summary

The Multi-Moduli Testing Device (MTD) was designed to independently measure three different wave velocities in a sand subjected to isotropic and biaxial states of stress. The MTD has the capability to vary the axial stress of the sample in compression or extension and yet, through a vibration isolation assembly, still allows the top of the specimen to move dynamically in response to the excitation of the base.

The MTD is divided into three main systems, which are the Confinement, Excitation, and Monitoring Systems. The Confinement System is composed of the following: (1) a pressure and a vacuum transducer to monitor the confining pressure on the specimen, (2) two proximeters to determine changes in the length of the specimen, (3) a load cell to determine the axial load on the specimen, and (4) the pressure and vacuum panels and the pressure chamber which apply the state of stress in the specimen.

There are two wave motion generators in the Excitation System. The first is a piezoelectric vibration generator, which is mounted vertically in the base of the MTD and connected to the sample base pedestal. The shaker vibrates the sample longitudinally using impulse (for constrained modulus) or sinusoidal (for Young's modulus) signals input by a function generator. The second wave motion generator is an electromechanical tapper which is mounted horizontally and strikes the side of the base pedestal (for shear modulus).

The Monitoring system is composed of the piezoelectric accelerometers that sense the motion of the specimen and the digital recording devices which capture and store the responses. Two accelerometers are mounted on the base, one vertically and one horizontally. Three accelerometers are mounted on the top cap, one vertically and two horizontally. A digital recording oscilloscope (DRO) is used to capture time records in the axial and shear pulse tests described in Chapter 6. A digital dynamic signal analyzer (DSA) is used to measure the frequency response of the sample in the longitudinal resonant column test described in Chapter 7. Time records and frequency responses are stored on diskettes for future analysis. A detailed list of the equipment used in the MTD is included in Appendix E.

The cohesionless sand specimens were prepared for testing using a Multiple Sieve Pluviating (MSP) column. The MSP column consists of a stack of six sieves, topped by a funnel, which sits atop the sample mold. The rate at which the sand falls, and to a lesser extent the height of fall,

determines the density of the specimen. The rate of fall is controlled by varying the size of the opening in the funnel at the top of the MSP. A small opening (slow rate) results in specimens with high relative density and a large opening (fast rate) results in specimens with low relative densities. A detailed description of the construction of a sand specimen using the MSP is contained in Appendix F.

## **Chapter Six**

### **Measuring Constrained and Shear Moduli Using Pulse Tests**

#### **6.1 Introduction**

The constrained modulus is commonly determined by measuring the compression or dilatational wave velocity using pulse testing methods. Two methods have been formalized by the American Society for Testing and Materials (ASTM) to determine wave velocities in civil engineering materials. First, ASTM C597-83, details test procedures to determine the pulse velocity in concrete, and the second, ASTM D2845-69, details testing using ultrasonics to determine the pulse velocities in rock.

All methods to determine pulse velocity consist of the same basic steps and equipment. An electromechanical generator and an electromechanical receiver are attached to, or held in contact with, the opposite sides/ends of a specimen. The generator produces a fast-rise-time displacement pulse, and the motion of the receiver is measured. By comparing the waveforms measured at the generator and receiver using the same time base, a time for the pulse to travel the distance between the generator and receiver can be determined. The distance travelled by the pulse, divided by the travel time corrected for any instrument delays is the pulse velocity.

The equipment used for pulse testing is described in detail in Chapter 5 and Appendix E and specific procedures are included in Appendix F. The tests are described here only in general to illustrate the process leading to determining the particular modulus.

## 6.2 Constrained Modulus from the Axial Pulse Test

### 6.2.1 Conducting the Axial Pulse Test

To conduct a pulse test to find the dilatational (or P-) wave velocity of a sand specimen, the function generator and digital recording oscilloscope(DRO) are used as configured in Figs. 5.5 and 5.9. The configuration of the MTD for this test is also illustrated in Fig. 6.1. The vertical accelerometers in the sample base and on the top cap are connected to separate channels of the oscilloscope. The function generator is connected to the vibration generator and also to a third channel of the oscilloscope. The function generator is set to produce one-half cycle of a square wave with a magnitude of 0.10 volts, a frequency of 2000 Hz and is triggered every 0.10 seconds. The resulting signal appears on the oscilloscope as a step function when compared to the travel times measured in the specimens.

The oscilloscope is set to trigger on the signal produced by the function generator because it provides a consistent trigger point. The oscilloscope is set to average 128 measurements and then stop. A direct

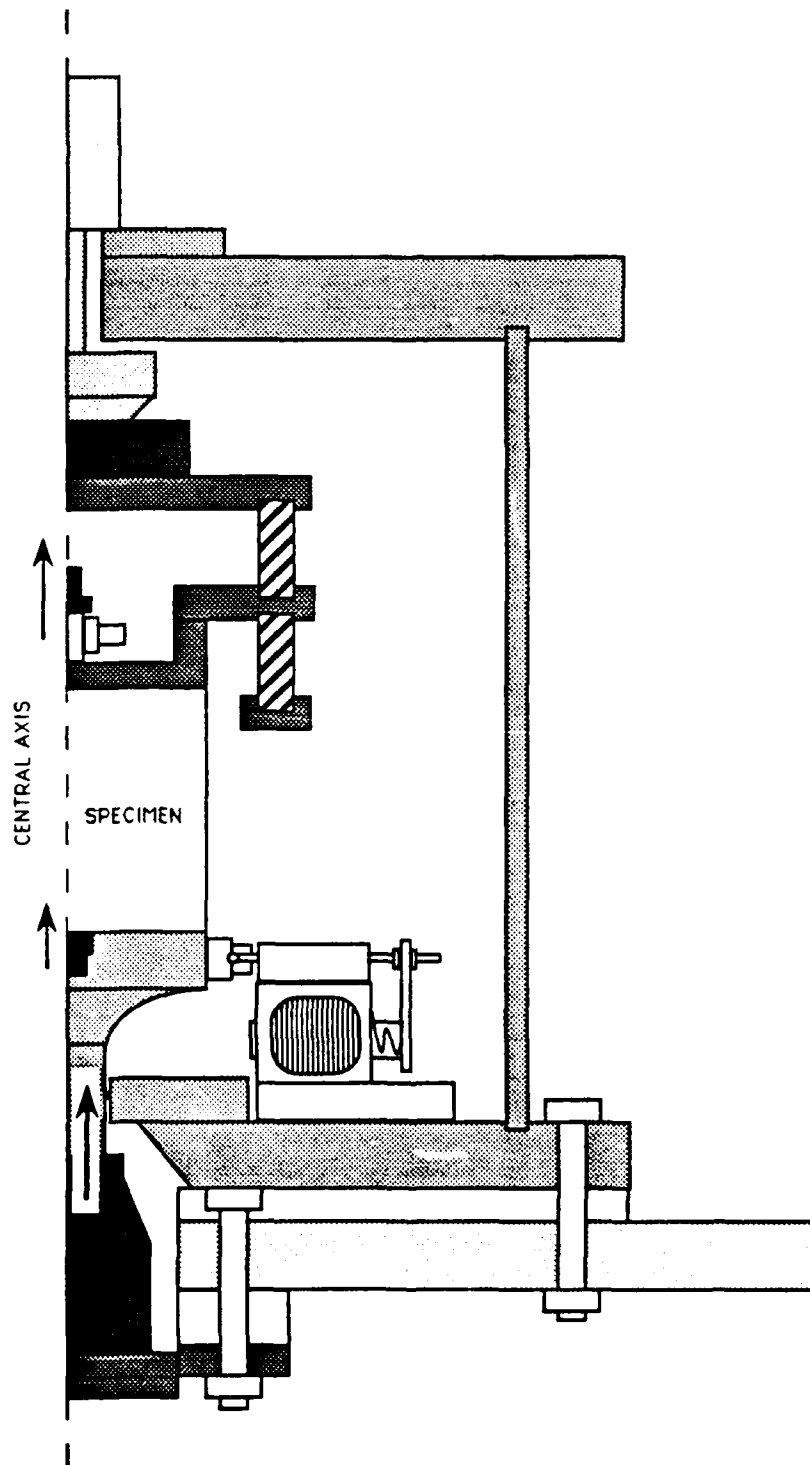


Fig. 6.1. Arrangement of MTD for Conducting Axial Pulse Test.

copy of the oscilloscope screen is provided as an example in Fig. 6.2. Displayed in Fig. 6.2 are the responses of the base and top accelerometers, with the trace for the top accelerometer highlighted (darkened in the figure). After the test is complete, each waveform is stored internally in the oscilloscope and the screen is cleared. The stored waveforms are recalled, and, using zoom and amplification functions on the oscilloscope, the waveforms are manipulated and expanded for easier examination.

The time interval,  $t_p$ , between the first arrivals of the pulse at the bottom and top accelerometers is easily determined using cursors. Figure 6.3 is an example of the oscilloscope configured to determine this travel time. The travel time for this example is  $372.5 \mu\text{s}$ . The length,  $L$ , of the sample is determined using the initial measured length, adjusted for any changes calculated using measurements from the proximeters. The calibrated time delay between the accelerometers,  $t_d$ , is determined in a separate test for each specific accelerometer configuration. In those calibration tests, the top cap is placed directly on the base with a very thin layer of vacuum grease between them and the same pulse test is conducted. The values of these delays typically ranged between 7 and  $10 \mu\text{s}$ . A value of  $9.5 \mu\text{s}$  was measured for this accelerometer configuration and is used in this example. The P-wave velocity,  $V_p$ , is then calculated using

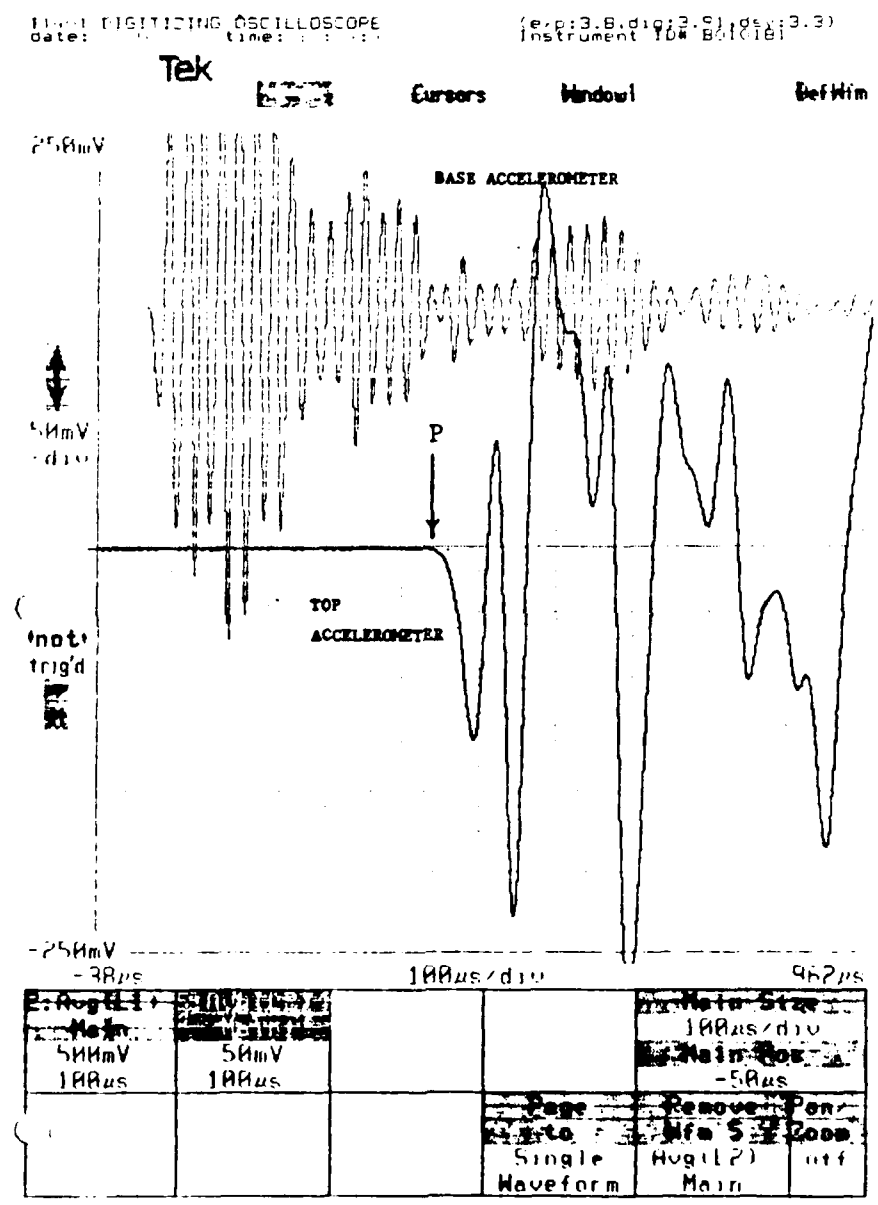


Fig. 6.2. Digital Oscilloscope Record of Axial Pulse Test on Loose Sand at 16 psi Confining Pressure (128 Averages).

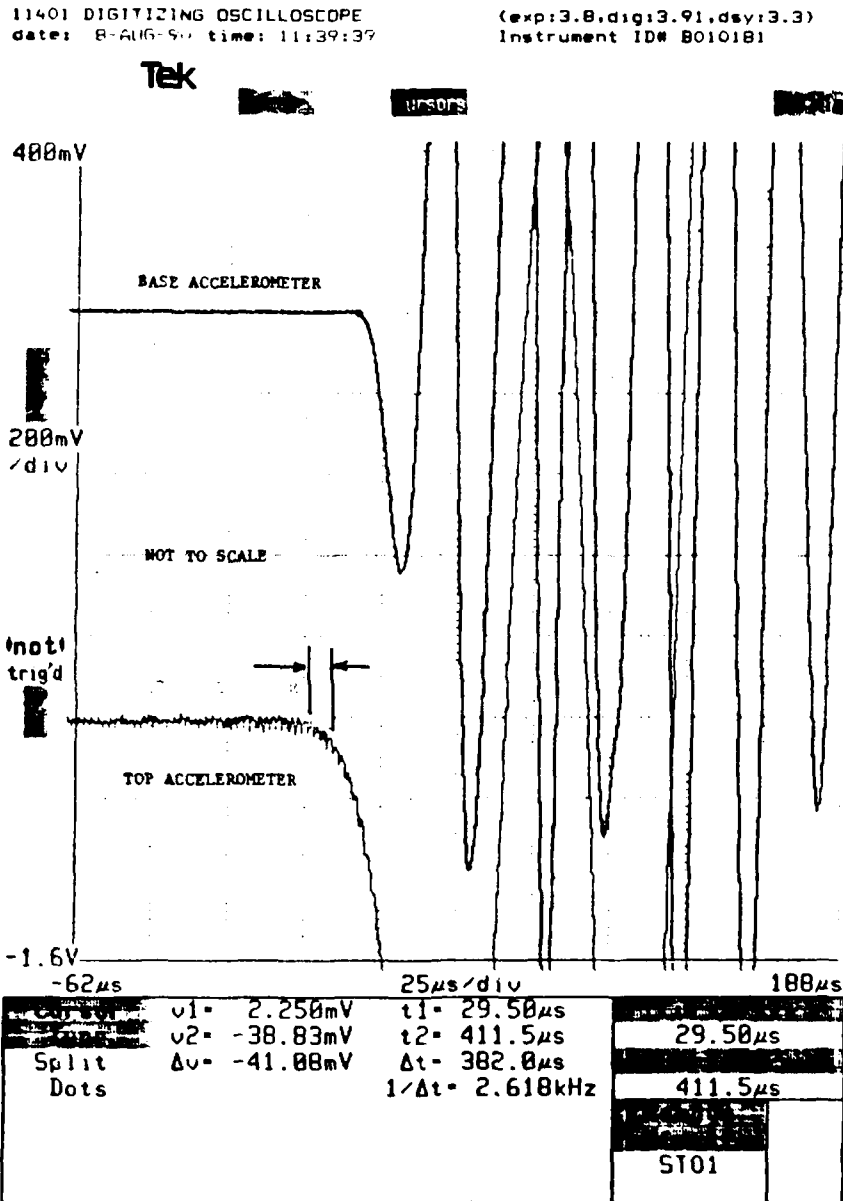


Fig. 6.3. Determining the P-wave Arrival From an Amplified Time Record on the Digital Recording Oscilloscope.

$$V_p = \frac{L}{(t_p - t_d)} \quad (6.1)$$

For the loose sand in Fig. 6.2,  $L = 0.2338$  ft, and the resulting velocity is 1458 fps. The constrained modulus,  $M$ , then follows from the equation

$$M = \rho V_p^2 \quad (6.2)$$

where  $\rho$  is the mass density.

Several assumptions have been made in the process of conducting and analyzing the axial pulse test. These include: 1) the first arrival is due to a disturbance travelling at the dilatational wave velocity, 2) the input motion has a sufficiently high frequency to appear as a step function, and 3) the strains in the specimen remain low enough to assume that the material responds linearly elastically. These assumptions are discussed in further detail in the following sections.

### 6.2.2 Justification for Identifying the First Arrival as the Compression Wave Arrival

A theoretical solution for transient waves propagating in a semi-infinite rod due to an impact on the end is presented in Chapter 3 and Appendix C. A computer program was written which numerically computes the solution for the particle velocity at positions relative to the wave front corresponding to the elementary solution. This solution can

be plotted versus time as done in Fig. 6.4 for Poisson's ratios of 0.25 and 0.49. The solutions are for a point in a rod that is at a distance four times the diameter from the impact end. The arrivals of the elementary rod wave,  $t_b$ , and the corresponding dilatational wave arrivals,  $t_p$ , are also shown. Here the dilatational wave arrival was computed using  $C_B$  and Poisson's ratio and assuming an isotropic linearly elastic material. It can be seen that motion at the observed point starts at about the time corresponding to the time of arrival for a dilatational wave. It is also observed, that as Poisson's ratio decreases, the time difference between the dilatational and elementary bar wave arrival decreases. The arrival of the dilatational wave appears to correspond to an amplitude which is on the order of 10 percent or less of the first peak amplitude in the waveform.

Therefore, for the purposes of this laboratory testing, the P- wave arrival time was assumed to occur at a point when the waveform makes a marked departure from the ambient level. This is illustrated in Fig. 6.3.

### 6.2.3 Impact of Input Frequency on the Measured Compression Wave Arrival.

In Fig. 6.2 it is obvious that the motion of the accelerometer in the base is very different from the step function input by the function generator. The time record for the base accelerometer has a sharply varying amplitude and dominant frequency. In addition, it should be

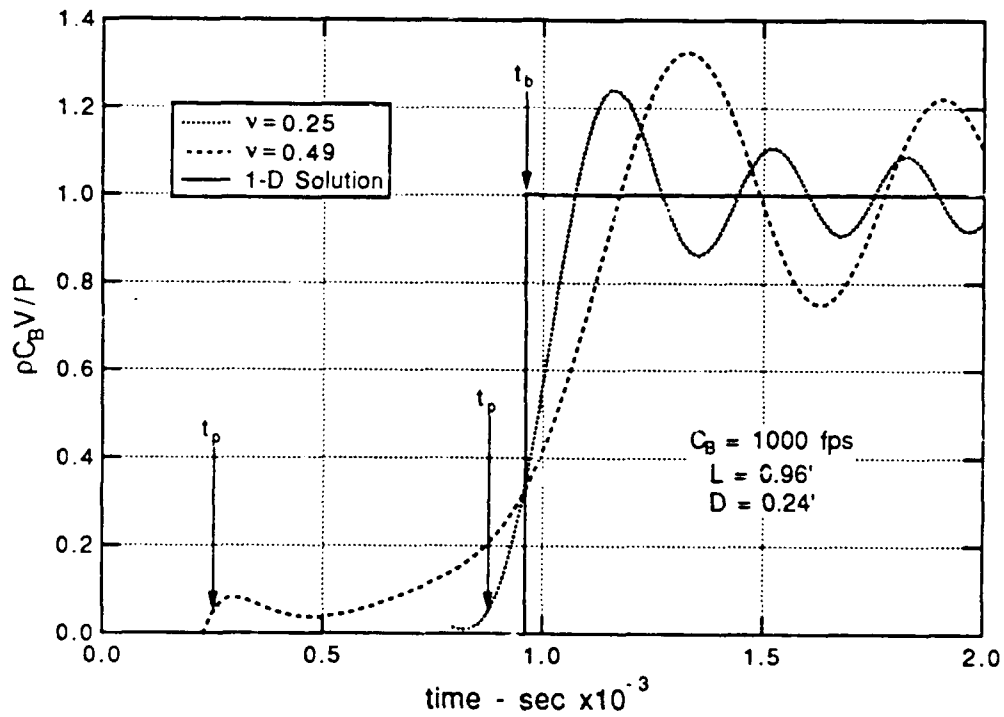


Fig. 6.4. Particle Velocity in the Vicinity of the Elementary Wave Front as a Function of Time from Three-Dimensional Theory for Transient Motion in a Rod.

noted that the wave arrives at the base accelerometer approximately 30  $\mu$ s after the time it is output from the function generator. This delay, and the resulting amplification and dominant frequency, are due to delays in the power amplifier and impedance matching network, inertial response of the piezoelectric crystals in the vibration generator, and the time it takes for the pulse to travel through the steel base piston and the base pedestal. The dominant frequency, about 45 kHz, appears to correspond to the expected resonant frequency of piezoelectric crystals in the vibration generator, subject to slight modification by the pulse's passage through the steel piston and base pedestal.

This observation leads to the assumption that although the input motion is not a true step function, it has a frequency sufficiently high in comparison to the natural frequency of the specimen that it appears as a step function. This conclusion is made noting that in Chapter 7 the first natural frequency for the loose sand in this sample is approximately 400 Hz, making the excitation frequency nearly two orders of magnitude higher. The study of the influence of input frequency on the observed P-wave arrival is beyond the scope of this research. However, the finite element model described in Chapter 4 should prove a useful tool. Fast Fourier Transform (FFT) algorithms can be used with the transfer function output by the finite element program to compute a time response at the top resulting from a specified input motion at the bottom.

#### 6.2.4 Assumption of Small Strains in the Axial Pulse Test

One fundamental assumption governing this research study is that the strain levels generated in the specimen are so small that the material behaves linearly elastically. For a typical sand this means that measured strains should be below  $10^{-3}$  percent.

It is a straightforward process to compute the maximum level of strain which occurs in the specimen. There are two points in the axial pulse test, the base and the top, where the acceleration amplitude is known accurately. If the displacement at any point is assumed to be governed by an equation of the form

$$w = Ae^{-i\omega t} = A(\cos\omega t - i \sin\omega t) \quad (6.3a)$$

then

$$\dot{w} = -A\omega e^{-i\omega t} \quad (6.3b)$$

and

$$\ddot{w} = +A\omega^2 e^{-i\omega t} \quad (6.3c)$$

so

$$\dot{w} = -\ddot{w}/\omega \quad \text{or} \quad \dot{w}_{\max} = \ddot{w}_{\max}/\omega \quad (6.4)$$

From the waveforms recorded in an axial pulse test, it is a simple matter to determine the maximum acceleration knowing the accelerometer constants and the signal amplification. It is noted that it is inherently

assumed that the maximum acceleration occurs on, or just after, the first arrival and the impact of wave reflections and their coincidences is ignored. For the example in Fig. 6.2, the maximum acceleration at the top is 0.28 g's and at the bottom is 1.33 g's (where 1 g = acceleration due to gravity). The corresponding dominant frequencies can also be scaled from Fig. 6.2. These are 20,000 Hz and 45,000 Hz for the top and bottom accelerometers, respectively.

It can be shown through simple manipulation of the one-dimensional equation of motion that

$$\dot{w} = \frac{\tau_z V_c}{E} = \epsilon_z V_c \quad (6.5)$$

where

- $\dot{w}$  = particle velocity in the z-direction,
- $\tau_z$  = stress in the z-direction,
- $V_c$  = bar wave velocity,
- $E$  = Young's modulus, and
- $\epsilon_z$  = strain in the z-direction.

Thus, if the bar velocity for a material is known, even approximately, the magnitude of the strain at maximum particle velocity can be computed from

$$\epsilon_{z\max} = \frac{\ddot{w}_{\max}}{\omega V_c} \quad (6.6)$$

The bar wave velocity for this test was determined in Chapter 7 to be approximately 1250 fps, thus the maximum strain was computed to be  $5.7 \times 10^{-6}$  percent at the top and  $1.2 \times 10^{-4}$  percent at the bottom, well within the small strain region for this material.

#### 6.2.5 Measurement Errors for the Axial Pulse Test and Their Influence on the Constrained Modulus

Table 6.1 is a summary of the approximate errors and their propagation through the calculations to the final computed value of the constrained modulus. The values presented in Table 6.1 are approximated for the sand used as an example in this and the following chapter.

##### 6.2.5.1 Errors in Specimen Dimension and Weight

The length is initially measured with an accuracy of  $\pm 0.01$  inches and adjusted for changes measured during a test series using the proximeters. As the accuracy of the proximeters is about  $\pm 0.0001$  inches, it is believed any error in the length will be dominated by the initial measurement.

Table 6.1. Propagation of Errors in the Axial Pulse Test for a Loose Sand at  $\bar{\sigma}_0 = 16.0$  psi (ISO2T7 Test)

<u>Parameter</u>	<u>Quantity</u>	<u>Error</u>	<u>Units</u>	<u>% Error</u>
Length, L	6.37	± 0.01	in	0.2%
Diameter, D	2.81	± 0.01	in	0.1%
Volume, V	39.41	± 0.12	in <sup>3</sup>	0.3%
Weight, W	983.0	± 1.0	gram	0.1%
Unit Weight, $\gamma$	95.10	± 0.3	pcf	0.3%
Added Mass, $W_m$	485.5	± 0.1	gram	0.02%
Travel Time, $t_p$	372.5	± 8.0	$\mu$ s	
Time Delay, $t_d$	9.5	± 0.25	$\mu$ s	
Net Travel Time, ( $t_p - t_d$ )	363.0	± 8.0	$\mu$ s	2.2%
Compression Wave Velocity, $V_s$	1462.2	± 32.2	fps	2.2%
Constrained Modulus, M	6312600	± 202000	psf	3.2%
	43830	± 1400	psi	3.2%

The diameter of the sample is also measured initially to  $\pm 0.001$  inches or less, using a Pi tape. The initial diameter is the average of at least three measurements which may range as high as  $\pm 0.005$  inches from their mean, thus, an assumed error of  $\pm 0.01$  inches is considered reasonable. However, unlike the length, the diameter is not adjusted

using direct measurement. Changes in the diameter are computed using the assumption that the strains experienced in the sample are equal in the axial and radial directions. For isotropic loading this is a reasonable assumption and not likely to introduce any appreciable error. However, in the case of biaxial loading, this assumption is inherently wrong.

For a material under biaxial loading one expects that as the axial dimension increases, the radial dimension will decrease in an amount proportional to the Poisson's ratio. Consequently, the data reduction program written to reduce test series data was written to account for this volume change behavior. For moderately equal changes in the axial and horizontal stresses (less than 0.5 psi), the diametrical strain is proportional to the longitudinal strain and in the same direction. For unequal changes in the respective stresses, the diametrical strain is proportional to the longitudinal strain and taken in the opposite direction. Further, a distinction is made whether the change is in the axial stress or the horizontal stress. An assumed value of Poisson's ratio is used as the proportionality constant. Typical values assumed for this study were between 0.26 and 0.30 for the loose sand and between 0.18 and 0.22 for the dense sand. For all tests on the sand, the largest change in length was less than  $\pm 0.015$  inches, which amounts to an axial strain of  $\pm 0.0025$  for the specimen lengths used in this study. If one assumes a Poisson's ratio of 0.30, then the diametrical strains would be on the order of  $\pm 0.001$ , or one tenth of a percent or less.

The error in the volume is simply the square root of the sum of the squares of the appropriate errors of the length and the diameter. An error in the sample weight is governed by the care used during sample preparation. With the preparation technique described in Section 5.4 and Appendix F, it is believed that the weight of the sand samples can be determined to within one gram. This is an error of about 0.1 percent for the sample size used in this study. The error in the unit weight is the square root of the sum of the squares of the appropriate errors for weight and volume, resulting in an error of approximately 0.3 percent for the sand samples used in this study.

#### 6.2.5.2 Determining the Error in the Constrained Modulus

The principal source of error in the travel time is determining the time of arrival at the top. An examination of Fig. 6.2 shows the starting time is easily determined from the base accelerometer time record. However, the first arrival of the wave at the top accelerometer is less clear and a range exists where the actual arrival may occur. This "arrival window" is illustrated in Fig. 6.3 and is about 8  $\mu$ s wide, which is a potential error amounting to approximately two percent for the sand in this example. Conceptually, a stiffer material will have a shorter travel time and the "arrival window" will constitute a larger percentage of that travel time. However, the author has observed that as a material

becomes stiffer, Poisson's ratio decreases and the relative size of the "arrival window" decreases. The exception to this is a material which has high Poisson's ratio (greater than 0.48). This material will have a relatively high constrained velocity, regardless of its stiffness, and the "arrival window" constitutes a larger percentage of the travel time. In such a case even the precision of the measurement (typically  $\pm 0.5 \mu\text{s}$ ) will constitute a larger proportional error.

It remains a straightforward step now to determine the error in the constrained velocity and subsequently the constrained modulus. The example listed in Table 6.1 suggests the ultimate error in the constrained modulus is on the order of three percent, low for typical geotechnical measurements.

### 6.3 Determining the Shear Modulus Using an Independent Shear Pulse Test

#### 6.3.1 Conducting the Shear Pulse Test

To conduct a shear pulse test to find the shear wave velocity in a specimen, the function generator and digital recording oscilloscope are used with a tapping device which is set up as shown in Figs. 5.7 and 5.9. The configuration of the specimen and the appropriate accelerometers

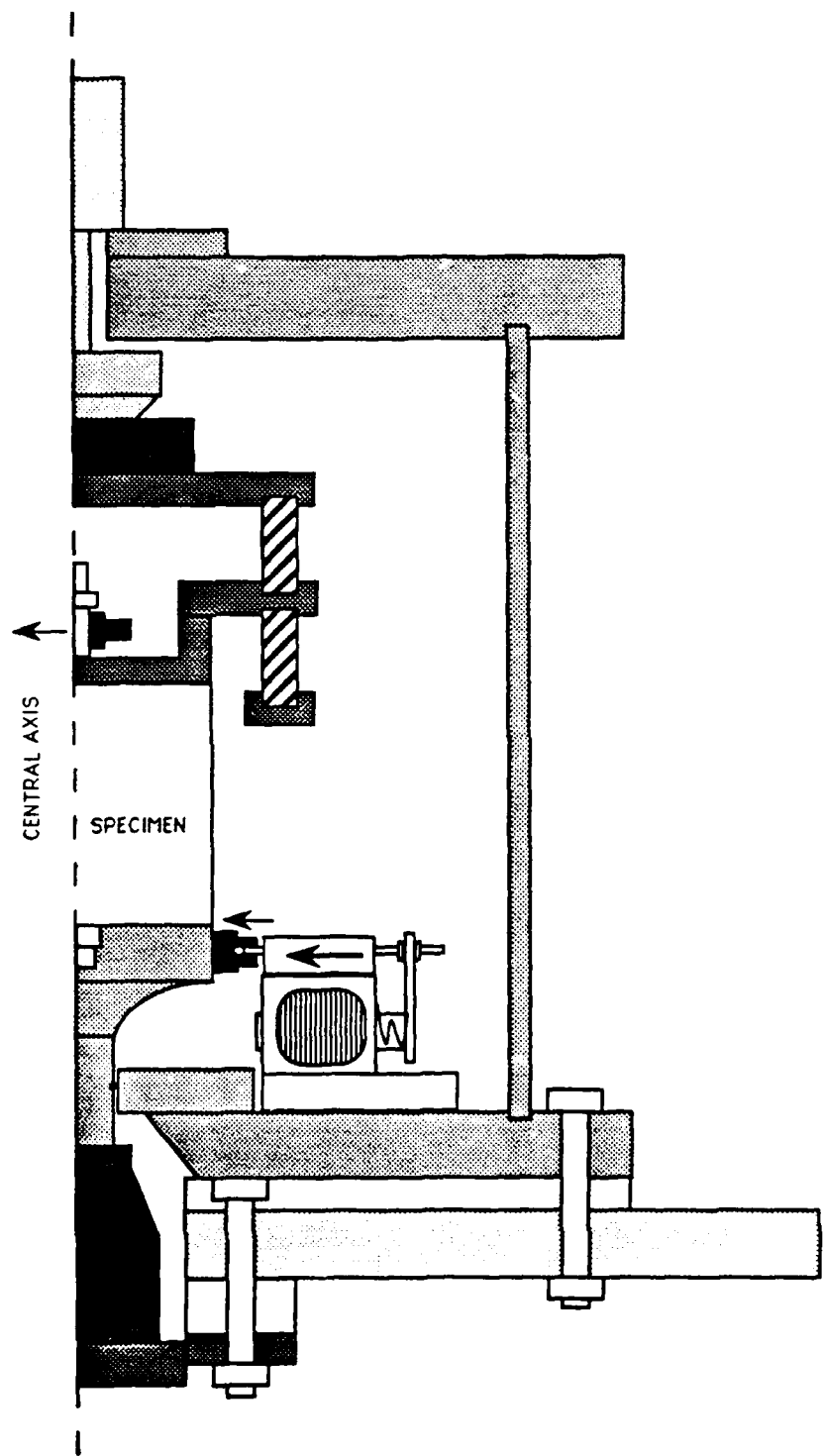


Fig. 6.5. Arrangement of MTD for Conducting Shear Pulse Test.

used for the test are shown in Fig. 6.5. The two horizontal accelerometers at the top and the horizontal accelerometer attached to the side of the base are connected to separate channels of the oscilloscope. The function generator is connected through a rectifier circuit to a variable amplifier/power supply and set to produce a 5.0-volt square wave at a frequency of 5.0 Hz. The rectifier acts to chop the negative half of the square wave, allowing only the positive voltage steps of the square wave to the amplifier. The amplifier is set to amplify the input signal 2 to 3 times and is connected, via an off-on switch, to the tapping device. The tapping device is made of a 0.125-inch diameter stainless steel rod mounted on a solenoid that was salvaged from an 8-track tape player. When the switch is closed, the positive voltage signal activates the solenoid and drives the rod against the side of the base pedestal. A small piece of steel is glued to the side of the base to protect its surface.

The oscilloscope is set to trigger on the signal produced by the horizontal accelerometer attached to the base next to where the tapper strikes. The oscilloscope is set to average 64 measurements and then stop. A direct copy of the oscilloscope screen is provided as an example in Fig. 6.6. Displayed in Fig. 6.6 are the responses of the base and two top accelerometers with the top accelerometer opposite the tapper being highlighted (darkened in the figure). After the test is complete, each waveform is stored internally in the oscilloscope and the screen is cleared. The stored waveforms are recalled, and using zoom and

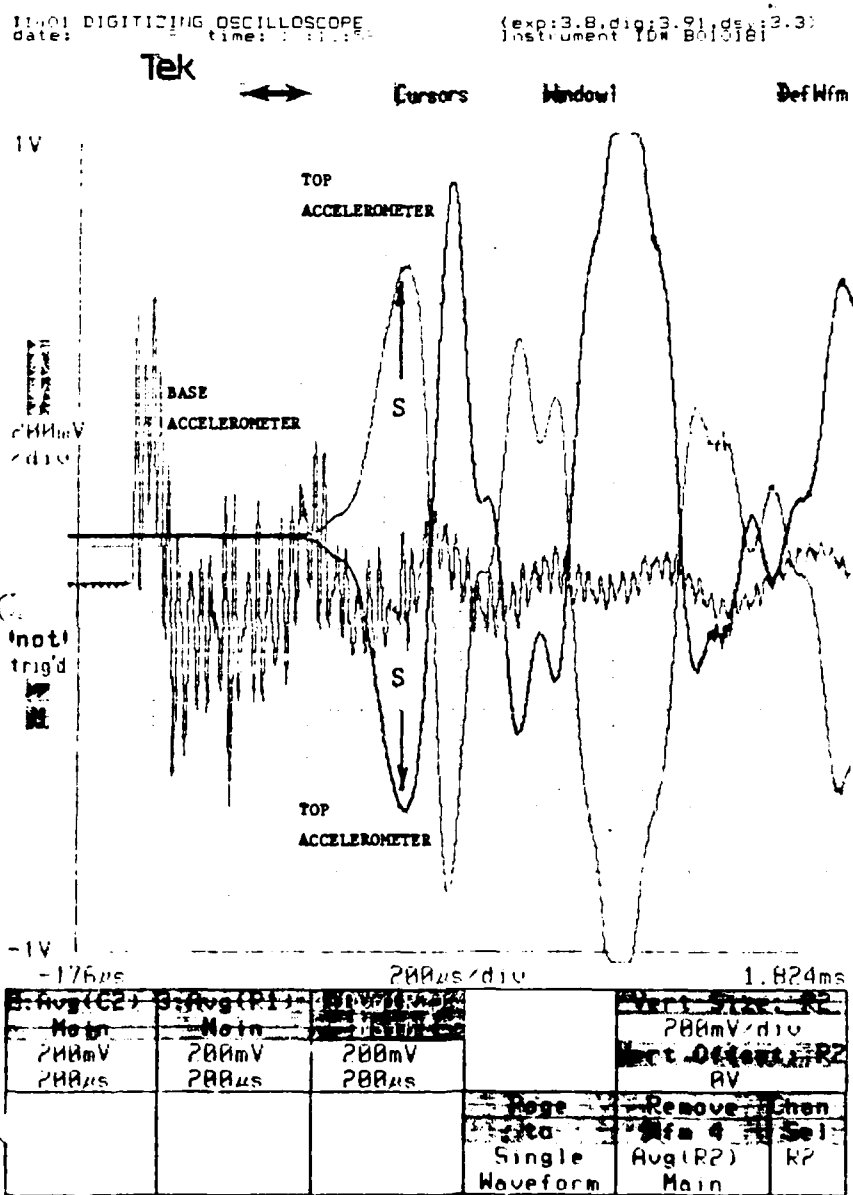


Fig. 6.5. Digital Oscilloscope Record of Shear Pulse Test on Loose Sand at 16 psi Confining Pressure (64 Averages).

amplification functions, the waveforms are manipulated and expanded for easier examination. The travel time,  $t_s$ , for the shear wave arrival is determined using the cursor functions. However, identification of the shear wave arrival at the top accelerometers is less straight forward than for the P-wave arrival and is discussed further in the next subsection.

The length of the sample,  $L$ , is determined using the initial measured length, adjusted for any changes determined from measurements using the proximeters as was described in the previous section for the axial pulse test. As before, the time delay,  $t_d$ , between the accelerometers was determined in a separate test without the soil sample present. The values of these delays typically ranged between 35 and 45  $\mu$ s. A value of 41  $\mu$ s was measured for this accelerometer configuration and is used in this example. The shear velocity,  $V_s$ , is then

$$V_s = \frac{L}{(t_s - t_d)}. \quad (6.7)$$

For the loose sand in Fig. 6.6,  $L = 0.2338$  ft, and the resulting shear wave velocity is 790 fps. The shear modulus,  $G$ , then follows from

$$G = \rho V_s^2 \quad (6.8)$$

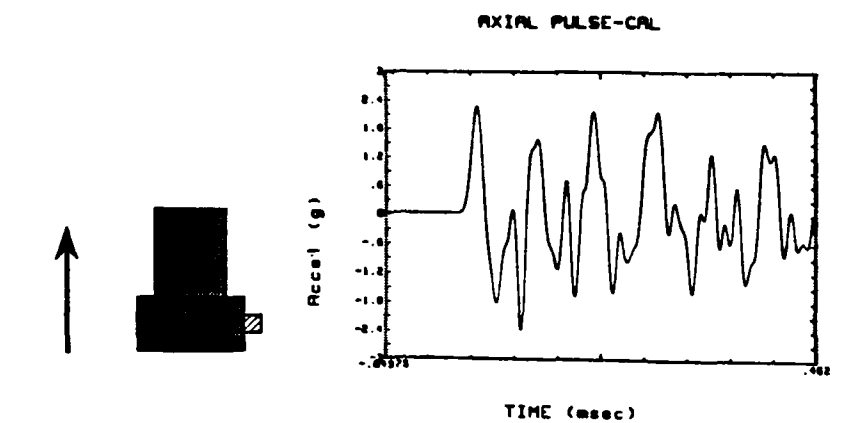
where  $\rho$  is the sample mass density.

Several assumptions have been made in the process of conducting the shear wave pulse test. These assumptions include clear identification of the shear wave arrival and that only small strains occur in the sample. Each of these is addressed separately in the following paragraphs.

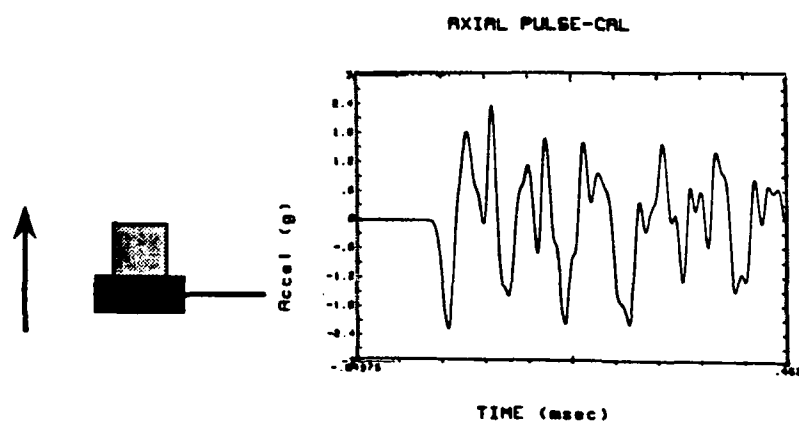
### 6.3.2 Identifying the Shear Wave Arrival

The shear wave is not the fastest travelling wave in the specimen. Consequently, its arrival at a receiver is often masked by the arrival of the dilatational wave. Also complicating this case is the presence of near-field shear waves, which are commonly observed when the receiver is less than two wavelengths from the source. Sanchez-Salinero (1987) showed that the near-field shear wave would travel at the P-wave velocity, further complicating identification of the far-field shear wave when making measurements close to the source.

To assist in identifying the shear wave arrival, each accelerometer used for this test was glued to the same base and subjected to an upward pulse. The relative orientation of the signal output is shown in Fig. 6.7. Using the accelerometer's base as the bottom reference an upward motion results initially in a positive signal for the top accelerometers and a negative signal for the base accelerometers. This suggests that, for the shear pulse test, the top horizontal accelerometer opposing the source should experience a significant positive signal



a) Low Impedance, Internally Amplified Accelerometer



b) High Impedance, Charge Output Accelerometer

Fig. 6.7. Relative Output for Accelerometer Used in the Shear Pulse Test.

corresponding to the main shear wave arrival. Figure 6.8 illustrates how the shear wave arrival was selected for a typical test. The second top accelerometer provides a check and aids in arrival identification. The travel time recorded was the average of the two separate measurements.

The P-wave and/or near-field shear wave arrival can also be seen at the top accelerometers, although this arrival can only be identified by magnifying the vertical scale of the recorded signal many more times than is necessary for the shear wave measurement. This has been done for the example and the P-wave arrival is also annotated in Fig. 6.8.

### 6.3.3 Assumption of Small Strains in the Shear Pulse Test

The strain level at the top and bottom of the specimen is computed in a manner analogous to that developed in Section 6.2.4. It is again noted that it is inherently assumed that the maximum acceleration occurs at, or just after, the first arrival and the impact of wave reflections and their coincidences is ignored. Then, assuming one-dimensional wave propagation, the shear strain,  $\gamma$ , at maximum horizontal particle velocity is computed from

$$\gamma_{\max} = \frac{\ddot{u}_{\max}}{\omega V_s} \quad (6.9)$$

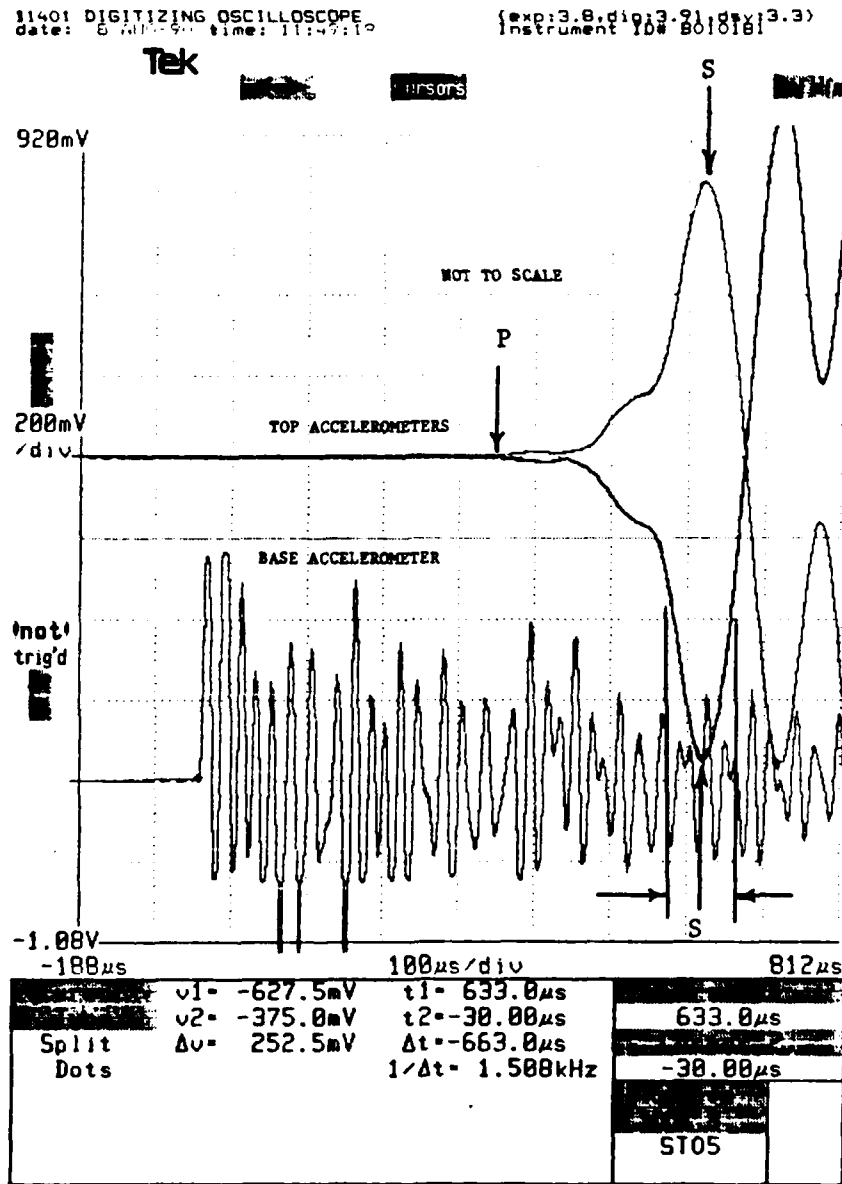


Fig. 6.8. Determining the Shear Wave Arrival From an Amplified Time Record on the Digital Recording Oscilloscope.

An examination of Fig. 6.6 shows at the top and bottom of the sample the maximum accelerations were 1.2 and 3.7 g's and the corresponding frequencies were 3,333 and 40,000 Hz, respectively. The shear wave velocity for this example was 790 fps, and the strains were computed to be  $2.3 \times 10^{-4}$  percent at the top and  $5.9 \times 10^{-5}$  percent at the bottom.

#### 6.3.4 Determining the Error in the Shear Modulus

Table 6.2 is a summary of the approximate errors and their propagation through the calculation of the independently measured shear modulus. The values in Table 6.2 are approximated for the loose sand confined isotropically that is used as an example in this and the following chapter. Comments pertaining to the errors in the sample dimensions and properties are included in Section 6.2.5.1 and are not repeated here.

The principal source of error in the measurement of the shear modulus is determining the arrival of the main (far-field) shear motion at the top horizontal accelerometers. The "arrival window" is illustrated in Fig. 6.8. An examination of the time record for the top accelerometer shows motion occurring well in advance of the larger far-field shear wave. Consequently, its arrival is obscured and could occur within a window 80 - 120  $\mu$ s wide. If the middle point in the window is chosen, and an average error is assumed of half the maximum window width,

Table 6.2. Propagation of Errors in the Shear Pulse Test for a Loose Sand at  $\bar{\sigma}_o = 16.0$  psi (ISO2T7 Test)

<u>Parameter</u>	<u>Quantity</u>	<u>Error</u>	<u>Units</u>	<u>% Error</u>
Length, L	6.37	± 0.01	in	0.2%
Diameter, D	2.81	± 0.01	in	0.1%
Volume, V	39.41	± 0.12	in <sup>3</sup>	0.3%
Weight, W	983.0	± 1.0	gram	0.1%
Unit Weight, $\gamma$	95.10	± 0.3	pcf	0.3%
Added Mass, $W_m$	485.5	± 0.1	gram	0.02%
Travel Time, $t_s$	713.5	± 60	$\mu$ s	
Time Delay, $t_d$	41.0	± 1.0	$\mu$ s	
Net Travel Time, $(t_s - t_d)$	672.5	± 57	$\mu$ s	8.5%
Shear Wave Velocity, $V_s$	789.9	± 67.1	fps	8.5%
Shear Modulus, $G_m$	1841970	± 222880	psf	12.1%
	12790	± 1550	psi	12.1%

say  $\pm 60 \mu$ s, then the error for the shear wave velocity of the loose sand at 16 psi confining pressure will be 8.5 percent. This results in a 12% error in the shear modulus.

This large an error is unacceptable and makes it difficult to draw any useful conclusions from the shear pulse test as it is currently configured in the MTD. To be useful, a shear wave source which does not generate so large a P-wave will need to be developed.

#### 6.4 Summary

Two of the three tests conducted in the Multi-Moduli Testing Device (MTD) are the axial and shear pulse tests which measure the dilatational and shear wave velocities that are used to calculate the constrained and shear modulus, respectively.

In the axial pulse test, the piezoelectric shaker applies a step function impulse to the base of the sample and the responses of the bottom and top vertical accelerometers are recorded by the digital recording oscilloscope. The travel time for the pulse is determined from the two time records, adjusted for any delay, and the dilatational wave velocity is computed from the sample length. The travel time is chosen as the time interval between the first arrivals at each accelerometer. The justification for picking the first arrival is based on the transient wave propagation theory discussed in Chapter 3. When the solution for transient motion in a rod (due to a sudden impact at the one end) is plotted as a function of time, it shows that particle motion begins at about the time corresponding to the theoretical arrival of the dilatational wave. Calculations for an example test on a loose sand confined at 16 psi showed that the maximum strains experienced by the sand were on the order  $1 \times 10^{-4}$  percent, or less. An examination of the errors in the axial pulse test suggest the error in the constrained modulus should not exceed three percent.

In the shear pulse test, a mechanical tapping device strikes the side of the base pedestal and the responses of the bottom and two top horizontal accelerometers are recorded by the digital recording oscilloscope. The travel time for the pulse is determined from the three time records, adjusted for any delay, and the shear wave velocity is computed from the sample length. The travel time is determined by observing the arrival of the polarized shear wave that corresponds to the direction of impact. However, motions travelling at the faster P-wave velocity obscure the shear wave arrival. This problem is likely due to the nature of the source and the size of the sample. Consequently, the error in the shear modulus is significantly greater than for the constrained modulus, and may be as large as 15 percent. A new dynamic source is needed which will generate a stronger shear wave that can be reversed.

## **Chapter Seven**

### **Young's Modulus from Longitudinal Resonant Column Testing**

#### **7.1 Introduction**

The use of resonant testing to determine the dynamic stiffness of civil engineering materials is slowly gaining acceptance in practice. The development of laboratory testing using dynamic techniques over the past 30 years is discussed in Chapter 2. The American Society for Testing and Materials has a formalized method, C215-85, to determine dynamic moduli of concrete specimens using the fundamental transverse, longitudinal and torsional frequencies.

The general procedure used in this research to measure multiple longitudinal natural frequencies of a typical soil specimen and to compute the elastic Young's modulus from those measured frequencies as discussed in this chapter. Detailed test procedures are included in Appendix F. A description of the test apparatus and equipment is included in Chapter 5 and Appendix E. Theoretical development of the equations used to backcalculate Young's modulus are contained in Chapter 3 and Appendices A and B.

## 7.2 Determining Young's Modulus of Soil Specimens

### 7.2.1 Conducting the Longitudinal Resonant Column Test

The arrangement of the MTD for conducting the longitudinal resonant column test is illustrated in Fig. 7.1, and the equipment set up is shown in Fig. 5.10. The base and top vertical accelerometers are connected to channels 1 and 2 of the dynamic signal analyzer, and the piezoelectric shaker is connected to the analyzer's internal function generator. The dynamic signal analyzer is set to conduct an upward frequency sweep with channel 1, the base accelerometer, used as the reference channel for frequency and amplitude control.

Table 7.1 is a listing of some of the pertinent settings that were used for the loose sand specimen used as an example in this chapter and for the pulse tests described in Chapter 6. The analyzer can be set to conduct the frequency sweep automatically, allowing the operator to perform other functions while the test is progressing. Depending on the properties of the test specimen, the operator may have to reset the source level or the range of the top accelerometer to insure good coherence between the accelerometer's signals. The settings in Table 7.1 were found to be appropriate for virtually all sand tests with adjustments only required for extreme variations, high or low, in material stiffness and damping. For all the tests on sand, loose or dense, the

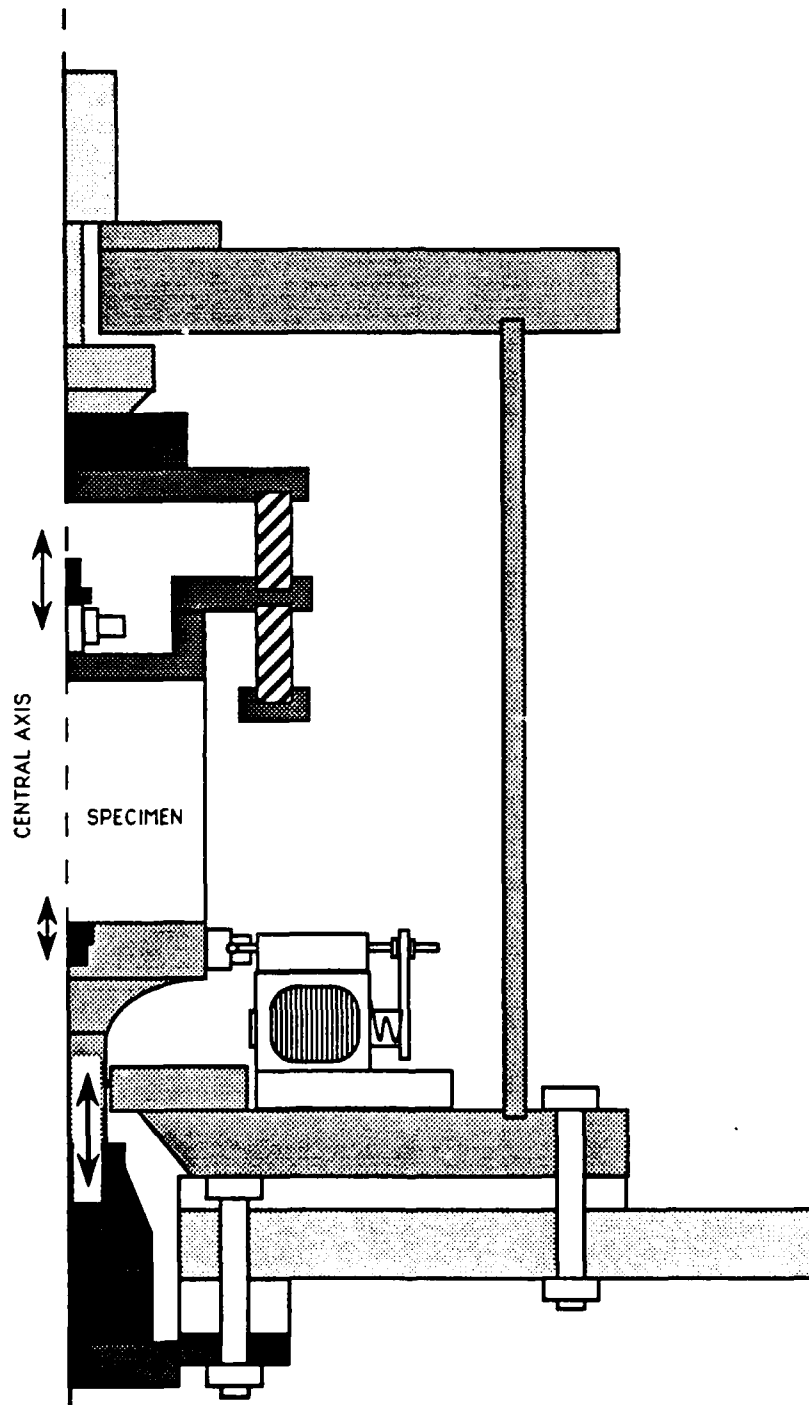


Fig. 7.1. Arrangement of MTD for Conducting Longitudinal Resonant Column Test.

**Table 7.1. Typical Settings for Dynamic Signal Analyzer for Longitudinal Resonant Column Test on Sand.**

<b>Measurement Mode:</b>	<b>Swept Sine - Linear Sweep</b>
<b>Auto Gain:</b>	<b>on</b>
<b>Ref Chan</b>	<b>Chan 1</b>
<b>Ref Level</b>	<b>15 mVpk</b>
<b>Source Limit</b>	<b>&lt; 2 Vpk</b>
<b>Average:</b>	
<b>Integration Time</b>	<b>50.0 ms</b>
<b># of Averages</b>	<b>8</b>
<b>Frequency:</b>	
<b>Start</b>	<b>100 Hz</b>
<b>Stop</b>	<b>5 kHz</b>
<b>Resolution</b>	<b>6.12 Hz/Point</b>
<b>Source:</b>	
<b>Sweep</b>	<b>Up</b>
<b>Offset</b>	<b>0.0 Vpk</b>
<b>Input:</b>	
<b>Chan 1</b>	<b>Auto Range Up</b>
<b>Chan 2</b>	<b>Auto Range Up</b>
<b>Chan 1</b>	<b>AC (Float) Coupling</b>
<b>Chan 2</b>	<b>AC (Float) Coupling</b>

settings in Table 7.1 were adequate for confining pressures ranging from 4 to 32 psi. Typically, the frequency range would have to be extended above 5000 Hz for sand under higher confining pressures (64+ psi) or stiffer materials such as polyvinylchloride and Portland cement concrete. It also was common to have to increase the reference level (15 mv) for highly damped materials such as the compacted clay and polyurethane specimens.

The analyzer performs a frequency sweep by driving the vibration generator at a specific frequency and amplitude referenced to a designated channel. In this example, the reference channel was the base accelerometer and the reference level was 15 mv, which was about 0.1 g. (The accelerometer constant, after amplification, was 150mv/g.) The source was also set to a maximum of  $\pm 2.0$  Volts peak to protect the piezoelectric shaker which has an input limit at the power amplifier of  $\pm 3.0$  Volts. The analyzer outputs a sine wave to the piezoelectric shaker in order to attain the prescribed test frequency at the base accelerometer. A typical test frequency range used for the natural soils was 100 to 5000 Hz, with a sweep consisting of 200 test frequencies. This resulted in a resolution of 6.12 Hz between test points. At each frequency, the analyzer took eight averages of the measured signals and then computed the relative amplitude and phase of the signals received at the two input channels. The analyzer could also display a variety of other waveform functions, including the coherence between channels, the

power spectrum of each channel, and the cross spectrum between the channels.

In the longitudinal resonant column test, the phase of the frequency spectrum is used to determine the natural frequencies of the sample. Figure 7.2 is the amplitude, phase and coherence plot for a longitudinal resonant column test on a loose sand ( $D_r = 26\%$ ) confined isotropically at 16.0 psi . The top curve is the ratio of the amplitudes of the top accelerometer to the bottom accelerometer in terms reduced to actual acceleration using the appropriate accelerometer constants and amplifier gains. The middle curve is the phase of the top accelerometer relative to the bottom accelerometer and is displayed in a form which wraps the plot between  $\pm 180$  degrees. The bottom curve is the coherence between the measured signals and is an indication of how well the signals relate to one another. A value close to 1.0 is an indication that the signals track each other well and the amplitude and phase measurements should be good. Low coherence can be the result of interference from other waves in the specimen, external noise and vibrations, or motion too small to be detected by one, or both, of the accelerometers. It is noted in Fig. 7.2 that the coherence is poor below about 300 Hz, a limitation attributable to both the accelerometer's inability to sense, and the piezoelectric shaker's inability to generate, low frequency motions.

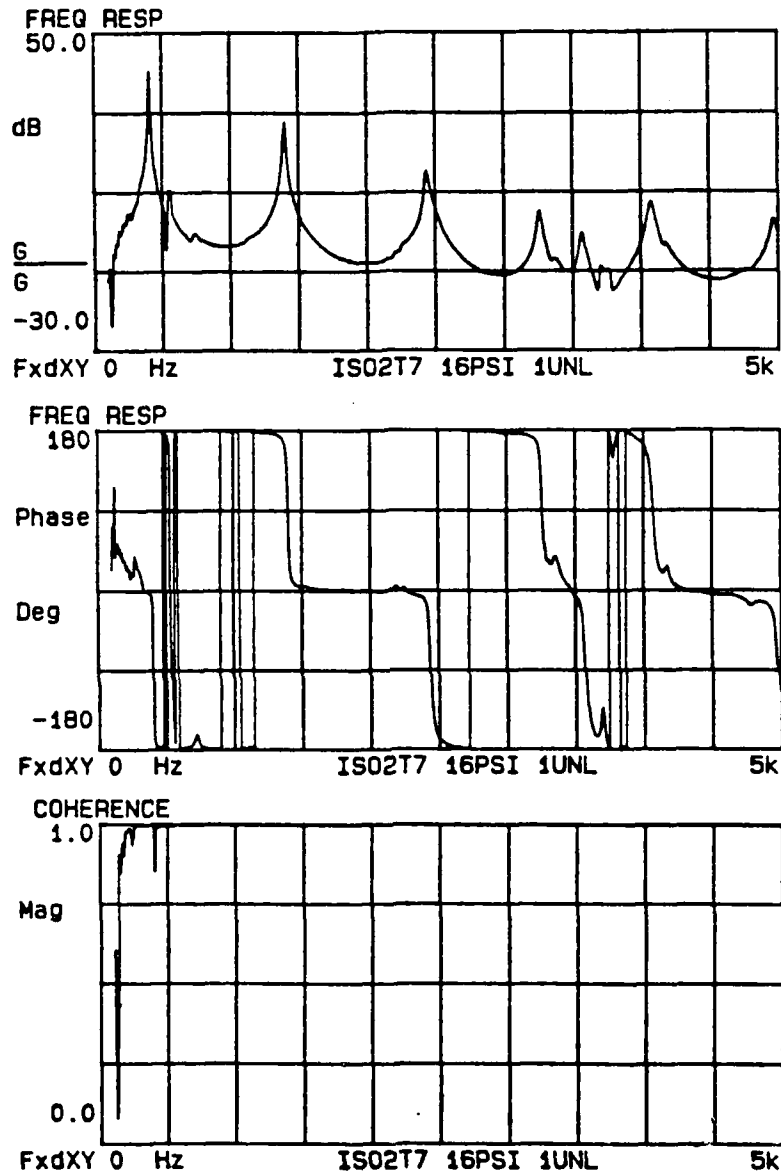


Fig. 7.2. Dynamic Signal Analyzer Record for Longitudinal Resonant Column Test on a Loose Sand Under 16 psi Confining Pressure (ISO2T7 test).



$$\frac{W_s}{W_m} = \beta_n \tan \beta_n, \quad n = 1, 2, 3, \dots \quad (7.1)$$

where

$$\beta_n = \frac{\omega_n L}{C_B} = \frac{2\pi f_n L}{C_B}, \quad n = 1, 2, 3, \dots \quad (7.2)$$

and where

- $W_s$  = weight of the specimen
- $W_m$  = weight of added mass,
- $L$  = length of specimen,
- $C_B$  = bar wave velocity,
- $\omega_n$  = resonant circular frequency in rad/sec, and
- $f_n$  = resonant frequency in cycles/sec.

Therefore, for any given  $W_s$ ,  $W_m$ ,  $L$ , and  $C_B$ , the value of  $f_n$  could be predicted by solving the transcendental equation. This is easily accomplished numerically by computer. Alternatively, if  $W_s$ ,  $W_m$ ,  $L$  and  $f_n$  are known, then  $C_B$  can be calculated. This has been done for the example test and the results listed in the third column of Table 7.2 and denoted as  $C_n$ . It is immediately obvious that the values calculated for  $C_n$  are not equal to each other as would be expected for one-dimensional wave propagation in a linearly elastic, finite rod. Therefore, an additional adjustment is required.

Table 7.2. Example of Data Reduction Steps for Longitudinal Resonant Column Test Using Data from ISO2T7 Test on Loose Sand Confined Isotropically at 16 psi.

(1) Mode n	(2) $f_n$ Hz	(3) $C_n^*$ fps	(4) $\lambda_n$ ft	(5) $2a/\lambda$	(6) $C_n/C_B^{**}$	(7) $V_c$ fps	(8) $E_n$ psi
1	403.6	1245.6	3.086	0.076	0.9990	1246.8	31,915
2	1397.7	1277.7	0.914	0.256	0.9867	1294.9	34,423
3	2438.9	1235.8	0.507	0.461	0.9427	1310.9	35,279
4	3259.5	1128.6	0.346	0.675	0.8371	1348.2	37,316

\*  $C_n = C_B$  where  $C_B$  is from  $\beta_n = \frac{2\pi f_n L}{C_B}$

\*\* For  $\nu = 0.27$

It was shown in Chapter 3 and Appendix B that dispersion occurs in an infinite rod subjected to a steady-state motion. It was also shown that the velocity of propagation is a function of the radius and stiffness properties of the rod and the frequency of the driving motion. Figure 7.3 is a plot of the dimensionless velocity ratio (the ratio of the phase velocity,  $C$ , to the theoretical bar velocity,  $C_B$ ), as a function of the dimensionless wavelength,  $2a/\lambda$ , for various values of Poisson's ratios. Only the first longitudinal mode of propagation is shown. Thus, for any given radius,  $a$ , wavelength,  $\lambda$ , and Poisson's ratio,  $\nu$ , three-dimensional theory predicts the dimensionless velocity ratio. Finally, if the phase velocity is known, then the theoretical bar velocity can be computed from the dimensionless velocity ratio.

Using this approach for the example test on the loose sand, the wavelength can be determined for each longitudinal mode of propagation using a variation of Eq. 7.2. By noting  $f\lambda = C$ , and substituting  $C_n$  for  $C_B$ , the wavelength for each mode can be computed directly from

$$\lambda_n = \frac{2\pi L}{\beta_n} . \quad (7.3)$$

Then, assuming a value for Poisson's ratio, a dimensionless velocity ratio can be determined for each natural frequency using the curves in Fig. 7.3. Finally, by assuming that the velocity computed from the first

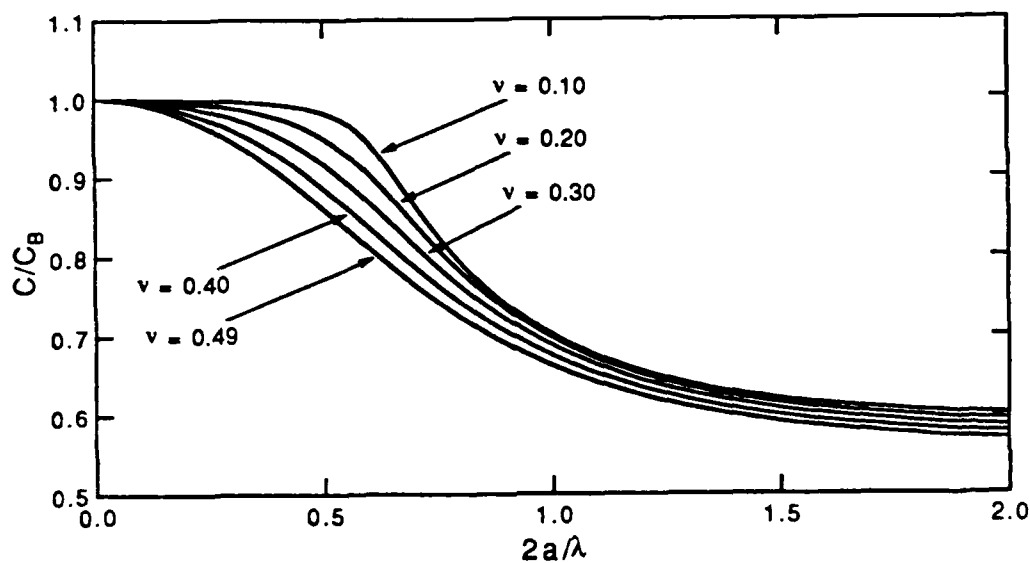


Fig. 7.3. Dimensionless Velocity Ratio as a Function of the Dimensionless Wavelength For Various Poisson's Ratios (Fundamental Mode Only).

approximation is the phase velocity, the bar velocity is calculated. The fourth through seventh columns of Table 7.2 reflect these steps. Here the values for  $C_T/C_B$  were computed numerically using an assumed value of Poisson's ratio equal to 0.27. The bar velocity computed in this manner is listed in the seventh column of Table 7.2 and is denoted as  $V_c$  to reflect the fact it is a measured quantity.

The final step is to compute Young's modulus using the relationship developed earlier for one-dimensional motion

$$E = \rho V_c^2 \quad (7.4)$$

where  $\rho$ , the mass density, is taken from the appropriate measurements. Consequently, there will be a different value of  $E_n$  for each longitudinal mode of propagation,  $n$ . Which value of  $E_n$  is the most correct is discussed in Section 7.3. The values for Young's modulus computed for the loose sand in the test example are shown in the eighth column of Table 7.2.

### 7.2.3 Computing Poisson's Ratio and the Shear Modulus

The adjustment to the phase velocity using the dimensionless velocity ratio requires a value for Poisson's ratio. In the earlier example, a Poisson's ratio of 0.27 was assumed. An examination of Fig. 7.3 shows that, for low and high values of the dimensionless wave number, an error in the estimate of Poisson's ratio should have only a small impact on the computed value of the bar velocity,  $V_c$ . Nevertheless, with the bar wave velocity from this test and the constrained wave velocity from the axial

pulse test described in Chapter 6, a possibly more accurate value of Poisson's ratio is available.

Poisson's ratio can be computed directly using the results from the axial pulse test. From linear elastic theory it can be shown

$$v = \frac{\sqrt{B^2 + 4B} - B}{2} \quad (7.5)$$

where

$$B = \frac{M - E}{2M} = \frac{V_p^2 - V_c^2}{2V_p^2} \quad (7.6)$$

- v = Poisson's ratio,
- M = constrained modulus from axial pulse test,
- E = Young's modulus from longitudinal resonant column test,
- V<sub>p</sub> = constrained velocity measured in pulse test,  
and
- V<sub>c</sub> = bar velocity computed from longitudinal resonant column test.

The computed value of Poisson's ratio can now be compared to that originally assumed and, if different, the computed value can be used to recompute the value of the bar wave velocity. By iteration in this manner the appropriate value of Poisson's ratio and the dimensionless velocity

ratio is quickly reached. This process is easily incorporated in a computer program and this has been done for all the laboratory test series. A copy of the source listing for the data reduction program is included in Appendix F. Figure 7.4 is a copy of the individual test printout for the loose sand at 16.0 psi that is used in this example (ISO2T7 test).

The shear wave velocity can now be calculated assuming isotropic linear elasticity from either

$$V_s = \frac{V_c}{\sqrt{2(1+\nu)}} \quad (7.7)$$

or

$$V_s = V_p \sqrt{\frac{(1-2\nu)}{2(1-\nu)}} \quad (7.8)$$

Finally, the shear modulus,  $G$ , follows from

$$G = \rho V_s^2 \quad (7.9)$$

where  $\rho$  is the sample mass density. As there was a different value of the bar velocity for each mode, there will also be a different value of the shear wave velocity and shear modulus backcalculated for each mode.

ISO2 TEST SERIES, 3-4 MAY 90

TEST NO. 7  
TIME(hr): 6.50

## STRESSES:

AXIAL = 16.16 psi  
 HORIZ. = 15.99 psi  
 MEAN = 16.05  
 K0 = 1.01

## SAMPLE PROPERTIES:

HEIGHT (in): 6.3695  
 DIAMETER (in): 2.8077  
 WEIGHT (lb): 2.1675  
 VOLUME (cf): .0228  
 UNIT WT. (pcf): 94.98  
 SPECIFIC GRAVITY: 2.670  
 WATER CONTENT: .001510  
 VOID RATIO: .7577  
 ADDED MASS (lb): 1.0703

MODE	fr(Hz)	C(fps)	Cb(fps)	Cp(fps)	POI. RAT.	Cs(fps)
1	403.6	1245.6	1247.3	1462.2	.3072	771.4
2	1397.7	1277.7	1295.9	1462.2	.2783	810.5
3	2438.9	1235.8	1310.4	1462.2	.2684	822.7
4	3259.5	1128.6	1338.0	1462.2	.2474	847.1

## MODULI (psf):

	YOUNGS	CONSTRAINED	SHEAR
1	4593047.	6312600.	1756849.
2	4958149.	6312600.	1939411.
3	5069600.	6312600.	1998447.
4	5285589.	6312600.	2118600.

## MODULI (psi):

	YOUNGS	CONSTRAINED	SHEAR
1	31896.	43838.	12200.
2	34432.	43838.	13468.
3	35206.	43838.	13878.
4	36705.	43838.	14713.

INDEPENDENT SHEAR WAVE VELOCITY: 789.9 fps  
 INDEPENDENT SHEAR MODULUS: 1841972. psf  
 INDEPENDENT SHEAR MODULUS: 12791. psi

Fig. 7.4. Individual Test Printout for ISO2T7 Test on a Loose Sand Under 16 psi Confining Pressure.

#### 7.2.4 The Assumption of Small Strains in the Longitudinal Resonant Column Test

It is important to determine that the strains experienced during this test are small enough so that the small-strain assumption remains valid. The process of computing the maximum strain in the specimen is analogous to that described in Section 6.2.4. However, the maximum acceleration and frequency are now known fairly accurately at each resonant mode. The acceleration at the bottom is 0.1 g, and is known because it is preset at the beginning of the test. An examination of Fig. 7.2 shows the maximum amplitude occurs at the first resonant mode and the acceleration at the top can be computed from the equation defining the amplification

$$\text{Amplification (dB)} = 20 \log_{10} \left( \frac{\ddot{w}_{\text{top}}}{\ddot{w}_{\text{base}}} \right) \quad (7.10)$$

The amplification at the first resonant mode is approximately 40 dB, so the corresponding acceleration at the top is approximately 10.0 g's. The maximum strain at the top and bottom can now be computed using Eq. 6.5, the first natural frequency of 403.6 Hertz and the approximate bar velocity,  $V_c = 1250$  fps. The resulting axial strains are  $1.0 \times 10^{-4}$  percent and  $1 \times 10^{-2}$  percent at the bottom and top, respectively.

Table 7.3. Summary of Maximum Strains for Example Longitudinal Resonant Column Test

Mode	Natural Freq., Hz	Magnitude dB	Base* $\epsilon_{zmax}\%$	Top $\epsilon_{zmax}\%$
1	403.6	40	$1.0 \times 10^{-4}$	$1.0 \times 10^{-2}$
2	1397.7	27	$2.9 \times 10^{-5}$	$6.6 \times 10^{-4}$
3	2438.9	15	$1.7 \times 10^{-5}$	$9.4 \times 10^{-5}$
4	3259.5	6	$1.3 \times 10^{-5}$	$2.5 \times 10^{-5}$

\*Base acceleration set to 0.1 g's

A similar calculation can be conducted for the second, third, and fourth resonant modes. The corresponding maximum strains are summarized for each mode in Table 7.3. Note that except for the first resonant mode, all the maximum strains are less than  $1 \times 10^{-3}$  percent, the small-strain threshold for this sand.

### 7.2.5 Measurement Errors in the Longitudinal Resonant Column Test and Their Influence on the Calculation of Young's Modulus

A summary of the approximate errors and their propagation through the calculation of the Young's modulus for the loose sand used in this example is presented in Table 7.4. Comments pertaining to errors in the sample dimensions and weight are included in Section 6.2.5.1.

The principal source of error in the computation of Young's modulus is from the length measurement and the determination of the natural frequency. The example in Table 7.4 suggests the computation process only introduces an error in the Young's modulus that is on the order of 1-2 percent. However, the study using the finite element model that is described in Chapter 4 suggests the two-step reduction method and the effect of the various test parameters will introduce errors which may be attributable to the test method, the test apparatus and the data reduction method. In particular, the parametric model study showed that the potential error in backcalculating the correct bar velocity tends to increase for the higher modes. However, that error never exceeded one or two percent and normally remained below one percent for the first three modes. Consequently, it is possible to conclude the error in determining the Young's modulus will surely be less than five percent. This is further substantiated by the comparison discussed in the next section.

Table 7.4. Propagation of Errors in the Longitudinal Resonant Column Test (Values from 1st Mode of ISO2T7 Test)

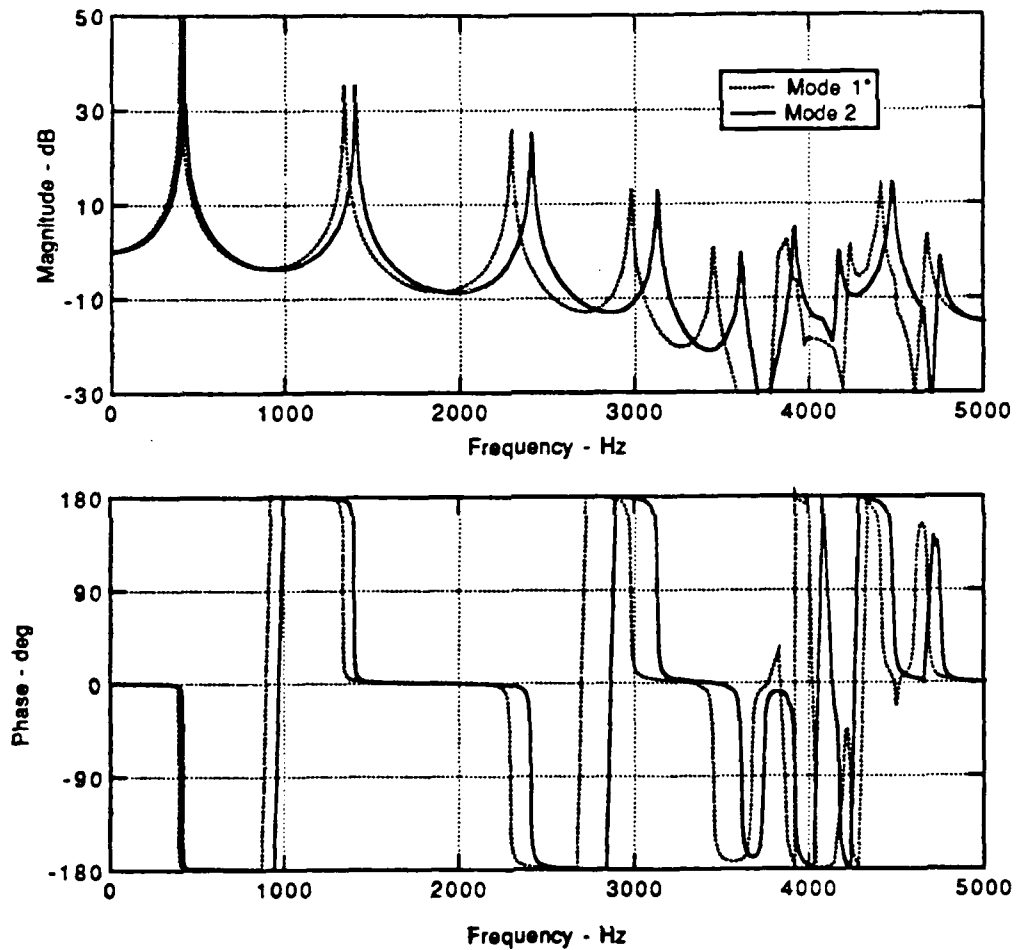
<u>Parameter</u>	<u>Quantity</u>	<u>Error</u>	<u>Units</u>	<u>% Error</u>
Length, L	6.37 ± 0.01		in	0.2%
Diameter, D	2.81 ± 0.01		in	0.4%
Volume, V	39.41 ± 0.24		in <sup>3</sup>	0.6%
Weight, W	983.0 ± 1.0		gram	0.1%
Unit Weight, $\gamma$	95.10 ± 0.5		pcf	0.6%
Added Mass, $W_m$	485.5 ± 0.1		gram	0.02%
Natural Frequency, $f_n$	403.6 ± 0.5		Hz	0.1%
Phase Velocity, $C_1$	1245.6 ± 2.9		fps	0.2%
Wavelength, $\lambda_1$	37.03 ± 0.08		in	0.2%
Wave Ratio, $2a/\lambda$	0.0338 ± 0.0003			0.5%
Velocity Ratio, $C/C_B$	0.9990 ± 0.0046			0.5%
Bar Velocity, $V_c$	1246.8 ± 6.1		fps	0.5%
Young's Modulus, $E_1$	4595400 ± 42100		psf	0.9%
	31915 ± 292		psi	0.9%

### 7.3 Comparing the Frequency Response Measured in the Laboratory to that Calculated by the Finite Element Model

Figure 7.5 is the transfer function computed using the finite element model described in Chapter 4. The input parameters for the program runs were taken directly from the test results for the loose sand used as an example in the preceding section. Two transfer functions are shown in Fig. 7.5, one each corresponding to the moduli computed from the first two natural frequencies found in the longitudinal resonant column test. The Young's modulus and shear modulus (computed from Eq. 7.9 using the measured constrained modulus) were used for the input stiffnesses. The damping ratio was calculated from the first mode noting the following from Fig. 4.10 for a single degree-of-freedom system

$$\left( \frac{\ddot{w}_{top}}{\ddot{w}_{base}} \right) = \frac{1}{2D} \quad (7.10)$$

where the left side of the equals sign represents the magnitude (amplification ratio), and  $D$  is the damping ratio. Recall that for this example, the magnitude of the first peak is approximately 40 dB, making the respective damping ratio approximately 0.05, or 5 percent. Other specimen parameters used for the input came directly from the laboratory results as summarized in Fig. 7.4. Table 7.5 summarizes the bar



\* Stiffness parameters based on Mode "n".

Fig. 7.5. Transfer Function for Loose Sand Computed Using Finite Element Model and Stiffness Parameters Determined in the Laboratory in the ISO2T7 Test.

Table 7.5. Comparison of Model Bar Velocities to Measured Bar Velocities for Loose Sand (ISO2T7)

	$V_c$ - fps			
	Mode 1	Mode 2	Mode 3	Mode 4
ISO2T7 (Lab Test)	1247.3	1295.6	1309.5	1336.7
FEM1*	1248.7 0.11%**	1249.7 -3.54%	1250.5 -4.51%	1251.1 -6.40%
FEM2	1297.3 4.01%	1298.1 0.19%	1298.7 -0.82%	1298.9 -2.83%
FEM3	1311.1 5.12%	1311.9 1.26%	1312.4 0.22%	1312.6 -1.80%
FEM4	1338.4 7.30%	1339.0 3.35%	1341.5 2.44%	1339.4 0.20%

\* FEM(n) represents program input corresponding to mode n from ISO2T7 test using  $E_n$  and  $G_n$ , where  $G_n$  is computed from  $M$  and  $E_n$ .

\*\* Percent difference from corresponding mode in ISO2T7 test.

velocities determined in the lab and resulting from the finite element model runs. It can be seen the best match for the lab data occurs when the moduli from the second or third modes are used for input.

It is noted now, that the bar wave velocities for the second and third mode are within one percent of each other, while the first mode is about five percent lower. There are two possible explanations. The first is that the strain level in the sand is above the small-strain range and a lower modulus is being measured. It is suggested in Section 7.2.4 that the axial strain at the top is on the order of  $1 \times 10^{-2}$  percent and, as can

be seen in Fig. 8.10, the stiffness of the loose sand begins to decrease when the axial strain is greater than  $1 \times 10^{-3}$  percent. The second explanation considers the one-dimensional wave propagation assumption which is made in the process of reducing the natural frequencies to the bar wave velocity. As the frequency increases for the higher modes of vibration, the wavelength becomes shorter with respect to the diameter and the long bar assumption associated with one-dimensional theory may no longer apply.

This comparison of laboratory and model results is important because it supports the use of the second or third natural frequencies to define the relationship between the various moduli and the stress state. In virtually all the longitudinal column tests in the biaxial test series, the first natural frequency was obscured by other resonances in the system. Further, in the BIAx1, BIAx2 and BIAx3 test series, the second mode was also obscured when the axial load was high (in tension or compression), and only results from the third natural frequency could be relied on for analysis. The BIAx4 and BIAx5 test series used a new dynamic isolation top cap assembly, and the second, third, and fourth (where present), natural frequencies were clearly identifiable.

#### 7.4 Summary

A longitudinal resonant column test is used in the Multi-Moduli Testing Device (MTD) to measure the bar wave velocity of a specimen, which is then used to calculate Young's modulus. A dynamic signal analyzer is used to control the dynamic excitation and record and display the response of the specimen. The analyzer drives the piezoelectric shaker at the base of the sample at a specified frequency and measures the relative amplitude and phase between the base and top vertical accelerometers. A typical linear sweep for a test on sand consists of 200 different frequencies and covers a range between 100 and 5000 Hz (resulting in a resolution of 6.12 Hz/point). The longitudinal natural frequencies are determined at phase angles of  $\pm 90$  degrees, in accordance with the theoretical development for one-dimensional motion in a finite rod described in Chapter 3.

The bar wave velocity of the specimen is determined from the measured natural frequencies in a two-step reduction method. In the first step, one-dimensional wave propagation is assumed and the phase velocity corresponding to each natural frequency is computed. The bar wave velocity is calculated in the second step by dividing the phase velocities by a dimensionless velocity ratio that is determined from the solution for the first longitudinal mode for three-dimensional wave propagation in an infinite rod. The values of Young's modulus computed

from the bar wave velocity for each natural frequency typically compare within five to ten percent.

The error in determining the Young's modulus from the longitudinal resonant column should be less than five percent. Also, it was shown that for the loose sand confined isotropically at 16 psi, that except for the first resonant mode, all the strains experienced by the specimen are less than  $1 \times 10^{-3}$  percent, the small-strain threshold for this sand.

Finally, a comparison was made between the bar wave velocities found in the MTD and the bar wave velocities determined using the finite element program developed in Chapter 4 and input parameters from the laboratory test on a loose sand. The comparison between the computed measured responses suggests it is appropriate to use values for Young's modulus that are computed from the second or third natural frequencies as well as the first. This is important because it was not always possible to observe the first natural frequency of the specimen.

## **Chapter Eight**

### **Test Materials**

#### **8.1 Introduction**

In the course of developing and evaluating the Multi-Moduli Testing Device (MTD), a variety of natural and man-made materials were tested. The list of man-made materials included plastics, such as polyurethane, polyvinylchloride and polyethylene, and Portland cement concrete. The synthetic materials provided a distinct advantage in that their stiffness did not change from test to test and they were easy to handle and set up. Further, the synthetic materials were available in a wide range of stiffnesses, allowing samples to be selected which approximate natural soils or other civil engineering materials. Most significantly, these specimens could be used repeatedly and could be tested in other laboratory test equipment using different methods such as used in cyclic triaxial (resilient modulus), torsional resonant column and torsional shear tests. Each of these materials were cast or formed in cylindrical shapes of various sizes and length-to-diameter ratios.

Each of the man-made materials is described in this chapter. Wherever available, their stiffness properties determined by other laboratory tests are presented. The results from the axial and shear pulse tests and the longitudinal resonant column tests are summarized in

this chapter when they are available. It is important to note that many tests on these synthetic materials were conducted in the early stages of the MTD's development and some results are incomplete or must be presented with qualifications.

A compacted clay and a washed mortar sand were the two natural materials used for the bulk of the laboratory tests after the MTD was completely developed. Both soils are being, or have been, used for other experimental investigations at The University of Texas at Austin. The results from the few tests conducted on the compacted clay are presented in this chapter along with results from torsional shear, torsional resonant column, and cyclic triaxial tests on the same samples. Tests on the washed mortar sand are by far the most extensive of the research study and the results are discussed in Chapters 9 and 10. However, the sand is described in this chapter and the results from torsional shear and torsional resonant column tests conducted on identically prepared samples are included.

## 8.2. Synthetic Calibration Specimens

### 8.2.1 Polyurethane Specimens

Stokoe, et al (1990) performed extensive tests on synthetic calibration specimens made of a two-component urethane elastomer

resin. Their tests were used for calibrating and comparing cyclic equipment used for resilient modulus testing. Three different urethane mixtures, Conathane® TU-700, TU-900, and TU-960 were used to construct cylindrical specimens. These three polyurethane specimens were tested in static axial compression, cyclic torsional shear and dynamic torsional resonant column tests. Their tests showed that the urethanes could be considered linear, viscoelastic materials with stiffness characteristics which were independent of confining pressure, strain amplitude and stress history. However, the tests showed that the urethane stiffness was dependent on loading frequency and specimen temperature. Therefore, any comparison of stiffness values determined by different test methods must make adjustments for these two effects.

Figure 8.1 is a plot of the stiffness variation of each urethane specimen as a function of strain amplitude and frequency from each of the dynamic tests. Young's modulus from the cyclic torsional shear and torsional resonant column tests was computed using Poisson's ratio from static tests. Also shown in Fig. 8.1 are the values for Young's modulus of the TU-700 and TU-900 measured in the MTD. Values of Young's modulus corresponding to each of the measured modes (except the first which was difficult to measure) are shown. It appears that the values of Young's modulus measured in the MTD fit well if one extends the trend for the stiffness to increase with frequency. Table 8.1 is a summary of test results for tests on several polyurethanes, including two additional specimens tested toward the end of this research study.

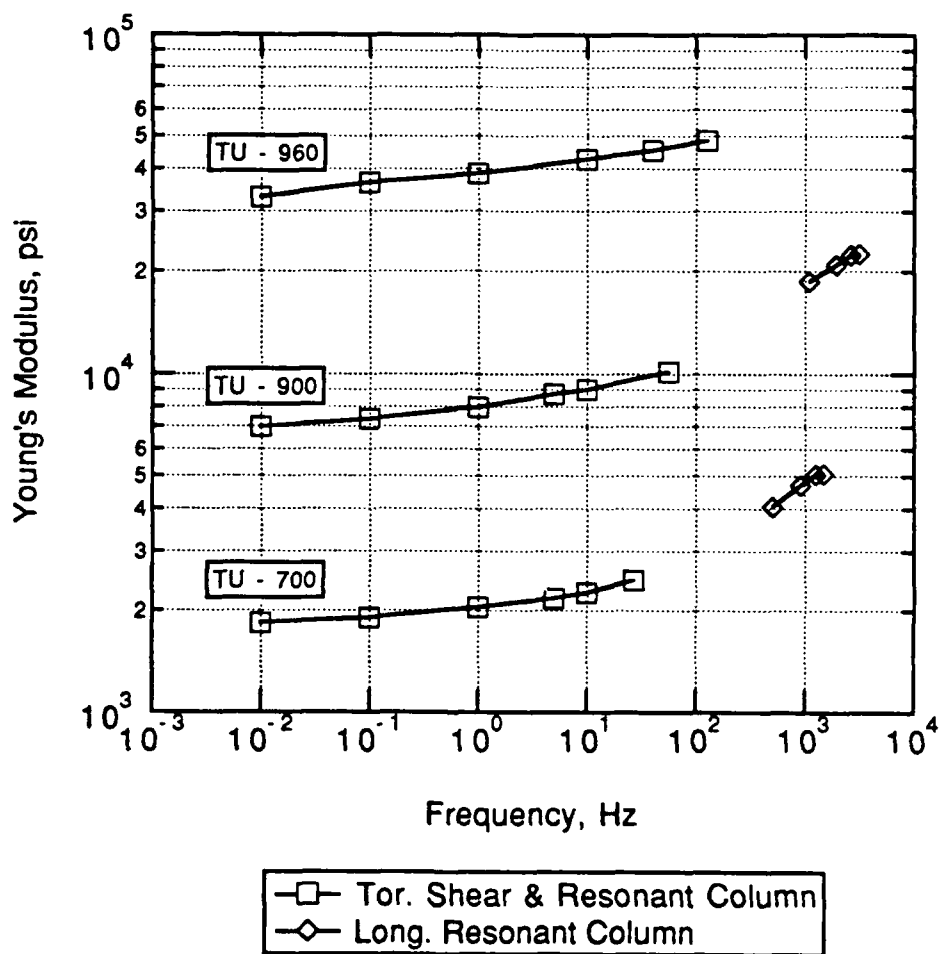


Fig. 8.1. Variations in Young's Modulus with Loading Frequency By Torsional Shear (0.0007%) and Longitudinal Resonant Column Tests at Zero Confining Pressure and Room Temperature (73°F).

Table 8.1. Summary of Moduli from Tests on Polyurethanes.

Sample	L in.	L/D	$\gamma$ pcf	Shore Hardness	M psi	E <sub>1</sub> psi	$\nu$	G <sub>b</sub> <sup>+</sup> psi	G <sub>m</sub> <sup>++</sup> psi
TU-700	6.96	2.49	65.21	72A	377500	4880	0.498	1620	1510
TU-900	6.90	2.46	66.36	90A	377300	16160	0.493	5380	6700
Orange*	13.08	3.23	71.02	50D	491600	33230	0.489	11080	10900
White*	12.63	3.11	73.70	60D	575500	91670	0.472	30930	30750

\* Base Ratio = 0.48, Accelerometer glued to specimen.

+ Backcalculated from M and E<sub>1</sub>.

++ Measured independently.

### 8.2.2 Polyvinylchloride (PVC) Specimens

A polyvinylchloride plastic, commonly referred to as PVC, was tested in a variety of length-to-diameter (L/D) ratios. A 4-inch diameter solid cylindrical rod of PVC industrial stock which was 24 inches long was purchased to make calibration specimens. Tests were performed on three PVC specimens, all of which came from the same piece of stock. The PVC specimens were 4-inch diameter by 24-inch long, 4-inch diameter by 12-inch long, and 2.8-inch diameter by 6-inch and long, which resulted in length-to-diameter ratios of about 6, 3, and 2 to 1, respectively.

Figure 8.2 illustrates the transfer function measured for the longest PVC specimen. The effect of the length on the transfer function is clearly evident by the presence of a large number of resonant modes. Table 8.2 summarizes the results from tests on all three PVC specimens. It is important to note that two of the samples have base ratios of 0.475 (base ratio = area of base pedestal/area of sample base). Although these two specimens show Young's moduli that are noticeably lower, it was shown in Chapter 4 that a base ratio of about 0.5 would result in a measured velocity for the first mode that is 10 percent lower than that measured for a base ratio of 1.0. Consequently, the Young's modulus would be on the order of 20 percent lower, approximately what is seen in Table 8.2.

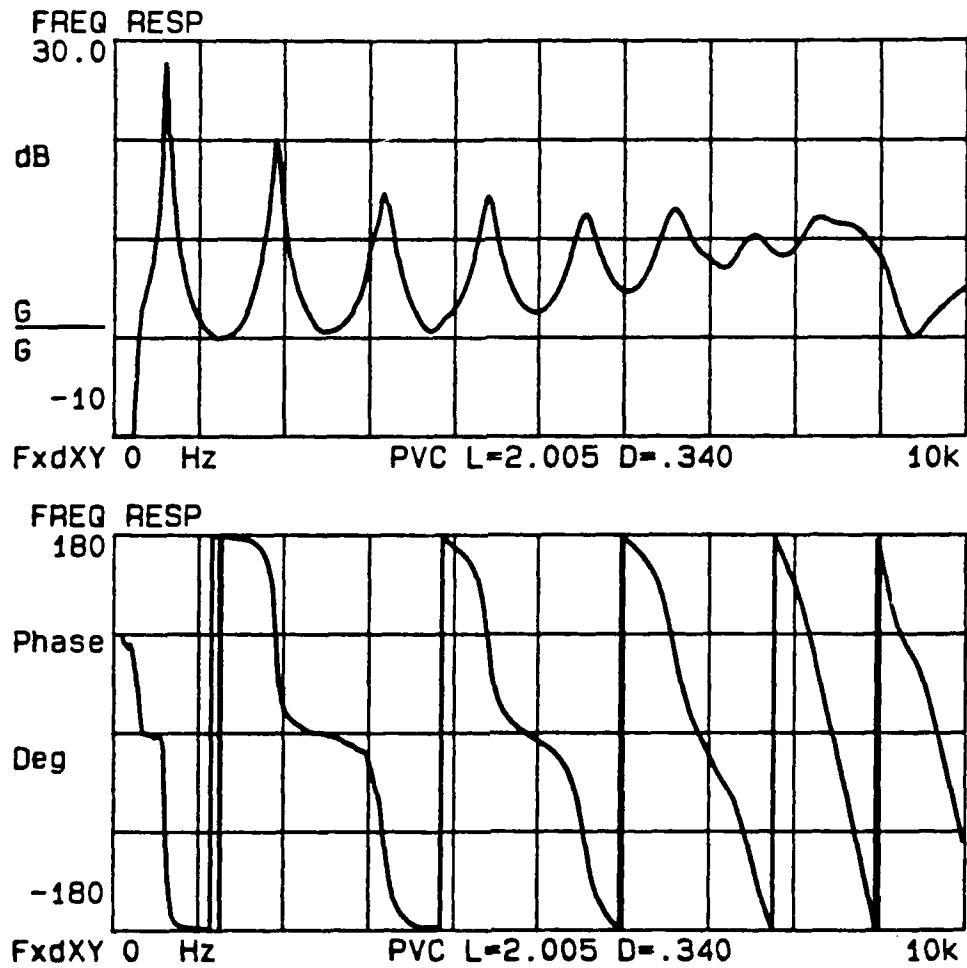


Fig. 8.2. Dynamic Signal Analyzer Record for Longitudinal Resonant Column Test on a Long PVC Specimen; Length = 2.005 ft, Diameter = 0.340 ft.

Table 8.2. Summary of Moduli from Tests on Polyvinylchloride (PVC).

Sample	L in.	L/D	$\gamma$ pcf	Base Ratio	M psi	$E_1$ psi	$\nu$	$G_b^*$ psi	$G_m^{**}$ psi
PVC1	24.06	5.90	86.4	0.475	903800	460500	0.388	165690	183010
PVC2	8.61	2.11	86.3	0.475	1051600	441100	0.413	156100	135040
PVC3	6.00	2.14	86.1	1.00	977900	535400	0.376	194590	143690

\* Backcalculated from M and  $E_1$ .

\*\* Measured independently.

### 8.2.3 Ultra-High Molecular Weight (UHMW) Polyethylene Specimens

An ultra-high molecular weight (UHMW) polyethylene was tested in a variety of length-to-diameter (L/D) ratios. A 4-inch diameter solid cylindrical rod of UHMW industrial stock 24 inches long was also purchased to make calibration specimens. Tests were performed on three UHMW specimens, all of which came from the same piece of stock. The UHMW specimens were 4-inch diameter by 24-inch long, 4-inch diameter by 12-inch long, and 2.8-inch diameter by 6-inch long, which resulted in length-to-diameter ratios of about 6, 3, and 2 to 1, respectively.

Table 8.3 lists the results from tests conducted on the three different sized UHMW samples. Again it is noted that two samples have base ratios of 0.463 and consequently their computed values of the Young's modulus are 20 to 25 percent lower than for the specimen with a base ratio equal to 1.0.

Table 8.3. Summary of Moduli from Tests on Ultra-High Molecular Weight (UHMW) Polyethylene.

Sample	L in	L/D	$\gamma$ pcf	Base Ratio	M psi	E <sub>1</sub> psi	$\nu$	G <sub>b</sub> <sup>*</sup> psi	G <sub>m</sub> <sup>**</sup> psi
UHMW1	23.84	5.77	58.1	0.463	663720	207500	0.439	71960	73630
UHMW2	8.41	2.04	58.1	0.463	651210	195250	0.443	66690	53740
UHMW3	6.02	2.14	58.1	1.00	638360	241960	0.423	85010	56630

\* Backcalculated from M and E<sub>1</sub>.

\*\* Measured independently.

#### 8.2.4 Portland Cement Concrete (PCC)

A series of axial pulse and longitudinal resonant column tests were conducted on a 3-inch diameter by 6-inch long cylinder of curing concrete. These tests were conducted primarily out of the curiosity of the writer at an early stage in the development of the MTD. However, the results are described here because they illustrate its unique capabilities.

The PCC sample was rodded into a 3-inch by 6-inch, thin-walled PVC mold, approximately one hour after it was initially mixed. The concrete was first sifted through a 3/8 inch sieve before rodding into the mold. A 2.9 inch diameter hole was precut in the bottom of the mold and the bottom was then taped back into the hole before the concrete was rodded into the mold. The bottom was carefully removed about five hours after rodding and the concrete cylinder (still in the mold) was set directly on the base pedestal of the MTD.

Axial pulse and longitudinal resonant column tests were conducted every 30 or 60 minutes for the next six hours and then less frequently over the next two days. The plastic mold was removed 48 hours after the specimen was prepared and tests continued daily for five more days.

Figure 8.3 shows the constrained and Young's modulus as a function of time from when the concrete specimen was prepared. Only one natural frequency was measured for each test so only one value of Young's modulus is reported. The shear modulus was backcalculated

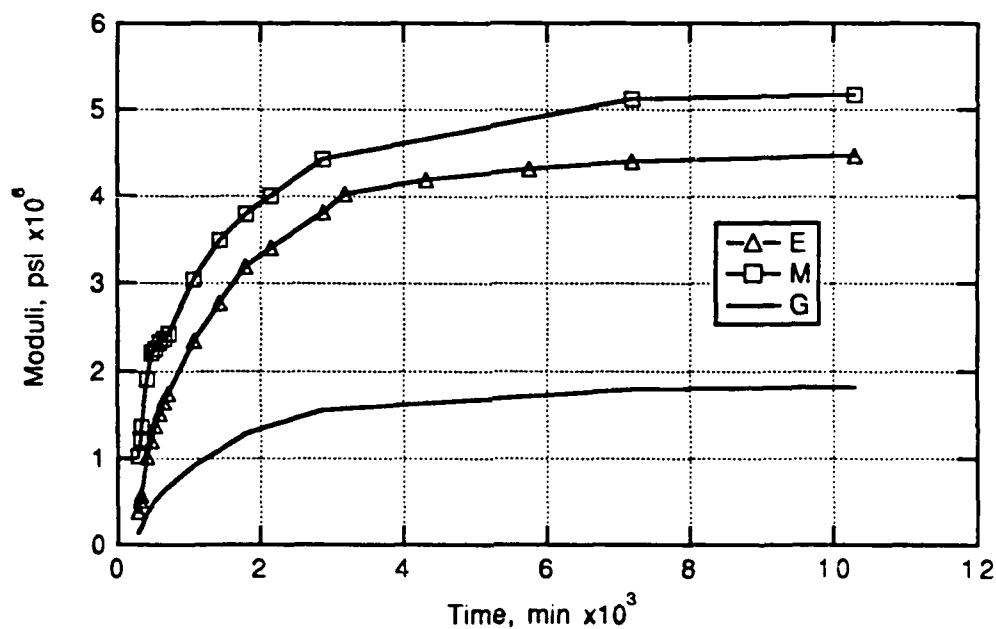


Fig. 8.3. Constrained, Young's and Backcalculated Shear Modulus of PCC as a Function of Curing Time.

from the constrained and Young's modulus assuming the specimen's properties are isotropic. Figure 8.4 shows the change in the Poisson's ratio as a function of time from specimen preparation. Both figures clearly illustrate the strength gain as the concrete cures. It is conceivable, with slight modification to the test setup, that strength measurements could be made from as early as one hour after sample preparation.

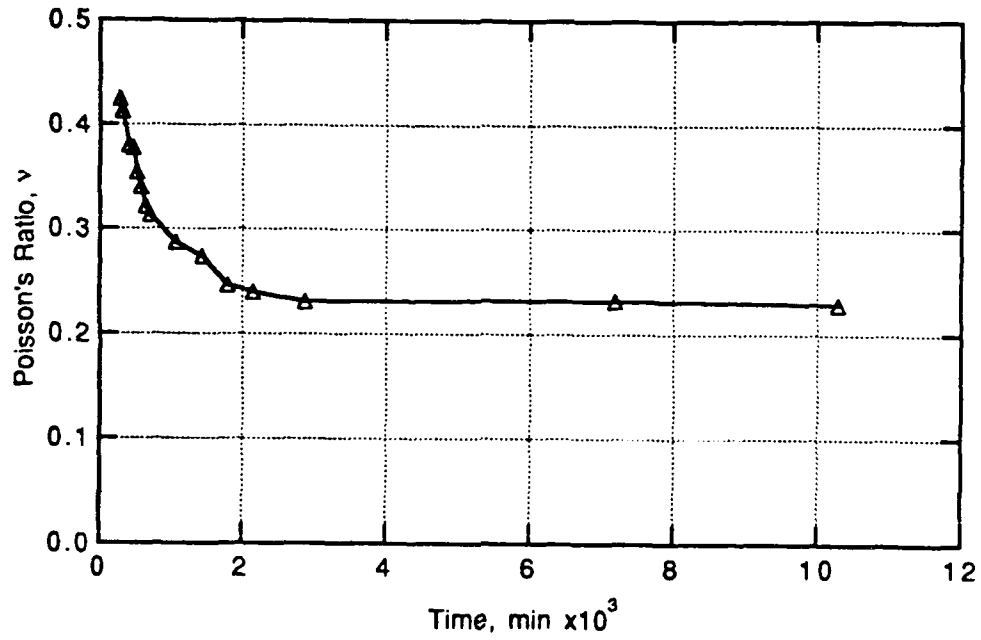


Fig. 8.4. Poisson's Ratio of PCC as a Function of Curing Time (as determined from M and E).

### 8.3 Soil Specimens

Two soils, a washed mortar sand and a medium plasticity, compacted clay were the focus of the laboratory investigation. Both soils have been used extensively in experimental investigations at The University of Texas at Austin.

#### 8.3.1 Compacted Clay

A medium plasticity, compacted clay, derived from a surficial subsoil at a local highway construction site, is being tested extensively at The University of Texas at Austin as part of a research program sponsored by the Texas State Department of Highways and Public Transportation (TSDHPT). Compacted specimens are being tested in cyclic compression, torsional shear and torsional resonance. It was decided to test the clay using the tests in the MTD in order to provide a side-by-side comparison.

The clay is classified as a CH (LL = 56, PI = 27) in the Unified Classification system and is an A-7-6 soil under the AASHTO classification system. One hundred percent of the material passes the #10 sieve, 93.6 percent passes the #40 sieve and 87.3 percent passes the #200 sieve. The clay was compacted in accordance with AASHTO T-99 specifications at moisture contents dry of, wet of, and near the optimum moisture content. The optimum moisture content was about 19

percent and the samples tested had moisture contents of 13, 19, 28 and 39 percent. All the clay samples were approximately 2.8 inches in diameter and 5.6 inches long. Cyclic triaxial testing was conducted at one and six days following compaction, torsional shear and resonant column testing was performed at two and six days following compaction and longitudinal resonant column and pulse testing was performed approximately five days following compaction.

Figure 8.5 is the transfer function measured for one clay specimen. It is immediately apparent that the clay has much higher damping than that observed in the loose sand used as an example in Chapter 7. Table 8.4 summarizes the results for the clay specimens from the tests conducted in the MTD. The trend in measured stiffnesses matches that expected for a compacted clay specimen. As the moisture content decreases from wet of optimum, the stiffness increases to a maximum at the optimum water content and then decreases. It can also be noted in Table 8.4 that the Poisson's ratio steadily decreases as the water content decreases.

The clay specimens were also tested using cyclic triaxial, torsional shear and torsional resonant column. The torsional shear and resonant column tests showed that the stiffness of the clay was both frequency- and strain-dependent. Consequently, any comparison of the test results will have to take this into account. Torsional shear and resonant column

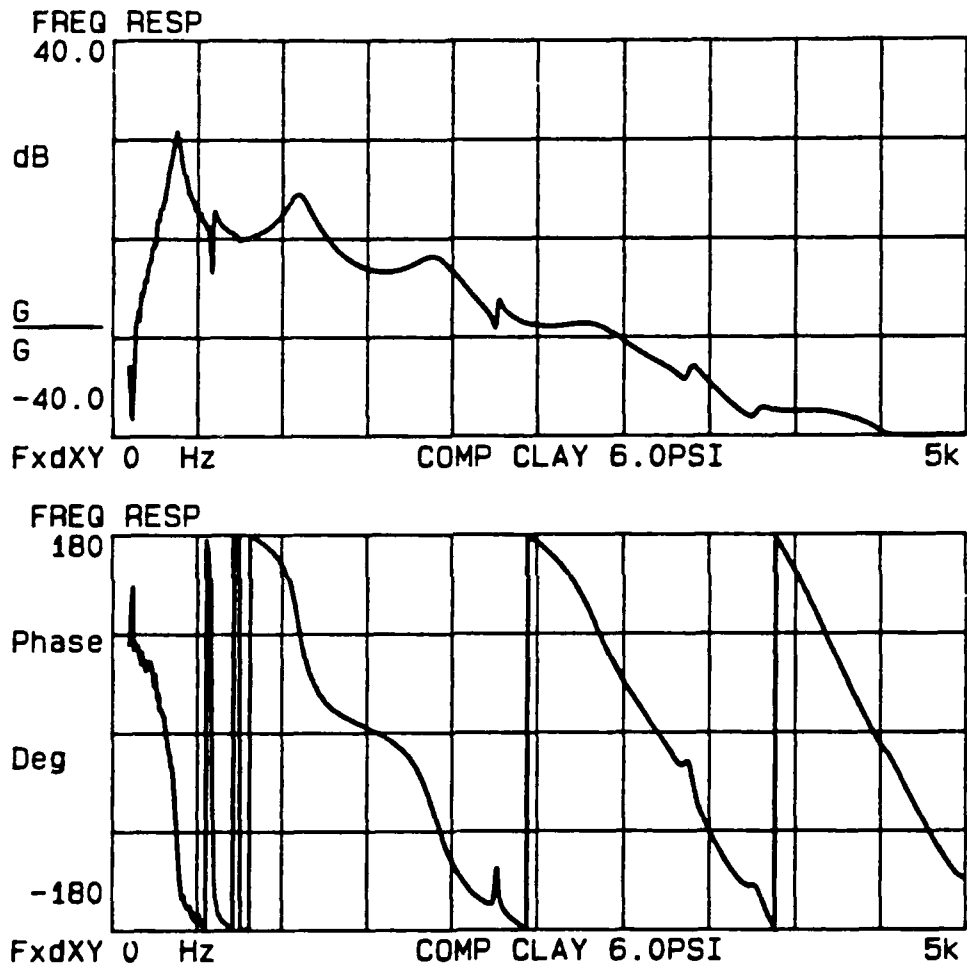


Fig. 8.5. Dynamic Signal Analyzer Record for Compacted Clay Specimen #3 at 6.0 psi Confining Pressure at Five Days Following Compaction.

Table 8.4. Summary of Moduli from Tests on Compacted Clay Specimens.

Sample	w %	$\gamma_d$ pcf	Void Ratio	S <sub>r</sub> %	M psi	E <sub>1</sub> psi	v	G <sub>b</sub> <sup>*</sup> psi
3	39	77.9	1.174	89	55520	8960**	0.471	3050
1	28	89.1	0.876	85	159100	29820	0.466	10170
4	19 <sup>+</sup>	93.9	0.741	69	246750	56680	0.457	19450
5	13	86.9	0.932	38	62460	24760	0.419	8730

(All tests at 6.0 psi confining pressure, 5 days after preparation)

\* Backcalculated from M and E<sub>1</sub>.

\*\* From Mode 2.

+ Optimum Moisture Content.

test results showed that the frequency dependency of Sample #3 amounted to a six percent gain per log cycle of frequency. Figure 8.6 plots the corrected values of Young's modulus for Sample #3 as a function of axial strain amplitude. The values in Fig. 8.6 have been normalized to a frequency of 10 Hz, the frequency at which the cyclic triaxial tests were conducted. The shear modulus and shear strain values determined by torsional shear and torsional resonant column tests have been converted to Young's modulus and axial strain using the Poisson's ratio calculated from tests in the MTD. The result for Young's modulus determined using the longitudinal resonant column is shown with an assumed strain amplitude of  $1.0 \times 10^{-6}$  ( $1 \times 10^{-4}$  percent) and was normalized to 10 Hz (from  $f_2 = 734$  Hz) and then increased 10 percent to account for aging that was exhibited by this clay.

The tests on the compacted clay using the various devices highlighted two problems which the researcher has to consider. The first was the integrity of the test specimen. The quality of the compacted clay specimens varied significantly with water content. Clay specimens compacted dry of optimum had lateral discontinuities and tended to ravel. This raises the question of whether the specimen can still be treated as a continuum. Any dynamic test method relies heavily on the assumption that the specimen is contiguous and internal flaws will tend to contaminate the test data. The second problem involves the impact of the end conditions on the observed stiffness. For particularly stiff

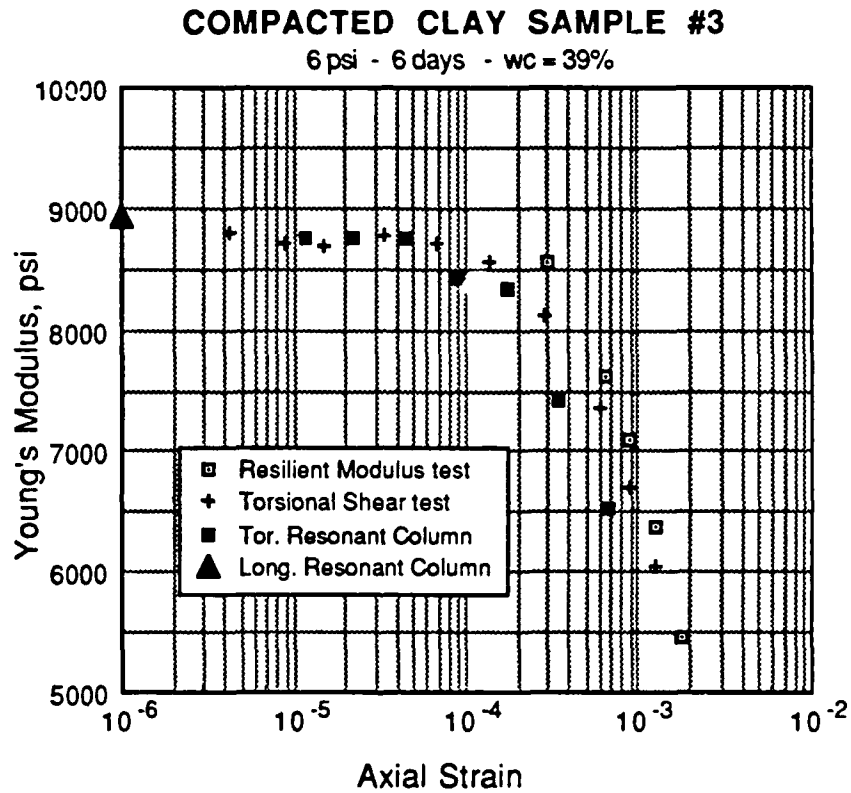


Fig. 8.6. Comparison of Young's Moduli for Compacted Clay Sample #3 ( $w_c = 39\%$ ) Determined by Cyclic Triaxial, Torsional Shear, and Torsional Resonant Column Tests at Six Days, at 6.0 psi Confining Pressure, and Normalized at 10 Hz. (After Pezo et al, 1990)

materials, the continuity between the specimen and the end caps has to be ensured. This is particularly important for torsional tests. The writer believes that one inherent strength of the longitudinal resonant column and axial pulse tests is that, as long as the strains are kept small and the contact between the specimen and base is uniformly continuous, the susceptibility of the measured stiffness to horizontal slippage at the ends is limited. As was shown by the analytical study described in Chapter 4, the horizontal fixity will have only a minor effect on the natural frequencies of the specimen, and that effect is confined to the higher modes.

### 8.3.2 Washed Mortar Sand

Washed mortar sand has been used for small- and large-scale laboratory wave propagation tests over the past decade (Stokoe et al, 1980; Knox et al, 1982, Allen and Stokoe, 1982; Lee and Stokoe 1986; and Ni, 1987). The sand is medium to fine with a subangular to subrounded grain shape. It is uniformly graded with a mean grain diameter,  $D_{50}$ , equal to about 0.35 mm and less than 1% passes the #200 sieve (0.074 mm). The specific gravity of the sand is 2.67. Rix (1984) performed sieve analyses during the course of his experiments and showed that the gradation was not significantly altered after repeated sample preparation using a simple raining process. The sand has a maximum dry density of 106.6 pcf and a minimum dry density of

90.6 pcf (as determined by ASTM D2049-69). The corresponding minimum and maximum void ratios are 0.563 and 0.839, respectively. Figure 8.7 shows the average grain size distribution for the sand. A summary of soil characteristics and properties are presented in Table 8.5.

The washed mortar sand was recently tested using cyclic triaxial, torsional shear and torsional resonant column methods. The sand samples for these tests were prepared using the multiple sieve pluviating (MSP) device developed for this research and described in Chapter 5. Consequently, the loose and dense sand samples had approximately the same structure and void ratio as those specimens tested in the MTD. Figure 8.8 shows the shear modulus measured in torsional shear and resonant column tests on loose sand and dense sand.

The shear moduli and shear strains from the torsional shear and torsional resonant column tests were converted to Young's moduli and axial strains using Poisson's ratio values determined at comparable confining pressures (see Fig. 9.8) in the MTD. The Young's moduli are plotted versus axial strain in Fig. 8.9 along with the values for Young's moduli calculated using the  $\log E - \log \bar{\sigma}_0$  relationship and stiffness coefficients determined in Chapter 9. It can be seen that there is reasonably good agreement between the values, with differences less than 10 percent.

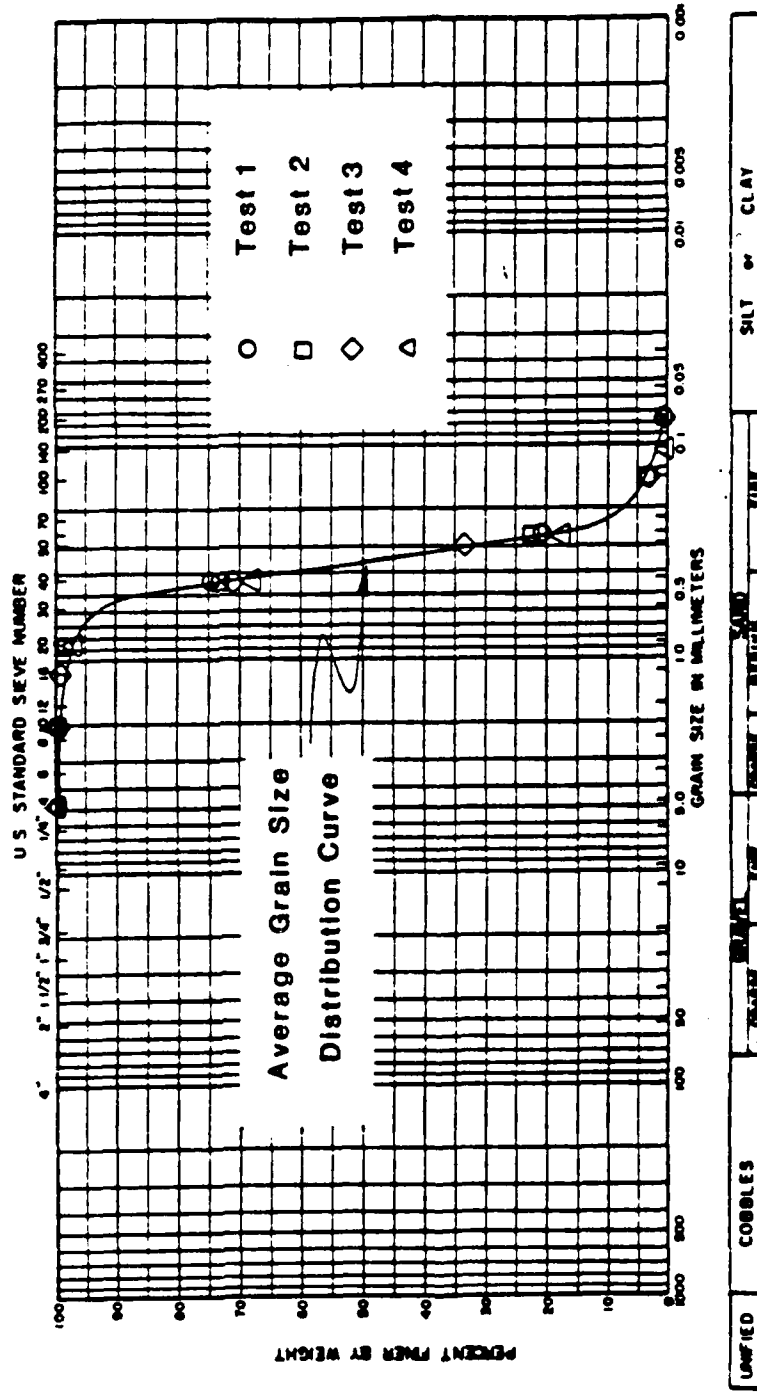


Figure 8.7. Average Grain Size Distribution Analyses of Washed Mortar Sand. (From Rix, 1984)

Table 8.5. Summary of Soil Characteristics and Properties of Washed Mortar Sand.(From Rix, 1984).

Soil Type:	Washed Mortar Sand
Unified Soil Classification	SP
Mean Grain Diameter, $D_{50}$	0.35 mm
Percent Passing #200 Sieve	< 1 %
Specific Gravity	2.67
Maximum Dry Density	106.6 pcf
Minimum Dry Density	90.6 pcf
Maximum Void Ratio	0.839
Minimum Void Ratio	0.563
Grain Shape	subangular to subrounded

Relative Density, %

Angle of Internal Friction,  $\phi$

5.7	34.5
10.2	34.5
12.3	36.5
17.5	37.2
22.4	38.5
114.0	44.0

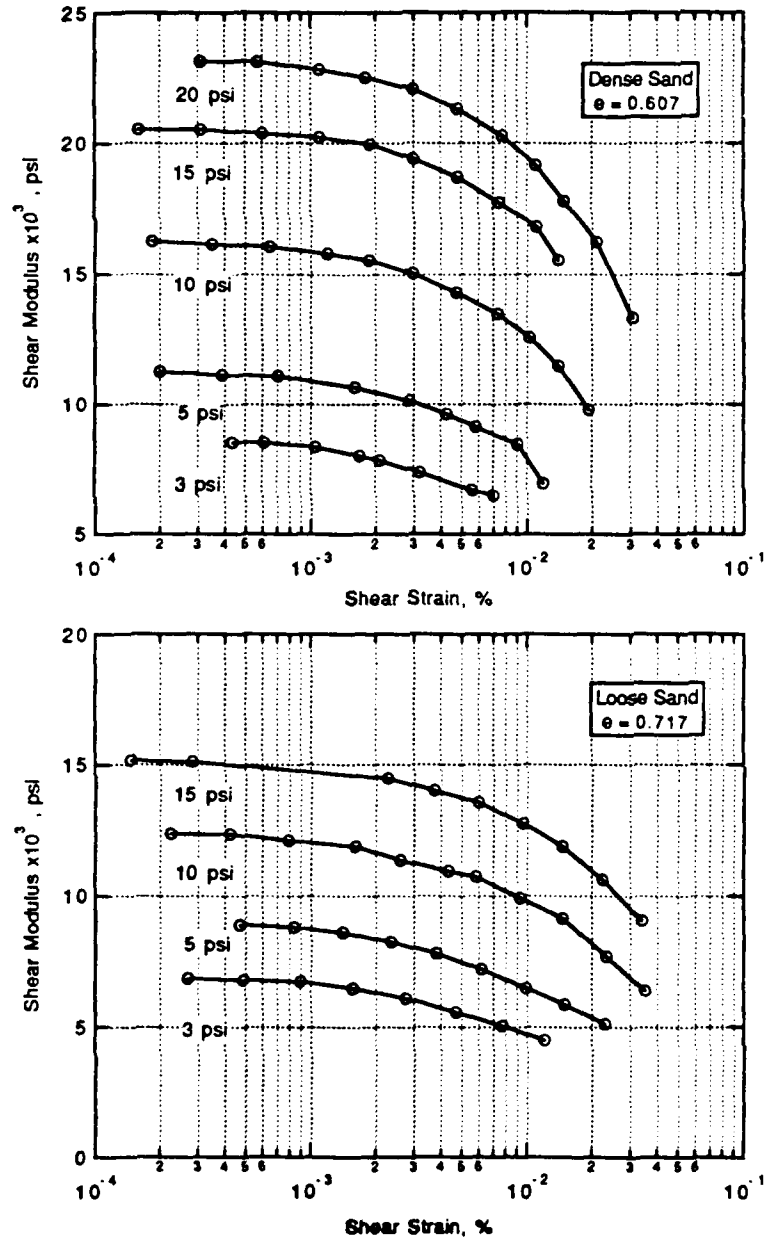


Fig. 8.8. Shear Modulus of Dense and Loose Washed Mortar Sand as a Function of Shear Strain Amplitude and Confining Pressure as Determined by Torsional Shear and Torsional Resonant Column Tests.

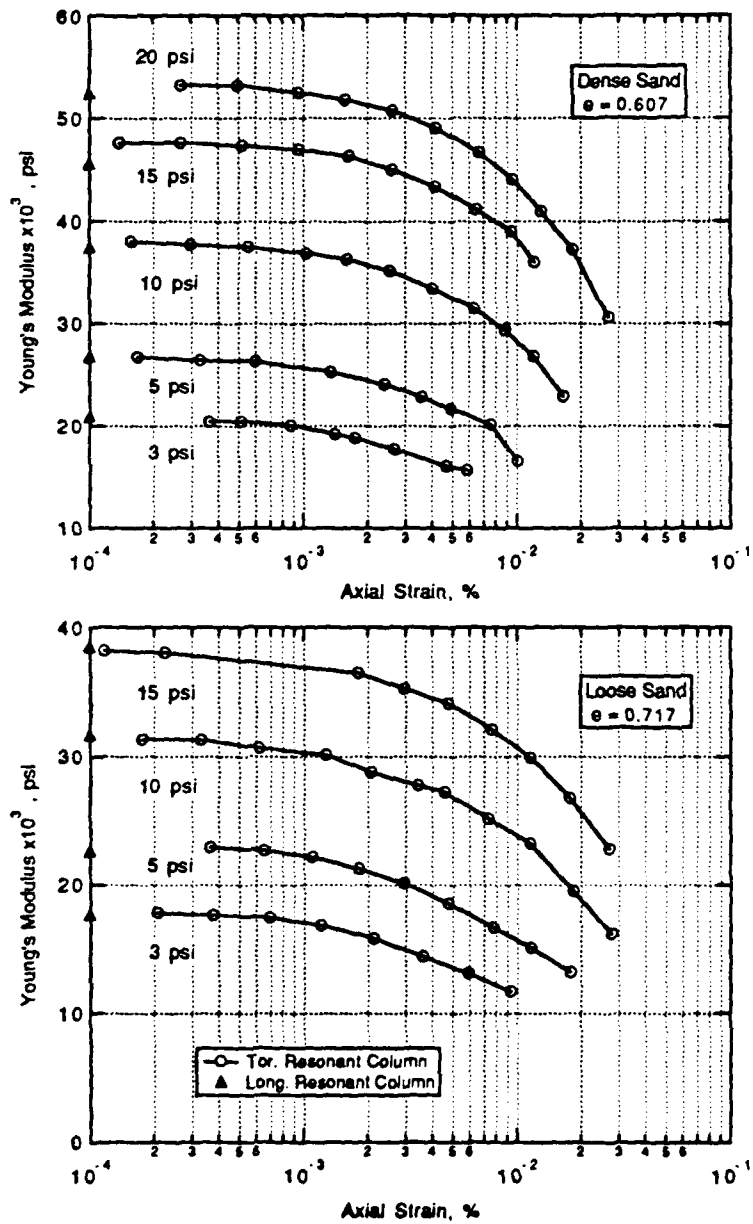


Fig. 8.9. Young's Modulus of Dense and Loose Washed Mortar Sand as a Function of Axial Strain Amplitude and Confining Pressure as Determined by Torsional Shear and Torsional Resonant Column Tests.

#### 8.4 Summary

A variety of natural and man-made materials were tested in the course of developing the Multi-Moduli Testing Device (MTD). The man-made materials that were tested included several plastic specimens (polyurethane, polyvinylchloride and polyethylene) and Portland cement concrete. The plastic specimens provided the following advantages: (1) a range of stiffnesses similar to soils and other civil engineering materials, (2) the capability for repeated use in the MTD and other laboratory test equipment, and (3) ease in test preparation and set up.

Tests on the plastic specimens were used to illustrate how well the moduli measured in the MTD compared with those measured by torsional shear and torsional resonant column devices. The single test on curing Portland cement concrete showed the versatility of the MTD to measure the stiffness of a broad range of materials.

Two natural soils were tested in the MTD, a medium plasticity, compacted clay, and an uncemented, dry sand. The compacted clay was also tested in cyclic triaxial, torsional shear and torsional resonant column devices. After making adjustments for the effect of frequency and aging, the Young's modulus determined by each small-strain device compared within two percent.

The main thrust of this research involved testing dry sand subjected to different stress states. Identically prepared sand samples

were also tested under isotropic loading using torsional shear and torsional resonant column devices. Those tests showed that the sand stiffness remained linear up to strains of about  $1 \times 10^{-3}$  percent. Young's modulus was computed from the shear modulus using the value for Poisson's ratio found in the MTD. The values for Young's modulus determined in the MTD were computed at the corresponding confining pressures using the  $\log E - \log \bar{\sigma}_0$  relationship determined in Chapter 9.4. The Young's modulus values typically compared to within ten percent.

## **Chapter Nine**

### **Stiffness of Sand Under Isotropic Confinement**

#### **9.1 Introduction**

Two series of tests were performed to determine the effect of the simplest stress state on the constrained, Young's, and shear modulus of a uniform, dry sand. The testing was performed to evaluate the effect of isotropic confinement, which is essentially equal to the confining pressure, on each of the moduli, and to compare these results with data from earlier tests on the same sand. The test series also provided insight into the effect of stress history and void ratio on the elastic moduli. Finally, it was possible to evaluate how applicable was the assumption that the sand behaved as an isotropic linear elastic material in these tests.

This chapter deals exclusively with testing on an uncemented, air-dried sand. However, a number of other materials were tested under isotropic loading conditions. These included compacted clay specimens, a variety of plastic specimens and Portland cement concrete. The results from tests on these materials are summarized in Appendix G and are discussed in Chapter 8.

## 9.2 Testing Sequence and Stress-State

Two test series were conducted utilizing only the top cap and accelerometers, i.e. the load cell, top cap frame, and axial loading piston were not installed. The hole in the top plate through which the axial loading piston normally passes was capped with a solid plate. Thus, aside from the minor weight of the top cap assembly itself, the test specimen was subjected to an isotropic state of stress. In an isotropic stress state the major, intermediate, and minor principal stresses are equal.

The isotropic stress state assumed for this case is illustrated in Fig. 9.1. For the purpose of discussion in this and the following chapters, the vertical or axial stress will be labelled  $\sigma_v$  and the horizontal stress (which is equal to the confining pressure) will be labelled  $\sigma_h$ . The major, intermediate and minor effective principal stresses will be labelled  $\sigma_1$ ,  $\sigma_2$ , and  $\sigma_3$ , respectively. In this case,  $\sigma_2 = \sigma_3 = \sigma_h = \sigma_{cell}$  and  $\sigma_1 = \sigma_v = \sigma_h = \sigma_{cell}$ . The weight of the top cap adds about 0.17 psi to the vertical stress for the top cap and sample sized used in these tests. This equates to a difference which ranges from 5.0 % to 0.3 %, respectively, as the confining pressure increases from 4 to 64 psi.

One test series was conducted on a dense sand sample and the other was conducted on a loose sand sample. These are denoted hereafter as ISO1 and ISO2, respectively. Each test series was made up of tests conducted at confining pressures of 4, 8, 16, 32, and 64 psi.

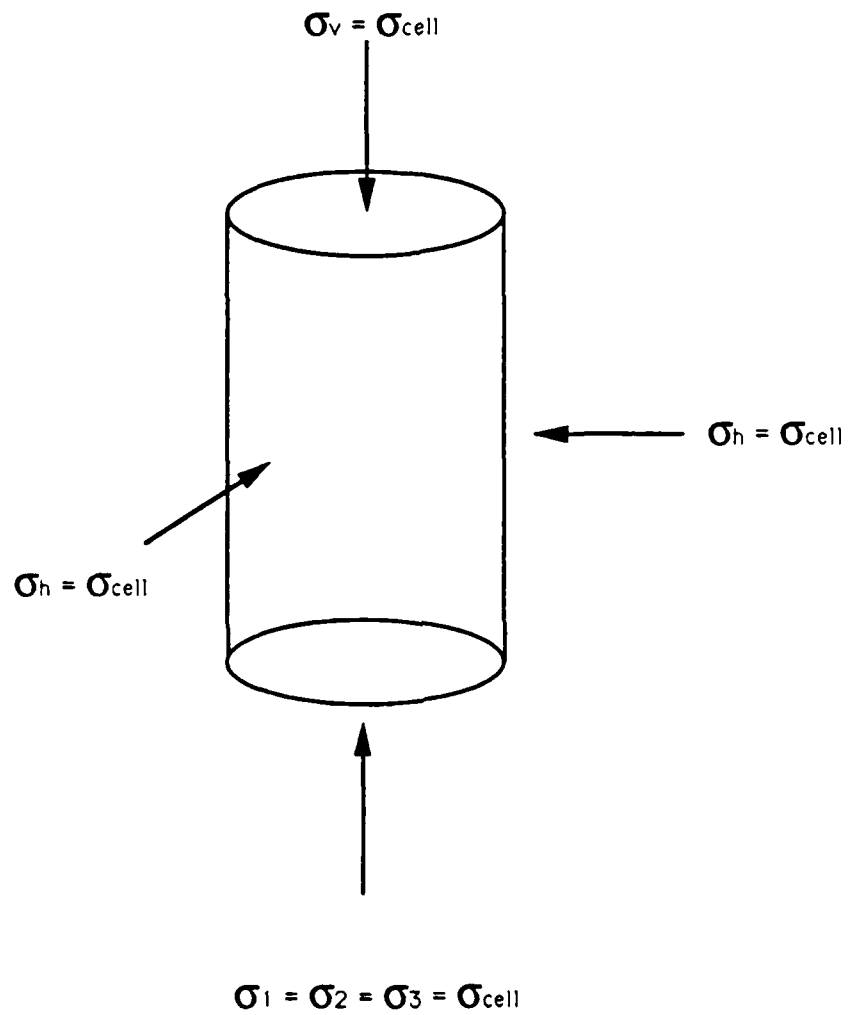


Fig. 9.1. Assumed Isotropic Stress-State for Tests on Sand Specimens.

Table 9.1. Summary of Loading Sequence for Dense Sand Specimen (ISO1 Test Series).

Test #	Void Ratio e	Axial Stress psi	Horizontal Stress psi	Ko	Mean Stress psi
1	0.594	4.13	3.96	1.04	4.02
2	0.594	8.17	7.99	1.02	8.05
3	0.594	16.17	16.00	1.01	16.06
4	0.593	32.18	32.01	1.01	32.07
5	0.592	64.16	63.98	1.00	64.04
6	0.593	32.18	32.00	1.01	32.06
7	0.593	16.17	16.00	1.01	16.06
8	0.594	8.17	7.99	1.02	8.05
9	0.594	4.15	3.98	1.04	4.04
10	0.594	8.19	8.02	1.02	8.07
11	0.593	16.18	16.01	1.01	16.06
12	0.593	32.15	31.97	1.01	32.03
13	0.592	64.17	63.99	1.00	64.05
14	0.593	32.18	32.00	1.01	32.06
15	0.593	16.18	16.00	1.01	16.06
16	0.594	8.18	8.01	1.02	8.07
17	0.594	4.17	4.00	1.04	4.06
18	0.594	16.18	16.01	1.01	16.06
19	0.592	64.14	63.97	1.00	64.03
20	0.593	16.18	16.01	1.01	16.07
21	0.594	4.21	4.04	1.04	4.09
22	0.592	64.15	63.98	1.00	64.04
23	0.594	4.20	4.03	1.04	4.09

Average  
Void Ratio = 0.593

Table 9.2. Summary of Loading Sequence for Loose Sand Specimen (ISO2 Test Series).

Test #	Void Ratio e	Axial Stress psi	Horizontal Stress psi	Ko	Mean Stress psi
1	0.760	4.18	4.01	1.04	4.06
2	0.759	8.19	8.01	1.02	8.07
3	0.759	16.16	15.99	1.01	16.05
4	0.757	32.18	32.00	1.01	32.06
5	0.756	64.14	63.97	1.00	64.02
6	0.757	32.18	32.00	1.01	32.06
7	0.758	16.16	15.99	1.01	16.05
8	0.758	8.18	8.01	1.02	8.07
9	0.759	4.18	4.01	1.04	4.07
10	0.758	16.17	16.00	1.01	16.05
11	0.756	64.17	64.00	1.00	64.05
12	0.758	16.17	16.00	1.01	16.05
13	0.759	4.18	4.01	1.04	4.06

Average  
Void Ratio = 0.758

Axial pulse, shear pulse and longitudinal resonant column tests were conducted at each pressure step. The two test series are summarized in Table 9.1 and Table 9.2. The ISO1 test series contained 23 test steps in four load and unload cycles. The ISO2 test series contained 13 test steps in two load and unload cycles.

### 9.3 Constrained Modulus of Sand Under Isotropic Confinement

The values of constrained modulus measured for each test series are plotted versus the mean effective stress in Fig. 9.2. It is immediately apparent that the  $\log M - \log \bar{\sigma}_0$  relationship is different for the first loading cycle (tests 1 - 5) than for the subsequent unloading and reloading cycles. In Fig. 9.2, the dashed lines represent the first load cycle and the solid lines represent the first unload and subsequent reloading cycles. The phenomena appears in both the dense and loose sand. The sand exhibits a decrease in stiffness after the first load cycle when unloaded to confining pressures below about 16 psi. This behavior was also noted by Ni (1987) and Lee and Stokoe (1986) in tests on this same sand.

There are several possible causes for this behavior. It could be due to particle rearrangement, seating of the top and bottom caps or complex and sensitive stress conditions in the vicinity of the base and top caps. It also could be attributed to the sample preparation technique. However, Lee and Stokoe prepared their test specimen in a large scale triaxial cube (7 ft x 7 ft x 7 ft) by raining, whereas, Ni prepared torsional resonant column samples using raining and an under-compaction technique (Ladd 1978). Lastly, the phenomenon cannot be attributed to a change in void ratio because that change was insignificant from the beginning to the end of a test series in this research study. Nevertheless,

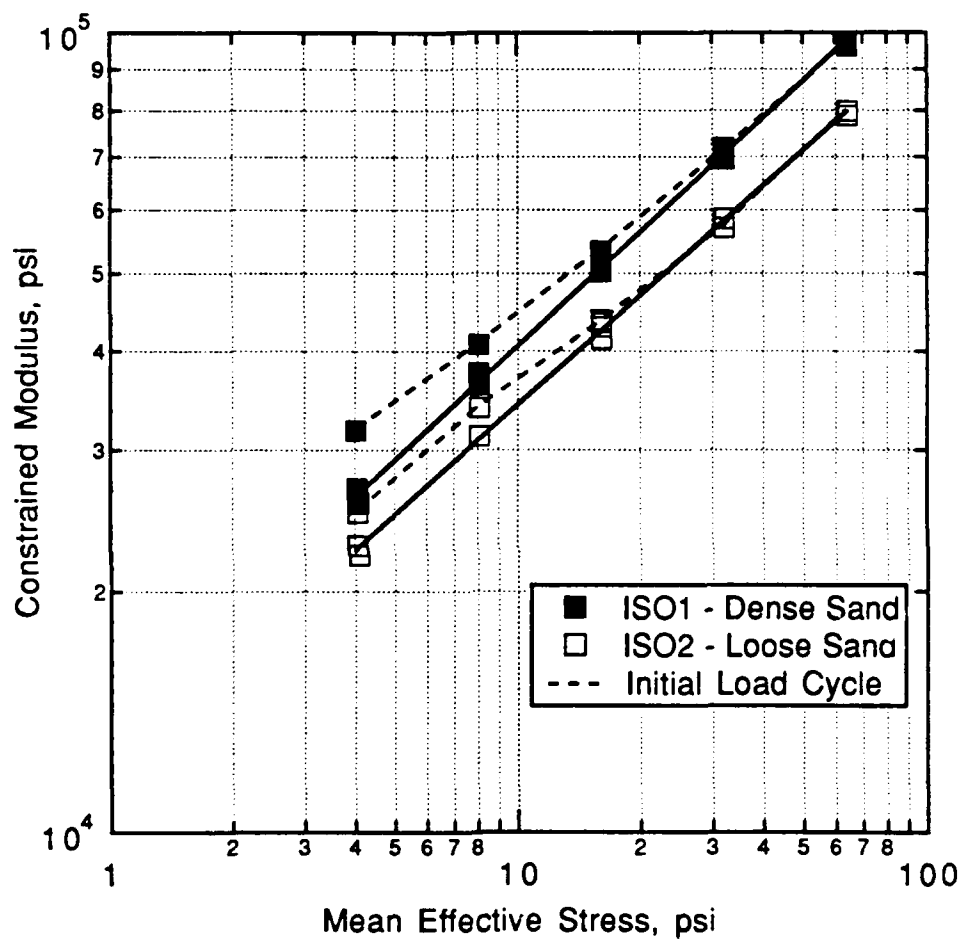


Fig. 9.2. Variation of Constrained Modulus with Mean Effective Stress for ISO1 and ISO2 Test Series on Sand.

the same behavior appeared in both research studies when the sand was unloaded to low confining pressures. Whatever the cause, its effect appears to be erased after the first loading cycle as is clearly shown in Fig. 9.2. As a result, the stiffness parameters reported hereafter are computed for the loading and unloading cycles after the initial loading cycle, i.e., excluding the first four tests at 4, 8, 16, and 32 psi.

The dynamic stiffness equation representing the constrained modulus as a function of the mean effective stress is cast in the form

$$M = C_M \bar{\sigma}_0^{nm} Pa^{1-nm} / F(e) \quad (9.1)$$

where,

- M = constrained modulus,
- $C_M, nm$  = stiffness coefficients,
- $\bar{\sigma}_0$  = mean effective stress,
- Pa = atmospheric pressure in same units as  $\bar{\sigma}_0$ , and
- F(e) = function of void ratio,  $F(e) = 0.3 + 0.7e^2$ .

Equation 9.1 is a straight line relationship when plotted on a log-log scale, and lends itself to a simple least squares fitting technique. The log M-log  $\bar{\sigma}_0$  relationships for both isotropic test series are shown as straight lines in Fig. 9.2. The resulting values for the coefficients  $C_M$  and  $nm$  are summarized in Table 9.3 for each test series. The stiffness coefficients computed from the test steps in the biaxial test series

Table 9.3. Comparison of Stiffness Coefficients for Log M - Log  $\bar{\sigma}_0$  Relationship\* for Isotropic Confinement

Test Series	$e_{Average}$	$C_M$	$nm$	S.E.E.#
ISO1 - 1L**	0.593	1941	0.388	736
ISO1+		1813	0.476	1046
ISO2 - 1L**	0.758	2020	0.395	561
ISO2+		1953	0.458	970
BIAX1++	0.760	2150	0.408	1022
BIAX2	0.771	2013	0.441	1993
BIAX3	0.586	2031	0.450	2019
BIAX4	0.582	2059	0.410	1341
BIAX5	0.750	2000	0.459	2021

\*  $M = C_M \bar{\sigma}_0^{nm} Pa^{1-nm}/F(e)$  ,  $F(e) = 0.3 + 0.7e^2$

\*\* From first four tests at 4, 8, 16, and 32 psi confining pressure

+ From all tests except first four

++ From tests in the biaxial series which are under isotropic confinement

# Standard Error of the Estimate in psi

(described in Chapter 10) that were at isotropic states of stress have also been included in Table 9.3.

It has been shown by Roesler (1979), Knox, et al (1982), and Lee and Stokoe (1986), that the constrained modulus is determined almost solely by the state of stress in the direction of particle motion and wave propagation for dilatational waves propagating along principal stress

directions. This coincides with the axial stress so Eq. 9.1 can be written as

$$M = C_A \bar{\sigma}_a^{na} P a^{1-na} / F(e) \quad (9.2)$$

where  $\bar{\sigma}_a$  is now the effective stress in the axial direction and  $C_A$  and  $na$  are the coefficients corresponding to a single stress in the three-stress model described in Chapter 2. The values resulting from a least squares fit are summarized in Table 9.4.

It can be seen the stiffness coefficients for the  $\log M - \log \bar{\sigma}_0$  and  $\log M - \log \bar{\sigma}_a$  relationships are similar, with the slope of the latter marginally higher and the constant marginally lower, than the former. However, comparison of the stiffness coefficients in Tables 9.3 and 9.4 suggests that either of these models is appropriate for the constrained modulus over the range of stresses at which these tests were performed. Further, it suggests there is little difference whether the axial or the mean effective stress is used to predict the constrained modulus when the sand is under an isotropic state of stress.

#### 9.4 Young's Modulus of a Sand Under Isotropic Confinement

The values of the Young's modulus (calculated at the third mode) measured in the ISO1 and ISO2 test series are plotted together in Fig. 9.3. Again, it is obvious that the sand appears stiffer on the first load

Table 9.4. Comparison of Stiffness Coefficients for Log M - Log  $\bar{\sigma}_a$  Relationship\* for Isotropic Confinement

Test Series	$e_{Average}$	$C_A$	$na$	S.E.E.#
ISO1 - 1L**	0.593	1933	0.393	672
ISO1+		1803	0.480	1114
ISO2 - 1L**	0.758	2011	0.400	601
ISO2+		1943	0.462	836
BIAX1++	0.760	2148	0.407	1020
BIAX2	0.771	2013	0.441	1989
BIAX3	0.586	2018	0.452	2008
BIAX4	0.582	2058	0.410	1335
BIAX5	0.750	2000	0.459	2020

\*  $M = C_A \bar{\sigma}_a^{na} Pa^{1-na}/F(e)$ ,  $F(e) = 0.3 + 0.7e^2$

\*\* From first four tests at 4, 8, 16, and 32 psi confining pressure

+ From all tests except first four

++ From tests in the biaxial series which are under isotropic confinement

# Standard Error of the Estimate in psi

cycle than in subsequent loading and unloading cycles, suggesting the same phenomenon affects both constrained and Young's moduli.

The dynamic stiffness equation relating Young's modulus to the mean effective stress is written as

$$E = C_E \bar{\sigma}_0^{nm} Pa^{1-nm} / F(e) \quad (9.3)$$

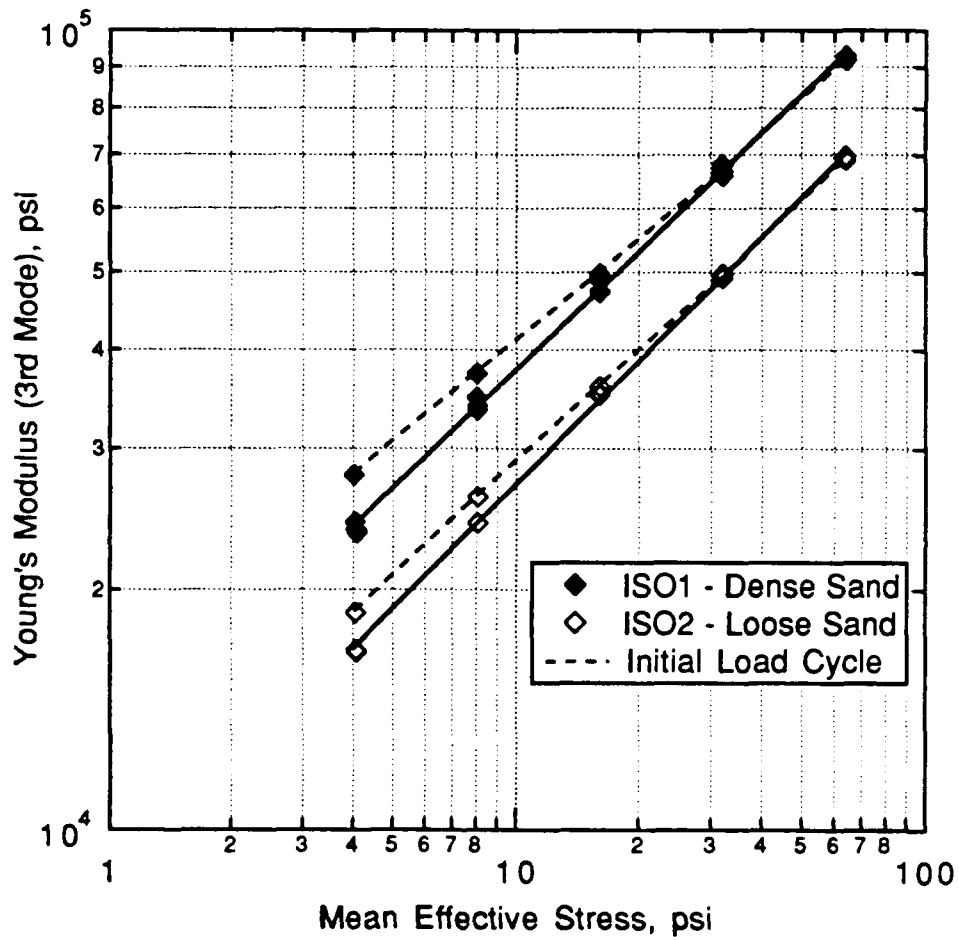


Fig. 9.3. Variation of Young's Modulus with Mean Effective Stress for ISO1 and ISO2 Test Series on Sand.

where

- E = Young's modulus,
- $C_E, nm$  = stiffness coefficients,
- $\bar{\sigma}_0$  = mean effective stress,
- $P_a$  = atmospheric pressure in same units as  $\bar{\sigma}_0$ , and
- $F(e)$  = function of void ratio,  $F(e) = 0.3 + 0.7e^2$ .

The values resulting from a least squares fit to a straight line  $\log E - \log \bar{\sigma}_0$  relationship yields the stiffness coefficients  $C_E$  and  $nm$  which are summarized in Table 9.5 for the ISO1 and ISO2 test series and for the tests from the biaxial test series which were conducted at isotropic states of stress. However, now there are as many as four relationships for each test series, one corresponding to each observed mode. The coefficients for the second and third modes in the ISO1 and ISO2 test series are included in Table 9.5. Only the third mode is included for the biaxial tests for the sake of brevity. In any event, not all the data was reliable, particularly at low and high frequencies, and these two modes had the most complete data (as was discussed in Chapter 7). The  $\log E - \log \bar{\sigma}_0$  relationships for mode 3 from both test series are shown as solid lines in Fig. 9.3.

Two observations can be made by examining Fig. 9.3 and Table 9.5. First, the slope of the lines relating the Young's modulus and the mean effective stress are about the same for both the dense and loose sand. Second, there appears to be a general trend for the slope to

Table 9.5 Comparison of Stiffness Coefficients for Log E - Log  $\bar{\sigma}_0$  Relationship\* for Isotropic Confinement

Test Series - Mode	eAverage	C <sub>E</sub>	nm	S.E.E.#
ISO1-2-1L** ISO1 - 2+	0.593	1745 1648	0.425 0.499	164 1416
ISO1-3-1L** ISO1 - 3+	0.593	1785 1692	0.421 0.493	107 1234
ISO2-2-1L** ISO2 - 2+	0.758	1622 1546	0.464 0.511	330 768
ISO2-3-1L** ISO2 - 3+	0.758	1639 1575	0.468 0.516	234 795
BIAX1 - 3++	0.760	1685	0.491	871
BIAX2 - 3	0.771	1681	0.506	1796
BIAX3 - 3	0.586	1850	0.470	1975
BIAX4 - 2	0.582	1692	0.481	1816
BIAX5 - 2	0.750	1545	0.526	1534

\*  $E = C_E \bar{\sigma}_0^{nm} \text{ Pa}^{1-nm} / F(e)$ ,  $F(e) = 0.3 + 0.7e^2$

\*\* From first four tests at 4, 8, 16, and 32 psi confining pressure

+ From all tests except first four

++ From tests in the biaxial series which are under isotropic confinement

# Standard Error of the Estimate in psi

decrease and the corresponding intercept to increase for subsequently higher modes. It is interesting to note that the slopes are lower, and the intercepts are higher, for the biaxial test series. This implies that stress history may have an impact on the observed behavior of the sand.

#### 9.5 Shear Modulus of a Sand Under Isotropic Confinement

The values of shear modulus measured using the shear pulse test in the ISO1 and ISO2 test series are plotted together versus the mean effective stress in Fig. 9.4. Here also, it is obvious the sand appears stiffer on the first load cycle than subsequent loading and unloading cycles, suggesting the same phenomenon affects all three moduli.

The dynamic stiffness equation relating the shear modulus to the mean effective stress can be written as

$$G = C_G \bar{\sigma}_0^{nm} Pa^{1-nm} / F(e) \quad (9.4)$$

where

$G$  = shear modulus,

$C_G$  and  $nm$  = stiffness coefficients,

$\bar{\sigma}_0$  = mean effective stress,

$Pa$  = atmospheric pressure in same units as  $\bar{\sigma}_0$ , and

$F(e)$  = function of void ratio,  $F(e) = 0.3 + 0.7e^2$ .

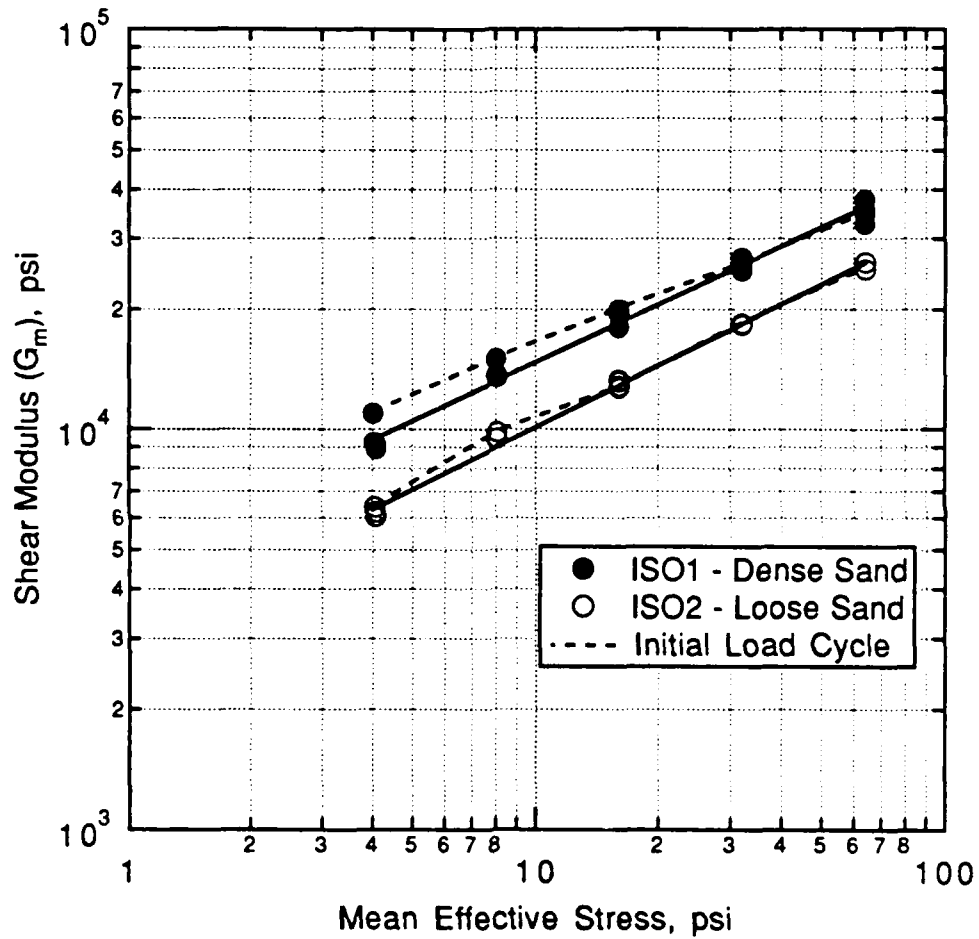


Fig. 9.4. Variation of Measured Shear Modulus ( $G_m$ ) with Mean Effective Stress for ISO1 and ISO2 Test Series on Sand.

Table 9.6 Comparison of Stiffness Coefficients for Log  $G_m$  - Log  $\bar{\sigma}_0$  Relationship\* Measured by Shear Pulse Test for Isotropic Confinement

Test Series	$e_{Average}$	$C_{Gm}$	$nm$	S.E.E.#
ISO1 - 1L**	0.593	703	0.414	311
ISO1+		655	0.486	1185
ISO2 - 1L**	0.758	595	0.498	489
ISO2+		584	0.515	471
BIAX1++	0.760	634	0.487	837
BIAX2	0.771	674	0.484	685
BIAX3	0.586	761	0.457	772
BIAX4	0.582	755	0.474	1356
BIAX5	0.750	647	0.531	1034

\*  $G_m = C_{Gm} \bar{\sigma}_0^{nm} \text{ Pa}^{1-nm} / F(e)$ ,  $F(e) = 0.3 + 0.7e^2$

\*\* From first four tests at 4, 8, 16, and 32 psi confining pressure

+ From all tests except first four

++ From tests in the biaxial series which are under isotropic confinement

# Standard Error of the Estimate in psi

The values resulting from a least squares fit to the straight line log  $G$  - log  $\bar{\sigma}_0$  relationship yields the stiffness coefficients  $C_{Gm}$  and  $nm$  which are summarized in Table 9.6 for the ISO1 and ISO2 test series and the tests from for the biaxial test series which were conducted at isotropic states of stress. The independently measured log  $G$  - log  $\bar{\sigma}_0$

relationships for the ISO1 and ISO2 test series are shown as lines in Fig. 9.4.

The shear modulus can also be backcalculated from the constrained and Young's modulus using Eq. 7.9. The backcalculated values of the shear modulus are plotted in Fig. 9.5 and the stiffness coefficients computed using Eq. 9.4 are included in Table 9.7 and also shown as solid lines on Fig. 9.5. A comparison of the measured and backcalculated values of the shear modulus is discussed in the next section.

#### 9.6 The Validity of the Isotropic Linear Elastic Assumption

To backcalculate the shear modulus from the measured constrained and Young's moduli, the simplest assumption is to assume the sand sample is homogeneous, isotropic and linear elastic. If this were true, the measured shear modulus and the backcalculated shear modulus should be equal. The measured and backcalculated shear moduli (from the third mode only) are plotted against each other in Fig. 9.6 and Fig. 9.7 for the ISO1 and ISO2 test series, respectively. Similar trends are evident for the other modes as is noted by comparing the stiffness coefficients in Tables 9.6 and 9.7. In addition, the biaxial test series also show the same trends in shear moduli.

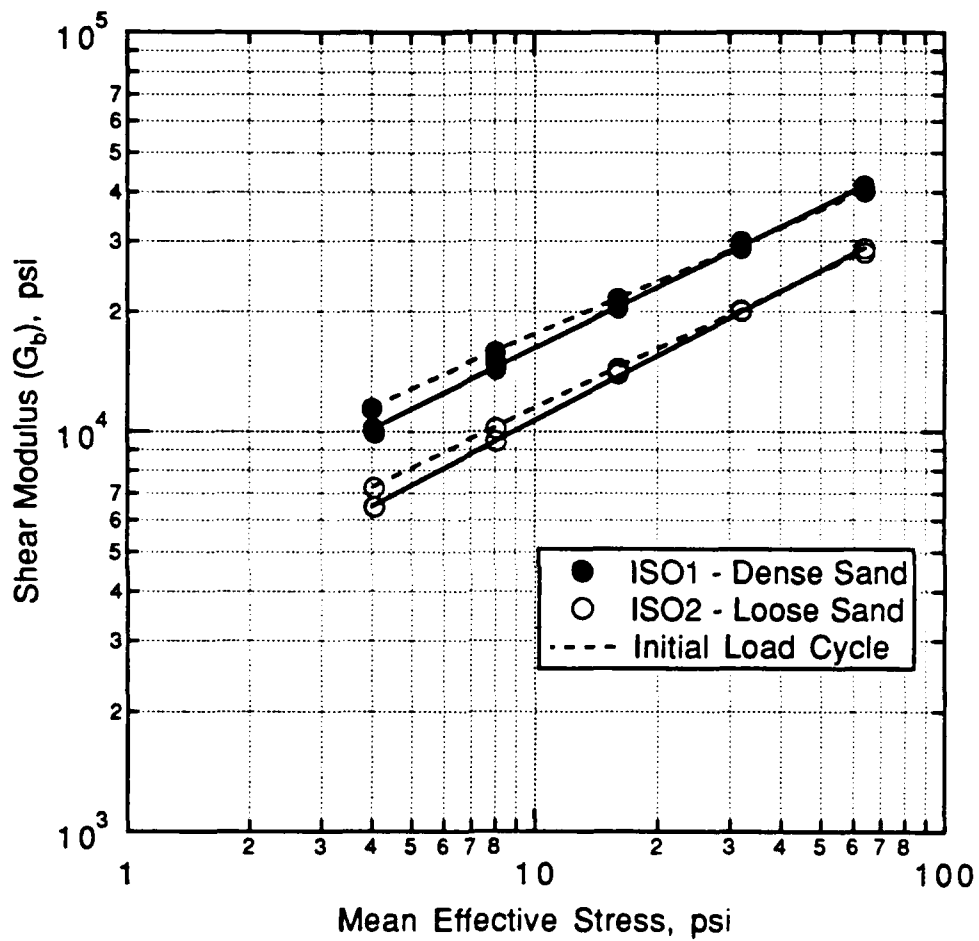


Fig. 9.5. Variation of Backcalculated Shear Modulus ( $G_b$ ) with Mean Effective Stress for ISO1 and ISO2 Test Series on Sand.

Table 9.7. Comparison of Stiffness Coefficients for Log  $G_b$  - Log  $\bar{\sigma}_o$  Relationship\* (Backcalculated From the Constrained and Young's Moduli) for Isotropic Confinement

Test Series - Mode	$e_{Average}$	$C_{Gb}$	nm	S.E.E.#
ISO1-2-1L**	0.593	727	0.446	79
ISO1 - 2+		693	0.515	774
ISO1-3-1L**	0.593	757	.0445	139
ISO1 - 3+		726	0.507	656
ISO2-2-1L**	0.758	641	0.488	102
ISO2 - 2+		608	0.529	390
ISO2-3-1L**	0.758	650	0.494	73
ISO2 - 3+		624	0.538	392
BIAX1 - 3++	0.760	662	0.518	236
BIAX2 - 3	0.771	677	0.534	417
BIAX3 - 3	0.586	778	0.485	259
BIAX4 - 2	0.582	677	0.508	387
BIAX5 - 2	0.750	603	0.547	280

\*  $G_b = C_{Gb} \bar{\sigma}_o^{nm} \text{ Pa}^{1-nm}/F(e)$  ,  $F(e) = 0.3 + 0.7e^2$

\*\* From first four tests at 4, 8, 16, and 32 psi confining pressure

+ From all tests except first four

++ From tests in the biaxial series which are under isotropic confinement

# Standard Error of the Estimate in psi

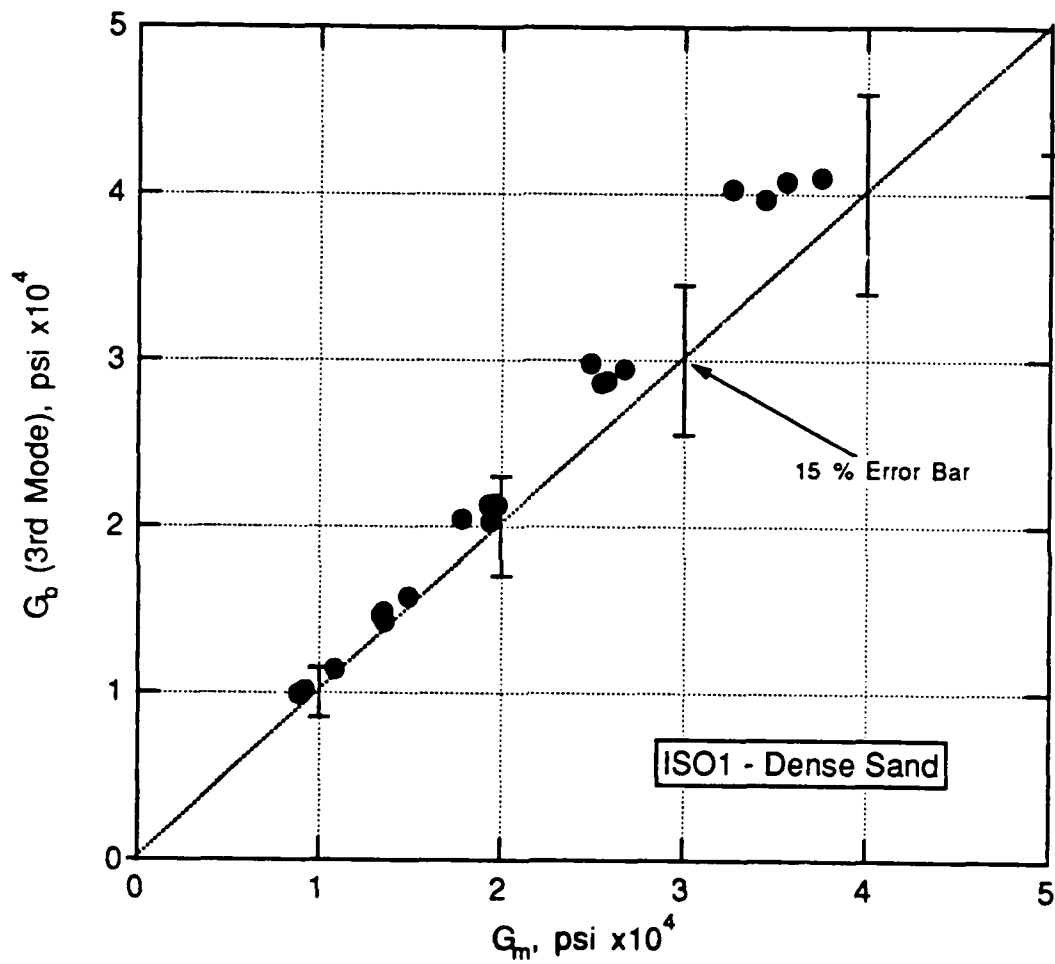


Fig. 9.6. Comparison of Backcalculated ( $G_b$ ) and Measured ( $G_m$ ) Shear Moduli for ISO1 Test Series on Dense Sand.

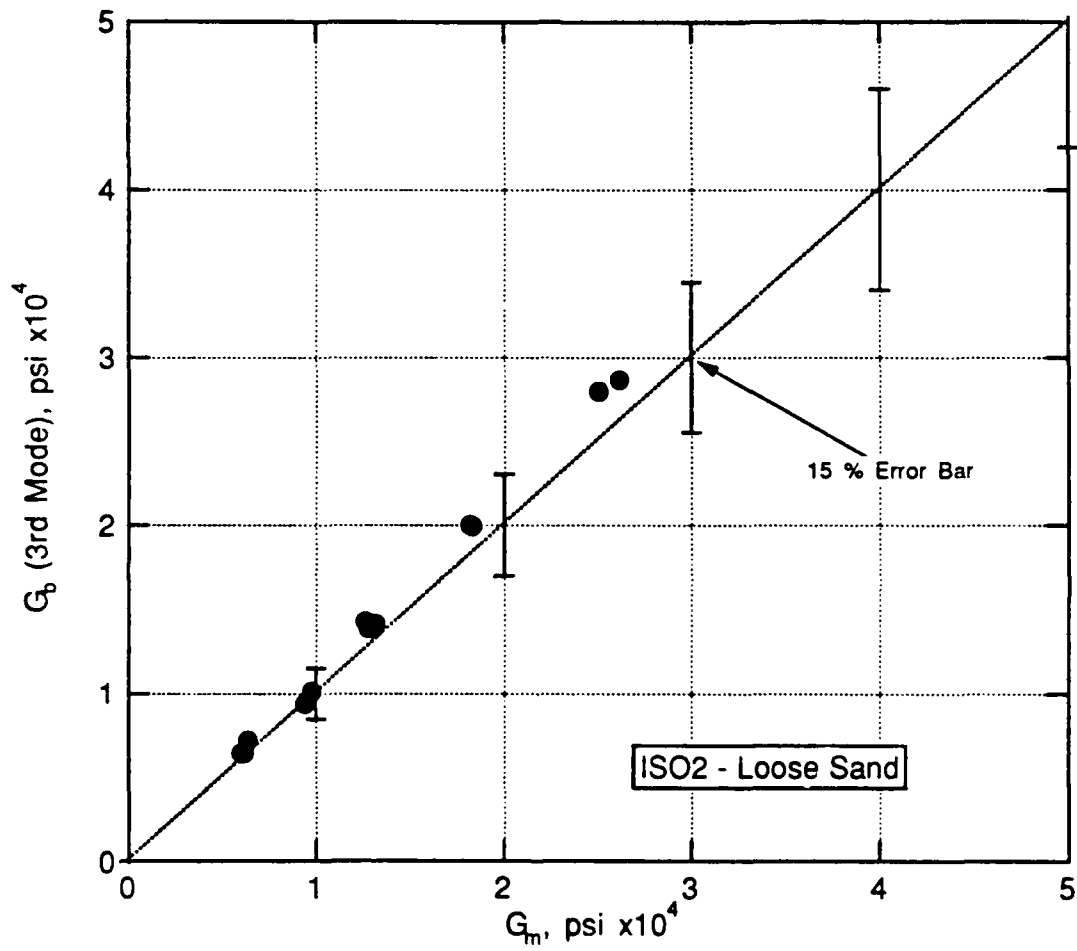


Fig. 9.7. Comparison of Backcalculated ( $G_b$ ) and Measured ( $G_m$ ) Shear Moduli for ISO2 Test Series on Loose Sand.

Figures 9.6 and 9.7 show that the measured shear modulus and backcalculated shear modulus tend to agree with each other within about  $\pm 10$  percent. The general trend is for the backcalculated shear modulus to be slightly higher (10 - 15 percent) than the measured value, however, this difference corresponds to a 5 to 7.5 percent difference in shear wave velocity, an error which is well within the range that can be expected from the shear pulse test (see discussion in Chapter 6.3.4.).

Figure 9.8 shows the variation in the Poisson's ratio as a function of the mean effective stress for the ISO1 and ISO2 test series. Poisson's ratio was computed from the constrained and Young's moduli (3rd Mode) using Eq.s 7.5 and 7.6 . An examination of the test summaries in Appendix G shows that Poisson's ratio decreases slightly for the higher modes in a longitudinal resonant column test, a decrease which probably reflects the increase in Young's modulus computed for each higher mode. It is also noted that there were cases when the computed Young's modulus was higher than the constrained modulus. In that event, the entries for the Poisson's ratio were set to zero primarily to act as a flag to the writer to discard that data. This occurred most often for the Young's moduli computed for the first and fourth modes, principally because of limitations in the ability of the equipment at low frequencies near the first mode, and interference from high frequency motions in the vicinity of the fourth mode (if it was observed at all).

Figure 9.8 shows a trend for the Poisson's ratio to decrease with increasing mean effective stress. This trend is also reflected in the

slopes of the  $\log M - \log \bar{\sigma}_0$  and  $\log E - \log \bar{\sigma}_0$  relationships in Table 9.3 and Table 9.5, respectively. The slope of the  $\log E - \log \bar{\sigma}_0$  relationship is consistently a bit higher than the  $\log M - \log \bar{\sigma}_0$  relationship. This trend is illustrated in Fig. 9.9 for the ISO2 test series. Based on theoretical considerations, it is not possible for these two relationships to intersect at very high confining pressures. (The moduli, E and M, can become equal for  $\nu = 0$ .) However, it is possible to postulate that they may become about parallel at high pressures and have a constant Poisson's ratio that approaches that of the solid particles of the sand. In effect, this suggests the properties of the sand fabric will approach those of its solid constituency, which suggests that any effect attributable to particle interfaces might become negligible at higher confining pressures. However, the pressure levels at which this might occur are well above those used in this study.

#### 9.7 Comparison of Stiffness Equations with Previous Research on Washed Mortar Sand

A comparison of the stiffness coefficients for the  $\log M - \log \bar{\sigma}_0$  relationship for research work completed using the same washed mortar sand that was used in this study is presented in Table 9.8. It can be seen the values of the stiffness coefficients from this research are similar to those from previous studies.

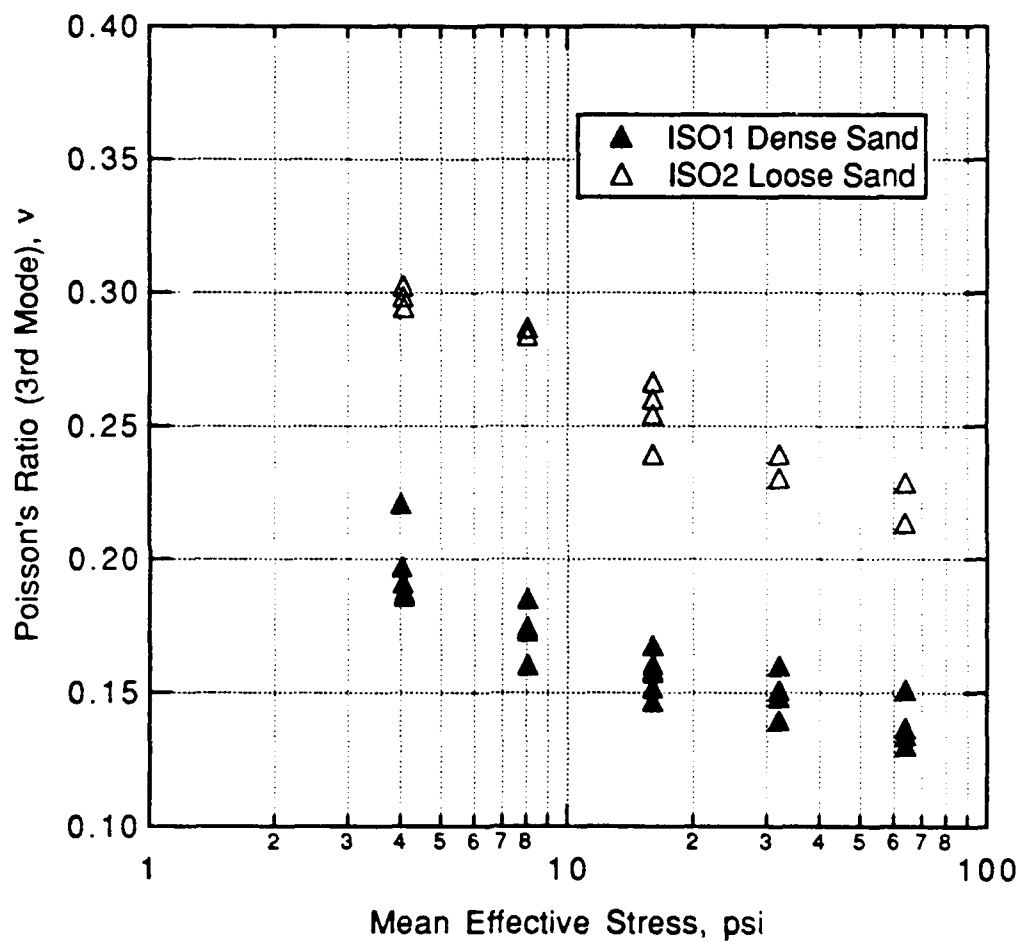


Fig. 9.8. Variation of Poisson's Ratio with Mean Effective Stress for ISO1 and ISO2 Test Series on Sand (3rd mode only)

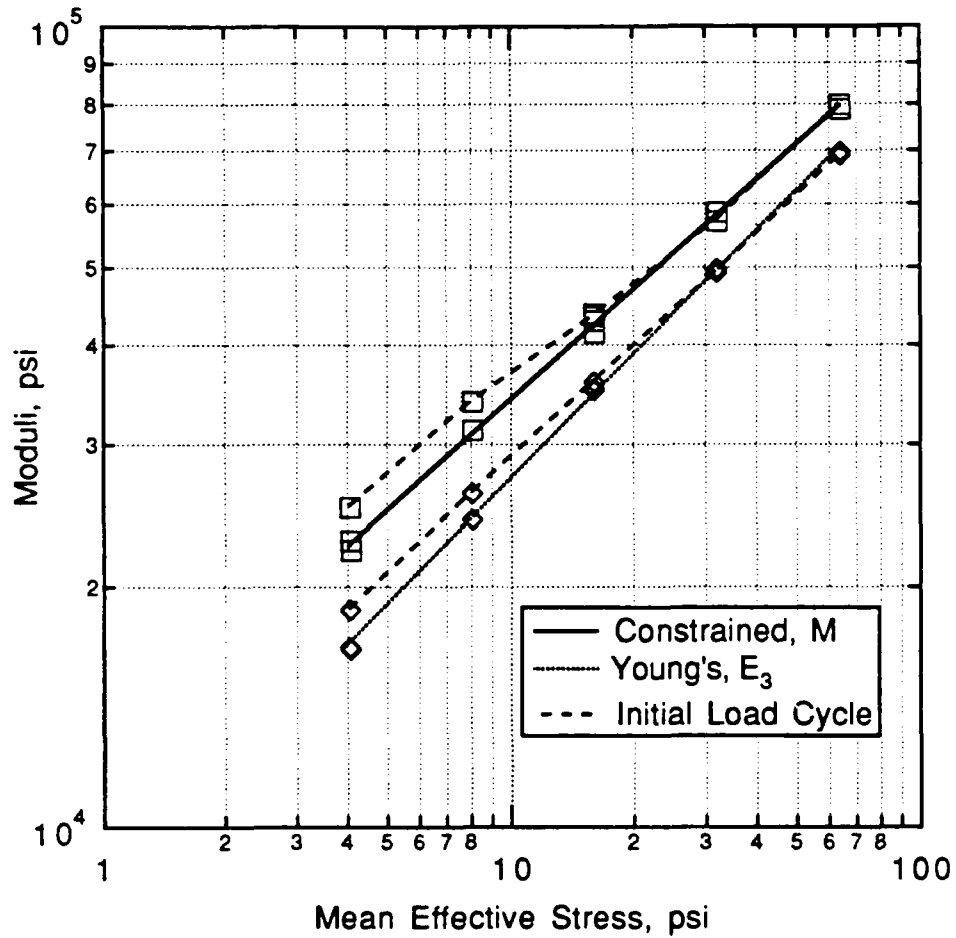


Fig. 9.9. Comparison of Constrained and Young's (3rd mode) Moduli for ISO2 Test Series on Loose Sand.

Table 9.9 is a comparison of the stiffness coefficients for the  $\log E - \log \bar{\sigma}_0$  relationship for research work completed during this study and previous studies on cohesionless soils. Only the slope coefficient is reported in the literature, so no comparison can be made of the constant coefficient. The slope of the  $\log E - \log \bar{\sigma}_0$  relationship determined in this study compares well with those reported by earlier researchers.

Table 9.10 is a comparison of the stiffness coefficients for the  $\log G - \log \bar{\sigma}_0$  relationship for research work completed using the same washed mortar sand that was used in this study. Two sets of coefficients are shown for this research, one representing the shear modulus ( $G_m$ ) computed from the independent shear pulse test described in Chapter 6.3 and the other representing the shear modulus ( $G_b$ ) backcalculated using the Young's modulus and constrained modulus from the longitudinal resonant column and axial pulse tests, respectively. It appears the directly measured shear modulus has a similar constant but a slightly higher slope than found in previous studies. This is probably due to the difficulty in identifying the far-field shear wave arrival. The backcalculated shear modulus has a steeper slope, but a similar value for the constant, which probably reflects the influence of the Young's and constrained moduli from which it is calculated. It is noted that the stiffness coefficients measured in the smaller laboratory devices tend to be slightly higher than those measured in the large-scale triaxial device. Figure 9.10 is a comparison of the values of the shear moduli computed from the various research studies using the washed mortar sand.

Table 9.8. Comparison of Stiffness Coefficients for Log M - Log  $\bar{\sigma}_0$  Relationship\* from Various Research Studies Using Washed Mortar Sand

Study	Void Ratio, e	$C_M$	nm	Range of Stress, psi	Test **
Kopperman (1983)	---	---	0.40	10 - 40	a
Chu, et al (1984)	0.64	1661-2129	0.41-0.43	15 - 30	a
This Research	0.59	1968	0.45	4 - 64	b
	0.76	2029	0.44	4 - 64	

\*  $M = C_M \bar{\sigma}_0^{nm} \text{ Pa}^{1-nm} / F(e)$  ,  $F(e) = 0.3 + 0.7e^2$

- \*\* a. Pulse tests in Large Scale Triaxial Device (LSTD)  
 b. Axial pulse tests in Multi-Moduli Testing Device (MTD)

Table 9.9. Comparison of Stiffness Coefficients for Log E - Log  $\bar{\sigma}_0$  Relationship\* for Soils under Isotropic Confinement from Various Research Studies.

Reference	$C_E$	nm	Confining Pressure	Test**
Duffy and Mindlin (1957)	---	0.50	< 5 psi	a
	---	0.34	> 5 psi	
Shannon, et al (1959)	---	0.50	> 4 psi	a
Hardin (1961)	---	0.46 - 0.62	3 - 55 psi	a
Smoots and Stickel (1962)	---	0.32 - 0.56	> 4 psi	a
Wilson and Miller (1962)	---	0.40 - 0.50	> 4 psi	a
Hardin and Richart (1963)	---	0.54 - 0.70	< 14 psi	a
		0.46 - 0.50	> 14 psi	
This Research e = 0.59 e = 0.77	1721	0.49	4 - 64 psi	a
	1606	0.51	4 - 64 psi	a

\*  $E = C_E \bar{\sigma}_0^{nm} \text{ Pa}^{1-nm}/F(e)$ ,  $F(e) = 0.3 + 0.7e^2$

\*\* a. Longitudinal Resonant Column Tests

Table 9.10. Comparison of Stiffness Coefficients for Log G - Log  $\bar{\sigma}_0$  Relationship\* from Various Research Studies Using Washed Mortar Sand

Study	Void Ratio, e	$C_G$	nm	Range of Stress, psi	Test**
Allen & Stokoe (1982)	0.62-0.70	720	0.48	4 - 64	a
Knox, et al (1982)	---	---	0.40	10 - 40	b
Stokoe & Ni (1985)	0.69	721	0.44	3 - 55	a
Lee & Stokoe (1986)	0.64	635	0.36	10 - 40	b
Ni (1987)	0.64-0.72	687	0.44	2 - 55	a
This Research	0.59	724	0.47	4 - 64	c
	0.76	635	0.50	4 - 64	c
This Research	0.59	719	0.50	4 - 64	d
	0.76	635	0.53	4 - 64	d

\*  $G = C_G \bar{\sigma}_0^{nm} \text{ Pa}^{1-nm} / F(e)$ ,  $F(e) = 0.3 + 0.7e^2$

- \*\*
- a. Torsional Resonant Column Tests
  - b. Shear Pulse tests in Large Scale Triaxial Device (LSTD)
  - c. Shear Pulse tests in Multi-Moduli Testing Device (MTD)
  - d. Longitudinal Resonant Column and Axial Pulse Tests in MTD

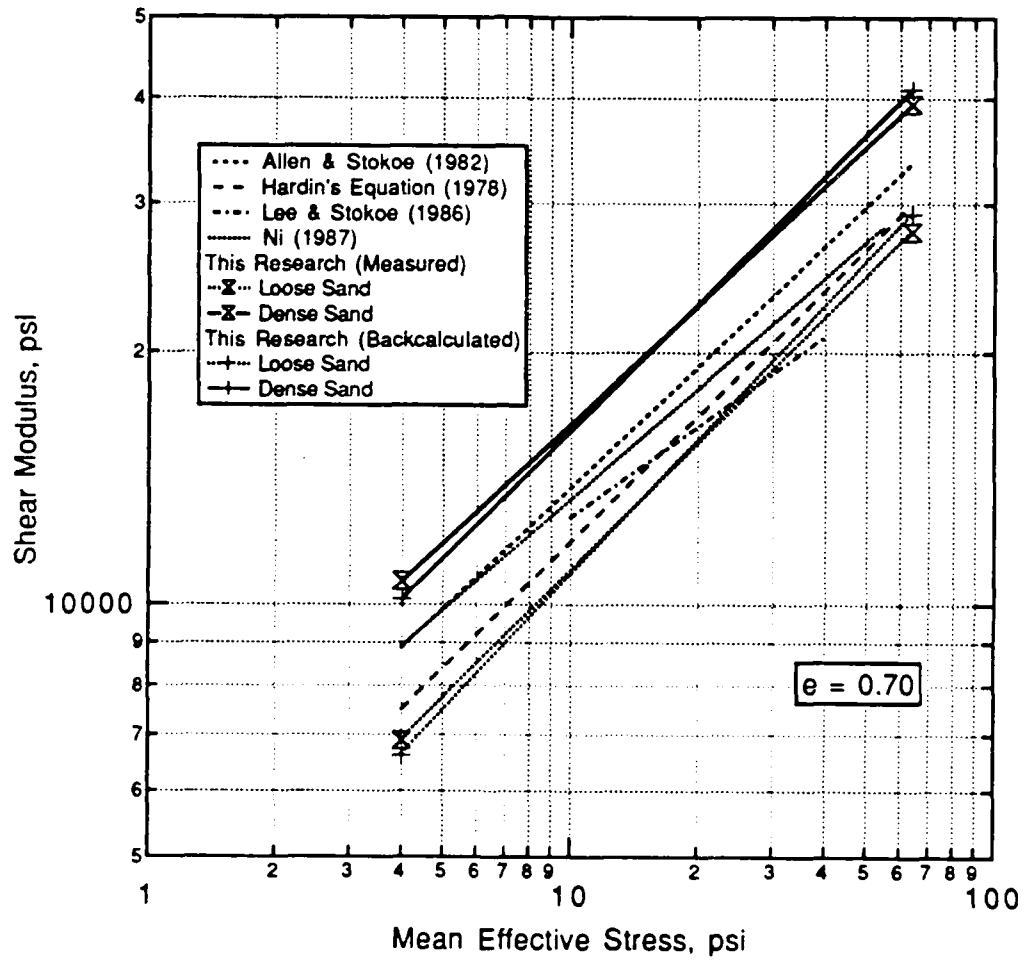


Fig. 9.10. Comparison of Shear Modulus - Mean Effective Stress Relationships from Research Studies on Washed Mortar Sand.

## 9.8 Summary

Tests were performed in the Multi-Moduli Testing Device (MTD) to determine the stiffness of sand under isotropic loading. Two test series were conducted, one on a dense sand and one on a loose sand. In each series, an axial and shear pulse test and a longitudinal resonant column test were each conducted at confining pressures of 4.0, 8.0, 16.0, 32.0 and 64.0 psi in several cycles of increasing and decreasing confining pressures. It was observed that the stiffness of the sand was significantly different for the first loading cycle (4.0, 8.0, 16.0 and 32.0 psi) than for the first unloading and subsequent loading and reloading cycles. This phenomenon suggests that the sand stiffness is susceptible to stress history and similar behavior was noted in tests by others on the same sand. The cause for this stress history dependent behavior may be attributed to sample construction technique, particle rearrangement, seating of the top cap or complex and sensitive stress conditions in the vicinity of the specimen ends. Therefore, a distinction is made between first load and subsequent loading when expressing the stiffness-stress relationships.

The tests showed that the small-strain constrained ( $M$ ), Young's ( $E$ ), and shear ( $G$ ) moduli could all be expressed by a constant times the mean effective stress,  $\bar{\sigma}_0$ , raised to a power ranging between 0.44 and 0.53. These relationships are straight lines when plotted as the log of the modulus versus the log of the mean effective stress, with the slope of the

line the power of the mean effective stress. The  $\log M - \log \bar{\sigma}_0$  relationship had slopes of 0.44 and 0.45 for the loose and the dense sand, respectively. The  $\log E - \log \bar{\sigma}_0$  relationship had slopes of 0.51 and 0.49 for the loose and dense sand, respectively. Finally, the independently measured shear modulus had slopes of 0.50 and 0.47 for the loose and dense sand, respectively.

The stiffness-stress relationships for those tests in the biaxial tests series (described in Chapter 10) which were conducted at isotropic states of stress were also determined. In general, for all moduli, the slopes were lower, and the constants higher, than for the test series where the sand was subjected only to isotropic loadings. This observation lends support to the thesis that stress history may have significant impact on the stiffness of a sand.

It is noted the slopes for the Young's modulus were steeper than for the constrained modulus, illustrating the decrease in Poisson's ratio that was observed as the confining pressure increased. Poisson's ratio was computed by invoking the assumption the sand is linear elastic. The shear modulus can be computed from the constrained and Young's modulus by making the same assumption. The shear moduli thus computed were generally within the 10 -15 percent of those measured independently, an error which is mostly attributable to the difficulty in determining the shear wave arrival in the shear pulse test used to determine the shear modulus.

The values for constrained modulus measured in the MTD compared well with previous research on the same washed mortar sand. The slope of the relationship was slightly higher than for previous work, however, that work has been exclusively pulse tests in a large (7 ft) cubic triaxial test device. Further, the previous work was limited to tests in a narrower range of confining pressures.

No direct comparison can be made between the values for Young's modulus measured in this research and those determined for similar soils by earlier researchers. However, the slopes of the log E-log  $\bar{\sigma}_0$  relationship determined in this study compare well with those reported in other studies.

The values for shear modulus measured in the MTD were similar to those reported in previous research. It is noted again that the trend for higher values appears to be related to the size of the test device. Further, the absolute values for the measured shear modulus have to be qualified by the possible error that is attributable to the shear pulse test as it is currently conducted in the MTD.

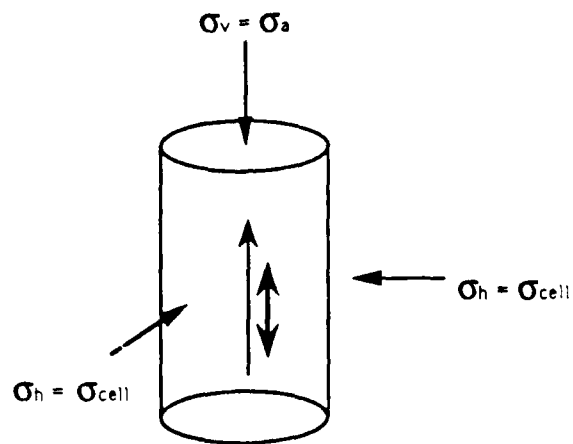
## Chapter Ten

### Stiffness of Sand Under Biaxial Loading

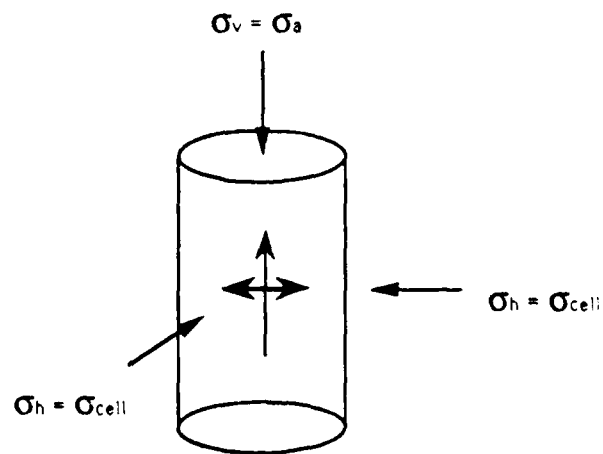
#### 10.1 Introduction

Five series of tests were performed to examine the effect of a biaxial stress state on the constrained, Young's and shear moduli of a uniform dry sand. The testing was conducted to evaluate the effect of the axial and horizontal stress on longitudinal, compression, and shear waves propagating in the axial direction of the specimen. The goal of the test series was to evaluate separately the influence of axial and horizontal stresses on Young's modulus. However, extensive data were also gathered which enabled the effect of these two stresses on the constrained and shear moduli to be studied.

It is assumed in this study that the principal stresses are aligned with, and perpendicular to, the axis of the specimen as illustrated in Fig. 10.1. It is further assumed that: (1) the direction of wave propagation is parallel to the longitudinal axis of the specimen and consequently parallel to one of the principal stresses, and (2) the direction of particle motion is either parallel to (for compression waves), or perpendicular to (for shear waves), the axis of the specimen. Finally, it is assumed that the rod wave propagates in a direction that is parallel to the axis of the



a) Constrained Wave from Axial Pulse Test



b) Shear Wave from Shear Pulse Test

Fig. 10.1. Directions of Wave Propagation and Particle Motion Assumed for Biaxial Testing with MTD.

specimen and that even though it has a complicated particle motion, the major motion is parallel to the axis of the specimen and only a minor component may be perpendicular to the axis of the specimen.

This chapter deals exclusively with testing on an uncemented air-dried sand. The test sequence used in each of the test series is described initially. This description is followed by an analysis of the effect of the biaxial state of stress on the constrained, Young's and shear moduli. Complete summaries of the test results for each test series are included in Appendix G and only representative examples are discussed in this chapter.

## 10.2 Biaxial Testing Sequence and Stress State

Five biaxial test series were conducted, and these are denoted BIAX1, BIAX2, BIAX3, BIAX4, and BIAX5. Only two of these, BIAX4 and BIAX5, were conducted with the vibration isolation assembly illustrated in Fig. 5.4. The BIAX1, BIAX2 and BIAX3 test series were conducted with an earlier less effective isolation assembly which may have influenced the results from those tests. Table 10.1 is a summary of the loading sequence for the BIAX2 test series and is included here as an example. The BIAX1 test series was conducted on the same loose sand sample as the ISO2 test series. The remaining biaxial test series were conducted on newly prepared samples, BIAX2 and BIAX5 on a loose sand, BIAX3 and BIAX4 on a dense sand. The average void ratios and relative

Table 10.1. Summary of Loading Sequence for Loose Sand Specimen.  
(BIAX2 Test Series)

Test #	Void Ratio e	Axial Stress psi	Horizontal Stress psi	Ko	Mean Stress psi
1	0.775	4.01	4.00	1.00	4.00
2	0.773	15.99	16.00	1.00	15.99
3	0.770	64.00	64.00	1.00	64.00
4	0.772	16.01	16.01	1.00	16.01
5	0.773	4.02	4.00	1.00	4.01
6	0.772	16.00	16.00	1.00	16.00
7	0.772	18.31	16.00	1.14	16.77
8	0.772	21.39	16.01	1.34	17.80
9	0.771	25.68	16.01	1.60	19.23
10	0.771	32.09	16.00	2.01	21.36
11	0.770	32.10	20.00	1.60	24.03
12	0.769	32.08	24.00	1.34	26.69
13	0.767	32.04	28.01	1.14	29.35
14	0.764	32.00	32.00	1.00	32.00
15	0.763	64.00	63.99	1.00	63.99
16	0.765	32.02	32.01	1.00	32.01
17	0.765	25.54	32.00	0.80	29.85
18	0.765	21.20	31.98	0.66	28.39
19	0.766	18.15	32.00	0.57	27.38
20	0.767	15.81	32.01	0.49	26.61
21	0.767	15.84	28.01	0.57	23.95
22	0.768	15.89	24.00	0.66	21.30
23	0.770	15.96	20.00	0.80	18.66
24	0.791	16.00	16.00	1.00	16.00
25	0.796	4.00	4.01	1.00	4.00

Average  
Void Ratio = 0.771

Table 10.2. Summary of Void Ratios and Densities for Test Series on Sand.

Test Series	$e_{Average}$	$\gamma_{Average}$ , pcf	Relative Density, $D_r$ %
ISO1	0.593	104.7	88
ISO2	0.758	94.9	27
BIAX1	0.760	94.8	26
BIAX2	0.771	94.2	23
BIAX3	0.586	105.2	91
BIAX4	0.582	105.5	93
BIAX5	0.750	95.3	29

$$* D_r = \frac{\gamma_{Average} - \gamma_{min}}{\gamma_{max} - \gamma_{min}}, \text{ where } \gamma_{min} = 90.6 \text{ pcf and } \gamma_{max} = 106.6 \text{ pcf}$$

Figure 10.2 illustrates the axial and horizontal stress paths for the BIAX2 and BIAX3 test series. Each test series started with five isotropic test steps at confining pressures of approximately 4.0, 16.0, 64.0, 16.0, and 4.0 psi. This was intended to eliminate the effect of stress history described in Section 9.3. Each biaxial test series consisted of a loading and unloading cycle during which the axial or horizontal stress was increased or decreased while the other was held constant. The biaxial portion of the test series actually started isotropically by increasing the confining pressure to 16.0 psi (after finishing the first five tests). The axial stress was then increased in increments for the next four tests while the

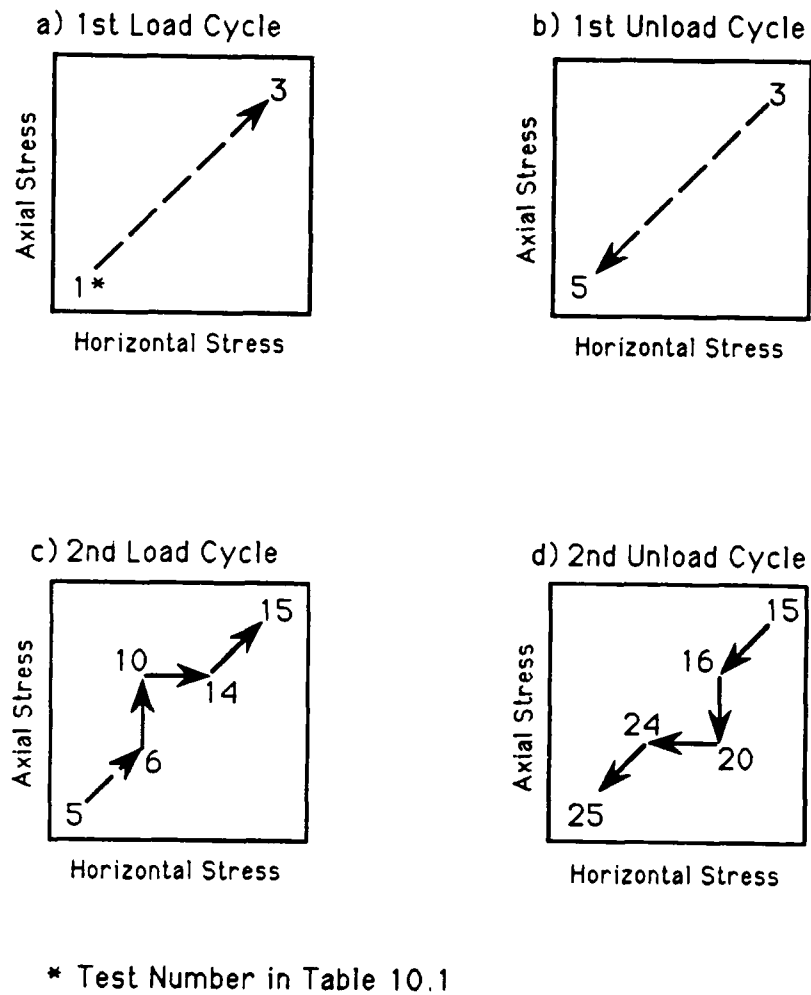


Fig. 10.2. Loading Sequence for BIAx2 and BIAx3 Test Series.

confining pressure was held constant. The axial stress was increased to a maximum of twice the confining pressure ( $K_0 = \sigma_h/\sigma_a = 0.5$ ). Then for the next four tests, the confining pressure was increased incrementally while holding the axial stress constant, until the horizontal stress again equaled the axial stress at 32.0 psi. The remaining test in the loading half of the test series included a test under isotropic conditions at a confining pressure of 64.0 psi to allow comparison with the isotropic test series.

The unloading half of the test began by decreasing the confining pressure to 32.0 psi. Then the axial stress was reduced in four increments while holding the confining pressure constant until the horizontal stress was twice the axial stress ( $K_0 = 2.0$ ). Next, the confining pressure was reduced in increments until the horizontal stress again equaled the axial stress at 16.0 psi. The final step in the unloading sequence was to reduce the confining pressure and test at the lowest isotropic state of 4.0 psi.

The BIAx4 and BIAx5 test series contained two biaxial "loops" like the one just described for the BIAx2 and BIAx3 test series. The BIAx4 and BIAx5 test series had a biaxial "loop" between 8.0 and 16.0 psi, in addition to the one between 16.0 and 32.0 psi that was just described. The BIAx4 and BIAx5 test series are illustrated in Fig. 10.3 where they are plotted on a two-dimensional diagram that is a representation of the three-dimensional state of stress. The horizontal axis is the square root of two times the radial stress because the two principal stresses equal

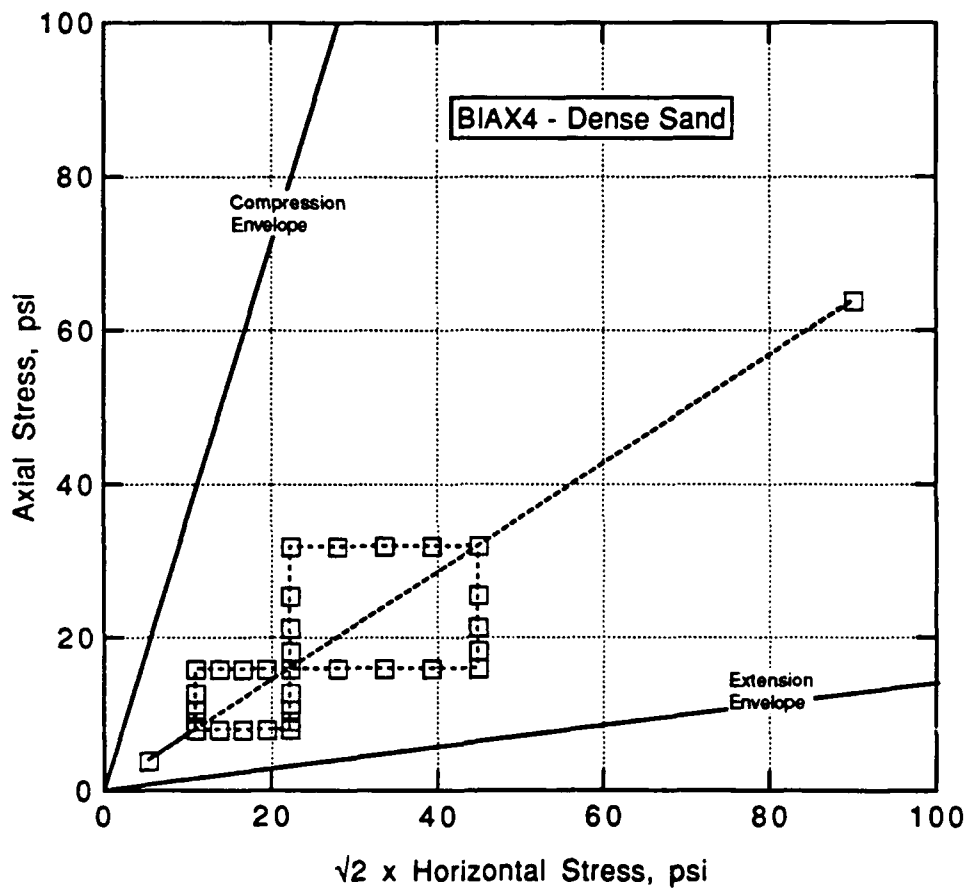


Fig. 10.3. Loading Sequence for BIAx4 and BIAx5 Test Series on Sand.

each other. Consequently, the stress path for the biaxial test series will be confined to a plane in three-dimensional stress space which contains one principal stress axis and the stress space diagonal. The Mohr-Coulomb failure envelopes for compression and extension are also shown on Fig. 10.3.

Whenever testing was conducted with the axial loading piston, load cell, and vibration isolation assembly in place, it was possible to correct the axial stress for any additional weight on the top of the sample. Thus, it was possible to adjust the axial load in order to achieve a more ideal isotropic balance of stresses in the sample. A correction was also required to account for the imbalance of forces on the sample due to the confining pressure acting against the cross sectional area of the loading piston. By knowing the appropriate constants and zero readings for the transducers and load cell, it was possible to predetermine the necessary readings to achieve the desired state of stress for each test step in a test series.

### 10.3 The Constrained Modulus Under a Biaxial State of Stress

Figure 10.4 illustrates the results from tests in the BIAx4 test series and shows the variation of  $M$  with the mean stress (Fig. 10.4a), the axial stress (Fig. 10.4b), and the horizontal stress (Fig. 10.4c). It is immediately obvious that constrained modulus appears to be almost solely a function

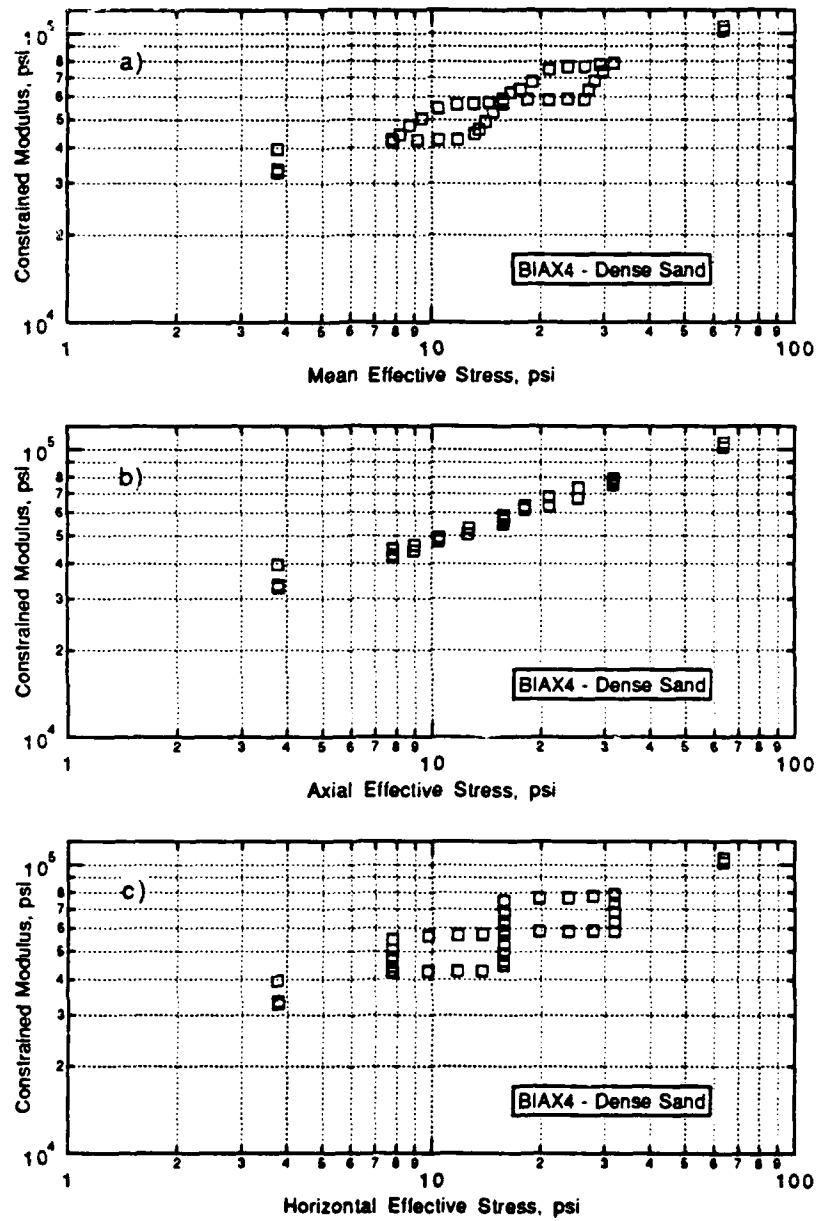


Fig. 10.4. Variation of Constrained Modulus with Mean, Axial and Horizontal Effective Stress for BIAx4 Test Series on Dense Sand.

Table 10.3. Stiffness Coefficients for Log M - Log  $\bar{\sigma}_a$  Relationship\* for Sand Under Biaxial Loading

Test Series	$e_{Average}$	$C_A$	$na$	S.E.E**
BIAX1	0.760	2082	0.453	544
BIAX2	0.771	1894	0.570	1142
BIAX3	0.586	2031	0.487	1815
BIAX4	0.582	2040	0.422	1490
BIAX5	0.750	1961	0.527	1769

\*  $M = C_A \bar{\sigma}_a^{na} Pa^{1-na} / F(e)$  ,  $F(e) = 0.3 + 0.7e^2$

\*\* Standard Error of the Estimate in psi

of the axial stress. In this case then the dynamic stiffness equation representing the constrained modulus as a function of the axial effective stress is taken in the form of equation 9.2

$$M = C_A \bar{\sigma}_a^{na} Pa^{1-na} / F(e) \quad (10.1)$$

where

- M = constrained modulus,
- $C_A$  ,  $na$  = stiffness coefficients,
- $\bar{\sigma}_a$  = axial effective stress,
- $Pa$  = atmospheric pressure in same units as  $\bar{\sigma}_a$ , and
- $F(e)$  = function of void ratio,  $F(e) = 0.3 + 0.7e^2$ .

Equation 10.1 is a straight line relationship when plotted on a log-log scale and lends itself to a simple least squares fitting technique. The resulting values for the stiffness coefficients  $C_A$  and  $n_a$  are summarized for each biaxial test series in Table 10.3. The stiffness coefficients in Table 10.3 are for all test steps, excluding the first two, tests 1 and 2, at 4.0 and 16.0 psi confining pressure, respectively.

It is also possible to represent the constrained modulus using a relationship containing both the axial and horizontal stresses. This two-stress relationship is of the form

$$M = C_M \bar{\sigma}_a^{n_a} \bar{\sigma}_b^{n_b} P_a^{1-n_a-n_b} / F(e) \quad (10.2)$$

where

- $M$  = constrained modulus,
- $C_M, n_a$  and  $n_b$  = stiffness coefficients,
- $\bar{\sigma}_a$  = axial effective stress,
- $\bar{\sigma}_b$  = horizontal effective stress,
- $P_a$  = atmospheric pressure in same units as  $\bar{\sigma}_a$  and  $\bar{\sigma}_b$ ,  
and,
- $F(e)$  = function of void ratio,  $F(e)=0.3+0.7e^2$ .

This relationship can be transformed into a linear equation by taking the common logarithm of both sides and a simple least squares regression then finds the coefficients. The resulting values for the stiffness coefficients are shown for each biaxial test series in Table 10.4.

Table 10.4. Stiffness Coefficients for Constrained Modulus (M) of Sand Under Biaxial Loading Using a Two-Stress Model\*

Test Series	$e_{Average}$	$C_M$	na	nb	S.E.E.**
BIAX1	0.760	2082	0.451	0.002	574
BIAX2	0.771	1898	0.570	-0.006	1189
BIAX3	0.586	2005	0.448	0.079	1246
BIAX4	0.582	2034	0.384	0.058	657
BIAX5	0.750	1969	0.577	-0.077	1536

\*  $M = C_M \bar{\sigma}_a^{na} \bar{\sigma}_b^{nb} P a^{1-na-nb} / F(e)$  ,  $F(e) = 0.3 + 0.7e^2$

\*\* Standard Error of the Estimate in psi

The stiffness coefficients in Table 10.4 are computed using only the tests which were part of the biaxial loading sequence, i.e. tests 6 - 14 and 16 - 24 for the BIAX2 and BIAX3 test series, and tests 6 - 22 and 24 - 40 for the BIAX4 and BIAX5 test series. The corresponding stress levels were 16 - 32 psi for the BIAX2 and BIAX3 test series, and 8 - 32 psi for the BIAX4 and BIAX5 test series.

There appears to be a significant difference in the values of the slopes for the axial stress between the one-stress and two stress relationships for the constrained modulus, however, most of this may be attributable to the different stress ranges over which the relationships are fitted and the possibility that the earlier, less effective, version of the

vibration isolation assembly influenced the results. However, there is also the possibility that the loose sand behaves differently under biaxial stress loadings.

#### 10.4 The Young's Modulus under a Biaxial State of Stress

Figure 10.5 illustrates the effect of the mean (Fig. 10.5a), axial (Fig. 10.5b), and horizontal (Fig. 10.5c) effective stresses on the Young's modulus for the BIAx4 test series. By examining Fig. 10.5, it can be seen that Young's modulus is dominated by the axial stress. However, there appears to be a slight influence from the horizontal stress.

Therefore, the dynamic stiffness equation is again taken in the two-stress form

$$E = C_E \bar{\sigma}_a^{n_a} \bar{\sigma}_b^{n_b} P_a^{1-n_a-n_b} / F(e) \quad (10.3)$$

where  $E$  is Young's modulus and  $C_E$ ,  $n_a$  and  $n_b$  are the corresponding stiffness coefficients.

As before, equation 10.3 is transformed into a linear relationship by taking the common logarithm of both sides. The resulting  $\log E - \log \bar{\sigma}_a - \log \bar{\sigma}_b$  relationship lends itself to a least squares fitting technique.

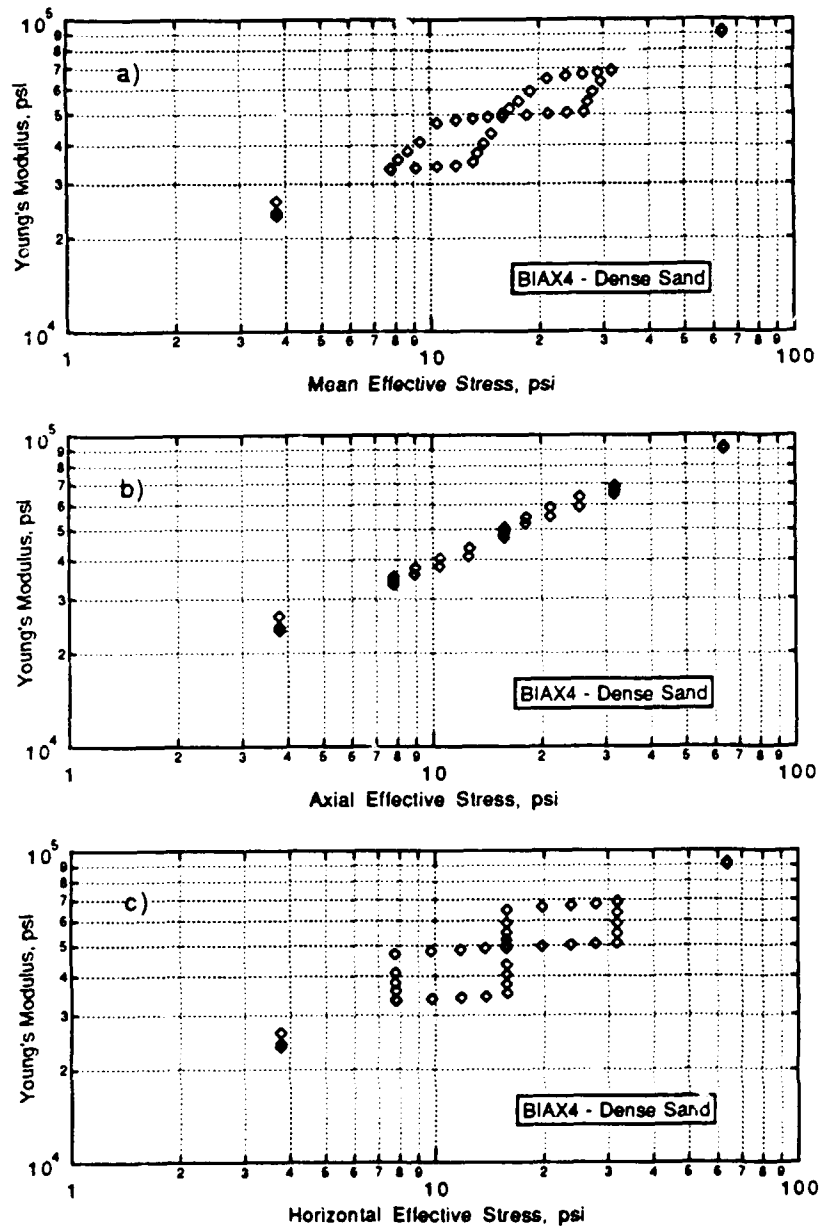


Fig. 10.5. Variation of Young's Modulus with Mean, Axial and Horizontal Effective Stress for BIAx4 Test Series on Dense Sand.

Table 10.5. Stiffness Coefficients for Young's Modulus of Sand Under Biaxial Loading Using a Two-Stress Model\*

Test Series - Mode	$e_{Average}$	$C_E$	$n_a$	$n_b$	S.E.E**
BIAX1 - 3	0.760	1679	0.441	0.055	420
BIAX2 - 3	0.771	1621	0.571	0.039	993
BIAX3 - 3	0.586	1806	0.451	0.098	517
BIAX4 - 2	0.582	1700	0.446	0.069	741
BIAX4 - 3	0.582	1798	0.424	0.077	581
BIAX5 - 2	0.750	1543	0.582	-0.021	794
BIAX5 - 3	0.750	1603	0.558	-0.011	977

\*  $E = C_E \bar{\sigma}_a^{n_a} \bar{\sigma}_b^{n_b} P a^{1-n_a-n_b} / F(e)$ ,  $F(e) = 0.3 + 0.7e^2$

\*\* Standard Error of the Estimate in psi

The resulting values for the stiffness coefficients are summarized in Table 10.5 for each biaxial test series. Again, the stiffness coefficients include only those tests which were part of the biaxial loading sequence.

The slope coefficients are higher, and the constants lower, for the loose sand compared to the dense sand. This trend is similar to that observed for the constrained modulus and may be attributable to the possibility that the earlier, less effective, version of the vibration isolation assembly influenced the results. Again, there is also the possibility that

the loose sand behaves differently than the dense sand under biaxial stress loadings.

### 10.5 The Shear Modulus Under a Biaxial State of Stress

Figure 10.6 illustrates the effect of the mean (10.6a), axial (10.6b), and horizontal (10.6c) effective stresses on the independently measured shear modulus for the BIAx4 test series. It is apparent that the mean stress alone is only a fair indicator for the shear modulus. It is also apparent both the axial stress and horizontal stress affect the shear modulus.

The dynamic stiffness equation is again taken in the form

$$G_m = C_{Gm} \bar{\sigma}_a^{na} \bar{\sigma}_b^{nb} P_a^{1-na-nb} / F(e) \quad (10.4)$$

where  $G_m$  is the shear modulus and  $C_{Gm}$ ,  $na$  and  $nb$  are the corresponding stiffness coefficients.

Equation 10.4 is again transformed into a linear equation by taking the common logarithm of both sides and the resulting  $\log G_m - \log \bar{\sigma}_a - \log \bar{\sigma}_b$  relationship is fitted using least squares regression. The resulting values for the stiffness coefficients are summarized in Table 10.6 for each

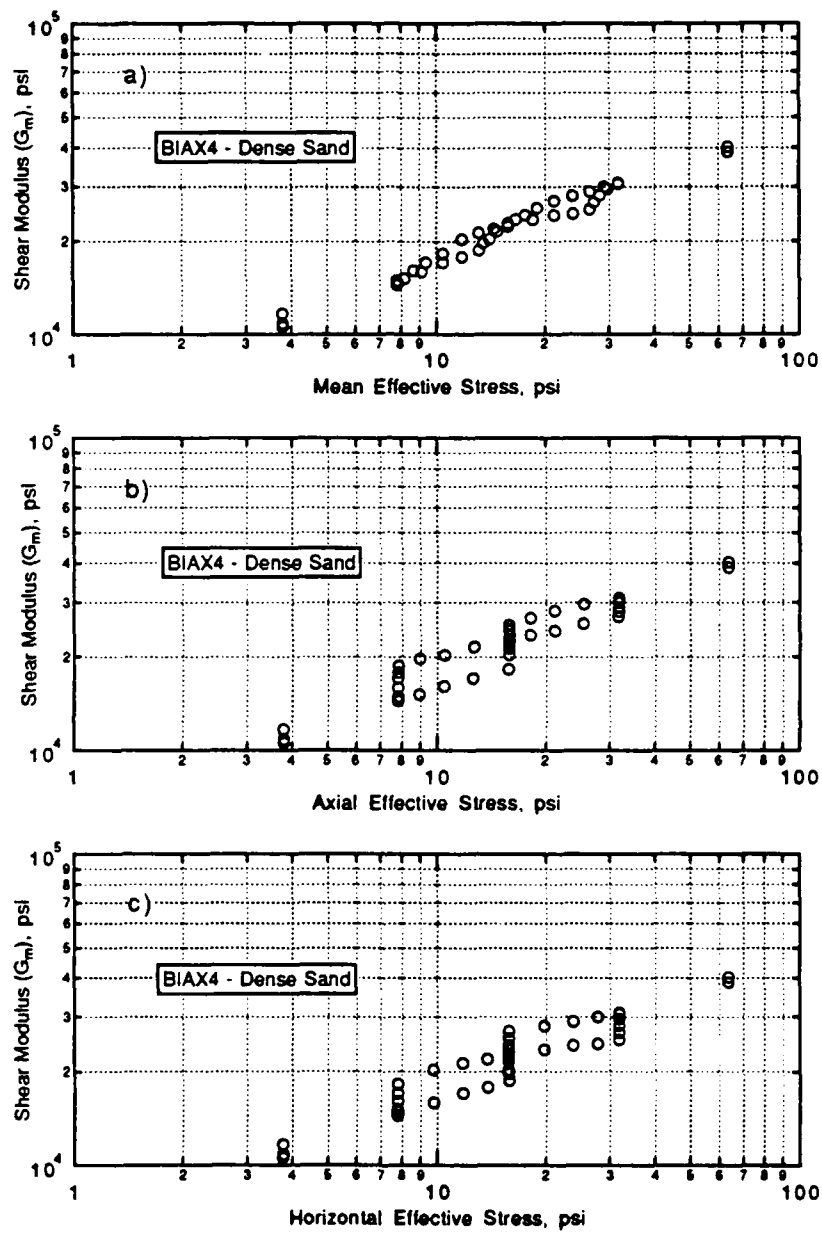


Fig. 10.6. Variation of Measured Shear Modulus with Mean, Axial and Horizontal Effective Stress for BIAx4 Test Series on Dense Sand.

Table 10.6. Stiffness Coefficients for Independently Measured Shear Modulus of Sand Under Biaxial Loading Using a Two-Stress Model\*

Test Series	$e_{Average}$	$C_{Gm}$	$na$	$nb$	S.E.E.**
BIAX1	0.758	636	0.321	0.177	313
BIAX2	0.771	661	0.406	0.160	228
BIAX3	0.586	759	0.297	0.208	221
BIAX4	0.582	775	0.270	0.244	585
BIAX5	0.750	676	0.438	0.100	709

\*  $G_m = C_{Gm} \bar{\sigma}_a^{na} \bar{\sigma}_b^{nb} Pa^{1-na-nb}/F(e)$  ,  $F(e) = 0.3 + 0.7e^2$ .

\*\* Standard Error of the Estimate in psi

biaxial test series. The stiffness coefficients in Table 10.6 are for all only the test steps that were part of the biaxial loading sequence.

The shear modulus can also be calculated from the constrained and Young's moduli in the manner described in Section 7.2.3 by assuming the sand is linear elastic. The resulting backcalculated shear modulus,  $G_b$ , can be expressed using the same two-stress model used for the measured shear modulus. The values of the stiffness coefficients for the  $\log G_b - \log \bar{\sigma}_a - \log \bar{\sigma}_b$  relationship are summarized in Table 10.7.

Table 10.7. Stiffness Coefficients for Backcalculated\* Shear Modulus of Sand Under Biaxial Loading Using a Two-Stress Model\*\*

Test Series - Mode	e <sub>Average</sub>	C <sub>Gb</sub>	na	nb	S.E.E.+
BIAX1 - 3	0.760	663	0.438	0.076	236
BIAX2 - 3	0.771	649	0.571	0.063	417
BIAX3 - 3	0.586	755	0.445	0.117	259
BIAX4 - 2	0.582	682	0.472	0.074	387
BIAX4 - 3	0.582	722	0.445	0.087	287
BIAX5 - 2	0.750	603	0.583	-0.003	280
BIAX5 - 3	0.750	636	0.551	0.015	362

\* Computed from constrained and Young's moduli.

\*\*  $G_b = C_{Gb} \bar{\sigma}_a^{na} \bar{\sigma}_b^{nb} P_a^{1-na-nb} / F(e)$ ,  $F(e) = 0.3 + 0.7e^2$ .

+ Standard Error of the Estimate in psi

Table 10.6 shows that the relative contribution of the principal effective stresses to the shear stiffness is different for the loose and dense sands. It appears that for the loose sand, the axial stress has greater influence on shear stiffness than the horizontal stress. However, the relative influence of each stress is about equal for the dense sand. This trend does not appear to be the same for the backcalculated shear modulus, where the axial stress seems to dominate more.

## 10.6 Comparison of Relationships for Sand Under Biaxial States of Stress with Previous Research

The stiffness coefficients for the moduli of washed mortar sand under biaxial loading using the two-stress model are summarized in Table 10.8. The stiffness coefficients listed in Table 10.8 have been averaged from the values of each test series for the dense and loose sand, respectively.

The stiffness coefficients for constrained modulus are similar to those of earlier research on this sand. However, a direct comparison is not possible because previous results are not typically presented using the two-stress model used in this study. A review of previous studies shows a trend for the  $n_b$  coefficient (the exponent of the principal effective stress perpendicular to the direction of wave propagation) to be very close to zero. The values for the  $n_b$  coefficient in this research bounded zero, and their slightly larger magnitude may reflect the impact of the extreme void ratios of the specimens used in this research.

A comparison of the stiffness coefficients for shear modulus from various research studies of the washed mortar sand under biaxial (and triaxial) loadings is included in Table 10.9. The stiffness coefficients for the dense sand measured in this study compare fairly well with those from earlier studies. However, the principal effective stresses appear to influence the shear modulus of the loose sand differently. For the dense sand, the influence of the axial stress is about equal to that of the

Table 10.8. Summary of Stiffness Coefficients for Tests on Washed Mortar Sand Under Biaxial Loading Using a Two-Stress Model\*\*

Modulus	C	na	nb
Dense Sand $e = 0.587$			
M	2020	0.416	0.069
E	1758	0.440	0.081
$G_b^+$	720	0.454	0.093
$G_m^{++}$	767	0.284	0.226
Loose Sand $e = 0.760$			
M	1983	0.533	-0.027
E	1609	0.538	0.014
$G_b^+$	638	0.536	0.038
$G_m^{++}$	658	0.388	0.146

\*\* Modulus =  $C \bar{\sigma}_a^{na} \bar{\sigma}_b^{nb} Pa^{1-na-nb}/F(e)$  ,  $F(e) = 0.3 + 0.7e^2$ .

+ Calculated from M and E

++ Measured in Shear Pulse Test

Table 10.9. Comparison of Stiffness Coefficients for Log  $G - \text{Log } \bar{\sigma}_c \cdot \text{Log } \bar{\sigma}_b - \text{Log } \bar{\sigma}_c$  Relationship\* from Various Research Studies Using Washed Mortar Sand

Study	Void Ratio, e	$C_G$	na	nb	nc	nm**	Range of Stress, psi	Test+
Allen & Stokoe (1982)	0.62-0.70	720	0.24	0.22	---	0.48	4 - 64	a
Knox, et al (1982)	---	---	0.24	0.18	0.02	0.40	10 - 40	b
Stokoe & Ni (1985)	0.69	721	0.22	0.22	0.00	0.44	3 - 55	a
Lee & Stokoe (1986)	0.62-0.70	---	0.20	0.20	---	0.40	10 - 40	b
Ni (1987)	0.64-0.72	687	0.22	0.23	0.02	0.44	2 - 55	a
Lee (1990)							10 - 40	b
This Research	0.59 0.76	767 658	0.28 0.39	0.23 0.15	---	0.47 0.50	8 - 32 8 - 32	c
This Research	0.59 0.76	720 638	0.45 0.54	0.09 0.04	---	0.50 0.53	8 - 32 8 - 32	d

\*  $G = C_G \bar{\sigma}_a^{na} P \bar{\sigma}_b^{nb} P \bar{\sigma}_c^{nc} P a^{1-na-nb-nc} / F(e)$

\*\*  $G = C_G \bar{\sigma}_c^{nm} P a^{1-nm} / F(e)$ ,  $F(e) = 0.3 + 0.7e^2$

+ a. Torsion Resonant Column Tests

b. Shear Pulse tests in Large Scale Triaxial Device (LSTD)

c. Shear Pulse tests in Multi-Moduli Testing Device (MTD)

d. Longitudinal Resonant Column and Axial Pulse Tests in MTD

horizontal stress. Conversely, the axial stress is definitely more dominant than the horizontal stress for loose sand.

The axial stress appears to almost solely control the shear modulus which is backcalculated from the constrained and Young's moduli. This is most likely due to the fact that the constrained and Young's moduli depend almost solely on the axial stress. This apparent difference highlights the problem of applying isotropic linear elastic assumptions to a structurally or stress-induced anisotropic medium.

#### 10.7 Summary

Five series of tests were performed to examine the effect of biaxial loading on the constrained, Young's and shear moduli of a uniform dry sand. The testing was conducted to evaluate the effect of the axial and horizontal stress on longitudinal, compression, and shear waves propagating in the axial direction of the specimen. For tests conducted with the MTD, it is assumed that: (1) the direction of wave propagation is parallel to the longitudinal axis of the specimen and consequently parallel to one of the principal stresses, and (2) the direction of particle motion is either parallel to (for compression waves), or perpendicular to (for shear waves), the axis of the specimen. It is further assumed that the major motion of a bar wave propagating longitudinally in the specimen is also parallel to the axis of the specimen.

Each biaxial test series consisted of an initial isotropic loading cycle followed by a biaxial loading cycle. The first isotropic loading cycle, which consisted of tests at 4, 16, 64, 16, and 4 psi confining pressure, was performed to remove any effects which may be attributable to stress history (as observed and discussed in Chapter 9). In the loading portion of the biaxial cycle, first the axial stress was increased while the horizontal stress was held constant, and then the horizontal stress was increased while the axial stress was held constant. In the unloading portion of the biaxial cycle, first the axial stress was decreased and the horizontal stress was held constant, and then the horizontal stress was decreased while the axial stress was held constant. Three of the test series contained one biaxial "loop" between 16 and 32 psi, and two contained two biaxial "loops", one between 8 and 16 psi and one between 16 and 32 psi. The maximum effective principal stress ratio did not exceed 2.0.

Stiffness coefficients for the constrained, Young's and shear moduli were determined using a two-stress model of the following form

$$\text{Modulus} = C \bar{\sigma}_a^{na} \bar{\sigma}_b^{nb} P a^{1-na-nb} / F(e) \quad (10.5)$$

where

$C, na$  and  $nb$  = stiffness coefficients,

$\bar{\sigma}_a$  = axial effective stress,

$\bar{\sigma}_b$  = horizontal effective stress,

$P_a$  = atmospheric pressure in same units as  $\bar{\sigma}_a$  and  $\bar{\sigma}_b$ ,  
and,

$F(e)$  = function of void ratio,  $F(e)=0.3+0.7e^2$ .

The stiffness coefficients were determined using multiple linear regression analysis and are summarized in Table 10.8. The regression analysis included only the tests which were part of the biaxial loading cycle.

The constrained modulus and Young's modulus are controlled almost solely by the axial stress. The horizontal stress appears to have slightly more influence on Young's modulus than constrained modulus. However, for practical applications this difference is negligible. The almost sole dependence of constrained modulus on the principal stress in the direction of wave propagation and particle motion agrees with that reported by others for tests on this same sand.

There is a notable difference between the stiffness coefficients for the shear modulus measured in the MTD and those reported by others, especially the coefficients for the loose sand. Earlier research on this same sand, has shown the shear modulus depends almost equally on the effective principal stresses in the direction of wave propagation and particle motion. However, the shear modulus measured by the shear pulse test in the MTD shows nearly a one to one correspondence for the dense sand and almost a three to one correspondence for the loose sand. This discrepancy may be caused by the difficulty in identifying the

arrival of the far-field shear wave, which was often obscured by waves travelling at the faster dilatational wave velocity.

The shear modulus that is backcalculated from the constrained and Young's moduli shows more impact from the axial stress than the directly measured shear modulus. This was probably due to the fact that both constrained and Young's moduli are dominated by the axial stress.

## Chapter Eleven

### Summary, Conclusions and Recommendations

#### 11.1 Summary

##### 11.1.1 Background

Research over the past three decades using seismic wave propagation testing on laboratory-sized soil specimens has focused on finding the constitutive relationships which best characterize soil. Early research showed that for small shear strains (less than about 0.001%), soil would behave as a linear, elastic continuum. Most of the early dynamic laboratory test devices were limited to testing under isotropic conditions, and as an indirect result, it was generally believed all elastic moduli (constrained, Young's, and shear) were controlled in a similar manner by the mean effective stress. Research over the past decade has shown this is not the case for constrained and shear moduli. However, until this research was conducted, no study had been made of the effect of stress state on Young's modulus.

Dynamic laboratory testing devices can be divided into two general groups: those which use pulse methods, and those which use resonant methods. The pulse devices measure stiffness by determining the time for a polarized body wave (dilatational or shear) to travel through

the material between a dynamic source and receiver. The distance, divided by the corrected travel time, yields the body wave velocity which is then used to calculate stiffness.

Resonant method devices measure stiffness by finding a characteristic resonant frequency of the material from which a wave velocity is computed by applying one-dimensional wave propagation theory. Typically, resonant devices only find the first resonant frequency, either torsional or longitudinal, and no adjustment is made for dispersion which occurs due to the three-dimensional nature of the wave propagation problem. This adjustment is normally insignificant if tests are limited to the first resonant mode where the wavelength is usually long with respect to the sample diameter.

Pulse method devices using cubical samples have the unique capability of being able to vary the three orthogonal stresses independently, allowing testing under isotropic ( $\bar{\sigma}_1 = \bar{\sigma}_2 = \bar{\sigma}_3$ ), biaxial ( $\bar{\sigma}_1 > \bar{\sigma}_2 = \bar{\sigma}_3$  or  $\bar{\sigma}_1 = \bar{\sigma}_2 > \bar{\sigma}_3$ ), or triaxial ( $\bar{\sigma}_1 > \bar{\sigma}_2 > \bar{\sigma}_3$ ) loadings. Torsional resonant devices can, with modification, apply biaxial (compression only) and triaxial loadings. However, all longitudinal resonant devices are used only under isotropic loading because of the difficulty associated making them capable of biaxial or triaxial loading.

Research over the past decade, in which pulse and resonant devices were used to study soils under biaxial and triaxial loading conditions, have shown that the elastic moduli are affected differently by the different principal stresses. That research, which was confined

primarily to dry sands, has shown that for waves propagating along principal stress directions, the constrained modulus is controlled almost solely by the principal stress in the direction of wave propagation and particle motion. It was also found the shear modulus is controlled about equally by the principal stresses in the direction of wave propagation and particle motion, and is virtually unaffected by the third principal stress. No research has been conducted to demonstrate how the state of stress influences Young's modulus of soil.

#### 11.1.2 Theoretical and Analytical Studies

A review was made of wave propagation theory for wave guides, particularly the theory for waves propagating in a solid cylindrical rod. A particular one-dimensional case was developed where one end of the sample is subjected to a longitudinal steady-state displacement and the other is capped by a rigid end mass. The resulting development showed at resonance that the problem reduced to the simpler case of vibration in a fixed-free rod. In that problem, the ratio between the sample and added masses is related to the frequency, sample length and the bar wave velocity by a simple transcendental equation.

The three-dimensional problem for steady-state longitudinal waves in an infinite rod shows that the velocity of propagation is a function of frequency, rod size, and the Poisson's ratio. The theory shows that, for the fundamental longitudinal mode, the phase (or

apparent) velocity approaches the value of the bar wave velocity as the wave number goes to zero, i.e. long wavelengths. Alternatively, as the wave number goes to infinity, i.e. short wavelengths, the phase velocity approaches the Rayleigh wave velocity.

Finally, it is possible to obtain an approximate solution using integral transforms for the case of transient waves travelling in a semi-infinite rod due to a sudden impact on the end. This solution is for the particle velocity in the vicinity of the elementary wave front. The solution suggests that there is motion preceding the elementary wave front which travel at velocities as high as the dilatational velocity. Therefore, theory shows it is possible to measure the dilatational velocity by identifying the initial wave arrival from a longitudinal pulse in a cylindrical specimen.

A finite element program, constructed with axisymmetric elements, was used to study what effect specimen parameters (such as stiffness, length, diameter, damping and Poisson's ratio) and specimen end conditions would have on the frequency response of a cylindrical specimen. The finite element program was used to model the longitudinal resonant column test. The study showed that: (1) the natural frequency of a specimen is roughly proportional to the square root of the stiffness and inversely proportional to the length, (2) the number of clearly observable resonant frequencies decreases as the diameter increases, relative to the length, (3) material damping less than five percent has little impact on the natural frequency, and (4) for a given

stiffness (E), changes in Poisson's ratio would have little effect on the natural frequency or the computed bar wave velocity.

The finite element program had the versatility to change the end conditions of the model specimen. A study of the effect of end conditions showed that: (1) the presence of an added mass significantly reduced the natural frequencies, (2) the presence of the added mass improved the accuracy of the computed bar wave velocities, (3) Young's modulus is underestimated if the base support is less than 90 percent of the diameter of the sample, and (4) the horizontal displacement condition at the ends has only a minor impact on the measurement of Young's modulus, overestimating it by one or two percent if the end is fixed rather than free.

### 11.1.3 Multi-Moduli Testing Device (MTD)

With the expressed goal of finding how the state of stress affects the Young's modulus of a dry sand, a laboratory device was designed and built which has the ability to measure the constrained, Young's, and shear modulus of a cylindrical sample without changing the state of stress on the sample. This device, called the Multi-Moduli Testing Device (MTD), uses axial pulse and shear pulse tests to determine the dilatational and shear wave velocities, respectively, and it uses a longitudinal resonant column test to determine the bar wave velocity. The MTD has the capability to perform these three tests under biaxial

loading conditions through the use of a vertical vibration isolation assembly, which can be used to apply a static axial load, in compression or extension, and still allow the top of the specimen to "vibrate" freely in the longitudinal direction.

The MTD has a pressure chamber that is 14 inches in diameter and 18 inches high in which specimens can be confined by air pressure or internal vacuum. There is a double acting air piston in the top of the cell which applies to the specimen an axial loading that is measured by a load cell. Cell and vacuum pressure are monitored by transducers and changes in sample length are measured by two proximeters mounted on opposite sides of the specimen.

The constrained modulus is determined from the dilatational wave velocity which is measured using an axial pulse test. In the axial pulse test, a piezoelectric shaker applies a step function impulse to the base of the sample, and the time domain motions of vertical accelerometers at the base and top of the specimen are recorded by a digital oscilloscope. The time between the first arrivals of the impulse at each accelerometer is adjusted for any delays, and divided into the sample length to compute the dilatational wave velocity. The error in the constrained modulus is estimated to be about two percent, with the largest contribution coming from finding the travel time.

The shear modulus is determined from the shear wave velocity which is measured using a shear pulse test. In the shear pulse test, an electromechanical tapper applies a horizontal impulse to the side of the

sample base pedestal and the time domain motions of the horizontal accelerometers are recorded by a digital oscilloscope. The time between the arrivals of the polarized motion at each accelerometer is adjusted for any delays and divided into the sample length to compute the shear wave velocity and the shear modulus. The possible error in the shear modulus determined in the MTD is as high as fifteen percent. This error is attributable to the difficulty in identifying the far-field shear wave arrival at the top accelerometers, since the arrival is obscured by the presence of wave motions travelling at faster velocities.

Young's modulus is determined from the bar wave velocity which is measured by the longitudinal resonant column test. A frequency sweep is conducted by a dynamic signal analyzer in which the piezoelectric shaker is driven at specified frequencies and the relative amplitude and phase between the top and bottom vertical accelerometers is recorded. The natural frequencies of the specimen are interpolated at  $\pm 90$  degrees of phase and the corresponding phase velocities are calculated using one-dimensional theory. The phase velocities are then adjusted to find the bar wave velocities by using the solution for the fundamental mode in three-dimensional theory for longitudinal waves in an infinite rod. The resulting values for the bar wave velocity, one for each natural frequency, typically agree within five percent.

For one example, a test on a loose sand confined isotropically at 16.0 psi, the specimen parameters determined in the MTD were used as

input for the finite element model. Transfer functions were determined using the stiffness values from each of the four resonant modes observed in the laboratory test and the bar wave velocity was computed for the natural frequencies using the same two-step reduction method used in the laboratory test. For this example, the bar wave velocities computed by the model compared very well with those measured in the laboratory.

#### 11.1.4 Tests on Sand and Other Materials

Several man-made materials and two natural soils were tested in the course of this research. The man-made materials tested included three plastics (polyurethane, polyvinylchloride and polyethylene) and Portland cement concrete. The tests on plastic afforded the opportunity to compare Young's modulus values measured in the MTD to those computed from the shear modulus measured in the torsional shear and torsional resonant column test. When adjusted for frequency and temperature dependency, the Young's modulus values usually compared within five percent. Tests were conducted on a curing sample of Portland cement concrete. The tests began approximately five hours after mixing and continued for seven days. This test illustrated the ability of the MTD to test materials over a broad range of stiffnesses and values of Poisson's ratio. A medium plasticity, compacted clay was also tested by cyclic triaxial, torsional shear, torsional resonant column and in the

MTD. The values for Young's modulus agreed well when adjustments were made for frequency, strain, and aging effects.

An uncemented, uniform dry washed mortar sand was the focus of this research. A total of seven test series were conducted on loose ( $D_r \equiv 23-29\%$ ) and dense ( $D_r \equiv 88-93\%$ ) sand specimens. Consistent sand specimens were constructed using a multiple sieve pluviator (MSP). The MSP is a column of six sieves (oriented 45 degrees to each other), topped by a funnel that has a variable size opening. The rate at which the sand is released from the funnel governs how dense the sand specimen will be, with fast rates yielding loose density specimens and slow rates yielding high density specimens.

Two test series were conducted in which a loose and a dense sand were confined isotropically at confining pressures of 4.0, 8.0, 16.0, 32.0, and 64.0 psi in several cycles of increasing and decreasing confining pressures. The stiffness of both the loose and dense sand was notably higher on the first load cycle (4.0, 8.0, 16.0, and 32.0 psi) than the first unloading and subsequent reloading cycles. This stress history dependent behavior had been noted by others in tests on the same sand and is possibly attributed to sample construction technique, particle rearrangement, seating of the top cap and base pedestal, or complex and sensitive stress conditions in the vicinity of the specimen ends.

### 11.1.5 Effect of Stress State on Elastic Moduli of Sand

The tests on the dry sand under isotropic loading showed that the constrained, Young's, and shear moduli (of the soil skeleton) could all be expressed by a constant times the mean effective stress,  $\bar{\sigma}_0$ , raised to a power. These relationships are a straight line, with the power representing the slope, when plotted log of the modulus versus log of the stress. The log M - log  $\bar{\sigma}_0$  relationship had slopes from 0.44 to 0.45, the log E - log  $\bar{\sigma}_0$  relationship had slopes from 0.49 to 0.51 and the log G - log  $\bar{\sigma}_0$  relationship had slopes from 0.47 to 0.50. It was noted that the slope for Young's modulus relationship was slightly greater than for the constrained modulus, illustrating an observed decrease in Poisson's ratio (computed from M and E) as the confining pressure increased. If one knows the Poisson's ratio, it is possible to calculate the shear modulus, assuming the sand is isotropic. These "backcalculated" values for the shear modulus were within 10-15 percent of those measured independently by the shear pulse test, with the backcalculated values slightly higher.

The log M - log  $\bar{\sigma}_0$  and log G - log  $\bar{\sigma}_0$  relationships have slopes which are slightly higher than those reported by others conducting research on the same sand. This could be due in part to the fact that the bulk of the previous tests were conducted in a large (7 feet) cubic triaxial

test device over a narrower range of confining pressures in which there may be less effect from end conditions.

Five biaxial test series were conducted in which the washed mortar sand was subjected first to a cycle of tests at isotropic confining pressures (4.0-64.0-4.0 psi). Then a biaxial cycle of tests was conducted in which first the axial stress was varied and the horizontal stress was held constant, and then the horizontal stress was varied while the axial stress was held constant. This load path was done first by increasing the respective stresses in a loading cycle and then decreasing the respective stresses in an unloading cycle.

The log modulus - log stress relationship was expressed using a two-stress model of the form

$$\text{Modulus} = C \bar{\sigma}_a^{na} \bar{\sigma}_b^{nb} P_a^{1-na-nb} / F(e) \quad (11.1)$$

where

$C, na, nb$  = stiffness coefficients,

$\bar{\sigma}_a$  = axial effective stress,

$\bar{\sigma}_b$  = horizontal effective stress,

$P_a$  = atmospheric pressure in same units as  $\bar{\sigma}_a$  and  $\bar{\sigma}_b$ ,  
and

$F(e)$  = function of void ratio  $F(e) = 0.3 + 0.7e^2$ .

The stiffness coefficients for the loose and dense sand are summarized for the isotropic and biaxial test series in Table 11.1. The constrained modulus and Young's modulus are controlled almost solely by the axial stress. The horizontal stress appears to have slightly more influence on Young's modulus than constrained modulus. The shear modulus calculated from the constrained and Young's moduli shows more impact from the axial stress than the directly measured shear modulus. This is probably due to the fact that both constrained and Young's moduli are dominated by the axial stress which is subsequently reflected in the behavior of the calculated shear modulus.

The almost sole dependence of constrained modulus on the principal stress in the direction of wave propagation and particle motion agrees with that reported by others for tests on this same sand. However, there is a notable difference between the stiffness coefficients for the shear modulus measured in the MTD and those reported by others, especially the coefficients for the loose sand. It has been shown the shear modulus depends almost equally on the effective principal stresses in the direction of wave propagation and particle motion. However, the shear modulus measured by the shear pulse test in the MTD shows a little more than one to one correspondence for the dense sand and a three to one correspondence for the loose sand. This discrepancy was most likely caused by the difficulty in identifying the arrival of the far-field shear wave, which was often obscured by waves travelling at the faster dilatational wave velocity.

Table 11.1. Summary of Stiffness Coefficients for Tests on Washed Mortar Sand.

	Isotropic Test Series*		Biaxial Test Series**		
	4 - 64 psi		8 - 32 psi		
	C	nm	C	na	nb
Dense Sand e = 0.587					
M	1968	0.445	2020	0.416	0.069
E	1721	0.486	1758	0.440	0.081
G <sub>b</sub> <sup>+</sup>	719	0.504	720	0.454	0.093
G <sub>m</sub> <sup>++</sup>	724	0.472	767	0.284	0.226
Loose Sand e = 0.760					
M	2029	0.442	1983	0.533	-0.027
E	1606	0.510	1609	0.538	0.014
G <sub>b</sub> <sup>+</sup>	635	0.533	638	0.536	0.038
G <sub>m</sub> <sup>++</sup>	635	0.504	658	0.388	0.146

\* Modulus =  $C \bar{\sigma}_0^{nm} Pa^{1-na}/F(e)$ ,  $F(e) = 0.3 + 0.7e^2$

\*\* Modulus =  $C \bar{\sigma}_a^{na} \bar{\sigma}_a^{nb} Pa^{1-na-nb}/F(e)$ ,  $F(e) = 0.3 + 0.7e^2$

+ Calculated from M and E

++ Measured in Shear Pulse Test

## 11.2 Conclusions

The following conclusions can be made as a result of this research.

1. The solution for one-dimensional motion in a finite rod subjected to steady-state longitudinal motion at one end and having a rigid mass at the other is, at resonance, identical to that of a fixed-free rod with an added mass. This makes it possible to compute the bar wave velocity based on the assumption of one-dimensional longitudinal motion in the specimen.

2. The solution for longitudinal waves in an infinite cylindrical rod shows that the phase velocity is a function of frequency (wave number), rod radius, and Poisson's ratio. For the fundamental mode, the phase velocity approaches the bar wave velocity for long wavelengths and the Rayleigh wave velocity at short wavelengths (with respect to bar radius).

3. An approximate solution for transient wave propagation in a semi-infinite bar caused by a sudden impact at the end suggests that some wave motion will travel at velocities approaching the dilatational wave velocity. Therefore, it is possible to identify the first arrival of a pulse travelling longitudinally in a cylindrical specimen as that which corresponds to the dilatational wave.

4. A finite element model, constructed with axisymmetric finite elements is a valuable tool to study the steady-state behavior of a typical laboratory-sized soil sample. Employed as such a tool, the finite element

model leads to the following conclusions about the effect of different specimen parameters and end conditions on the response at the top of the specimen due to longitudinal excitation at the base:

- a. The natural frequencies are roughly proportional to the square root of Young's modulus of the material specimen.
- b. The natural frequencies are inversely proportional to the length.
- c. The number of clearly observable natural frequencies decreases with increasing diameter (length staying the same).
- d. Changes in damping (hysteretic) within a range from 0.5% to 5.0% will not significantly affect the observed natural frequencies.
- e. For a constant Young's modulus, changes in Poisson's ratio have only a minor effect on the observed natural frequencies.
- f. The presence of a rigid mass reduces the natural frequency of the specimen and increases the respective wavelength.
- g. Estimations of the bar wave velocity appear to be significantly improved by the presence of the added mass.
- h. Young's modulus will be significantly underestimated if the base pedestal diameter is less than 90 percent of the sample diameter.
- i. The difference in bar wave velocities for end conditions ranging from a free to fixed horizontal displacement conditions is two percent or less. The fixed condition results in slightly higher velocities.

5. It is feasible to construct a test device which can measure three small-strain moduli independently without changing the stress state or end conditions of the sample.

6. It is feasible to measure multiple longitudinal natural frequencies in a specimen using a piezoelectric vibration generator and accelerometers mounted along the centerline at each end of a soil specimen.

7. It is possible to calculate the theoretical bar wave velocity from any of the first three natural frequencies using a two-step reduction method which first determines the phase velocity using one-dimensional theory. The second step computes the bar wave velocity from the phase velocity based on the frequency spectrum of the fundamental mode found from three-dimensional theory. This adjusts for the dispersion in the phase velocity for waves travelling in cylindrical rods as predicted by theory and observed in the laboratory testing.

8. Tests on plastics and compacted clay show the values for Young's modulus measured in the Multi-Moduli Test Device (MTD) compare within five percent to those measured, or derived from, cyclic triaxial, torsional shear, and torsional resonant column tests.

9. The MTD can measure the elastic moduli of a broad range of civil engineering materials including soils, asphalt concrete, and Portland cement concrete.

10. The dilatational wave velocity can be measured by exciting the entire base axially with a step function pulse and observing the first

arrival at the top accelerometer. For the instrumentation used in this study, the resulting constrained modulus has a measurement error on the order of two percent or less.

11. Tests on dry, uncemented sand, subjected to isotropic and biaxial stress conditions showed that when confined isotropically, all three moduli (M, E and G) could be adequately described by a relationship involving a constant times the mean effective stress raised to a power ranging between 0.44 and 0.50. A summary of the average stiffness coefficients for the dense and loose sands is included in Table 11.1.

12. Poisson's ratio of the sand decreases as confining pressure increases for tests under isotropic loading.

13. Stress history has an impact on the stiffness of the sand for initial loading conditions at confining pressures below 32 psi.

14. When the sand was subjected to biaxial compression or extension, it was shown that the effective principal stresses influenced each modulus differently. It was found that:

a. For M, the principal stress in the direction of wave propagation almost solely controls the modulus.

b. For E, the principal stress in the direction of wave propagation dominates the modulus. However, the principal stresses perpendicular to the direction of wave propagation have marginally more influence on the Young's modulus than the constrained modulus.

c. For  $G$ , both principal effective stresses influence the shear modulus. However, this study shows the influence of the stress in the direction of wave propagation could be more influential than the stresses perpendicular to the direction of wave propagation. This is contrary to research by others on this same sand, which showed the shear modulus was about equally influenced by the principal effective stresses in the plane containing the direction of wave propagation and the direction of particle motion. This difference could be due to the fact that the MTD can only load the specimen biaxially and this will require further study.

15. The shear wave tapper used for the shear pulse test is not an adequate source to generate the clean, polarized shear waves necessary to identify a shear wave arrival in the size of sample used in the MTD.

### 11.3 Recommendations for Future Research

The following recommendations are broken into three general groups: (1) changes to the MTD, (2) theoretical development and analytical studies using the finite element program, and (3) studies of soils and other civil engineering materials using the MTD.

1. Changes to the MTD. The MTD continuously evolved as this research progressed. It was not possible to incorporate the following

specific modifications within the time allowed for this research. However, they are recommended because the modifications should improve the accuracy of the results measured and extend the capabilities of the MTD.

a. The axial and shear pulse tests and the longitudinal resonant column tests should be automated. The ability to set and run automatically will reduce the work load on the operator, reduce the possibility of error and increase the speed of testing.

b. Replace the current load cell with a static piezoelectric load cell. This will allow taller samples in the cell and eliminate a cumbersome sensor cable.

c. Install case-isolated feed-throughs for sensor leads in the cell casing, versus their current location in the top plate. This will greatly simplify the set-up process.

d. Use proximeters to measure changes in diameter. This will reduce the error introduced by assumptions made to compute volume change.

e. Modify the sample top cap to install an accelerometer flush with the top of the sample like the one that is currently installed in the base.

f. Design a new shear wave source. The current tapping device generates both dilatational and shear waves in the sample. Consider the use of piezoelectric crystals mounted in the base pedestal.

g. Improve the top cap vibration isolation assembly.

h. Modify the base plate to allow testing of saturated samples.

- i. Modify the sample base pedestal to allow tests where only a point on the central axis is excited.

2. Theoretical and Analytical Studies. Two avenues are available to further investigate the theory as it was applied in this research.

- a. Develop a closed-form solution for a solid cylindrical rod subjected to a steady-state longitudinal displacement at one end and having a rigid mass at the other. Investigate ways to apply that solution to reducing laboratory data.

- b. Study the impact of specimen parameters on the arrival of the dilatational wave.

- c. Develop a reduction method which optimizes use of the multiple natural frequencies measured by the longitudinal resonant column test to find the bar wave velocity and damping in the specimen.

- d. Study the distribution of strain in a model specimen resonating at its natural frequencies.

3. Studies of Soils and other Civil Engineering Materials. This research demonstrated the ability of the MTD to measure the elastic moduli of civil engineering materials with a broad range of stiffness properties. Potential studies in the MTD may include:

- a. Development of damping measurements in the MTD. As currently configured, the MTD has the possibility of performing three independent damping measurements by using: (1) the logarithmic

decrement (of a free vibration curve), (2) the half-power bandwidth method, and (3) the difference between the resonant and natural frequencies of each mode.

b. Further studies on the behavior of sand under anisotropic states of stress should be conducted including:

(1) more tests to study the effect of stress state on Young's modulus,

(2) more tests at different void ratios (densities), and

(3) tests to study the effect of stress path on Young's and other elastic moduli.

c. Further studies of the effect of axial strain level on the stiffness of sand under isotropic and biaxial stress states.

d. Tests on other soils such as clays, silts, and gravels. Also tests on saturated soils.

**Appendix A**  
**Theoretical Solution of Elasticity for an Isotropic Material**

### A.1 Elastic Solution for Isotropic Materials

In its most general form the relationship between the components of the stress tensor,  $\tau_{ij}$ , and the components of the strain tensor,  $\epsilon_{kl}$  is given by

$$\tau_{ij} = C_{ijkl} \epsilon_{kl} \quad (\text{A.1})$$

where

$$C_{ijkl} = C_{jikl} = C_{klij} = C_{ijlk} \quad (\text{A.2})$$

and  $C_{ijkl}$  is a tensor having 81 separate components. Equation A.1 is recognized as the generalized Hooke's law. Here  $i, j, k$  and  $l$  represent commonly used index notation and can each take values of 1, 2 or 3 in correspondence to the three reference directions in Cartesian coordinates. Equation A.2 actually limits  $C_{ijkl}$  to 21 independent components. This reduction occurs by imposing the assumptions the material is homogeneous ( $C_{ijkl}$  is independent of location) and that the material behaves linearly elastically ( $C_{ijkl}$  is constant). Finally, by recognizing the symmetry of the stress and strain tensors, and recognizing the existence of a linear strain energy density function, we arrive at the 21 independent constants which represent a fully anisotropic material. If a material is elastically isotropic, it is assumed there are no preferred directions and the elastic constants are the same whatever the

orientation of the Cartesian coordinate system in which  $\tau_{ij}$  and  $\epsilon_{ij}$  are evaluated. This implies that the constants  $C_{ijkl}$  can be expressed as

$$C_{ijkl} = \lambda \delta_{ij} \delta_{kl} + \mu (\delta_{ik} \delta_{jl} + \delta_{il} \delta_{jk}) \quad (\text{A.3})$$

where  $\delta_{ij}$  is the special tensor known as the Kronecker delta, which is equal to 1 when  $i = j$  and equal to 0 when  $i \neq j$ , and  $\lambda$  and  $\mu$  are Lamé's constants. Hooke's generalized law then assumes the well-known form

$$\tau_{ij} = \lambda \epsilon_{kk} \delta_{ij} + 2\mu \epsilon_{ij} \quad (\text{A.4})$$

Now consider two cases;  $i \neq j$  and  $i = j$ . If  $i \neq j$ , a state of pure shear exists and

$$\tau_{ij} = 2\mu \epsilon_{ij} \quad (\text{A.5a})$$

or alternatively

$$\tau_{ij} = G \gamma_{ij} \quad (\text{A.5b})$$

where  $\mu = G$  and is known as the shear modulus.

If  $i = j$ , Eq. A.4 becomes

$$\tau_{ii} = 3\lambda \epsilon_{ii} + 2\mu \epsilon_{ii} \quad (\text{A.6a})$$

or

$$\tau_{ii} = (3\lambda + 2\mu) \varepsilon_{ii} \quad (\text{A.6b})$$

and if we perform the implied summation letting  $\tau_{11} = \tau_{22} = \tau_{33} = -p$ , a state of hydrostatic compression occurs and

$$p = -\left(\frac{3\lambda + 2\mu}{3}\right) \varepsilon_{ii} \quad (\text{A.6c})$$

Here

$$B = \lambda + \frac{2}{3}\mu > 0 \quad (\text{A.7})$$

where B is known as the modulus of compression or the bulk modulus.

Another special state of stress assumes all strains except  $\varepsilon_{11}$  equal zero. In this case, Eq. A.4 becomes

$$\tau_{11} = \lambda \varepsilon_{11} + 2\mu \varepsilon_{11} = (\lambda + 2\mu) \varepsilon_{11} \quad (\text{A.8})$$

Here

$$M = (\lambda + 2\mu) \varepsilon_{11} \quad (\text{A.9})$$

where M is known as the constrained modulus.

One final special stress state warrants discussion. If the strain tensor is written in terms of the stress tensor by substituting Eq. A.6b in Eq. A.4, it results in

$$\epsilon_{ij} = \frac{1}{2\mu} \tau_{ij} - \frac{\lambda \delta_{ij}}{2\mu(3\lambda+2\mu)} \tau_{kk} \quad (\text{A.10})$$

If  $\tau_{ij} \neq 0$ , and all other  $\tau_{ij} = 0$ , a case of pure tension exists. Equation A.10 yields

$$\epsilon_{11} = \frac{\lambda + \mu}{\mu(3\lambda+2\mu)} \tau_{11} = \frac{1}{E} \tau_{11} \quad (\text{A.11a})$$

$$\epsilon_{22} = \epsilon_{33} = \frac{-\lambda}{2\mu(3\lambda+2\mu)} \tau_{11} \quad (\text{A.11b})$$

and substituting Eq. A.11b into Eq. A.11a

$$\epsilon_{22} = \epsilon_{33} = \frac{-\lambda}{2(\lambda+\mu)} \epsilon_{11} \quad (\text{A.11c})$$

Equations A.11a and A.11c yield the constants known as Young's modulus and Poisson's ratio:

$$E = \frac{\mu(3\lambda+2\mu)}{\lambda+\mu} \quad (\text{A.12})$$

$$\nu = \frac{-\epsilon_{22}}{\epsilon_{11}} = \frac{\lambda}{2(\lambda+\mu)} \quad (\text{A.13})$$

The fundamental point to note is that a homogeneous isotropic linear elastic material can be completely characterized by two elastic constants. Table 3.1 relates common constants for an isotropic linear elastic material.

## A.2 Elastic Solution in Cylindrical Coordinates

Whereas Eq. A.4 is frequently presented in terms of Cartesian coordinates, using  $x$ ,  $y$ , and  $z$  to represent the orthogonal coordinate directions and  $u$ ,  $v$ , and  $w$ , the respective displacements in those directions, it is often convenient to represent the three-dimensional problem using cylindrical coordinates. In this case the coordinate directions are denoted by (see Fig. 3.1)  $r$ ,  $\theta$ , and  $z$ . Denoting the displacements in the coordinate directions as  $u$ ,  $v$ , and  $w$ , respectively, the strain-displacement relationships are given by

$$\epsilon_r = \frac{\partial u}{\partial r}, \quad \epsilon_\theta = \frac{u}{r} + \frac{1}{r} \frac{\partial v}{\partial \theta}, \quad \epsilon_z = \frac{\partial w}{\partial z} \quad (\text{A.14 a,b,c})$$

$$2\epsilon_{r\theta} = 2\epsilon_{\theta r} = \frac{\partial v}{\partial r} - \frac{v}{r} + \frac{1}{r} \frac{\partial u}{\partial \theta} \quad (\text{A.15})$$

$$2\varepsilon_{\theta z} = 2\varepsilon_{z\theta} = \frac{1}{r} \frac{\partial w}{\partial \theta} + \frac{\partial v}{\partial z} \quad (\text{A.16})$$

$$2\varepsilon_{rz} = 2\varepsilon_{zr} = \frac{\partial u}{\partial z} + \frac{\partial w}{\partial r} \quad (\text{A.17})$$

and the stress-strain relations following from Eq. A.4 are of the form

$$\tau_r = \lambda \Delta + 2\mu \frac{\partial u}{\partial r} \quad (\text{A.18})$$

$$\tau_{\theta} = \lambda \Delta + 2\mu \left( \frac{u}{r} + \frac{1}{r} \frac{\partial v}{\partial \theta} \right) \quad (\text{A.19})$$

$$\tau_z = \lambda \Delta + 2\mu \frac{\partial w}{\partial z} \quad (\text{A.20})$$

$$\tau_{r\theta} = \mu \left[ \frac{\partial v}{\partial r} - \frac{v}{r} + \frac{1}{r} \frac{\partial u}{\partial \theta} \right] \quad (\text{A.21})$$

$$\tau_{\theta z} = \mu \left[ \frac{1}{r} \frac{\partial w}{\partial \theta} + \frac{\partial v}{\partial z} \right] \quad (\text{A.22})$$

$$\tau_{rz} = \mu \left[ \frac{\partial u}{\partial z} + \frac{\partial w}{\partial r} \right] \quad (\text{A.23})$$

where,  $\Delta$ , the dilatation is defined as

$$\Delta = \frac{\partial u}{\partial r} + \frac{u}{r} + \frac{1}{r} \frac{\partial v}{\partial \theta} + \frac{\partial w}{\partial z} \quad (\text{A.24})$$

**Appendix B**  
**Theoretical Solution for Waves Propagating in a Cylindrical**  
**Elastic Rod**

### B.1 Equations of Motion for a Linearly Elastic Body

Derivation of the equations of motion in a continuous media begins with the principle of balance of linear momentum. That principle states that the instantaneous change of the linear momentum of a body is equal to the resultant external force acting on the body at the particular instant of time. Mathematically this can be stated as

$$\int_S \mathbf{t} \, dS + \int_V \rho \mathbf{f} \, dV = \int_V \rho \ddot{\mathbf{u}} \, dV \quad (\text{B.1})$$

where  $V$  represents an arbitrary contiguous volume enclosed by the surface  $S$ . Here  $\mathbf{t}$  is the distribution of surface tractions on  $S$ ,  $\mathbf{f}$  is the distribution of body forces acting on  $V$  and  $\ddot{\mathbf{u}}$  is the distribution of the acceleration in  $V$ .

The Cauchy stress formula relates the stress tensor,  $\tau$ , to the surface tractions by

$$\mathbf{t} = \tau \mathbf{n} \quad (\text{B.2})$$

where  $\mathbf{n}$  is the unit normal vector to the surface  $S$ . Substituting Eq. B.2 in Eq. B.1 and writing in indicial notation, the balance of linear momentum can be written as

$$\int_S \tau_{ij} n_i dS + \int_V \rho f_j dV = \int_V \rho \ddot{u}_j dV \quad (\text{B.3})$$

Transforming the surface integral into a volume integral using Gauss' theorem which states

$$\int_V \tau_{ij,i} dV = \int_S \tau_{ij} n_i dS \quad (\text{B.4})$$

This Eq. B.3 becomes

$$\int_V (\tau_{ij,i} + \rho f_j - \rho \ddot{u}_j) dV = 0 \quad (\text{B.5})$$

which for a continuous volume yields Cauchy's first law of motion

$$\tau_{ij,i} + \rho f_j = \rho \ddot{u}_j \quad (\text{B.6})$$

The problem statement for the motion of a homogeneous isotropic, linear elastic body consists of the stress equations of motion (Eq. B.6), Hooke's generalized equation relating stresses and strains (Eq. A.4) and the strain-displacement equations, given by

$$\epsilon_{ij} = \frac{1}{2} (u_{i,j} + u_{j,i}) \quad (\text{B.7})$$

Equation B.7 invokes the common assumption of "small" strains associated with linear elastic theory. If Eq. B.7 is substituted into Eq. A.4, which is then substituted into Eq. B.6, it yields the displacement equations of motion

$$\mu u_{i,jj} + (\lambda + \mu) u_{j,ji} + \rho f_i = \rho \ddot{u}_j \quad (\text{B.8})$$

## B.2 The Equations of Motion Expressed in Displacement Potentials

The displacement equations of motion as written in Eq. B.8 are difficult to deal with because they couple the three displacement components. It is a common practice to express the components of the displacement vector in terms of the derivatives of potentials which themselves satisfy uncoupled wave equations.

The displacement equations of motion in the absence of body forces, can be written in vector notation as

$$\mu \nabla^2 \mathbf{u} + (\lambda + \mu) \nabla \nabla \cdot \mathbf{u} = \rho \ddot{\mathbf{u}} \quad (\text{B.9})$$

If we decompose the displacement vector into the sum of a scalar,  $\phi$ , and a vector,  $\psi$ , potential such that

$$\mathbf{u} = \nabla\phi + \nabla \wedge \psi \quad (\text{B.10})$$

and substitute Eq. B.10 into Eq. B.9, it yields

$$\begin{aligned} \mu \nabla^2 [\nabla\phi + \nabla \wedge \psi] + (\lambda + \mu) \nabla \nabla \cdot [\nabla\phi + \nabla \wedge \psi] \\ = \rho \frac{\partial^2}{\partial t^2} [\nabla\ddot{\phi} + \nabla \wedge \ddot{\psi}] \end{aligned} \quad (\text{B.11})$$

Noting that  $\nabla \nabla \cdot \phi = \nabla^2 \phi$  and  $\nabla \cdot \nabla \wedge \psi = 0$ , we obtain after rearranging Eq. B.11

$$\nabla [(\lambda + 2\mu) \nabla^2 \phi - \rho \ddot{\phi}] + \nabla \wedge [\mu \nabla^2 \psi - \rho \ddot{\psi}] = 0 \quad (\text{B.12})$$

By inspection, for Eq. B.12 to be true, the terms in brackets must each equal zero and with rearranging yields

$$\nabla^2 \phi = \frac{\rho}{\lambda + 2\mu} \ddot{\phi} = \frac{1}{C_L^2} \ddot{\phi} \quad (\text{B.13})$$

$$\nabla^2 \psi = \frac{\rho}{\mu} \ddot{\psi} = \frac{1}{C_T^2} \ddot{\psi} \quad (\text{B.14})$$

where

$$C_L^2 = \frac{\lambda + 2\mu}{\rho} \quad \text{and} \quad C_T^2 = \frac{\mu}{\rho} \quad (\text{B.15a,b})$$

Equations B.13 and B.14 are uncoupled equations of motion in  $\phi$  and  $\psi$ . The scalar potential and the three components of the vector potential are generally coupled through the boundary conditions of any particular problem. However, if the boundary conditions can be adequately described in terms of the potential functions then a unique solution can be found. It should be noted that  $\phi$  and  $\psi$  together contain four functions which are related by Eq. B.10 to the three displacement functions. This implies an additional constraint condition is required and usually, but not always, the components of  $\psi$  are related by

$$\nabla \cdot \psi = 0 \quad (\text{B.16})$$

### B.3 The Problem Statement for Waves in a Rod of Circular Cross Section

In cylindrical coordinates the relation between the displacements  $u$ ,  $v$ , and  $w$  in the  $r$ ,  $\theta$ , and  $z$  directions follow from Eq. B.10 as

$$u = \frac{\partial \phi}{\partial r} + \frac{1}{r} \frac{\partial \psi_z}{\partial \theta} - \frac{\partial \psi_\theta}{\partial z} \quad (\text{B.17})$$

$$v = \frac{1}{r} \frac{\partial \phi}{\partial \theta} + \frac{\partial \psi_r}{\partial z} - \frac{\partial \psi_z}{\partial r} \quad (\text{B.18})$$

$$w = \frac{\partial \phi}{\partial z} + \frac{1}{r} \frac{\partial (\psi_\theta r)}{\partial r} - \frac{1}{r} \frac{\partial \psi_r}{\partial \theta} \quad (\text{B.19})$$

The four equations of motion in terms of the displacement potential are

$$\nabla^2 \phi = \frac{1}{C_L^2} \frac{\partial^2 \phi}{\partial t^2} \quad (\text{B.20})$$

$$\nabla^2 \psi_r - \frac{\psi_r}{r^2} - \frac{2}{r^2} \frac{\partial \psi_\theta}{\partial \theta} = \frac{1}{C_T^2} \frac{\partial^2 \psi_r}{\partial t^2} \quad (\text{B.21})$$

$$\nabla^2 \psi_\theta - \frac{\psi_\theta}{r^2} - \frac{2}{r^2} \frac{\partial \psi_r}{\partial \theta} = \frac{1}{C_T^2} \frac{\partial^2 \psi_\theta}{\partial t^2} \quad (\text{B.22})$$

$$\nabla^2 \psi_z = \frac{1}{C_T^2} \frac{\partial^2 \psi_z}{\partial t^2} \quad (\text{B.23})$$

Note two equations, Eq. B.20 and Eq. B.23 are uncoupled. The components of the vector potential must also satisfy a constraint condition such as that given by Eq. B.16.

The displacement equations of motion written in terms of the displacements  $u$ ,  $v$ , and  $w$  are

$$\nabla^2 u - \frac{u}{r^2} - \frac{2}{r^2} \frac{\partial v}{\partial \theta} + \frac{1}{1-2\nu} \frac{\partial \Delta}{\partial r} = \frac{1}{C_T^2} \frac{\partial^2 u}{\partial t^2} \quad (\text{B.24})$$

$$\nabla^2 v - \frac{v}{r^2} - \frac{2}{r^2} \frac{\partial u}{\partial \theta} + \frac{1}{1-2\nu} \frac{1}{r} \frac{\partial \Delta}{\partial \theta} = \frac{1}{C_T^2} \frac{\partial^2 v}{\partial t^2} \quad (\text{B.25})$$

$$\nabla^2 w - \frac{1}{1-2\nu} \frac{\partial \Delta}{\partial r} = \frac{1}{C_T^2} \frac{\partial^2 w}{\partial t^2} \quad (\text{B.26})$$

where  $\nabla^2$  is the Laplacian and is defined by

$$\nabla^2 = \frac{\partial^2}{\partial r^2} + \frac{1}{r} \frac{\partial}{\partial r} + \frac{1}{r^2} \frac{\partial^2}{\partial \theta^2} + \frac{\partial^2}{\partial z^2} \quad (\text{B.27})$$

and the dilatation,  $\Delta$ , is as defined in Eq. A.24 and Poisson's ratio,  $\nu$ , is defined in Eq. A.13.

The pertinent stress-strain relations are

$$\tau_r = \lambda \Delta + 2\mu \frac{\partial u}{\partial r} \quad (\text{B.28})$$

$$\tau_{r\theta} = \mu \left[ \frac{\partial v}{\partial r} - \frac{v}{r} + \frac{1}{r} \frac{\partial u}{\partial \theta} \right] \quad (\text{B.29})$$

$$\tau_{rz} = \mu \left[ \frac{\partial u}{\partial z} + \frac{\partial w}{\partial r} \right] \quad (\text{B.30})$$

#### B.4 General Solution for Time-Harmonic Motion in a Long Cylindrical Rod with Solid Cross Section

For the case of an infinitely long cylinder of solid cross section and radius  $a$ , the boundary conditions at  $r = a$  are

$$\tau_r = 0, \quad \tau_{r\theta} = 0, \quad \tau_{rz} = 0 \quad (\text{B.31a,b,c})$$

provided no surface tractions exist.

Considering the scalar potential  $\varphi(r, \theta, z, t)$  and a wave propagating in the positive  $z$  direction is of the form

$$\varphi = \Phi(r)\Theta(\theta)e^{-i(kz - \omega t)} \quad (\text{B.32})$$

which presumes a separation of variables type solution in  $r$  and  $\theta$ . Substituting this function for  $\varphi$  into Eq. B.20 and rearranging yields

separate second order differential equations for the functions of  $\Phi$  and  $\Theta$ . The solutions for  $\Theta(\theta)$  are sines and cosines of the argument  $n\theta$  where  $n$  can only be zero or an integer. The solutions of  $\Phi(r)$  are ordinary Bessel functions which by necessity are only of the first kind because of the solid cross section (the displacement at  $r = 0$  must be finite). The solution for  $\varphi$  then is of the form

$$\varphi = [A_1 \cos(n\theta) + A_2 \sin(n\theta)] J_n(pr) e^{-i(kz - \omega t)} \quad (\text{B.33})$$

where  $J_n$  are Bessel functions of the first kind and order  $n$ ,  $A_1$  and  $A_2$  are constants and  $p$  is defined by

$$p^2 = \frac{\omega^2}{C_L^2} - k^2 \quad (\text{B.34})$$

A similar treatment of the other uncoupled wave equation given by Eq. B.23 yields a solution for  $\psi_z$  of the form

$$\psi_z = [B_1 \cos(n\theta) + B_2 \sin(n\theta)] J_n(qr) e^{-i(kz - \omega t)} \quad (\text{B.35})$$

where  $q$  is defined by

$$q^2 = \frac{\omega^2}{C_T^2} - k^2 \quad (\text{B.36})$$

The solutions for  $\psi_r$  and  $\psi_\theta$  are necessarily difficult because they are coupled by Eqs. B.21 and B.22. On further investigation it becomes evident  $\psi_r$  and  $\psi_\theta$  also contain trigonometric expressions of  $\theta$ . However, it is noted that a sine-dependence on  $\theta$  of one potential is consistent with a cosine dependence on  $\theta$  of the other. The converse can also be true.

Substituting functions for one possible pair having the form

$$\psi_r = \Psi_r(r)\sin(n\theta) e^{-i(kz-\omega t)} \quad (\text{B.37})$$

$$\psi_\theta = \Psi_\theta(r)\cos(n\theta) e^{-i(kz-\omega t)} \quad (\text{B.38})$$

into Eqs. B.21 and B.22 and imposing the constraint condition,  $\Psi_r = -\Psi_\theta$  (as opposed to that represented by Eq. B.16), yields

$$\psi_r = C_2 J_{n+1}(qr)\sin(n\theta) e^{-i(kz-\omega t)} \quad (\text{B.39})$$

$$\psi_\theta = -C_2 J_{n+1}(qr)\cos(n\theta) e^{-i(kz-\omega t)} \quad (\text{B.40})$$

If the following pair of equations derived from Eq. B.33 and Eq. B.35

$$\varphi = A_1 J_n(pr)\cos(n\theta) e^{-i(kz-\omega t)} \quad (\text{B.41})$$

$$\psi_z = B_2 J_n(qr)\sin(n\theta) e^{-i(kz-\omega t)} \quad (\text{B.42})$$

are considered together with Eqs. B.39 and B.40, the general motion in the cylindrical rod is completely defined. These four equations can be used to express the stresses in terms of the potentials. By applying the boundary conditions of Eq. B.31a,b&c, three homogeneous equations can be obtained to determine the values of the constants  $A_1$ ,  $B_2$ , and  $C_2$ . The requirement that the determinant of coefficients vanishes provides a complicated frequency equation which relates  $\omega$ ,  $n$ , and  $k$ . It is noted that an alternate set of equations similar to Eqs. B.39 - B.42 can be chosen merely by exchanging the sine and cosine functions of  $n\theta$ .

It is further noted that the analysis for a hollow cylindrical rod can be accomplished in the same manner. However, now the solutions containing the Bessel functions must retain Bessel functions of the second kind. The corresponding expressions for the potentials now contain six arbitrary constants which can be solved for if the stresses on the inner wall vanish as well, thus yielding six homogeneous equations. The frequency equation is then obtained from the requirement that the determinant of the coefficients vanishes.

**Appendix C**  
**Theoretical Solution for a Transient Wave Propagating in a**  
**Semi-infinite Solid Cylindrical Rod**

C.1 Theoretical Solution for a Transient Wave  
Propagating in a Semi-infinite Solid Cylindrical  
Rod

The simplest solution for transient waves in a rod assumes a one-dimensional state of stress and the applicable equation of motion (Eq. B.26), derived in Appendix B, is

$$\frac{\partial^2 w}{\partial z^2} = \frac{1}{C_B^2} \frac{\partial^2 w}{\partial t^2} \quad (\text{C.1})$$

where  $w$  is the displacement parallel to the longitudinal axis of the rod and  $C_B$  is the theoretical bar wave velocity defined by Eq. 3.12. This wave equation predicts that a pulse will not change shape as it propagates along a rod. However, if the pulse is applied rapidly, the resulting waveform shows dispersion as it travels along the rod.

Casting the problem in terms of the displacement potentials following the manner of Achenbach (1973) the pertinent expressions relating the displacements to the potentials for the axisymmetric case ( $v = \frac{\partial}{\partial \theta} = 0$ ) from Eqs. B.20 - B.23

$$u(r,z,t) = \frac{\partial \phi}{\partial r} - \frac{\partial \psi}{\partial z} \quad (\text{C.2})$$

$$w(r,z,t) = \frac{\partial \varphi}{\partial z} + \frac{1}{r} \frac{\partial(r\psi)}{\partial r} \quad (\text{C.3})$$

where the single remaining component of the vector potential  $\psi_\theta$  is now denoted by  $\psi$ . Only two of the four equations of motion remain. These are

$$\nabla^2 \varphi = \frac{1}{C_L^2} \frac{\partial^2 \varphi}{\partial t^2} \quad (\text{C.4})$$

$$\nabla^2 \psi - \frac{\psi}{r^2} = \frac{1}{C_T^2} \frac{\partial^2 \psi}{\partial t^2} \quad (\text{C.5})$$

and the Laplacian is now defined by

$$\nabla^2 = \frac{\partial^2}{\partial r^2} + \frac{1}{r} \frac{\partial}{\partial r} + \frac{\partial^2}{\partial z^2} \quad (\text{C.6})$$

The pertinent components of the stress tensor in terms of the potentials follow from Eqs. B.28-B.30 and Eq. C.2 and Eq. C.3. These are

$$\tau_r = \lambda \nabla^2 \varphi + 2\mu \frac{\partial}{\partial r} \left[ \frac{\partial \varphi}{\partial r} - \frac{\partial \psi}{\partial z} \right] \quad (\text{C.7})$$

$$\tau_z = \lambda \nabla^2 \varphi + 2\mu \frac{\partial}{\partial z} \left[ \frac{\partial \varphi}{\partial z} + \frac{1}{r} \frac{\partial(r\psi)}{\partial r} \right] \quad (\text{C.8})$$

$$\tau_{rz} = \mu \left[ \frac{\partial}{\partial z} \left( \frac{\partial \phi}{\partial r} - \frac{\partial \psi}{\partial z} \right) + \frac{\partial}{\partial r} \left( \frac{\partial \phi}{\partial z} + \frac{1}{r} \frac{\partial (r\psi)}{\partial r} \right) \right] \quad (\text{C.9})$$

Solutions to these equations must satisfy the boundary conditions at the end of the rod, at the lateral surface and at a point an infinite distance along the rod. Summarizing these we have

$$\text{for } 0 \leq r \leq a \quad \tau_z(r,0,t) = -PH(t) \quad (\text{C.10a})$$

$$\text{for } 0 \leq r \leq a \quad u(r,0,t) = 0 \quad (\text{C.10b})$$

$$\text{for } z \geq 0 \quad \tau_r(a,z,t) = 0 \quad (\text{C.10c})$$

$$\text{for } z \geq 0 \quad \tau_{rz}(a,z,t) = 0 \quad (\text{C.10d})$$

$$\text{for } 0 \leq r \leq a \quad u(r,\infty,t) = 0 \quad (\text{C.10e})$$

$$\text{for } 0 \leq r \leq a \quad w(r,\infty,t) = 0 \quad (\text{C.10f})$$

As the rod is at rest at time  $t = 0$ , the initial conditions are

$$u = w = \dot{u} = \dot{w} = \tau_r = \tau_z = \tau_{rz} = 0 \quad (\text{C.11})$$

Substitution of the displacement and stress tensor equations into the boundary conditions given by Eqs. C.10a and C.10b and the stress tensor for  $\tau_z$  in Eq. C.8 and recognizing that  $\phi$  also satisfies the equation of motion in Eq. C.4, it is possible to write the boundary conditions at  $z = 0$  in terms of the potentials  $\phi$  and  $\psi$ . Doing so then,

$$\text{at } z = 0, \text{ for } 0 \leq r \leq a \quad \rho \ddot{\phi} = -PH(t) \quad (\text{C.12})$$

$$\text{at } z = 0, \text{ for } 0 \leq r \leq a \quad \frac{\partial \psi}{\partial z} = 0 \quad (\text{C.13})$$

Integral transforms are a common method of solution used in these types of wave propagation problems. For this problem, Fourier sine and cosine transforms are used with respect to  $z$  and a one-sided Laplace transform is used with respect to  $t$ . The appropriate transform pairs are defined for  $0 \leq z \leq \infty$  and  $0 \leq t \leq \infty$  as:

$$\text{sine transform; } f^s(\xi) = \int_0^{\infty} f(x) \sin \xi x dx \quad (\text{C.14a})$$

$$f(x) = \frac{2}{\pi} \int_0^{\infty} f^s(\xi) \sin \xi x d\xi \quad (\text{C.14b})$$

$$\text{cosine transform; } f^c(\xi) = \int_0^{\infty} f(x) \cos \xi x dx \quad (\text{C.15a})$$

$$f(x) = \frac{2}{\pi} \int_0^{\infty} f^c(\xi) \sin \xi x d\xi \quad (\text{C.15b})$$

$$\text{Laplace transform; } \bar{f}(p) = \int_0^{\infty} f(t) e^{-pt} dt \quad (\text{C.16a})$$

$$f(t) = \frac{1}{2\pi i} \int_{\gamma-i\infty}^{\gamma+i\infty} \bar{f}(p) e^{pt} dp \quad (\text{C.16b})$$

The form of the boundary conditions given at  $z = 0$  in Eq. C.12 and Eq. C.13 suggest the use of a cosine transform for  $\psi$  and a sine transform for  $\phi$ . The one-sided Laplace transform is also applied to eliminate the dependence on time  $t$ . Transforming the equations of motion in Eq. C.2 and Eq. C.3 and applying the initial conditions in Eq. C.11 and the boundary conditions in Eq. C.12 and Eq. C.13 yields

$$\frac{d^2 \bar{\phi}^s}{dr^2} + \frac{1}{r} \frac{d \bar{\phi}^s}{dr} + \alpha^2 \bar{\phi}^s = \frac{P}{\rho} \frac{\xi}{p^3} \quad (\text{C.17})$$

$$\frac{d^2 \bar{\psi}^c}{dr^2} + \frac{1}{r} \frac{d \bar{\psi}^c}{dr} + \left( \beta^2 - \frac{1}{r^2} \right) \bar{\psi}^c = 0 \quad (\text{C.18})$$

where

$$\alpha^2 = \frac{-p^2}{C_L^2} - \xi^2, \quad \beta^2 = \frac{-p^2}{C_T^2} - \xi^2 \quad (\text{C.19a,b})$$

It is noted the solutions of  $\bar{\varphi}^s$  and  $\bar{\psi}^c$  will involve Bessel functions and for a solid rod must remain bounded at the center. Thus,

$$\bar{\varphi}^s = A J_0(\alpha r) + \frac{P \xi}{\rho p^3} \quad (\text{C.20})$$

and

$$\bar{\psi}^c = B J_1(\beta r) \quad (\text{C.21})$$

The remaining boundary conditions at  $r = a$  also need to be satisfied. Transforming Eq. C.10c using the Laplace and Fourier sine transforms and substituting Eqs. C.20 and C.21 yields at  $r = a$

$$\begin{aligned} & \left[ -(\beta^2 - \xi^2) J_0(\alpha a) + \frac{2\alpha}{a} J_1(\alpha a) \right] A + 2 \left[ \beta x J_0(\beta a) - \frac{\xi}{a} J_1(\beta a) \right] B \\ & = -\frac{\lambda}{\lambda + 2\mu} \frac{P \xi}{\rho \alpha^2} \quad (\text{C.22}) \end{aligned}$$

And similarly applying the Laplace and Fourier cosine transform to Eq. C.10d and again substituting Eqs. C.20 and C.21 yields at  $r = a$ ,

$$2\alpha \xi J_1(\alpha a) A + (\beta^2 - \xi^2) J_1(\beta a) B = 0 \quad (\text{C.23})$$

The solutions for A and B follow from these two equations and are

$$A = -\frac{\lambda}{\lambda+2\mu} \frac{P \xi}{\mu \rho} \frac{\beta^2 - \xi^2}{\alpha^2} \frac{J_1(\beta a)}{D} \quad (\text{C.24})$$

$$B = \frac{2\lambda}{\lambda+2\mu} \frac{P}{\mu \rho} \frac{1}{\alpha} \frac{\xi^2}{\alpha} \frac{J_1(\alpha a)}{D} \quad (\text{C.25})$$

where

$$D = \frac{2\alpha}{a} (\beta^2 + \xi^2) J_1(\alpha a) J_1(\beta a) - (\beta^2 - \xi^2)^2 J_0(\alpha a) J_1(\beta a) \\ - 4\alpha \beta \xi^2 J_1(\alpha a) J_0(\beta a) \quad (\text{C.26})$$

The particle velocity, V, in the axial direction will be the focus of remaining development. In terms of the potentials it can be defined from Eq. C.3 as

$$V(r,z,t) = \frac{\partial w}{\partial t} = \frac{\partial \varphi}{\partial z} + \frac{1}{r} \frac{\partial (r\psi)}{\partial r} \quad (\text{C.27})$$

Applying the Fourier Cosine and Laplace Transforms results in

$$\tilde{V}^c = \frac{P}{\rho} \frac{1}{p^2} + p \xi \tilde{\varphi}^s + \frac{P}{r} \frac{\partial}{\partial r} (r \tilde{\psi}^c) \quad (\text{C.28})$$

which can be rewritten by substituting the solutions for  $\bar{\varphi}^s$  and  $\bar{\psi}^c$  given by Eqs. C.20 and C.21 as

$$\bar{V}^c = \frac{P}{\rho} \frac{1}{p^2 + \xi^2 C_L^2} - \frac{\lambda}{\lambda + 2\mu} \frac{P \xi}{\mu} \frac{\xi^2}{\rho \alpha^2} \frac{N}{D} \quad (\text{C.29})$$

where D is defined by Eq. C.26 and

$$N = (\beta^2 - \xi^2) J_0(\alpha r) J_1(\beta a) - 2\alpha\beta J_0(\beta r) J_1(\alpha a) \quad (\text{C.30})$$

Inversion of the transforms to find  $V(r,z,t)$  now remains the only task, however, it is a formidable one. First consider the inversion of the Laplace transform in accordance with Eq. C.16b. It is possible to perform the integration in the complex  $p$ -plane by applying Cauchy's residue theorem where the path of integration is closed by a semicircle of infinite radius about the origin in the left half-plane.

It can be shown by manipulating Eq. C.30 that only even powers of  $\alpha$  and  $\beta$  appear so there are no branch points in the complex  $p$ -plane. Further, by replacing the Bessel functions by their appropriate asymptotic forms for large arguments the integral over the infinite semi-circle vanishes. Therefore, the original integral is equal to  $2\pi i$  times the sum of the residues in the left plane.

With close examination, both terms of Eq. C.30 have poles at  $\pm i\xi C_L$ , however, it can be verified the residues of these poles cancel

each other and the remaining poles occur where the function  $D(p, \xi)$  vanishes. If the substitution  $p = i\omega$  is made in Eqs. C.26 and C.19a,b the equation  $D(p, \xi) = 0$  takes the same form as that for the frequency equation for longitudinal motions of a rod that is presented in Section 3.4.2 (Eq. 3.55) with the only difference being the transformed variable  $\xi$  in the location of the wave number  $k$ . As a result, for any value of  $\xi$  there are an infinite number of poles along the imaginary axis of the  $p$ -plane at positions defined by  $p = i\omega_n$ , where the functions  $\omega_n(\xi)$  are the circular frequencies of longitudinal modes in a rod. The contributions of these poles leads to a summation for the solution for  $V^c$  given by

$$V^c = -\frac{\lambda}{\lambda+2\mu} \frac{P}{\mu} \sum_{n=1}^{\infty} 2i\xi^2 M_n(\omega_n, \xi) \sin(\omega_n t) \quad (C.31)$$

where

$$M_n(\omega_n, \xi) = \left[ \frac{1}{\alpha^2} \frac{N}{\partial D / \partial p} \right]_{p=i\omega_n} \quad (C.32)$$

It is relatively simple now to apply the inversion integral for the Fourier cosine transform to the infinite series for  $V^c$  yielding

$$V = \frac{\lambda}{\lambda+2\mu} \frac{P}{\mu} \sum_{n=1}^{\infty} I_n \quad (C.33)$$

where

$$I_n = -\frac{4i}{\pi} \int_0^{\infty} \xi^2 M_n(\omega_n, \xi) \sin(\omega_n t) \cos(\xi z) d\xi \quad (C.34)$$

To evaluate the particle velocity at large time the integrals in Eq. C.33 can be recast in the form

$$I_n = \frac{2i}{\pi} \int_0^{\infty} \xi^2 M_n(\omega_n, \xi) \Upsilon [e^{i(\xi z - \omega_n t)} - e^{i(\xi z + \omega_n t)}] d\xi \quad (C.35)$$

At large values of dimensionless time, such as  $C_L t/a$  an approximate evaluation can be accomplished using the stationary phase method. This approximate method is outlined by Achenbach(1973) and discussed in some detail by Skalak(1957) when applied to transient motions in a rod. Borrowing on a development by Jones(1964) for transient motion in a layer, it can be shown that the contributions of the various branches of the frequency spectrum will at most be on the order of  $(C_L t/a)^{-1/2}$ , except at positions of stationary group velocity where the contributions are of the order  $(C_L t/a)^{-1/3}$ . Additional contributions may come from poles on the real  $\xi$ -axis but Skalak(1957) presents an argument for the case of a rod in that  $\partial D/\partial p$  cannot vanish for real values of  $\xi$ . In the present problem it should also be noted that for the lowest mode  $\omega_1$ , that the contribution is proportional to  $\xi$  in the vicinity of  $\xi = 0$  and the presence of  $\alpha^2$  in  $\partial D/\partial p$  in

the denominator causes a simple pole at  $\xi = 0$ , which also coincidentally is a point of stationary phase. It can be further demonstrated that the group velocity is also stationary at  $\xi = 0$ . As a result, the contribution of the lowest mode at small values of  $\xi$  predominates over the contributions from large modes particularly because it does not decay with time.

Following Skalak's (1957) development, it can be noted the frequency for the lowest longitudinal mode can be approximated by

$$\omega_1 = C_B \xi - \gamma \xi^3 \quad (\text{C.36})$$

where  $C_B$  is the bar velocity and  $\gamma$  is defined as

$$\gamma = \frac{1}{4} v^2 C_B \alpha^2 \quad (\text{C.37})$$

Here  $v$  is the Poisson's ratio. By substituting  $\omega_1 = C_B \xi$  into  $M(\omega_1, \xi)$ , and taking the limit as  $\xi$  goes to zero, the essential contribution to  $I_1$ , can be determined from Eq. C.35 by limiting the range of integration to  $\xi < \epsilon$  where  $\epsilon$  is small. Thus

$$I_1 = -\frac{1}{\pi} \frac{\mu}{\lambda} \frac{C_L^2}{C_B} \gamma \int_0^{+\epsilon} \frac{1}{\xi} [e^{i(\xi z - \omega_1 t)} - e^{i(\xi z + \omega_1 t)}] d\xi \quad (\text{C.38})$$

Next the upper limit of these integrals are extended to infinity because the integrals so added are of the order  $(C_L t/a)^{-1/2}$ . If just the first term of Eq. C.36 is substituted into Eq. C.38 it yields

$$V(z,t) = \frac{1}{C_B} \frac{P}{\rho} H(C_B t - z) \quad (\text{C.39})$$

which is the solution according to elementary theory. Note, the waveform in the elementary solution is independent of  $\xi$ , or stated differently, the velocity is independent of the frequency, and the waveform will not disperse as it travels along the rod.

A better approximation is obtained if both terms of Eq. C.36 are used. This results in

$$I_1 = -\frac{\mu}{\lambda} \frac{C_L^2}{C_B} [F_1 + F_2] \quad (\text{C.40})$$

where  $F_1$  and  $F_2$  are given by

$$F_1 = \frac{1}{\pi} \int_0^{\infty} \frac{\sin[\xi(z - C_B t) + \gamma \xi^3 t]}{\xi} d\xi \quad (\text{C.41a})$$

$$F_2 = \frac{1}{\pi} \int_0^{\infty} \frac{\sin[-\xi(z + C_B t) + \gamma \xi^3 t]}{\xi} d\xi \quad (\text{C.41b})$$

By changing the variable the expressions for  $F_1$  and  $F_2$  can be written as

$$F_n = \frac{1}{\pi} \int_0^{\infty} \frac{\sin(q_n \eta + \eta^3/3)}{\eta} d\eta \quad (\text{C.42})$$

where

$$q_1 = \frac{z - C_b t}{(3\gamma t)^{1/3}}, \quad q_2 = -\frac{z + C_b t}{(3\gamma t)^{1/3}} \quad (\text{C.43a,b})$$

and  $\gamma$  is defined in Eq. C.37. In this form  $F_1$  and  $F_2$  can be recognized as integrals of Airy's integral

$$\text{Ai}(q_n) = \frac{1}{\pi} \int_0^{\infty} \cos(q_n \eta + \eta^3/3) d\eta \quad (\text{C.44})$$

Thus we can rewrite the expressions for  $F_1$  and  $F_2$  as

$$F_1 = \int_0^{q_1} \text{Ai}(s) ds + \frac{1}{6} \quad (\text{C.45})$$

$$F_2 = \int_0^{q_2} \text{Ai}(s) ds + \frac{1}{6} \quad (\text{C.46})$$

where the  $1/6$  terms enter as the values for  $F_1$  and  $F_2$  for  $q_1 = 0$  and  $q_2 = 0$ , respectively.

**Appendix D**  
**Developing an Axisymmetric Finite Element**

### D.1 Developing an Axisymmetric Finite Element

The equations for the strain-displacement ( $u,v,w$ ) and stress-strain relationships expressed in cylindrical coordinates ( $r,\theta,z$ ) were developed and presented in Appendix A. These relationships can be derived for the axisymmetric case by setting  $v$  and any derivatives with respect to  $\theta$  equal to zero. The strain-displacement equations then become

$$\epsilon_r = \frac{\partial u}{\partial r}, \quad \epsilon_\theta = \frac{u}{r}, \quad \epsilon_z = \frac{\partial w}{\partial z} \quad (\text{D.1a,b,c})$$

and

$$\gamma_{rz} = 2\epsilon_{rz} = \frac{\partial u}{\partial z} + \frac{\partial w}{\partial r} \quad (\text{D.2})$$

The stress-strain relationships are given in matrix form by

$$\begin{Bmatrix} \tau_r \\ \tau_\theta \\ \tau_z \\ \tau_{rz} \end{Bmatrix} = \begin{bmatrix} \lambda+2\mu & \lambda & \lambda & 0 \\ \lambda & \lambda+2\mu & \lambda & 0 \\ \lambda & \lambda & \lambda+2\mu & 0 \\ 0 & 0 & 0 & \mu \end{bmatrix} \begin{Bmatrix} \epsilon_r \\ \epsilon_\theta \\ \epsilon_z \\ \gamma_{rz} \end{Bmatrix} \quad (\text{D.3})$$

or in matrix notation

$$\tau = \mathbf{D} \epsilon \quad (\text{D.4})$$

Now define a two-dimensional, 4-node, linear, finite element (see Figure D.1) where the z-axis corresponds to the central axis of the cylindrical specimen and the r-axis is perpendicular to it. The nodes are numbered 1 to 4, counter-clockwise from the lower left and  $r_1, r_2, z_1$  and  $z_2$  are the global coordinates corresponding to the sides of element.

If  $u$  is the displacement in the r-direction and  $w$  is the displacement in the z direction we can define

$$u = f_1u_1 + f_2u_2 + f_3u_3 + f_4u_4 \quad (D.5)$$

and

$$w = f_1w_1 + f_2w_2 + f_3w_3 + f_4w_4 \quad (D.6)$$

where  $f_n$  are prescribed interpolation functions and  $u_n$  and  $w_n$  are the respective nodal displacements. In matrix form these are

$$\begin{Bmatrix} u \\ w \end{Bmatrix} = \begin{bmatrix} f_1 & 0 & f_2 & 0 & f_3 & 0 & f_4 & 0 \\ 0 & f_1 & 0 & f_2 & 0 & f_3 & 0 & f_4 \end{bmatrix} \begin{Bmatrix} u_1 \\ w_1 \\ u_2 \\ w_2 \\ u_3 \\ w_3 \\ u_4 \\ w_4 \end{Bmatrix} \quad (D.7)$$

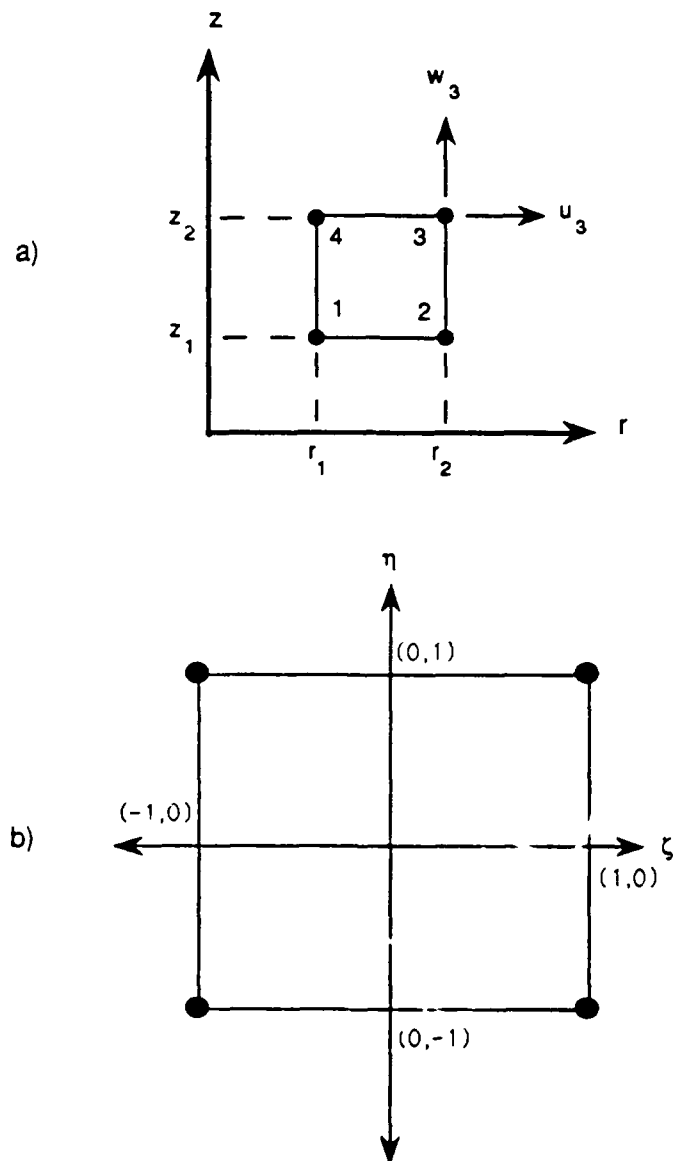


Figure D.1. Description of Finite Element Coordinate System; (a) Global Coordinates, and (b) Local Coordinates.

or in matrix notation

$$\begin{Bmatrix} u \\ w \end{Bmatrix} = \mathbf{N}^T \mathbf{U} \quad (\text{D.8})$$

For a linear element the interpolation functions,  $f_n$ , can be defined

$$f_1 = \left( \frac{r_2 - r}{\Delta r} \right) \left( \frac{z_2 - z}{\Delta z} \right) = \frac{1}{4} (1 - \xi) (1 - \eta) \quad (\text{D.9a})$$

$$f_2 = \left( \frac{r - r_1}{\Delta r} \right) \left( \frac{z_2 - z}{\Delta z} \right) = \frac{1}{4} (1 + \xi) (1 - \eta) \quad (\text{D.9b})$$

$$f_3 = \left( \frac{r - r_1}{\Delta r} \right) \left( \frac{z - z_1}{\Delta z} \right) = \frac{1}{4} (1 + \xi) (1 + \eta) \quad (\text{D.9c})$$

$$f_4 = \left( \frac{r_2 - r}{\Delta r} \right) \left( \frac{z - z_1}{\Delta z} \right) = \frac{1}{4} (1 - \xi) (1 + \eta) \quad (\text{D.9d})$$

where

$$\Delta r = r_2 - r_1, \text{ and } \Delta z = z_2 - z_1. \quad (\text{D.9e,f})$$

$\xi$  and  $\eta$  represent local variables relative to the center of a particular element as illustrated in Figure D.1 such that,

$$r = r_1 \left( \frac{1 - \xi}{2} \right) + r_2 \left( \frac{1 + \xi}{2} \right), \quad -1 \leq \xi \leq 1 \quad (\text{D.10a})$$

and

$$z = z_1 \left( \frac{1 - \eta}{2} \right) + z_2 \left( \frac{1 + \eta}{2} \right), \quad -1 \leq \eta \leq 1 \quad (\text{D.10b})$$

and

$$dr = \frac{\Delta r}{2} d\xi, \quad dz = \frac{\Delta z}{2} d\eta. \quad (\text{D.11a,b})$$

By denoting the partial derivatives of  $f_n$  with respect to  $r$  and with respect to  $z$  as  $f'_{nr}$  and  $f'_{nz}$ , respectively, we can determine using the chain rule

$$f'_{nr} = \frac{df_n}{dr} = \frac{df_n}{d\xi} \frac{d\xi}{dr} = \frac{df_n}{d\xi} \left( \frac{2}{\Delta r} \right) \quad (\text{D.12})$$

and

$$f'_{nz} = \frac{df_n}{dz} = \frac{df_n}{d\eta} \frac{d\eta}{dz} = \frac{df_n}{d\eta} \left( \frac{2}{\Delta z} \right) \quad (\text{D.13})$$

The derivatives of the interpolation functions then become

$$f'_{1r} = -\frac{1}{2\Delta r} (1 - \eta), \quad f'_{1z} = -\frac{1}{2\Delta z} (1 - \xi) \quad (\text{D.14a,b})$$

$$f'_{2r} = \frac{1}{2\Delta r} (1 - \eta), \quad f'_{2z} = -\frac{1}{2\Delta z} (1 + \xi) \quad (\text{D.14c,d})$$

$$f'_{3r} = \frac{1}{2\Delta r} (1 + \eta), \quad f'_{3z} = \frac{1}{2\Delta z} (1 + \xi) \quad (\text{D.14e,f})$$

$$f_{4r} = -\frac{1}{2\Delta r}(1 + \eta), \quad f_{4z} = \frac{1}{2\Delta z}(1 - \xi). \quad (\text{D.14g,h})$$

It is now possible to write the strain-displacement equations given in Eq. D.1 using the interpolation functions and their partial derivatives.

These are then

$$\epsilon_r = f_{nr}u_n, \quad \epsilon_\theta = \frac{1}{r}f_n u_n, \quad \epsilon_z = f_{nz}w_n, \quad (\text{D.15a,b,c})$$

and

$$\gamma_{rz} = f_{nz}u_n + f_{nr}w_n. \quad (\text{D.16})$$

Equations D.15 and D.16 can be combined in matrix form

$$\begin{Bmatrix} \epsilon_r \\ \epsilon_\theta \\ \epsilon_z \\ \gamma_{rz} \end{Bmatrix} = \begin{bmatrix} f'_{1r} & 0 & f'_{2r} & 0 & f'_{3r} & 0 & f'_{4r} & 0 \\ \frac{f_1}{r} & 0 & \frac{f_2}{r} & 0 & \frac{f_3}{r} & 0 & \frac{f_4}{r} & 0 \\ 0 & f'_{1z} & 0 & f'_{2z} & 0 & f'_{3z} & 0 & f'_{4z} \\ f'_{1z} & f'_{1r} & f'_{2z} & f'_{2r} & f'_{3z} & f'_{3r} & f'_{4z} & f'_{4r} \end{bmatrix} \begin{Bmatrix} u_1 \\ w_1 \\ u_2 \\ w_2 \\ u_3 \\ w_3 \\ u_4 \\ w_4 \end{Bmatrix} \quad (\text{D.17})$$

which in matrix notation is

$$\epsilon = \mathbf{B} \mathbf{U} \quad (\text{D.18})$$

To form the element stiffness matrix, it is first noted that

$$\tau = \mathbf{D} \varepsilon = \mathbf{D} \mathbf{B} \mathbf{U} \quad (\text{D.19})$$

and

$$\varepsilon^T = \mathbf{U}^T \mathbf{B}^T \quad (\text{D.20})$$

If the equations of motions for this element are stated in matrix form they are

$$\mathbf{M} \mathbf{U} + \mathbf{K} \mathbf{U} = \mathbf{P} \quad (\text{D.21})$$

where

- $\mathbf{M}$  = element mass matrix,
- $\mathbf{K}$  = element stiffness matrix,
- $\mathbf{U}$  = nodal displacement matrix,
- $\ddot{\mathbf{U}}$  = nodal acceleration matrix, and
- $\mathbf{P}$  = external forcing functions.

For steady state motions equation D.21 can be rewritten as

$$\mathbf{P} = (\mathbf{K} - \omega^2 \mathbf{M}) \mathbf{U} \quad (\text{D.22})$$

By virtue of the conservation of work, we have

$$\delta \mathbf{U}^T \mathbf{P} = \delta \mathbf{U}^T \mathbf{K} - \omega^2 \delta \mathbf{U}^T \mathbf{M} \mathbf{U} \quad (\text{D.23})$$

Also, the internal work in the element is given by

$$\delta W = \int_V \delta \boldsymbol{\varepsilon}^T \boldsymbol{\tau} = \int_V \delta \boldsymbol{\varepsilon}^T \boldsymbol{\tau} \mathbf{D} \boldsymbol{\varepsilon} = \int_V \delta \mathbf{U}^T \mathbf{B}^T \mathbf{D} \mathbf{B} \mathbf{U} \quad (\text{D.24})$$

It is then obvious from equations D.23 and D.24 that the element stiffness matrix is given by

$$\mathbf{K} = \int_V \mathbf{B}^T \mathbf{D} \mathbf{B} \, dV \quad (\text{D.25})$$

which in global cylindrical coordinates is given by

$$\mathbf{K} = \int_0^{2\pi} \int_{z_1}^{z_2} \int_{r_1}^{r_2} \mathbf{B}^T \mathbf{D} \mathbf{B} \, r \, dr \, dz \, d\theta \quad (\text{D.26})$$

In local coordinates, the axisymmetric case becomes

$$\mathbf{K} = 2\pi \left( \frac{\Delta r \Delta z}{4} \right) \int_{-1}^1 \int_{-1}^1 \mathbf{B}^T \mathbf{D} \mathbf{B} \, r \, d\xi \, d\eta \quad (\text{D.27})$$

It can be shown similarly the element mass matrix can be determined in local coordinates by

$$\mathbf{K} = 2\pi \left( \frac{\Delta r \Delta z}{4} \right) \int_{-1}^1 \int_{-1}^1 \mathbf{N} \mathbf{N}^T r \, d\xi d\eta, \quad (\text{D.28})$$

where  $\mathbf{N}^T$  is the matrix of interpolation functions defined in equation D.7.

For the purpose of numerical computation, the integrals in equations D.27 and D.28 can be replaced by the following summation

$$\int_{-1}^1 \int_{-1}^1 f(\xi, \eta) \, d\xi d\eta = \sum_i A_i \sum_j A_j f(\xi, \eta) \quad (\text{D.29})$$

where  $A_i, A_j$  are the appropriate constants from the quadrature formula. The resulting element matrices are 8x8, which corresponds to the four nodes multiplied by the two degrees of freedom at each node.

**Appendix E**  
**Equipment Used in the Multi-Moduli Testing Device**

## E.1 Equipment Used in the Multi-Moduli Testing Device

### 1. Specimen Confinement System

<u>Component</u>	<u>Purpose</u>	<u>Manufacturer</u>
Pressure Regulator	To control air supply to axial air piston and confinement cell	Fairchild M30 pressure regulator
Vacuum Regulator	To control internal specimen vacuum	Farchild M30 vacuum regulator
Pressure/Vacuum Transducer	To measure chamber pressure and specimen vacuum	Validyne DP15 pressure transducer
Multichannel Carrier Demodulator	To input excitation signals to pressure transducer for conditioning	Validyne CD 280
Proximeter Probe 11-mm diameter	To measure changes in length	Bentley-Nevada 7200 Series
Proximeter Conditioner	To condition the probe signal	Bentley-Nevada 19048-00-10-05-02
Load Cell	To measure axial load	Lebow M3397 w/ 50 or 300 lb capacity
DC Power Amplifier	To amplify load cell signal	NEFF Model 128
Voltmeter	To read output from load cell, proximeters and transducers	HP 3478 Multimeter
DC Power Supply	To power Load Cell and Proximeters	LAMDA power supply M-LL-902

## 2. Dynamic Excitation System

<u>Component</u>	<u>Purpose</u>	<u>Manufacturer</u>
Piezoelectric Vibration Generator (Shaker)	To provide transient and steady-state longitudinal excitation	Wilcoxon Research F7 Shaker
Power Amplifier	To amplify input signals to shaker	Wilcoxon Research PA8
Matching Network	To balance impedance of shaker	Wilcoxon Research N8HF
Transverse Shear Wave Exciter	To generate shear waves in the specimen	MDL
Power Supply/Amplifier	To amplify signal to shear wave exciter	HP 6825A
Function Generator	To supply excitation signal for shear wave exciter and shaker	HP 3314A

## 3. Dynamic Monitoring System

<u>Component</u>	<u>Purpose</u>	<u>Manufacturer</u>
Low Impedance, High output Accelerometer	To measure dynamic motion of specimen	Wilcoxon Research 736
High Impedance Charge Accelerometer	To measure dynamic motion of specimen	Wilcoxon Research 111A
Power Unit/Amplifier	To provide DC power to accelerometers	Wilcoxon Research P702

## 3. Dynamic Monitoring System (continued)

<u>Component</u>	<u>Purpose</u>	<u>Manufacturer</u>
In-Line Charge Converter	To convert high impedance charge output to low impedance voltage signal (for 111A)	Wilcoxon Research CC701
Line adapter	To provide DC power to P702 amplifiers	Wilcoxon Research LA703
Digital Recording Oscilloscope	To capture, store and analyze time records for pulse tests	Tektronix 11401
Dynamic Signal Analyzer	To control and measure frequency response	HP 3562A
Computer (Test Control)	To control transfer and storage of pulse time records	HP+ 200 series desktop microcomputer
Disc Drive	To store programs and data files	HP 9133D Winchester disc or HP 9122D disc drive
Printer	To make hardcopies copies of oscilloscope records and print data and results	IBM Proprinter or HP 82906A graphic printer
Plotter	To plot time and frequency records	HP 7475A or HP 7470A plotter
Computer (Data Reduction)	To perform data reduction	IBM AT or equivalent

**Appendix F**  
**Sample Preparation and Test Procedures for the Multi-Moduli**  
**Testing Device (MTD)**

## F.1 Preparation of a Sand Sample

### 1. Collect the following items needed to construct a sand sample.

- Filter paper
- Scissors
- Super glue
- Latex membrane
- A ruler
- Vacuum grease
- O-rings
- O-ring spreader
- Sample mold with fittings
- A small level
- 3/16 in. allen wrench
- Pluviating device with appropriate screens
- Vacuum source and gage
- Sand
- Beaker, 1 liter
- A scale accurate to + 0.1 grams
- Erlenmeyer flask, 1 liter
- Initial data sheet
- Steel straight edge
- The top cap assembly
- Yard stick

2. Make sure that the shaker is mounted properly in the base of the test cell, that the sample base pedestal is installed properly, and has been cleaned.

3. Cut two small circles of filter paper approximately 1/4 in. in diameter and tack one over each hole in the sample base pedestal using one or two drops of super glue.

4. Cut the membrane to a length of 8.3 in. (dictated by sample mold size). Also, on the uncut end of the membrane, cut a small rectangular notch approximately 1/4 in. into the membrane and 1 in. long.
5. Apply a small amount of vacuum grease around the sides of the base pedestal. Stretch the uncut end of the membrane over the base pedestal and align it so that the notch in the membrane spans the tapping plate for the shear wave tapper. Carefully align the bottom of the membrane so that it is even with the bottom edge of the base pedestal. If the notch in the membrane is large enough, the shear tapper plate should be exposed and there should be a small 1/4 square inch area of the base exposed next to it. This is where the base horizontal accelerometer will be glued.
6. Install an O-ring on the base over the membrane using an O-ring spreader.
7. Disassemble the sample mold and apply vacuum grease to the two sides where they touch. Be sure to clean any excess vacuum grease from the inside of the mold. Now assemble the two halves of the mold around the base and the membrane. Be careful that the membrane is not pinched between the two halves of the mold and that the O-ring on the base fits snugly into the groove for it in the mold. Finger tighten the four bolts holding the two halves of the mold together.
8. Using a small level adjust the legs of the mold to level the mold.
9. When the mold is level, tighten the bolts using the 3/16 allen wrench.
10. Carefully pull the membrane up and fold it over the top of the mold, ensuring there are no wrinkles in the membrane inside the mold.
11. Fit the aluminum capture ring from the pluviating device over the top of the mold and membrane.
12. Attach the vacuum source to the ports on the side of the mold and draw a 1.0-1.5 psi vacuum, ensuring that the membrane is pulled smoothly against the sides of the mold. Again check to see there are no wrinkles in the membrane.

13. Recheck the level at the top of the mold before installing the pluviating column.
14. Set up the pluviating column on top of the sample mold. Begin by putting the acrylic base alignment ring over the aluminum capture ring on top of the sample mold. Continue assembling the pluviating device with the bottom free-fall section, the sieve stack and the top free-fall section on top of the sample mold. Ensure that the sieves in the sieve stack have been oriented at 45 degrees to each other and that the correct size sieves are installed to achieve the desired density.
15. Install the funnel on the top of the pluviating column and insert the funnel opening (plastic insert) that will give the desired density. For high relative densities, use a small funnel opening, and for low relative densities use a large funnel opening.
16. Place sand in the liter beaker and weigh. Also weigh the Erlenmeyer flask. Record these weights on the initial data sheet.
17. Pour the sand from the liter beaker into the funnel, ensuring that it doesn't fall through by first stopping the hole.
18. When ready, remove the stopper and allow the sand to fall. After pouring the sand into the funnel, weigh the beaker again and record this weight on the initial data sheet.
19. When the sand has completed falling into the mold, there should be 1-2 inches of sand above the top of the mold inside the pluviating column.
20. Start disassembling the pluviating column. Connect the Erlenmeyer flask to the vacuum source. (It is possible to disconnect the vacuum to the sample mold at this time.) Disassemble the pluviating column one piece at a time being sure to capture all the loose sand with the vacuum in the Erlenmeyer flask. When removing the sieves it is convenient to reassemble them in reverse order, so that they are ready to use for the next sample construction. Before removing the bottom free-fall section of the pluviating column, remove the excess sand to within about 1/2 in. of the top of the mold. After removing the free fall section, carefully vacuum

the remaining sand on the top of the mold down to just above the top surface of the mold and remove the acrylic alignment ring. Again, be careful to capture all loose sand with the vacuum. Now, carefully remove the aluminum capture ring.

21. Using the steel straight edge, carefully strike off the top of the sand sample, capturing any excess sand with the vacuum.
22. Ensure that the top cap has been assembled with the necessary accelerometers and mounts. The horizontal accelerometers should align with the bolt holes in the top cap. Apply a light layer of vacuum grease to the sides of the top cap.
23. Carefully place the top cap on top of the sand in the mold. Align it, using a yard stick, between the two vertical connecting rods on either side so that the horizontal accelerometers are aligned with the mounting location for the shear wave source.
24. Inch the membrane up along the sides of the top cap, being careful not to rock the top cap excessively, and making sure that the membrane is smooth along the side surface of the top cap.
25. Install an O-ring on the top cap using the O-ring spreader.
26. Attach the vacuum to the ports in the base of the sample base. Then apply a 1.5 to 2.0 psi vacuum to the sample. With the sample under a vacuum, remove the bolts connecting the mold and carefully remove the mold without disturbing the sample.
27. Ensure that all spilt sand is collected with the vacuum. Weigh the Erlenmeyer flask and record the weight on the initial data sheet.
28. Add a second O-ring to the top and the bottom of the sample using the O-ring spreader. This completes the construction of the sample.

## F.2 Assembling the MTD and Preparing a Sample for Test

### 1. To start, collect the following items:

Digital calipers

Pi tape

A large adjustable wrench

Vacuum grease

Allen wrenches (sizes 3/32, 9/64, and 5/32)

Super glue

Cotton swabs

Equipment listed in Appendix E

2. The following equipment should be calibrated ahead of time: the two proximeters, the load cell, the pressure transducer, and the vacuum transducer.

3. To measure the initial dimensions of the sample, increase the internal vacuum in the sample to 3.5 psi. Measure the length between the top and the bottom caps on opposing sides of the sample using the digital calipers and average the two measurements for the initial length. Using the Pi tape, measure the diameter at a minimum of three locations along the sample and average the measurements for the initial diameter, being sure to subtract twice the membrane thickness. Note the pressure on the sample indicated by the vacuum transducer so that it is possible to return the sample to this pressure at a later time during the setup procedure.

4. Glue the horizontal accelerometer next to the taper shield on the side of the base pedestal. It may be necessary to trim the membrane slightly to make sure that it will glue securely to the base.

5. Install the shear wave taper. Mount the shear wave taper so that it is aligned with the horizontal accelerometers on the top cap.

6. Very carefully install the top vibration isolation assembly, ensuring that the proximeter targets align with the proximeter locations. Very carefully

install and tighten the cap screws that attach the vibration isolation assembly to the top cap using the 9/64 allen wrench. Be careful not to twist the top of the sample.

7. Attach the three internal accelerometer cables to the top three accelerometers. Make sure that they are tightened securely.
8. Install the proximeters in their proximeter mounts. Screw the mounts to the base plate of the cell and adjust the proximeters so that they are centered in the middle of the targets on the top cap assembly. Use the 3/32 allen wrench to space the proximeter from the target. This should give an initial reading of -8 to -9 volts.
9. Connect all of the proximeters and the accelerometers to their appropriate amplifiers and determine that they are operating properly. Also check that the shear wave tapper is operating.
10. Disconnect all of the connected proximeters and accelerometers. Clean the O-ring groove (for cell casing) in the base plate using cotton swabs.
11. Install the acrylic wire guard around the sample by carefully lowering it down around the sample and feeding the bottom wires through the holes in the bottom of the guard.
12. Apply a liberal amount of vacuum grease to the O-ring groove in the base plate. It is convenient to tie all loose accelerometer cables in a bundle and carefully rest them on the vibration isolation assembly on top of the sample. Lower the cell casing down around the wire guard being sure not to damage any of the wires.
13. With the cell case in place, drape all of the wires from the bottom and the top accelerometers over the top of the cell casing. Also, work the proximeter leads into a position where they can be easily reached. Feed the top accelerometer leads through the holes in the top of the wire guard.
15. Note the zero reading for the load cell and install it on top of the vibration isolation assembly. Also install the gimble joint on top of the

load cell. Screw both down snugly but be careful not to push down on, or twist, the top of the sample.

16. Lift the top plate onto the top of the cell and prop it on the upright connecting rods.
17. Attach all of the internal cables to the feedthrus in the top plate. Also, connect the internal proximiter and the load cell cables to the cables passing through the fittings in the top plate.
18. Connect all of the external leads to the outside of the top plate. Test each of the accelerometers and proximiters again to make sure that they are operating.
19. Extend the shaft on the axial air piston and screw it down into the connecting rod on top of the gimble joint.
20. Having ensured that all sensors are working properly, liberally grease the top of the cell casing and carefully lower the top plate onto the container cell.
21. Carefully lower the piston and screw it down into the mount on the top plate.
22. Before tightening down the nuts securing the top plate, again test all of the accelerometers and proximiters and other instruments.
23. Tighten the nuts on the top evenly so that it does not warp the top plate.
24. Connect the pressure panel to the pressure cell and the two ends of the axial loading piston.
25. Incrementally decrease the vacuum in the sample and increase the pressure in the test cell in 0.5 psi steps until the cell pressure is at 3.5 psi, or at the same pressure used initially when the height of the sample was measured. When the vacuum has been reduced to atmospheric pressure, disconnect the line and open the vacuum port in the base plate.
26. Record the initial reading for the two proximiters.

These steps complete the setting up of the test cell and the preparation for a test series.

### F.3 Beginning a Test Series in the MTD and Conducting Tests at a Single Stress State

1. Decide on the stress state for each test step in the test series. Having chosen the desired stress states, prepare a transducer reading calculation sheet. This sheet will give the transducer readings for the pressure transducer and the load cell for each test step in the test series.
2. From the preparation pressure, in this case 3.5 psi, adjust the cell pressure and the axial loading piston until the readings from the pressure transducer and load cell equal those on the transducer calculation sheet for the first test step. All tests in this study started at 4 psi cell pressure. After adjusting the cell pressure and the pressure in the axial piston to get the correct load cell readings for the desired stress state, record the time, the pressure transducer reading, the load cell reading, and the reading on the two proximeters at the beginning of the test step.

#### F.3.1 Conducting the Axial Pulse Test.

1. Connect the base and top vertical accelerometers to two channels on the digital recording oscilloscope. (See Fig. 5.9) Connect the shaker amplifier to the function generator (See Fig. 5.5.) and recall the preset settings saved in the scope and the function generator for the axial pulse test. The typical settings for the function generator to conduct an axial pulse test in sand are listed in Table F.1. Also, note at the beginning of the test, the amplification settings of the accelerometer amplifiers. When multiplied by the accelerometer constant, these will be the accelerometer constant requested when the wave forms are saved to disk storage.
2. Activate the internal trigger on the function generator and adjust the oscilloscope so that two clear signals are observed for the bottom and the top vertical accelerometers. The oscilloscope should make the

Table F.1. Typical Settings for the Function Generator to Conduct an Axial Pulse Test on Sand.

Frequency	2 kHz
Amplitude	0.100 V
Offset	0.00 V
Symmetry	50 %
Phase	-90.0 deg
Number	001
Trigger Interval	100 ms
Trigger	Internal
Mode	1/2 Cycle
Wave	Square

prescribed number of averages and stop. (128 averages were used in this test program.)

3. Store the two recorded wave forms in the first and second internal storage locations of the oscilloscope.
4. Turn off the internal trigger on the function generator.
5. To permanently store the recorded wave forms for the axial pulse test, load the PSAVE storage program into the active bank of the computer and execute. The program will ask you for the name and the storage location for the file in which to store the wave forms. It will then request the accelerometer constants for each of the accelerometers. The computer will transfer the wave forms and necessary wave form data in storage locations 1 and 2 of the oscilloscope and put them in the file that has been identified on the mass storage unit. The source code for PSAVE, which is written in HP Basic®, is provided in Fig. F.1 at the end of this appendix.
6. The final step in the axial pulse test is to determine the compression wave travel time. To accomplish this, clear the oscilloscope screen, and

recall the waves stored in storage locations 1 and 2. Then, using the cursor functions it is possible to determine the travel time between the two accelerometers in the sample. Record the travel time on the test data sheet. Calculation of the P-wave velocity is in accordance with the procedures outlined in Chapter 6.

### F.3.2 Conducting the Shear Pulse Test.

1. Connect the base and two top horizontal accelerometers to three channels on the digital recording oscilloscope. (See Fig. 5.9) Connect the shear wave tapper to the function generator (See Fig. 5.7.) and recall the preset settings saved in the scope and the function generator. Typical settings for the function generator to conduct a shear pulse test in sand are listed in Table F.2. Also, note at the beginning of the test, the amplification settings of the accelerometer amplifiers, which when multiplied by the accelerometer constant will be the accelerometer constants requested when the wave forms are saved to disk storage.
2. Hold down the off/on button and adjust the oscilloscope so that three clear signals are observed for the bottom and two top horizontal accelerometers. The oscilloscope should make the prescribed number of averages and stop. (64 averages were used in this test program.)
3. Release the off/on button when the oscilloscope stops.
4. Store the three wave forms in the third, fourth, and fifth internal storage locations of the oscilloscope.
5. To permanently store the recorded wave forms for the shear pulse test, load the SSAVE storage program into the active bank of the computer and execute. The program will ask you for the name and the storage location for the file in which to store the wave forms. It will then request the accelerometer constants for each of the accelerometers. The computer will transfer the wave forms and necessary wave form data in

**Table F.2. Typical Settings for the Function Generator to Conduct a Shear Pulse Test on Sand.**

Frequency	5 Hz
Amplitude	5 V
Offset	0.00 V
Symmetry	50 %
Phase	-90.0 deg
Number	001
Trigger Interval	N/A
Trigger	N/A
Mode	Free Run
Wave	Square

storage locations 3, 4, and 5 of the oscilloscope and put them in the file that you have identified on the mass storage unit.

6. The final step in the shear pulse test is to determine the shear wave travel time. To accomplish this, clear the oscilloscope screen, and recall the waves stored in storage locations 3, 4, and 5. Then, using the the cursor functions, it is possible to determine the travel time between the bottom and top accelerometers. Record the travel time on test data sheet. Calculation of the shear wave velocity is in accordance with the procedures outlined in Chapter 6.

### F.3.3 Conducting the Longitudinal Resonant Column (LRC) Test

1. Connect the base and top vertical accelerometers to channels 1 and 2 of the Dynamic Signal Analyzer (DSA), respectively (See Fig. 5.10). Connect the shaker amplifier to the internal source of the DSA. Recall

the preset settings saved in the DSA for the LRC test as prescribed by Table 7.1. Note the amplification settings and determine the accelerometer constants for each accelerometer. Ensure the "engineering units valves" for each channel of DSA are set to the correct accelerometer constants.

2. Begin the frequency sweep. While the frequency sweep is being accomplished by the DSA, the operator can be determining the P-wave and S-wave travel times for the axial and shear pulse tests.
3. When the DSA has completed the frequency sweep, label the trace and store the frequency response and coherence on disk storage.
4. While the sweep is being conducted, the operator can be identifying and recording the natural frequencies of the specimen on the test data sheet. Calculation of the bar wave velocity is in accordance with the procedures outlined in Chapter 7.

#### F.4 Completing Tests at a Single Stress-State

1. After completing the axial and shear pulse tests and the longitudinal resonant column tests, again record the time and the readings from the pressure transducer, load cell, and two proximiters.
2. Check the transducer calculation sheet and adjust the cell pressure and axial air piston for the next stress state. Repeat until the last stress state is complete.

#### F.5 Reducing the Lab Data

1. All the manually recorded data for each test step in a test series is entered into a computer using an interactive program that automatically builds an input file that is read by the data reduction program. That program is called RCLIN and the source code is included in Fig. F.2. at

the end of this Appendix. The input program will first request initial test data which was recorded on the initial data sheets. It then requests test data for each test step in the test series, in sequential order.

2. When the input file is complete, the operator executes the data reduction file, RCL, which reads the input file and computes the wave velocities and moduli in accordance with the methods described in Chapter 6 and Chapter 7. The output from the program is an individual, one page summary for individual tests at each stress state in a test series and an overall summary of the moduli measured during the test series. An example of an individual stress state summary was given in Fig. 7.4 and test series summaries for the sand and clay can be found in Appendix G. The source code for the data reduction program is included in Fig. F.3 at the end of this Appendix.

#### F.6 Dismantling the MTD

1. When a test series is complete, reduce the cell pressure and increase the vacuum in the specimen (which has been reconnected) in 0.5 psi increments until the cell pressure is zero and the vacuum is at 3.5 psi or 4.0 psi. Open the cell pressure port to the atmosphere and disconnect the pressure lines to the axial load piston.
2. Disconnect all external sensor leads to the top plate and remove the retaining nuts.
3. Carefully lift the top plate and prop it on top of the connecting rods. Wipe off any excess vacuum grease.
4. Unscrew the axial load piston and remove.
5. Disconnect all internal sensor leads to the top plate and remove the top plate.
6. Unscrew gimble joint and load cell and remove.
7. Carefully coil loose cables on top of vibration isolation assembly.

8. Remove cell casing and wipe off any excess vacuum grease.
9. Disconnect the accelerometer leads from the top accelerometers.
10. Carefully remove acrylic wire guard, feeding cables back through holes in bottom.
11. Remove proximiters and their mounts.
12. Loosen cap screws and remove vibration isolation assembly from the top cap.
13. Remove shear wave tapper.
14. Reduce vacuum to zero and carefully remove top cap. The sand sample will stand in the membrane without a vacuum. Scoop sand from membrane into beaker, taking three 100 -150 gram samples for determining the moisture content.
15. Vacuum any excess sand into the Erlenmeyer flask and clean vacuum grease from top and bottom plates and the sample base pedestal.

```

OPTION BASE 1
CLEAR 7
PRINT "PROGRAM TO SAVE PULSE TEST WAVEFORMS"
PRINT " "
INPUT "INPUT FILE NAME TO SAVE P-WAVE DATA TO:" ,F$
PRINT " "
PRINT "DESTINATION STORAGE ADDRESSES"
PRINT " (1) FLEXIBLE DISC - : ,706,0"
PRINT " (2) HARD DISC - : ,700,0"
PRINT " (3) HP INTERNAL - : INTERNAL,4,0"
PRINT " (4) OTHER"
INPUT "SELECT DESTINATION DEVICE: " ,Save$
SELECT Save$
CASE "1"
F$=F$&" : ,706,0"
CASE "2"
F$=F$&" : ,700,0"
CASE "3"
F$=F$&" : INTERNAL,4,0"
CASE ELSE
INPUT "ENTER DESTINATION DEVICE: " ,D$
F$=F$&D$
END SELECT
ON ERROR GOTO Err
INPUT "ENTER ACCELEROMETER CONSTANT FOR WAVEFORM IN ST01(Volts/G):" ,Acc1
INPUT "ENTER ACCELEROMETER CONSTANT FOR WAVEFORM IN ST02(Volts/G):" ,Acc2
PRINT " "
PRINT "**** INSERT STORAGE DISK, HIT CONTINUE ****"
PAUSE
ASSIGN @Tek TO 716
ASSIGN @Tekbin TO 716;FORMAT OFF
PRINT " "
PRINT "TRANSFERRING WAVEFORM IN ST01"
OUTPUT @Tek;"ENCDG WAUFRM:BIN;BYT.OR MSB"
OUTPUT @Tek;"OUTPUT ST01"
OUTPUT @Tek;"CURVE?"
ENTER @Tek USING "#,7A,W" ;Head$,Bytcnt
Nr_pt1=(Bytcnt-1)/2
ALLOCATE INTEGER A(1:Nr_pt1)
ENTER @Tekbin;A(*)
ENTER @Tek USING "B" ;Cksum
OUTPUT @Tek;"WFMPRE? YMULT,YZERO,XZERO,XINCR"
ENTER @Tek;Ymul1,Yzer1,Xzer1,Xincl
PRINT " "

```

Fig. F.1. Source Code for Saving Axial Pulse Test Wave Forms - PSAVE.

```

PRINT "TRANSFERRING WAVEFORM IN STO2"
OUTPUT @Tek;"ENCDS WAUFRM:BIN;BYT.OR MSB"
OUTPUT @Tek;"OUTPUT STO2"
OUTPUT @Tek;"CURVE?"
ENTER @Tek USING "%,7A,W";Head$,Bytcnt
Nr_pt2=(Bytcnt-1)/2
ALLOCATE INTEGER B(1:Nr_pt2)
ENTER @Tekbin;B(*)
ENTER @Tek USING "B";Cksum
OUTPUT @Tek;"WFMPRE? YMULT,YZERO,XZERO,XINCR"
ENTER @Tek;Ymul2,Yzer2,Xzer2,Xinc2
CREATE BDAT F$,2,2*6*8+2*(Nr_pt1+Nr_pt2)
ASSIGN @Dest TO F$;FORMAT OFF
OUTPUT @Dest;Acc1,Ymul1,Yzer1,Xzer1,Xinc1,Nr_pt1
OUTPUT @Dest;A(*)
OUTPUT @Dest;Acc2,Ymul2,Yzer2,Xzer2,Xinc2,Nr_pt2
OUTPUT @Dest;B(*)
PRINT " "
PRINT " ***** TRANSFER TO "iF$;" COMPLETE *****"
GOTO 680
Err:  OFF ERROR
      IF ERRN=54 THEN
        INPUT "FILE EXISTS! OVERWRITE? (YorN):",Q$
        IF Q$="N" THEN GOTO 50
        PURGE F$
      END IF
      GOTO 520
DEALLOCATE A(*),B(*)
END

```

Fig. F.1. Source Code for Saving Axial Pulse Test Wave Forms - PSAVE(continued).

```

C*****PROGRAM TO BUILD INPUT DATA FILE FOR RCL TEST*****
C
  IMPLICIT REAL*8(A-H,O-Z)
  CHARACTER*50 TESTID
  INTEGER UNIT1,Q
C
  UNIT1=9
  OPEN(UNIT1,FILE=' ',STATUS='UNKNOWN')
  WRITE(6,*)'IS THIS A NEW INPUT FILE? (1-YES,0-NO):'
  READ(5,*)Q
  IF(Q.EQ.0)THEN
    REWIND UNIT1
    READ(UNIT1,*)TESTID
    CALL ENFIL(UNIT1)
    BACKSPACE UNIT1
    READ(UNIT1,*)ITEST
    GOTO 100
  ENDIF
  WRITE(6,5)
5 FORMAT(1X,'THIS IS A NEW INPUT FILE. YOU WILL HAVE TO ENTER',
  * ' TEST CONSTANTS FIRST.'//1X,'ENTER TEST NAME & DATES:')
  READ(5,*)TESTID
  WRITE(UNIT1,*)TESTID
  WRITE(6,*)'ENTER SAMPLE WEIGHT(gram):'
  READ(5,*)WT
  WRITE(UNIT1,*)WT
  WRITE(6,*)'ENTER INITIAL SAMPLE LENGTH(in) AND DIAMETER(in):'
  READ(5,*)Z,D
  WRITE(UNIT1,*)Z,D
  WRITE(6,*)'ENTER SAMPLE SPECIFIC GRAVITY AND WATER CONTENT'
  READ(5,*)GS,WC
  WRITE(UNIT1,*)GS,WC
  WRITE(6,*)'ENTER POISSON'S RATIO FOR VOLUME CHANGE COMPUTATION'
  READ(5,*)PR
  WRITE(UNIT1,*)PR
  WRITE(6,*)'ENTER ADDED MASS OF TOP CAP(gram):'
  READ(5,*)WM
  WRITE(UNIT1,*)WM
  WRITE(6,*)'ENTER MASS OF TOP CAP LOAD FRAME(gram):'
  READ(5,*)WF
  WRITE(UNIT1,*)WF
  WRITE(6,*)'ENTER P-WAVE DELAY(microsec):'
  READ(5,*)PD
  WRITE(UNIT1,*)PD
  WRITE(6,*)'ENTER S-WAVE DELAY(microsec):'
  READ(5,*)SD

```

Fig. F.2. Source Code to Build Lab Data File - RCLIN.

```

WRITE(6,*)'ENTER PRESSURE/VACUUM TRANSDUCER CONSTANT(psi/volt)',
** & ZERO READING(volts):'
READ(5,*)PTC,PTZERO
WRITE(UNIT1,*)PTC,PTZERO
WRITE(6,*)'ENTER AXIAL LOAD CELL CONSTANT(lbs/volt)',
** & ZERO READING(volt):'
READ(5,*)ALC,ALCZERO
WRITE(UNIT1,*)ALC,ALCZERO
WRITE(6,*)'ENTER PROXIMETER #2 CONSTANT(in/volt)',
** & INITIAL READING:'
READ(5,*)PX2C,PX2I
WRITE(UNIT1,*)PX2C,PX2I
WRITE(6,*)'ENTER PROXIMETER #3 CONSTANT(in/volt)',
** & INITIAL READING:'
READ(5,*)PX3C,PX3I
WRITE(UNIT1,*)PX3C,PX3I
WRITE(UNIT1,*)ITEST
GOTO 150
C
100 WRITE(6,*)'THIS IS AN INPUT FILE FOR - ',TESTID
WRITE(6,110)ITEST
110 FORMAT(1X,'THE LAST DATA ENTERED WAS FOR TEST ',I3,':')
C
150 ITEST=ITEST+1
WRITE(6,200)ITEST
200 FORMAT(1X,'ENTER DATA NOW FOR TEST ',I3,':')
WRITE(6,*)'ENTER TIME(hr) OF TEST FROM INITIAL START:'
READ(5,*)TIME
WRITE(UNIT1,*)TIME
WRITE(6,*)'ENTER PRESSURE/VACUUM TRANSDUCER READING(volt):'
READ(5,*)PT
WRITE(UNIT1,*)PT
WRITE(6,*)'ENTER AXIAL LOAD CELL READING(volt):'
READ(5,*)AL
WRITE(UNIT1,*)AL
WRITE(6,*)'ENTER PROXIMETER #2 READING(volt):'
READ(5,*)PX2
WRITE(UNIT1,*)PX2
WRITE(6,*)'ENTER PROXIMETER #3 READING(volt):'
READ(5,*)PX3
WRITE(UNIT1,*)PX3
WRITE(6,*)'ENTER P-WAVE INTERVAL TIME(microsec):'
READ(5,*)PW
WRITE(UNIT1,*)PW
WRITE(6,*)'ENTER S-WAVE INTERVAL TIME(microsec):'
READ(5,*)SW
WRITE(UNIT1,*)SW
WRITE(6,*)'ENTER NO. OF FIXED-FREE MODES MEASURED:'

```

Fig. F.2. Source Code to Build Lab Data File - RCLIN (continued).

```
WRITE(6,*)'ENTER NO. OF FIXED-FREE MODES MEASURED:'
READ(5,*)IC
WRITE(UNIT1,*)IC
DO 250 I=1,IC
WRITE(6,240)I
240 FORMAT(1X,'ENTER RESONANT FREQUENCY(Hz) FOR MODE ',I3,':')
READ(5,*)FX
250 WRITE(UNIT1,*)FX
WRITE(UNIT1,*)ITEST
WRITE(6,260)ITEST
260 FORMAT(1X,'YOU HAVE COMPLETED DATA ENTRY FOR TEST ',I3,':',
* /1X,'DO YOU WISH TO ENTER DATA FOR ANOTHER TEST? (1-YES,0-NO)')
READ(6,*)Q
IF(Q.EQ.1)GOTO 150
END
C
C*****SUBROUTINE TO ADVANCE TO END OF FILE*****
C
SUBROUTINE ENFIL(ID)
IMPLICIT REAL*8(A-H,O-Z)
C
100 IF(.NOT.EOF(ID))THEN
READ(ID,*)FILL
GOTO 100
ENDIF
RETURN
END
```

Fig. F.2. Source Code to Build Lab Data File - RCLIN (continued).

```

C*****PROGRAM TO REDUCE LONG. RES. COL. DATA*****
C
  IMPLICIT REAL*8(A-H,O-Z)
  CHARACTER*50 TESTID
  DIMENSION TIME(50),PT(50),AL(50),PX2(50),PX3(50),PW(50),SW(50)
  DIMENSION BETA(10),IC(50),CP(50),CB(10,50),C(10,50),POS(10,50)
  DIMENSION CS(10,50),FX(10,50),CSW(50),G(10,50),PM(50),E(10,50)
  DIMENSION GSW(50),SIGA(50),SIGC(50),SIGM(50),Z(50),D(50)
  DIMENSION V(50),GAM(50),VR(50)
  INTEGER UNIT1,UNIT
  DATA PV3.14159265358979/,UNIT1/9/,UNIT/10/
C
C*****READ INPUT FILE*****
C
  OPEN(UNIT1,FILE='  ';MODE='READ')
  REWIND UNIT1
  READ(UNIT1,*)TESTID
  READ(UNIT1,*)WT
  READ(UNIT1,*)ZI,DI
  READ(UNIT1,*)GS,WC
  READ(UNIT1,*)PR
  READ(UNIT1,*)WM
  READ(UNIT1,*)WF
  READ(UNIT1,*)PD
  READ(UNIT1,*)SD
  READ(UNIT1,*)PTC,PTZERO
  READ(UNIT1,*)ALC,ALZERO
  READ(UNIT1,*)PX2C,PX2I
  READ(UNIT1,*)PX3C,PX3I
  READ(UNIT1,*)ITEST
10 I=ITEST+1
  READ(UNIT1,*,END=30)TIME(I)
  READ(UNIT1,*)PT(I)
  READ(UNIT1,*)AL(I)
  READ(UNIT1,*)PX2(I)
  READ(UNIT1,*)PX3(I)
  READ(UNIT1,*)PW(I)
  READ(UNIT1,*)SW(I)
  READ(UNIT1,*)IC(I)
  DO 20 J=1,IC(I)
20 READ(UNIT1,*)FX(J,I)
  READ(UNIT1,*)ITEST
  WRITE(6,*)' JUST READ TEST,ITEST'
  GOTO 10
30 CONTINUE
C
C*****COMPUTE VALUES FOR EACH TEST*****
C

```

Fig. F.3. Source Code for Lab Data Reduction Program - RCL

```

CALL XFBETA(WT/WM,BETA)
C
DO 300 I=1,ITEST
C
WRITE(6,*)' COMPUTING TEST',I
C
C*****COMPUTE DIMENSION AND STRESS CHANGE*****
C
SIGC(I)=(PT(I)-PTZERO)*PTC
PL=ALC*(AL(I)-ALZERO)-SIGC(I)*0.19635
IF(ALC.EQ.0.0)PL=0.0
AS=DI*DI*PIV/4.0
SIGA(I)=SIGC(I)+(PL+(WM+WF)/453.6)/AS
C
DZ=(PX2I-PX2(I))*PX2C/2.0+(PX3I-PX3(I))*PX3C/2.0
Z(I)=(ZI-DZ)
IF(I.EQ.1)THEN
    DD=PR*DZ*DI/Z(I)
    D(1)=DI-DD
    GOTO 210
ENDIF
DL=(PX2(I-1)-PX2(I))*PX2C/2.0+(PX3(I-1)-PX3(I))*PX3C/2.0
DSIGA=SIGA(I)-SIGA(I-1)
DSIGC=SIGC(I)-SIGC(I-1)
IF(DABS(DSIGA)-DSIGC).LE.0.5)THEN
    DD=PR*DL*D(I-1)/Z(I)
    GOTO 200
ELSEIF(DABS(DSIGA).GE.DABS(DSIGC))THEN
    DD=-1.*PR*DL*D(I-1)/Z(I)
    GOTO 200
ELSEIF(DABS(DSIGA).LT.DABS(DSIGC))THEN
    DD=-1.*DL*D(I-1)/Z(I)/PR
    GOTO 200
ENDIF
C
200 D(I)=D(I-1)-DD
210 V(I)=PI*D(I)*D(I)*Z(I)/4.0/1728.0
    GAM(I)=WT/453.6/V(I)
    AS=D(I)*D(I)*PIV/4.0
    SIGA(I)=SIGC(I)+(PL+(WF+WM)/453.6)/AS
    SIGM(I)=(SIGA(I)+2.*SIGC(I))/3.0
    VR(I)=(62.43*(1.+WC)*GS/GAM(I))-1.0
C
ZFT=Z(I)/12.0
DFT=D(I)/12.0
C
C*****COMPUTE Vp AND Vs*****

```

Fig. F.3. Source Code for Lab Data Reduction Program - RCL  
(continued).

```

C
  CP(I)=1000000.*ZFT/(PW(I)-PD)
  CSW(I)=1000000.*ZFT/(SW(I)-SD)
  GSW(I)=GAM(I)*CSW(I)*CSW(I)/32.17
C
C*****COMPUTE Vc*****
C
  DO 300 J=1,IC(I)
  C(J,I)=2.0*PI*FX(J,I)*ZFT/BETA(J)
  ZR=FX(J,I)*DFT/C(J,I)
  IF(C(J,I).GT.CP(I))GOTO 250
  B=(CP(I)*CP(I)-C(J,I)*C(J,I))/2./CP(I)/CP(I)
  POI=DSQRT(B*B/4.+B)-B/2.
  225 CALL LM1(ZR,POI,CR)
  CB(J,I)=C(J,I)/CR
  IF(CB(J,I).GT.CP(I))GOTO 250
  B=(CP(I)*CP(I)-CB(J,I)*CB(J,I))/2./CP(I)/CP(I)
  POS(J,I)=DSQRT(B*B/4.+B)-B/2.
  IF(DABS(POS(J,I)-POI).LT.0.0001)GOTO 275
  POI=POS(J,I)
  GOTO 225
  250 POS(J,I)=0.0
  CB(J,I)=CP(I)
  275 CS(J,I)=CB(J,I)/DSQRT(2.*(1.+POS(J,I)))
  E(J,I)=GAM(I)*CB(J,I)*CB(J,I)/32.17
  G(J,I)=GAM(I)*CS(J,I)*CS(J,I)/32.17
  PM(I)=GAM(I)*CP(I)*CP(I)/32.17
  300 CONTINUE
C
C*****INDIVIDUAL TEST OUTPUT*****
C
  OPEN(UNIT,FILE=' ')
  DO 500 I=1,ITEST
C
  WRITE(UNIT,2)TESTID,I,TIME(I)
  2 FORMAT(A50,5X,TEST NO. ',I3,/55X,TIME(hr):',F6.2)
  WRITE(UNIT,5)SIGA(I),SIGC(I),SIGM(I),SIGA(I)/SIGC(I)
  5 FORMAT(/1X,
  '*STRESSES:',/5X,'AXIAL = ',F10.2,' psi',/5X,'HORIZ. = ',
  '*F10.2,' psi',/5X,'MEAN = ',F10.2,/5X,'K0 = ',3X,F10.2)
  WRITE(UNIT,15)Z(I),D(I),WT/453.6,V(I),GAM(I),
  *GS,WC,VR(I),WM/453.6
  15 FORMAT(/1X,'SAMPLE PROPERTIES:',/5X,'HEIGHT (in):',F10.4,
  */5X,'DIAMETER (in):',F10.4,/5X,'WEIGHT (lb):',F10.4,
  */5X,'VOLUME (cf):',F10.4,/5X,'UNIT WT. (pcf):',F10.2,
  */5X,'SPECIFIC GRAVITY:',F10.3,/5X,'WATER CONTENT:',F10.6,
  */5X,'VOID RATIO:',F10.4,/5X,'ADDED MASS (lb):',F10.4/)

```

Fig. F.3. Source Code for Lab Data Reduction Program - RCL  
(continued).

```

WRITE(UNIT,25)
25 FORMAT(/1X,'MODE',2X,'r(Hz)',4X,'C(fps)',4X,'Cb(fps)',
*3X,'Cp(fps)',2X,'POI. RAT.',2X,'Cs(fps)')
WRITE(UNIT,35)(J,FX(J,I),C(J,I),CB(J,I),CP(I),POS(J,I),
*CS(J,I),J=1,IC(I))
35 FORMAT(I3,4F10.1,F10.4,F10.1)
WRITE(UNIT,45)
45 FORMAT(/1X,'MODULI (psf):',/10X,'YOUNGS',8X,'CONSTRAINED',6X,
*'SHEAR')
WRITE(UNIT,55)(J,E(J,I),PM(I),G(J,I),J=1,IC(I))
55 FORMAT(I3,3F15.0)
WRITE(UNIT,65)
65 FORMAT(/1X,'MODULI (psi):',/10X,'YOUNGS',8X,'CONSTRAINED',
*6X,'SHEAR')
WRITE(UNIT,75)(J,E(J,I)/144.,PM(I)/144.,G(J,I)/144.,J=1,IC(I))
75 FORMAT(I3,3F15.0)
WRITE(UNIT,85)CSW(I),GSW(I),GSW(I)/144.
85 FORMAT(/1X,'INDEPENDENT SHEAR WAVE VELOCITY:',F9.1,' fps',/1X,
*'INDEPENDENT SHEAR MODULUS:',F11.0,' psf',/1X,
*'INDEPENDENT SHEAR MODULUS:',F11.0,' psi',//)
DO 450 K=1,30-3*IC(I)
450 WRITE(UNIT,*)
500 CONTINUE
C
C*****MODULI SUMMARY OUTPUT*****
C
DO 800 J=1,IC(ITEST)
WRITE(UNIT,105)TESTID,J
105 FORMAT(/20X,A50,/25X,'TEST SUMMARY FOR MODE ',I2,/27X,
*(ALL VALUES IN psi))
WRITE(UNIT,115)J,J
115 FORMAT(/1X,'# SIGA SIGC SIGM VR PR',
*6X,'M',8X,'GM',6X,'E',I2,6X,'GB',I2,/)
C
DO 700 I=1,ITEST
C
WRITE(UNIT,125)I,SIGA(I),SIGC(I),SIGM(I),VR(I),
*POS(J,I),PM(I)/144.,GSW(I)/144.,E(J,I)/144.,G(J,I)/144.
125 FORMAT(1X,I2,3F7.2,2F7.4,4F9.0)
700 CONTINUE
800 CONTINUE
C
C*****STRESS-STATE SUMMARY OUTPUT*****
C
WRITE(UNIT,135)TESTID
135 FORMAT(/20X,A50,/25X,'STRESS-STATE SUMMARY ',/27X,
*(ALL VALUES IN psi))

```

Fig. F.3. Source Code for Lab Data Reduction Program - RCL  
(continued).

```

WRITE(UNIT,145)PR
145 FORMAT(/1X,'COMPUTATION FOR ASSUMED VALUE OF POISSONS',
  * RATIO = ',F10.4)
WRITE(UNIT,155)
155 FORMAT(/1X,'# VR SIGA SIGC Ko SIGM LENGTH',
  * DIAMETER GAMMA',)
C
DO 900 I=1,ITEST
C
WRITE(UNIT,165)I,VR(I),SIGA(I),SIGC(I),SIGA(I)/SIGC(I),
  *SIGM(I),Z(I),D(I),GAM(I)
165 FORMAT(1X,I2,F7.4,4F7.2,2F9.4,F9.2)
900 CONTINUE
END
C
C*****SUBPROGRAM TO CALCULATE BETA VALUES*****
C
SUBROUTINE XFBETA(WR,B)
IMPLICIT REAL*8(A-H,O-Z)
DIMENSION B(10)
PI=3.14159265358979
DO 40 I=1,10
D=(I-1)*PI+0.00000001
DW=0.1
10 D1=D+DW
IF(D1.GE.(2*I-1)*PI/2)GOTO 20
W=D1*DTAN(D1)
SUM=WR-W
IF(DABS(SUM).LE.0.000001)GOTO 40
IF(SUM)20,20,30
20 DW=DW/2.
GOTO 10
30 D=D1
GOTO 10
40 B(I)=D
RETURN
END
C
C*****SUBPROGRAM TO CALCULATE C/Cb RATIO OF 1ST MODE*****
C
SUBROUTINE LM1(AK,POI,W1)
IMPLICIT REAL*8(A-H,O-Z)
G2=0.5/(1.+POI)
A2=(1.-POI)/(1.+POI)/(1.-2.*POI)
CTB=DSQRT(G2)
CRT=(0.862+1.14*POI)/(1.+POI)
CLB=DSQRT(A2)

```

Fig. F.3. Source Code for Lab Data Reduction Program - RCL  
(continued).

```

CLT=CLB/CTB
CRB=CRT*CTB
AK2=AK*AK
W=CRB
CALL SUMP(SUM,W,G2,A2,AK2)
DW=0.1*POI
10 W1=W+DW
   IF(DW.LE.0.00001)GOTO 60
   CALL SUMP(SUM1,W1,G2,A2,AK2)
   IF(SUM*SUM1)40,50,50
40 DW=DW/2.
   GOTO 10
50 SUM=SUM1
   W=W1
   GOTO 10
60 CONTINUE
   RETURN
   END
C
C.....BESSEL FUNCTION, 1ST KIND, ORDER ZERO.....
C
SUBROUTINE BESJ0(X,Y)
IMPLICIT REAL*8(A-H,O-Z)
X2=X*X/4
DY=-X2
Y=1+DY
M=0
10 M=M+1
   AN=M+1
   AN2=AN*AN
   DY=-1.*DY*X2/AN2
   Y=Y+DY
   IF(DABS(DY/Y).GT.1.E-06)GOTO 10
   RETURN
   END
C
C.....BESSEL FUNCTION, 1ST KIND, ORDER ONE.....
C
SUBROUTINE BESJ1(X,Y)
IMPLICIT REAL*8(A-H,O-Z)
X2=X*X/4
AM=1.
SUM=AM
M=0
10 M=M+1
   DM=M*(M+1)
   AM=-AM*X2/DM

```

Fig. F.3. Source Code for Lab Data Reduction Program - RCL  
(continued).

```

SUM=SUM+AM
IF(DABS(AM/SUM).GT.1.E-06)GOTO 10
Y=X*SUM/2.
RETURN
END
C
C.....MODIFIED BESSEL FUNCTION, ORDER ZERO.....
C
SUBROUTINE BESI0(X,Y)
IMPLICIT REAL*8(A-H,O-Z)
X2=X*X/4
DY=X2
Y=1+DY
M=0
10 M=M+1
A=M+1
A2=A*A
DY=DY*X2/A2
Y=Y+DY
IF(DABS(DY/Y).GT.1.E-06)GOTO 10
RETURN
END
C
C.....MODIFIED BESSEL FUNCTION, ORDER ONE.....
C
SUBROUTINE BESI1(X,Y)
IMPLICIT REAL*8(A-H,O-Z)
X2=X*X/4
DY=1.
SUM=DY
M=0
10 M=M+1
A=M
A1=A+1.
DY=DY*X2/A/A1
SUM=SUM+DY
Y=SUM*X2
IF(DABS(DY/Y).GT.1.E-06)GOTO 10
RETURN
END
C
C.....SUBPROGRAM TO CALCULATE SUM.....
C
SUBROUTINE SUMP(SUM,W,G2,A2,AK2)
IMPLICIT REAL*8(A-H,O-Z)
TPI=6.28318530717958
PI2=TPI*TPI/4.

```

Fig. F.3. Source Code for Lab Data Reduction Program - RCL  
(continued).

```

Q2=AK2*PI2*(W*W/G2-1.)
P2=AK2*PI2*(W*W/A2-1.)
Q=DSQRT(DABS(Q2))
P=DSQRT(DABS(P2))
TERM1=4.*P*Q*AK2*PI2
TERM2=2.*P*(Q2+AK2*PI2)
TERM3=(Q2-AK2*PI2)*(Q2-AK2*PI2)
IF(P2)20,10,10
10 CALL BESJ0(P,BP0)
   CALL BESJ1(P,BP1)
   CALL BESJ0(Q,BQ0)
   CALL BESJ1(Q,BQ1)
   SUM=TERM1*BQ0/BQ1-TERM2+TERM3*BP0/BP1
   GOTO 50
20 IF(Q2)40,30,30
30 CALL BESJ0(P,BIP0)
   CALL BESJ1(P,BIP1)
   CALL BESJ0(Q,BQ0)
   CALL BESJ1(Q,BQ1)
   SUM=TERM1*BQ0/BQ1-TERM2-TERM3*BIP0/BIP1
   GOTO 50
40 CALL BESJ0(P,BIP0)
   CALL BESJ1(P,BIP1)
   CALL BESJ0(Q,BIQ0)
   CALL BESJ1(Q,BIQ1)
   SUM=TERM1*BIQ0/BIQ1-TERM2-TERM3*BIP0/BIP1
50 CONTINUE
   RETURN
   END

```

Fig. F.3. Source Code for Lab Data Reduction Program - RCL  
(continued).

**Appendix G**  
**Test Data**

## ISO1 Test Series, 19-21 April 90

## Test Summary

Test #	$\sigma_a$ psi	$\sigma_h$ psi	$\sigma_o$ psi	void ratio	$v$	M psi	$G_m$ psi	E psi	$G_b$ psi
--------	-------------------	-------------------	-------------------	---------------	-----	----------	--------------	----------	--------------

## Mode 1

1	4.13	3.96	4.02	0.594	0.239	31904	10924	27109	10939
2	8.17	7.99	8.05	0.594	0.215	40903	14926	36110	14866
3	16.17	16.00	16.06	0.594	0.194	53550	19841	48569	20344
4	32.18	32.01	32.07	0.593	0.215	71440	25820	62987	25911
5	64.16	63.98	64.04	0.592	0.089	97366	34491	95662	43910
6	32.18	32.00	32.06	0.593	0.215	72144	26765	63646	26192
7	16.17	16.00	16.06	0.593	0.193	52941	19703	48084	20161
8	8.17	7.99	8.05	0.594	0.197	37637	13582	34012	14211
9	4.15	3.98	4.04	0.594	0.197	26939	9232	24351	10176
10	8.19	8.02	8.07	0.594	0.189	36319	13660	33105	13916
11	16.18	16.01	16.06	0.593	0.184	50613	17921	46428	19612
12	32.15	31.97	32.03	0.593	0.201	69812	25514	62764	26133
13	64.17	63.99	64.05	0.592	0.000	96619	32668	96619	48309
14	32.18	32.00	32.06	0.593	0.199	71666	24919	64558	26916
15	16.18	16.00	16.06	0.593	0.180	51608	19364	47513	20127
16	8.18	8.01	8.07	0.594	0.167	36318	13426	33898	14528
17	4.17	4.00	4.06	0.594	0.198	26190	9123	23627	9861
18	16.18	16.01	16.06	0.594	0.184	50475	19433	46314	19567
19	64.14	63.97	64.03	0.592	0.000	97371	35628	97371	48686
20	16.18	16.01	16.07	0.593	0.168	52195	19365	48652	20826
21	4.21	4.04	4.09	0.594	0.188	25931	9081	23668	9960
22	64.15	63.98	64.04	0.592	0.000	97368	37527	97368	48684
23	4.20	4.03	4.09	0.594	0.188	25777	8891	23541	9910

## ISO1 Test Series, 19-21 April 90

## Test Summary (continued)

Test #	$\sigma_a$ psi	$\sigma_h$ psi	$\sigma_o$ psi	void ratio	$v$	M psi	$G_m$ psi	E psi	$G_b$ psi
--------	-------------------	-------------------	-------------------	---------------	-----	----------	--------------	----------	--------------

## Mode 2

1	4.13	3.96	4.02	0.594	0.238	31904	10924	27146	10961
2	8.17	7.99	8.05	0.594	0.213	40903	14926	36184	14914
3	16.17	16.00	16.06	0.594	0.191	53550	19841	48724	20456
4	32.18	32.01	32.07	0.593	0.183	71440	25820	65557	27699
5	64.16	63.98	64.04	0.592	0.184	97366	34491	89337	37743
6	32.18	32.00	32.06	0.593	0.181	72144	26765	66357	28089
7	16.17	16.00	16.06	0.593	0.186	52941	19703	48456	20433
8	8.17	7.99	8.05	0.594	0.200	37637	13582	33858	14103
9	4.15	3.98	4.04	0.594	0.232	26939	9232	23182	9412
10	8.19	8.02	8.07	0.594	0.192	36319	13660	33002	13842
11	16.18	16.01	16.06	0.593	0.183	50613	17921	46487	19656
12	32.15	31.97	32.03	0.593	0.172	69812	25514	64857	27682
13	64.17	63.99	64.05	0.592	0.165	96619	32668	90357	38796
14	32.18	32.00	32.06	0.593	0.166	71666	24919	66935	28705
15	16.18	16.00	16.06	0.593	0.174	51608	19364	47851	20389
16	8.18	8.01	8.07	0.594	0.179	36318	13426	33478	14196
17	4.17	4.00	4.06	0.594	0.227	26190	9123	22696	9248
18	16.18	16.01	16.06	0.594	0.185	50475	19433	46248	19518
19	64.14	63.97	64.03	0.592	0.166	97371	35628	90930	38989
20	16.18	16.01	16.07	0.593	0.178	52195	19365	48151	20431
21	4.21	4.04	4.09	0.594	0.220	25931	9081	22699	9300
22	64.15	63.98	64.04	0.592	0.162	97368	37527	91253	39258
23	4.20	4.03	4.09	0.594	0.219	25777	8891	22621	9281

## ISO1 Test Series, 19-21 April 90

## Test Summary (continued)

Test #	$\sigma_a$ psi	$\sigma_h$ psi	$\sigma_o$ psi	void ratio	$\nu$	M psi	$G_m$ psi	E psi	$G_o$ psi
--------	-------------------	-------------------	-------------------	---------------	-------	----------	--------------	----------	--------------

## Mode 3

1	4.13	3.96	4.02	0.594	0.223	31904	10924	27824	11376
2	8.17	7.99	8.05	0.594	0.188	40903	14926	37339	15714
3	16.17	16.00	16.06	0.594	0.171	53550	19841	49756	21239
4	32.18	32.01	32.07	0.593	0.164	71440	25820	66823	28696
5	64.16	63.98	64.04	0.592	0.156	97366	34491	91722	39659
6	32.18	32.00	32.06	0.593	0.156	72144	26765	68015	29432
7	16.17	16.00	16.06	0.593	0.161	52941	19703	49656	21379
8	8.17	7.99	8.05	0.594	0.176	37637	13582	34803	14796
9	4.15	3.98	4.04	0.594	0.199	26939	9232	24272	10121
10	8.19	8.02	8.07	0.594	0.178	36319	13660	33538	14242
11	16.18	16.01	16.06	0.593	0.162	50613	17921	47438	20411
12	32.15	31.97	32.03	0.593	0.153	69812	25514	65952	28600
13	64.17	63.99	64.05	0.592	0.143	96619	32668	92033	40272
14	32.18	32.00	32.06	0.593	0.145	71666	24919	68160	29773
15	16.18	16.00	16.06	0.593	0.151	51608	19364	48644	21221
16	8.18	8.01	8.07	0.594	0.163	36318	13426	33998	14611
17	4.17	4.00	4.06	0.594	0.193	26190	9123	23764	9958
18	16.18	16.01	16.06	0.594	0.164	50475	19433	47217	20278
19	64.14	63.97	64.03	0.592	0.140	97371	35628	92907	40735
20	16.18	16.01	16.07	0.593	0.156	52195	19365	49202	21289
21	4.21	4.04	4.09	0.594	0.190	25931	9081	23628	9930
22	64.15	63.98	64.04	0.592	0.137	97368	37527	93159	40981
23	4.20	4.03	4.09	0.594	0.189	25777	8891	23521	9895

## ISO1 Test Series, 19-21 April 90

## Test Summary (continued)

Test #	$\sigma_a$ psi	$\sigma_h$ psi	$\sigma_o$ psi	void ratio	$v$	M psi	$G_m$ psi	E psi	$G_b$ psi
--------	-------------------	-------------------	-------------------	---------------	-----	----------	--------------	----------	--------------

## Mode 4

1	4.13	3.96	4.02	0.594	0.000	31904	10924	31904	15952
2	8.17	7.99	8.05	0.594	0.000	40903	14926	40903	20451
3	16.17	16.00	16.06	0.594	0.000	53550	19841	53550	26775
4	32.18	32.01	32.07	0.593	0.000	71440	25820	71440	35720
5	64.16	63.98	64.04	0.592	0.000	97366	34491	97366	48683
6	32.18	32.00	32.06	0.593	0.000	72144	26765	72144	36072
7	16.17	16.00	16.06	0.593	0.000	52941	19703	52941	26470
8	8.17	7.99	8.05	0.594	0.000	37637	13582	37637	18818
9	4.15	3.98	4.04	0.594	0.000	26939	9232	26939	13470
10	8.19	8.02	8.07	0.594	0.000	36319	13660	36319	18160
11	16.18	16.01	16.06	0.593	0.000	50613	17921	50613	25306
12	32.15	31.97	32.03	0.593	0.000	69812	25514	69812	34906
13	64.17	63.99	64.05	0.592	0.000	96619	32668	96619	48309
14	32.18	32.00	32.06	0.593	0.000	71666	24919	71666	35833
15	16.18	16.00	16.06	0.593	0.000	51608	19364	51608	25804
16	8.18	8.01	8.07	0.594	0.000	36318	13426	36318	18159
17	4.17	4.00	4.06	0.594	0.000	26190	9123	26190	13095
18	16.18	16.01	16.06	0.594	0.000	50475	19433	50475	25238
19	64.14	63.97	64.03	0.592	0.000	97371	35628	97371	48686
20	16.18	16.01	16.07	0.593	0.000	52195	19365	52195	26098
21	4.21	4.04	4.09	0.594	0.000	25931	9081	25931	12966
22	64.15	63.98	64.04	0.592	0.000	97368	37527	97368	48684
23	4.20	4.03	4.09	0.594	0.000	25777	8891	25777	12888

## ISO2 Test Series, 3-4 May 90

## Test Summary

Test #	$\sigma_a$ psi	$\sigma_h$ psi	$\sigma_o$ psi	void ratio	$\nu$	M psi	$G_m$ psi	E psi	$G_o$ psi
--------	----------------	----------------	----------------	------------	-------	-------	-----------	-------	-----------

## Mode 1

1	4.18	4.01	4.06	0.760	0.310	25133	6376	18116	6913
2	8.19	8.01	8.07	0.759	0.312	34040	9796	24423	9309
3	16.16	15.99	16.05	0.759	0.294	43604	12643	32962	12740
4	32.18	32.00	32.06	0.757	0.286	57300	18353	44163	17170
5	64.14	63.97	64.02	0.756	0.218	80098	25063	70374	28892
6	32.18	32.00	32.06	0.757	0.296	58765	18221	44165	17042
7	16.16	15.99	16.05	0.758	0.307	43838	12791	31896	12200
8	8.18	8.01	8.07	0.758	0.309	31317	9423	22653	8652
9	4.18	4.01	4.07	0.759	0.306	22213	6191	16199	6200
10	16.17	16.00	16.05	0.758	0.300	43009	13103	31975	12301
11	64.17	64.00	64.05	0.756	0.210	79215	26142	70371	29079
12	16.17	16.00	16.05	0.758	0.279	41520	13181	32582	12741
13	4.18	4.01	4.06	0.759	0.301	22836	6041	16916	6501

## Mode 2

1	4.18	4.01	4.06	0.760	0.303	25133	6376	18515	7105
2	8.19	8.01	8.07	0.759	0.289	34040	9796	26041	10101
3	16.16	15.99	16.05	0.759	0.263	43604	12643	35427	14026
4	32.18	32.00	32.06	0.757	0.242	57300	18353	48488	19528
5	64.14	63.97	64.02	0.756	0.247	80098	25063	67068	26883
6	32.18	32.00	32.06	0.757	0.254	58765	18221	48595	19375
7	16.16	15.99	16.05	0.758	0.278	43838	12791	34432	13468
8	8.18	8.01	8.07	0.758	0.292	31317	9423	23782	9204
9	4.18	4.01	4.07	0.759	0.299	22213	6191	16570	6380
10	16.17	16.00	16.05	0.758	0.272	43009	13103	34285	13479
11	64.17	64.00	64.05	0.756	0.233	79215	26142	68036	27597
12	16.17	16.00	16.05	0.758	0.250	41520	13181	34608	13845
13	4.18	4.01	4.06	0.759	0.309	22836	6041	16549	6324

## ISO2 Test Series, 3-4 May 90

## Test Summary (continued)

Test #	$\sigma_a$ psi	$\sigma_h$ psi	$\sigma_o$ psi	void ratio	$v$	M psi	$G_m$ psi	E psi	$G_b$ psi
--------	-------------------	-------------------	-------------------	---------------	-----	----------	--------------	----------	--------------

## Mode 3

1	4.18	4.01	4.06	0.760	0.300	25133	6376	18698	7194
2	8.19	8.01	8.07	0.759	0.288	34040	9796	26095	10128
3	16.16	15.99	16.05	0.759	0.256	43604	12643	35901	14288
4	32.18	32.00	32.06	0.757	0.233	57300	18353	49169	19935
5	64.14	63.97	64.02	0.756	0.232	80098	25063	68854	27941
6	32.18	32.00	32.06	0.757	0.242	58765	18221	49701	20011
7	16.16	15.99	16.05	0.758	0.268	43838	12791	35206	13878
8	8.18	8.01	8.07	0.758	0.285	31317	9423	24187	9409
9	4.18	4.01	4.07	0.759	0.296	22213	6191	16707	6448
10	16.17	16.00	16.05	0.758	0.262	43009	13103	35017	13875
11	64.17	64.00	64.05	0.756	0.217	79215	26142	69664	28616
12	16.17	16.00	16.05	0.758	0.242	41520	13181	35136	14151
13	4.18	4.01	4.06	0.759	0.304	22836	6041	16796	6443

## Mode 4

1	4.18	4.01	4.06	0.760	0.287	25133	6376	19341	7516
2	8.19	8.01	8.07	0.759	0.274	34040	9796	26985	10589
3	16.16	15.99	16.05	0.759	0.239	43604	12643	37058	14955
4	32.18	32.00	32.06	0.757	0.206	57300	18353	51167	21212
5	64.14	63.97	64.02	0.756	0.204	80098	25063	71745	29801
6	32.18	32.00	32.06	0.757	0.214	58765	18221	51888	21363
7	16.16	15.99	16.05	0.758	0.247	43838	12791	36705	14713
8	8.18	8.01	8.07	0.758	0.264	31317	9423	25412	10056
9	4.18	4.01	4.07	0.759	0.276	22213	6191	17547	6877
10	16.17	16.00	16.05	0.758	0.238	43009	13103	36591	14774
11	64.17	64.00	64.05	0.756	0.000	79215	26142	79215	39608
12	16.17	16.00	16.05	0.758	0.216	41520	13181	36602	15056
13	4.18	4.01	4.06	0.759	0.283	22836	6041	17724	6906

## BIAX1 Test Series, 5-6 May 90

## Test Summary

Test #	$\sigma_a$ psi	$\sigma_h$ psi	$\sigma_o$ psi	void ratio	$\nu$	M psi	$G_m$ psi	E psi	$G_o$ psi
--------	-------------------	-------------------	-------------------	---------------	-------	----------	--------------	----------	--------------

## Mode 3

1	4.00	4.01	4.01	0.762	0.317	27030	7218	19081	7245
2	15.98	16.01	16.00	0.760	0.263	45485	13724	36951	14629
3	18.29	16.01	16.77	0.760	0.258	47306	14421	38821	15430
4	21.32	16.01	17.78	0.760	0.267	51623	14834	41584	16411
5	25.54	16.01	19.19	0.760	0.267	55502	16197	44728	17654
6	31.90	16.01	21.31	0.759	0.275	61971	17137	49084	19254
7	33.03	32.01	32.35	0.754	0.247	62592	19764	52452	21032
8	64.00	63.99	64.00	0.759	0.236	83045	25556	70972	28717
9	32.00	32.00	32.00	0.760	0.242	61793	20074	52236	21027
10	28.46	32.00	30.82	0.760	0.240	57776	18663	49001	19755
11	25.64	32.00	29.88	0.760	0.253	56527	18335	46868	18707
12	23.33	32.00	29.11	0.760	0.258	54474	17578	44689	17760
13	21.40	32.00	28.46	0.760	0.251	50982	16811	42402	16947
14	16.00	16.01	16.01	0.762	0.265	45112	14344	36501	14429
15	4.00	4.01	4.01	0.763	0.328	26386	6639	17965	6766

## BIAX2 Test Series, 21-22 May 90

## Test Summary

Test #	$\sigma_a$ psi	$\sigma_h$ psi	$\sigma_o$ psi	void ratio	$\nu$	M psi	$G_m$ psi	E psi	$G_o$ psi
--------	-------------------	-------------------	-------------------	---------------	-------	----------	--------------	----------	--------------

## Mode 3

1	4.01	4.00	4.00	0.775	0.301	28751	7728	21295	8184
2	15.99	16.00	15.99	0.773	0.228	44419	14854	38442	15653
3	64.00	64.00	64.00	0.770	0.194	77198	26902	70001	29317
4	16.01	16.01	16.01	0.772	0.232	42509	14432	36571	14846
5	4.02	4.00	4.01	0.773	0.287	24694	7585	19011	7388
6	16.00	16.00	16.00	0.772	0.229	42167	14208	36432	14822
7	18.31	16.00	16.77	0.772	0.242	46158	14939	39011	15702
8	21.39	16.01	17.80	0.772	0.240	49282	16315	41830	16871
9	25.68	16.01	19.23	0.771	0.229	52413	17397	45295	18430
10	32.09	16.00	21.36	0.771	0.238	58887	18714	50173	20272
11	32.10	20.00	24.03	0.770	0.233	60454	19631	51884	21037
12	32.08	24.00	26.69	0.769	0.229	60899	20164	52619	21408
13	32.04	28.01	29.35	0.767	0.226	61160	20185	53118	21670
14	32.00	32.00	32.00	0.764	0.224	61293	21004	53404	21824
15	64.00	63.99	63.99	0.763	0.198	80601	28172	72768	30384
16	32.02	32.01	32.01	0.765	0.209	59356	21005	52781	21824
17	25.54	32.00	29.85	0.765	0.213	53603	19581	47418	19545
18	21.20	31.98	28.39	0.765	0.218	49501	18232	43483	17850
19	18.15	32.00	27.38	0.766	0.216	44257	16799	38982	16027
20	15.81	32.01	26.61	0.767	0.221	39550	15550	34614	14180
21	15.84	28.01	23.95	0.767	0.220	39465	15456	34554	14158
22	15.89	24.00	21.30	0.768	0.225	39841	15243	34657	14151
23	15.96	20.00	18.66	0.770	0.235	40103	14559	34320	13896
24	16.00	16.00	16.00	0.791	0.243	40008	14200	33758	13578
25	4.00	4.01	4.00	0.796	0.300	22658	7120	16837	6476

## BIAX3 Test Series, 1-2 June 90

## Test Summary

Test #	$\sigma_a$ psi	$\sigma_h$ psi	$\sigma_o$ psi	void ratio	$\nu$	M psi	$G_m$ psi	E psi	$G_o$ psi
--------	-------------------	-------------------	-------------------	---------------	-------	----------	--------------	----------	--------------

## Mode 3

1	4.00	4.01	4.00	0.588	0.232	45072	15486	38743	15721
2	16.00	16.00	16.00	0.588	0.181	61930	22854	56968	24116
3	64.02	64.00	64.01	0.586	0.171	105440	39079	98008	41852
4	16.02	16.01	16.01	0.587	0.180	55430	21310	51073	21649
5	4.02	4.01	4.01	0.588	0.215	30916	11446	27264	11217
6	16.00	16.01	16.00	0.588	0.184	56090	21160	51427	21715
7	18.27	16.00	16.76	0.587	0.190	59684	22178	54361	22840
8	21.30	16.00	17.77	0.587	0.195	64450	23630	58339	24403
9	25.55	16.00	19.18	0.587	0.198	70038	24550	63230	26401
10	31.90	16.00	21.30	0.587	0.212	80158	26558	71062	29328
11	31.93	20.01	23.98	0.587	0.201	80457	27897	72330	30115
12	31.96	24.00	26.65	0.586	0.193	80514	28985	73119	30656
13	31.98	28.00	29.33	0.585	0.185	80540	29741	73740	31103
14	32.01	32.00	32.00	0.583	0.182	80931	30165	74357	31447
15	64.01	64.01	64.01	0.583	0.157	105620	39729	99433	42964
16	32.02	32.01	32.01	0.584	0.165	80935	30559	75631	32450
17	25.61	32.00	29.87	0.584	0.181	74041	28442	68136	28853
18	21.38	32.00	28.46	0.584	0.182	68425	27299	62906	26618
19	18.34	32.00	27.45	0.584	0.198	65447	25809	59061	24653
20	16.06	32.00	26.69	0.584	0.320	61516	24918	42943	16263
21	16.07	28.01	24.03	0.585	0.417	113340	24244	45598	16086
22	16.02	23.99	21.34	0.586	0.417	113270	23590	45577	16079
23	16.16	20.00	18.72	0.587	0.417	113180	22957	45549	16069
24	16.00	16.01	16.00	0.588	0.417	113050	21617	45510	16056
25	4.01	4.01	4.01	0.589	0.417	113080	11031	45514	16057

BIAX4 Test Series, 2-5 July 90  
Test Summary (Mode 2)

Test #	$\sigma_a$ psi	$\sigma_h$ psi	$\sigma_o$ psi	void ratio	$\nu$	M psi	$G_m$ psi	E psi	$G_b$ psi
1	3.78	3.77	3.77	0.584	0.333	39383	11676	26272	9853
2	15.79	15.78	15.78	0.583	0.242	58981	22285	49877	20081
3	63.77	63.76	63.77	0.581	0.213	101740	38600	90052	37129
4	15.80	15.79	15.79	0.582	0.230	57587	22528	49695	20205
5	3.79	3.78	3.78	0.583	0.310	33502	10852	24193	9236
6	7.79	7.77	7.78	0.583	0.278	42638	14441	33505	13108
7	8.92	7.78	8.16	0.583	0.266	44191	15148	35695	14101
8	10.46	7.78	8.68	0.583	0.271	47565	16056	37979	14940
9	12.56	7.78	9.37	0.583	0.264	50492	17048	40906	16178
10	15.74	7.78	10.43	0.583	0.236	54779	18253	46778	18920
11	15.76	9.78	11.77	0.582	0.241	56398	20220	47787	19257
12	15.76	11.77	13.10	0.582	0.237	56740	21252	48388	19559
13	15.77	13.77	14.43	0.582	0.235	57087	21880	48863	19786
14	15.79	15.77	15.78	0.581	0.233	57441	22290	49337	20012
15	18.07	15.78	16.54	0.581	0.242	61544	23482	52049	20957
16	21.10	15.78	17.55	0.581	0.228	63455	24203	54909	22357
17	25.35	15.78	18.97	0.581	0.224	67560	25547	58786	24006
18	31.72	15.78	21.09	0.581	0.228	74752	26893	64708	26351
19	31.74	19.77	23.76	0.581	0.226	76037	28015	65986	26907
20	31.76	23.78	26.44	0.580	0.222	76318	28849	66702	27304
21	31.77	27.78	29.11	0.580	0.226	77661	29849	67458	27522
22	31.79	31.78	31.78	0.579	0.224	78231	30507	68114	27825
23	63.78	63.78	63.78	0.579	0.222	105130	40181	91883	37612
24	31.79	31.78	31.79	0.579	0.220	78769	30902	68948	28247
25	25.41	31.78	29.66	0.579	0.230	73379	29492	63287	25724
26	21.15	31.78	28.23	0.580	0.231	68085	28060	58623	23808
27	18.11	31.78	27.22	0.580	0.232	63346	26624	54496	22123
28	15.83	31.78	26.46	0.580	0.231	58737	25296	50572	20538
29	15.82	27.78	23.79	0.580	0.234	58894	24516	50472	20450
30	15.82	23.78	21.13	0.581	0.236	58520	24225	50022	20242
31	15.81	19.78	18.46	0.581	0.242	58665	23489	49587	19960
32	15.78	15.77	15.78	0.582	0.230	56591	22784	48853	19867
33	12.61	15.78	14.72	0.582	0.259	52985	21495	43382	17227
34	10.48	15.78	14.02	0.582	0.258	49030	20239	40221	15984
35	8.96	15.78	13.51	0.582	0.263	46226	19686	37544	14862
36	7.83	15.78	13.13	0.582	0.277	44568	18646	35136	13761
37	7.82	13.79	11.80	0.583	0.268	42660	17797	34296	13525
38	7.80	11.78	10.45	0.583	0.271	42538	17057	33980	13369
39	7.81	9.79	9.13	0.583	0.275	42521	15907	33639	13190
40	7.82	7.81	7.81	0.584	0.276	42077	14869	33262	13039
41	3.79	3.77	3.78	0.584	0.310	32742	10573	23592	9002

BIAX4 Test Series, 2-5 July 90  
Test Summary (Mode 3)

Test #	$\sigma_a$ psi	$\sigma_h$ psi	$\sigma_o$ psi	void ratio	$\nu$	M psi	$G_m$ psi	E psi	$G_b$ psi
1	3.78	3.77	3.77	0.584	0.318	39383	11676	27692	10504
2	15.79	15.78	15.78	0.583	0.222	58981	22285	51475	21055
3	63.77	63.76	63.77	0.581	0.000	101740	38600	0	0
4	15.80	15.79	15.79	0.582	0.208	57587	22528	51302	21236
5	3.79	3.78	3.78	0.583	0.293	33502	10852	25402	9827
6	7.79	7.77	7.78	0.583	0.256	42638	14441	35096	13967
7	8.92	7.78	8.16	0.583	0.247	44191	15148	37063	14867
8	10.46	7.78	8.68	0.583	0.250	47565	16056	39613	15841
9	12.56	7.78	9.37	0.583	0.233	50492	17048	43354	17583
10	15.74	7.78	10.43	0.583	0.221	54779	18253	47879	19599
11	15.76	9.78	11.77	0.582	0.223	56398	20220	49167	20098
12	15.76	11.77	13.10	0.582	0.222	56740	21252	49585	20296
13	15.77	13.77	14.43	0.582	0.218	57087	21880	50146	20584
14	15.79	15.77	15.78	0.581	0.214	57441	22290	50718	20881
15	18.07	15.78	16.54	0.581	0.221	61544	23482	53844	22053
16	21.10	15.78	17.55	0.581	0.210	63455	24203	56405	23316
17	25.35	15.78	18.97	0.581	0.204	67560	25547	60480	25112
18	31.72	15.78	21.09	0.581	0.208	74752	26893	66548	27535
19	31.74	19.77	23.76	0.581	0.205	76037	28015	68032	28238
20	31.76	23.78	26.44	0.580	0.201	76318	28849	68618	28572
21	31.77	27.78	29.11	0.580	0.203	77661	29849	69606	28924
22	31.79	31.78	31.78	0.579	0.200	78231	30507	70388	29323
23	63.78	63.78	63.78	0.579	0.000	105130	40181	0	0
24	31.79	31.78	31.79	0.579	0.194	78769	30902	71424	29913
25	25.41	31.78	29.66	0.579	0.206	73379	29492	65544	27177
26	21.15	31.78	28.23	0.580	0.206	68085	28060	60807	25210
27	18.11	31.78	27.22	0.580	0.207	63346	26624	56536	23430
28	15.83	31.78	26.46	0.580	0.207	58737	25296	52359	21682
29	15.82	27.78	23.79	0.580	0.210	58894	24516	52303	21609
30	15.82	23.78	21.13	0.581	0.212	58520	24225	51874	21408
31	15.81	19.78	18.46	0.581	0.220	58665	23489	51393	21065
32	15.78	15.77	15.78	0.582	0.211	56591	22784	50240	20752
33	12.61	15.78	14.72	0.582	0.221	52985	21495	46374	18998
34	10.48	15.78	14.02	0.582	0.227	49030	20239	42517	17330
35	8.96	15.78	13.51	0.582	0.238	46226	19686	39347	15890
36	7.83	15.78	13.13	0.582	0.249	44568	18646	37184	14881
37	7.82	13.79	11.80	0.583	0.238	42660	17797	36291	14652
38	7.80	11.78	10.45	0.583	0.242	42538	17057	35979	14487
39	7.81	9.79	9.13	0.583	0.250	42521	15907	35462	14189
40	7.82	7.81	7.81	0.584	0.250	42077	14869	35061	14024
41	3.79	3.77	3.78	0.584	0.299	32742	10573	24378	9382

BIAX5 Test Series, 6-8 August 90  
Test Summary (Mode 2)

Test #	$\sigma_a$ psi	$\sigma_h$ psi	$\sigma_o$ psi	void ratio	$\nu$	M psi	$G_m$ psi	E psi	$G_o$ psi
1	4.03	4.02	4.02	0.753	0.332	26411	7217	17721	6654
2	16.01	16.01	16.01	0.753	0.286	45456	15290	35053	13630
3	64.00	64.00	64.00	0.749	0.242	80026	28027	67684	27252
4	16.02	16.01	16.01	0.752	0.288	45576	15253	34966	13575
5	3.99	4.01	4.00	0.753	0.324	24451	6774	16879	6376
6	8.04	8.02	8.03	0.752	0.299	32282	9177	24054	9259
7	9.15	8.01	8.39	0.752	0.302	34509	9458	25470	9779
8	10.68	8.02	8.91	0.752	0.296	36789	12703	27617	10653
9	12.79	8.01	9.60	0.752	0.296	40443	13321	30418	11740
10	15.98	8.01	10.67	0.752	0.293	45537	14887	34498	13342
11	15.98	10.00	12.00	0.752	0.293	46320	15278	35110	13582
12	16.00	12.00	13.34	0.751	0.293	46729	15483	35383	13683
13	16.01	14.00	14.67	0.751	0.292	46881	15692	35611	13784
14	16.01	16.00	16.00	0.750	0.291	46902	15907	35711	13832
15	18.29	16.01	16.77	0.750	0.283	48253	16443	37499	14617
16	21.33	16.01	17.78	0.750	0.267	50836	17121	40985	16180
17	25.59	16.02	19.21	0.750	0.268	54949	18093	44214	17441
18	31.96	16.01	21.33	0.749	0.265	61108	19280	49431	19538
19	31.99	20.01	24.00	0.749	0.267	61727	20007	49698	19609
20	32.01	24.01	26.68	0.748	0.266	61963	20318	49986	19737
21	32.02	28.02	29.36	0.747	0.263	62004	20637	50390	19953
22	32.01	32.01	32.01	0.746	0.260	62053	20967	50691	20112
23	64.00	64.00	64.00	0.745	0.245	82911	28842	69772	28029
24	32.01	32.00	32.00	0.746	0.257	62053	21127	50984	20274
25	25.61	32.00	29.87	0.746	0.258	55572	19762	45625	18138
26	21.34	32.00	28.45	0.747	0.256	50651	18527	41696	16594
27	18.31	32.02	27.45	0.747	0.267	45722	17289	36804	14520
28	16.01	32.00	26.67	0.747	0.263	41165	16393	33445	13241
29	16.01	28.01	24.01	0.748	0.264	41371	15854	33562	13280
30	16.02	24.01	21.35	0.749	0.265	41451	15435	33551	13264
31	16.01	20.01	18.68	0.750	0.264	41305	15322	33487	13247
32	16.00	16.00	16.00	0.751	0.273	42261	15108	33617	13207
33	12.82	16.01	14.94	0.752	0.271	37879	14186	30229	11889
34	10.70	16.02	14.25	0.752	0.281	34728	13186	27104	10580
35	9.18	16.01	13.74	0.752	0.283	31089	12081	24122	9398
36	8.04	16.02	13.36	0.752	0.276	28859	11229	22767	8918
37	8.02	14.01	12.01	0.752	0.275	28726	10864	22735	8916
38	8.03	12.01	10.68	0.753	0.278	28907	10514	22722	8890
39	7.98	9.98	9.32	0.753	0.281	29148	10178	22735	8872
40	8.01	7.99	8.00	0.755	0.281	29514	9653	23019	8983
41	4.02	4.02	4.02	0.755	0.320	22700	6759	15863	6009

BIAX5 Test Series, 6-8 August 90  
Test Summary (Mode 3)

Test #	$\sigma_a$ psi	$\sigma_h$ psi	$\sigma_o$ psi	void ratio	$\nu$	M psi	$G_m$ psi	E psi	$G_b$ psi
1	4.03	4.02	4.02	0.753	0.317	26411	7217	18673	7092
2	16.01	16.01	16.01	0.753	0.268	45456	15290	36549	14414
3	64.00	64.00	64.00	0.749	0.000	80026	28037	0	0
4	16.02	16.01	16.01	0.752	0.268	45576	15263	36605	14430
5	3.99	4.01	4.00	0.753	0.303	24451	6774	17992	6902
6	8.04	8.02	8.03	0.752	0.283	32282	9177	25097	9784
7	9.15	8.01	8.39	0.752	0.284	34509	9458	26759	10423
8	10.68	8.02	8.91	0.752	0.278	36789	12703	28923	11317
9	12.79	8.01	9.60	0.752	0.281	40443	13321	31526	12301
10	15.98	8.01	10.67	0.752	0.280	45537	14887	35627	13917
11	15.98	10.00	12.00	0.752	0.278	46320	15278	36392	14237
12	16.00	12.00	13.34	0.751	0.276	46729	15483	36899	14459
13	16.01	14.00	14.67	0.751	0.274	46881	15692	37198	14601
14	16.01	16.00	16.00	0.750	0.271	46902	15907	37423	14718
15	18.29	16.01	16.77	0.750	0.259	48253	16443	39507	15688
16	21.33	16.01	17.78	0.750	0.256	50836	17121	41897	16681
17	25.59	16.02	19.21	0.750	0.258	54949	18093	45065	17907
18	31.96	16.01	21.33	0.749	0.263	61108	19280	49689	19679
19	31.99	20.01	24.00	0.749	0.258	61727	20007	50632	20121
20	32.01	24.01	26.68	0.746	0.255	61963	20318	51194	20404
21	32.02	28.02	29.36	0.747	0.251	62004	20637	51599	20628
22	32.01	32.01	32.01	0.746	0.247	62053	20967	52011	20857
23	64.00	64.00	64.00	0.745	0.000	82911	28842	0	0
24	32.01	32.00	32.00	0.746	0.243	62053	21127	52409	21089
25	25.61	32.00	29.87	0.746	0.240	55572	19762	47172	19026
26	21.34	32.00	28.45	0.747	0.242	50651	18527	42843	17251
27	18.31	32.02	27.45	0.747	0.238	45722	17289	38924	15720
28	16.01	32.00	26.67	0.747	0.238	41165	16393	35019	14139
29	16.01	28.01	24.01	0.748	0.240	41371	15854	35096	14151
30	16.02	24.01	21.35	0.749	0.242	41451	15435	35071	14123
31	16.01	20.01	18.68	0.750	0.242	41305	15322	34915	14055
32	16.00	16.00	16.00	0.751	0.252	42261	15108	35087	14013
33	12.82	16.01	14.94	0.752	0.248	37879	14186	31696	12701
34	10.70	16.02	14.25	0.752	0.254	34728	13186	28706	11443
35	9.18	16.01	13.74	0.752	0.260	31089	12081	25419	10088
36	8.04	16.02	13.36	0.752	0.256	28859	11229	23762	9457
37	8.02	14.01	12.01	0.752	0.256	28726	10864	23651	9413
38	8.03	12.01	10.68	0.753	0.261	28907	10514	23603	9363
39	7.98	9.98	9.32	0.753	0.264	29148	10178	23644	9355
40	8.01	7.99	8.00	0.755	0.263	29514	9653	23982	9495
41	4.02	4.02	4.02	0.755	0.294	22700	6759	17127	6616

## References

- Abramowitz, M., and Stegun, I.A., Editors (1964), Handbook of Mathematical Functions, Dover Publications, Inc., New York, 1964.
- Achenbach, J.D. (1973), Wave Propagation in Elastic Solids, Elsevier Science Publishing Company, Inc., New York, 1984.
- Achenbach, J.D., and Fang, S.J. (1969), "Asymptotic Analysis of the Modes of Wave Propagation in a Solid Cylinder," The Journal of the Acoustical Society of America, Vol. 47, No. 5 (Part 2), 1970, pp. 1282-1289.
- Afifi, S.E.A., and Richart, F.E. Jr. (1973) "Stress-History Effects on Shear Modulus of Soils," Soils and Foundations, International Society of Soil Mechanics and Foundation Engineering, Vol. 13, No. 1, pp. 77-95.
- Allen, J.C. (1982) "Development of Resonant Column Apparatus with Anisotropic Loading," M.S. Report, The University of Texas at Austin, 150 pages.
- Allen, J. C., and Stokoe, K. H., II (1982), "Development of Resonant Column Apparatus with Anisotropic Loading," Report GR82-28, Civil Engineering Department, University of Texas at Austin.
- Anderson, D.G. (1974), "Dynamic Modulus of Cohesive Soils," Thesis presented to the University of Michigan, in partial fulfillment of the requirements for the degree of Doctor of Philosophy.
- Anderson, D.G., and Stokoe, K.H.,II, (1978), "Shear Modulus: A Time-Dependent Soil Property," Dynamic Geotechnical Testing, ASTM STP 654, American Society for Testing and Materials, 1978, pp. 66-90.
- Arango, I., Moriwaki, Y., and Brown, F. (1978), "In-Situ and Laboratory Shear Velocity and Modulus," Proceedings of the Earthquake Engineering and Soil Dynamics Conference, ASCE, Pasadena, CA, June 19-21, Vol. 1 pp. 198-212.
- Armenakas, A.E., Gazis, D.C., and Herrmann, G. (1969), Free Vibrations of Circular Shells, (Pergamon Press, Inc., 1969).

Bancroft, D. (1941), "The Velocity of Longitudinal Waves in Cylindrical Bars," Physical Review, Department of Geology and Geography, Harvard University, Cambridge, Massachusetts, April, Vol. 59, pp. 588-593.

Barry, B.A. (1964), Engineering Measurements, John Wiley and Sons, Inc., New York, 1964.

Bedford, A., and Sorenson, A.L. (1977), "Variational Solution for the Reflection and Transmission of Waves at a Material Interface Between Waveguides," Journal of the Acoustical Society of America, Vol. 62, No. 2, August 1977, pp. 370-374.

Berends, B. E. (1977), Development of a Multiaxial Testing Cell for Cohesive Soils," M.S. Thesis, University of Colorado, Boulder, 1977.

Bianchini, G. (1985), "Evaluating Nonlinear Soil Behavior Using the Resonant Column," Advances in Soils Testing, pp. 197-231.

Biot, M.A. (1956a), Theory of Propagation of Elastic Waves in a Fluid-Saturated Porous Solid. I.Low Frequency Range," The Journal of the Acoustical Society of America, Vol. 28, No.2, (1956), pp. 168-177.

Biot, M.A. (1956b), Theory of Propagation of Elastic Waves in a Fluid-Saturated Porous Solid. II.Higher Frequency Range," The Journal of the Acoustical Society of America, Vol. 28, No. 2, (1956), pp. 179-191.

Biot, M.A. (1962), Generalized Theory of Acoustic Propagation in Porous Dissipative Media," The Journal of the Acoustical Society of America, Vol. 34, No. 9, September 1962, pp. 1254-1264.

Bhatia, S.K., Schwab, J., and Ishibashi, I. (1985), "Cyclic Simple Shear, Torsional Shear and Triaxial - A Comparative Study," Advances in Soil Testing, pp.232-254.

Brunson, B.A., and Johnson, R.K. (1980), "Laboratory Measurements of Shear Wave Attenuation In Saturated Sand," The Journal of the Acoustical Society of America, 68(5), Nov. 1980, pp. 1371-1375.

Canales, A. R. (1980), "Measurement Techniques and Test Related Variables in Resonant Column Testing," Geotechnical Engineering Thesis, GT80-4, Civil Engineering Department, University of Texas at Austin, August, 240 pages.

- Carnahan, B., Luther, H.A., and Wilkes, J.O. (1969), Applied Numerical Methods, John Wiley & Sons, New York, 1969.
- Chen, W.T. (1966), "On Some Problems in Transversely Isotropic Elastic Materials," Journal of Applied Mechanics, June 1966, pp. 347-355.
- Chu, H.Y.F., Lee S.H.H., and Stokoe, K.H., II (1984), "Effects of Structural and Stress Anisotropy on Velocity of Low-Amplitude Compression Waves Propagating along Principal Stress Directions in Dry Sand," Report GR84-6, Civil Engineering Department, University of Texas at Austin.
- Curtis, C.W. (1954), "Second Mode Vibrations of the Pochhammer-Chree Frequency Equation," page 198.
- Dahlen, F.A. (1972a), "The Effect of an Initial Hypocentral Stress Upon the Radiation Patterns of P and S Waves," Bulletin of the Seismological Society of America, Vol. 62, No. 5, October, pp. 1173-1182.
- Dahlen, F.A. (1972b), "Elastic Velocity Anisotropy in the Presence of an Anisotropic Initial Stress," Bulletin of the Seismological Society of America, Vol. 62, No. 5, October, pp. 1183-1193.
- Davies, R.M. (1947), "A Critical Study of the Hopkinson Pressure Bar," The Engineering Laboratory, University of Cambridge, Vol. 240, A. 821, pp. 375-457.
- Drnevich, V.P., Hall, J.R., and Richart, F.E., Jr. (1967), "Effects of Amplitude of Vibration on the Shear Modulus of Sand," Proceedings, International Symposium on Wave Propagation and Dynamic Properties of Earth Materials, Albuquerque, NM, August.
- Duffy, J., and Mindlin, R. D. (1957), "Stress-Strain Relations of a Granular Medium," Journal of the Applied Mechanics, Transactions ASME, Dec., pp. 585-593.
- Dyvik, R., and Madshus, C. (1986), "Lab Measurements of  $G_{max}$  Using Bender Elements," Norwegian Geotechnical Institute Publication NR. 161, Oslo, 1986.
- Folk, R., Fox, G., Shook, C.A., and Curtis, C.W. (1958), "Elastic Strain Produced by Sudden Application of Pressure to One End of a Cylindrical

Bar. I. Theory," The Journal of the Acoustical Society of America, Vol 30, No. 6, June, 1958, pp. 552-558.

Graham, J., and Houlsby, G.T. (1983), "Anisotropic Elasticity of a Natural Clay," Geotechnique 33, No. 2, pp. 165-180.

Gregory, A.R., and Podio, A.L. (1970), "Dual-Mode Ultrasonic Apparatus for Measuring Compressional and Shear Wave Velocities of Rock Samples," IEEE Transactions on Sonics and Ultrasonics, Vol. SU-17, No. 2, April, pp. 77-85.

Hall, J.R., "Limits on Dynamic Measurements and Instrumentation," Stone and Webster Engineering Corporation, Boston, MA 02107, pp. 108-119.

Hall, J.R., Jr., and Richart, F.E. Jr. (1963), "Dissipation of Elastic Wave Energy in Granular Soils," Journal of Soil Mechanics and Foundations Division, ASCE, Vol. 89, No. SM1, Feb., pp. 33-65.

Hardin, B.O. (1961), "Study of Elastic Wave Propagation and Damping in Granular Materials," Ph.D. Dissertation, University of Florida, August, 207 pages.

Hardin, B.O. (1965), "The Nature of Damping in Sands," Journal of Soil Mechanics and Foundations Division, ASCE, Vol. 91, No. SM1, January, pp. 63-97.

Hardin, B.O. (1978), "The Nature of Stress-Strain Behavior of Soils," Proceedings of the Earthquake Engineering and Soil Dynamics Conference, ASCE, Pasadena, CA, June 19-21, 1978, Vol. 1, pp. 3-90.

Hardin, B.O., and Black, W.L. (1966), "Sand Stiffness Under Various Triaxial Stresses," Journal of the Soil Mechanics and Foundations Division, ASCE, Vol. 92, No. SM2, March, pp. 27-43.

Hardin, B.O., and Black, W.L. (1968), "Vibration Modulus of Normally Consolidated Clay," Journal of the Soil Mechanics and Foundations Division, ASCE, Vol. 94, No. SM2, March, pp. 353-369.

Hardin, B.O., and Drnevich, V.P. (1972a), "Shear Modulus and Damping in Soils: Measurement and Parameter Effects," Journal of the Soil Mechanics and Foundations Division, ASCE, Vol. 98, No. SM6, June, pp. 603-642.

Hardin, B.O., and Drnevich, V.P. (1972b), "Shear Modulus and Damping in Soils: Design Equations and Curves," Journal of the Soil Mechanics and Foundations Division, ASCE Vol. 98, No. SM7, July, pp. 667-692.

Hardin, B.O., and Music, J. (1965), "Apparatus for Vibration During the Triaxial Test," Symposium on Instruments and Apparatus for Soils and Rocks, ASTM STP, No. 392.

Hardin, B.O., and Richart, F.E., Jr. (1963) "Elastic Wave Velocities in Granular Soils," Journal of the Soil Mechanics and Foundations Division, ASCE, Vol. 89, No. SM1, February, pp. 33-65.

Heiniger, C. and Studer, J.A. (1985), "Resonant Column Apparatus for Coarse-Grained Materials," Geotechnical Testing Journal, GTJDJ, Vol. 8, No. 3, Sept. 1985, pp. 132-136.

Helbig, K., (1983), "Elliptical Anisotropy - Its Significance and Meaning," Geophysics, Vol. 48, No. 7, July 1983, pp.825-832.

Hensel, R.D., and Curtis, C.W. (1967), "Propagation of a Longitudinal Strain Pulse along a Single-Crystal Bar," Journal of Applied Physics, Vol. 38, No. 6, May 1967, pp. 2679-2686.

Hertelency, P., (1962), "Displacement and Strain Energy Distribution in Longitudinally Vibrating Cylindrical Rod With a Viscoelastic Coating," Journal of Applied Mechanics, March 1982, pp. 47-52.

Holden, A.N., (1951), "Longitudinal Modes of Elastic Waves in Isotropic Cylinders and Slabs," The Bell System Technical Journal, October 1951, pp. 956-969.

Hudson, G.E., (1943), "Dispersion of Elastic Waves in Solid Circular Cylinders," Physical Review, Vol. 63, January 1 and 15, 1943, pp. 46-51.

Iida, K. (1938), "The Velocity of Elastic Waves in Sand," Bulletin of the Earthquake Research Institute, Tokyo Imperial University, Vol. 16, pp. 131-144.

Iida, K. (1940), "On the Elastic Properties of Soil Particularly in Relation to Its Water Content," Bulletin of the Earthquake Research Institute, Tokyo Imperial University, Vol. 18, pp. 675-690.

Isenhower, W.M. (1979), "Torsional Simple Shear/Resonant Column Properties of San Francisco Bay Mud," Geotechnical Engineering Thesis

GT80-1, Civil Engineering Department, University of Texas at Austin, December, 307 pages.

Januskevicius, C.K. and Vey, E. (1965), Stresses and Strains in Triaxial Specimens," Instruments and Apparatus for Soil and Rock Mechanics, ASTM STP 392, American Society for Testing and Materials, pp. 37-54.

Kausel, E., and Roesset, J.M. (1977), "Semianalytic Hyperelement for Layered Strata," Journal of the Engineering Mechanics Division, August 1977, pp. 569-588.

Knox, D.P., Stokoe, K.H., II, and Kopperman, S.E. (1982), "Effect of State of Stress on Velocity of Low-Amplitude Shear Waves Propagating Along Principal Stress Directions in Dry Sand," Report GR82-23, Civil Engineering Department, University of Texas at Austin, 420 pages.

Kopperman, S.E., Stokoe, K.H., II, and Knox, D.P. (1982), "Effect of State of Stress on Velocity of Low-Amplitude Compression Waves Propagating Along Principal Stress Directions in Dry Sand," Report GR82-22, Civil Engineering Department, University of Texas at Austin, 267 pages.

Kossoff, G. (1966), "The Effects of Backing and Matching on the Performance of Piezoelectric Ceramic Transducers," IEEE Transactions on Sonics and Ultrasonics, Vol. SU 13, No. 1, March, 1966, pp. 20-30.

Ladd, R.S. (1978), "Preparing Test Specimens Using Undercompaction," Geotechnical Testing Journal, GTJODJ, Vol. 1, No. 1, March 1978, pp. 16-23.

Lapin, L.L. (1983), Probability and Statistics for Modern Engineering, Brooks/Cole Publishing Company, Monterey, California, 624 pages.

Lawrence, F.V. (1963), "The Response of Soils to Dynamic Loadings," Report 14: Propagation Velocity of Ultrasonic Waves through Sand, Massachusetts Institute of Technology, Department of Civil Engineering, Research Report R63-8, March, 54 pages.

Lawrence, F.V. (1965), "Ultrasonic Shear Wave Velocities in Sand and Clay," Massachusetts Institute of Technology, Department of Civil Engineering, Research Report R65-05, January, 24 pages.

Lee, S.H.H. (1985), "Investigation of Low-Amplitude Shear Wave Velocity in Anisotropic Material," Ph.D. Dissertation, Geotechnical Engineering,

Civil Engineering Department, University of Texas at Austin, December, 394 pages.

Lee, S.H.H., and Stokoe, K.H., II, (1986), "Effects of Structural and Stress Anisotropy on Velocity of Low-Amplitude Oblique Compression Wave in Dry Sand," GR86-16, Civil Engineering Department, University of Texas at Austin (In Preparation)

Levin, F.K. (1978), "The Reflection, Refraction, and Diffraction of Waves in Media with an Elliptical Velocity Dependence," Geophysics, Vol. 43, No.3, April 1978, pp. 528-537.

LoPresti, D ., and Pedroni, S. (1989) "Maximum Dry Density of Cohesionless Soils by Pluviation and by ASTM D4253-83: A Comparative Study" to be submitted to the Geotechnical Testing Journal. Letter dated Dec. 1989, 2 pages.

Love, A.E.H. (1927), A Treatise on the Mathematical Theory of Elasticity, Cambridge University Press, Cambridge, (reprinted by Dover Publication, Inc., 1944).

Lysmer, J. and Waas, G. (1972), "Shear Waves in Plane Infinite Structures," Journal of the Engineering Mechanics Division, February 1972, pp. 85-105.

Matsukawa, E., and Hunter, A.N. (1956), "The Variation of Sound Velocity with Stress in Sand," Proceedings of the Physical Society, Sect. B, Vol. 69, Part 8, No. 440.b, August, pp. 847-884.

McSkimin, H.J. (1961), "Notes and References for the Measurement of Elastic Moduli by Means of Ultrasonic Waves," Journal of Acoustical Society of America, Vol. 33, No. 5, pp. 606-627.

Miklowitz, J. (1962), "Transient Compressional Waves in an Infinite Elastic Plate or Elastic Layer Overlying a Rigid Half-Space," Journal of Applied Mechanics, March 1962, pp. 53-60.

Miklowitz, J. (1969), "Wave Propagation in Solids," presented at ASME Winter Annual Meeting, Los Angeles California, Copyright , 1969, by The American Society of Mechanical Engineers, pp. 44-70.

Mindlin, R.D., and Fox, E.A. (1960), "Vibrations and Waves in Elastic Bars of Rectangular Cross Section," Journal of Applied Mechanics, March 1960, pp. 152-158.

- Mindlin, R.D., and McNiven, H.D. (1960), "Axially Symmetric Waves in Elastic Rods," Journal of Applied Mechanics, March 1960, pp. 145-151.
- Miura, S., and Shosuke, T. (1982), "A Sample Preparation Method and Its Effect on Static and Cyclic Deformation-Strength Properties of Sand," Soils and Foundations, Japanese Society of Soil Mechanics and Foundation Engineering, Vol. 22, No. 1, March 1982, pp. 61-77.
- Ni, S.H. (1987) "Dynamic Properties of Sand Under True Triaxial Stress States from Resonant/Column Torsional Shear Tests," Ph. D. Dissertation, Civil Engineering Department, University of Texas at Austin, August, 421 pages.
- Nishio, S., and Tamaoki, K. (1988), "Shear Wave Velocities in Diluvial Gravel Samples During Triaxial Compression Tests," Proceedings of Ninth World Conference on Earthquake Engineering, August 2-9, 1988, (Vol. III), Tokyo-Kyoto, Japan.
- Nishio S., and Tamaoki, K. (1988), "Measurement of Shear Wave Velocities in Diluvial Gravel Samples Under Triaxial Conditions," Soils and Foundations, Japanese Society of Soil Mechanics and Foundation Engineering, Vol. 28, No. 2, June 1988, pp. 35-48.
- Norman-Gregory, G.M., and Selig, E.T. (1989), "Volume Change Behavior of Vibrated Sand Columns," Journal of Geotechnical Engineering, Vol. 115, No. 3, March 1989, pp. 289-303.
- Norman-Gregory, G.M., and Selig, E.T. (1989), "Analytical Model for Longitudinal Soil Vibration," Journal of Geotechnical Engineering, Vol. 115, No. 3, March 1989, pp. 304-321.
- Noureldin A.S., and Wood, L.E. (1990), "Laboratory Evaluation of Recycled Asphalt Pavement Using Non Destructive Tests," Transportation Research Board 69th Annual Meeting, January 7-II, 1990, Washington D.C.
- Onoe, M., McNiven, H.D., Mindlin, R.D. (1962), "Dispersion of Axially Symmetric Waves in Elastic Rods," Journal of Applied Mechanics, December 1962, pp. 729-734.
- Pezo, R.F., Dong-Soo, K., Stokoe, K. H., II, and Hudson, W.R. (1990), Developing a Reliable Resilient Modulus Testing System, A Paper

Proposed for Presentation at the 1991 Annual Meeting of the Transportation Research Board, 37 pages.

Pochhammer, L. (1876), "Ueber die Fortpflanzungsgeschwindigkeiten kleiner Schwingungen in einem unbegrenzten isotropen Kreiscylinder." *J. reine angew. Math.* 81, pp. 324-336.

Prange, B. (1981), Resonant Column Testing of Railroad Ballast," Soil Mechanics and Foundation Engineering Tenth International Conference, Volume 3, Rotterdam.

Lord Rayleigh (1945) The Theory of Sound, Vol. 1, Dover Publications, New York, 1945.

Redwood, M. (1960), Mechanical Waveguides, Pergamon Press, London, 1960.

Richart, F.E., Jr. (1975), "Some Effects of Dynamic Soil Properties on Soil-Structure Interaction," Journal Geotechnical Engineering Division, ASCE, Vol. 101, No. GT12, December, Proc. Paper 11764, pp. 1193-1240.

Richart, F.E., Jr., Hall, J.R., Jr., and Woods, R.D. (1970), Vibrations of Soils and Foundations, Prentice-Hall, 414 pages.

Rix, G.J. (1984), "Correlation of Elastic Moduli and Cone Penetration Resistance," Thesis presented in partial fulfillment of requirement for Masters of Science in Engineering, University of Texas at Austin, May, 110 pages.

Roesler, S.K. (1979), "Anisotropic Shear Modulus Due to Stress Anisotropy," Journal of the Geotechnical Engineering Division, ASCE, Vol. 105, No. GT5, July, pp. 871-880.

Roesset, J.M., Chang, D., Stokoe, K.H. II, and Aouad, M. (1990), "Modulus and Thickness of the Pavement Surface Layer from SASW Tests," A Paper Prepared for Presentation at the 1990 Annual Meeting of the Transportation Research Board, 31 pages.

Rosenfeld, R.L., and Miklowitz, J. (1965), "Elastic Wave Propagation in Rods of Arbitrary Cross Section," Journal of Applied Mechanics, June, pp. 290-294.

- Saada, A.S., Bianchini, G.F., and Shook, L.P. (1978), "The Dynamic Response of Anisotropic Clay", Proceedings of the Earthquake Engineering and Soil Dynamics Conference, ASCE, Pasadena, CA, June 19-21, Vol. 2, pp. 777-801.
- Sanchez-Salinerio, I., Roesset, J.M., and Stokoe, K.H., II (1986), "Analytical Studies of Body Wave Propagation and Attenuation," Report GR86-15, Civil Engineering Department, University of Texas at Austin.
- Saxena, S.K., Reddy, K.R., Avramidis, A.S. (1988) "Dynamic Behavior of Artificially Cemented Sands," Proceedings of Ninth World Conference on Earthquake Engineering, August 2-9, 1988, (Vol. III), Tokyo-Kyoto, Japan.
- Schmertmann, J.H. (1978), Effect of Shear Stress on Dynamic Bulk Modulus of Sand, U.S. Army Engineering Waterways Experiment Station, Technical Report S-78-16, October, 92 pages.
- Scott, R.A., and Miklowitz, J. (1967), "Transient Elastic Waves in Anisotropic Plates," Journal of Applied Mechanics, March 1967, pp. 104-110.
- Scott, R.A. (1969), "Transient Anisotropic Waves in Bounded Elastic Media," Wave Propagation in Solids, Presented at ASME Winter Meeting, Los Angeles, California, November 20, 1969, pp. 71-91.
- Shannon, W.L., Yamane, G., and Dietrich, R.J. (1959), "Dynamic Triaxial Tests on Sand," Proceedings, First Panamerican Conference on Soil Mechanics and Foundations Engineering, Mexico City, Vol. 1, pp. 473-486.
- Skalak, R. (1957), "Longitudinal Impact of a Semi-Infinite Circular Elastic Bar," Journal of Applied Mechanics, March 1957, pp. 59-64.
- Smoots, V.A., and Stickel, J.F. (1962), Discussion of "Foundation Vibrations," Transactions, ASCE, Vol. 127, Part 1, pp. 906-908.
- Spanier, J., and Oldham, K.B. (1987) An Atlas of Functions, Hemisphere Publishing Corporation, New York, 1987.
- Stephenson, R.W. (1978) "Ultrasonic Testing for Determining Dynamic Soil Moduli," Dynamic Geotechnical Testing, ASTM STP 654, American Society for Testing and Materials, 1978, pp. 179-195.

Stokoe, K.H., II, Anderson, D.G., Hoar, R.J., and Isenhowe, W.M. (1978), Discussion on "In-Situ and Laboratory Shear Velocity and Modulus," Proceedings of the Earthquake Engineering and Soil Dynamics Conference, ASCE, Pasadena, CA, June 19-21, Vol. 3, pp. 1498-1502.

Stokoe, K.H., II, and Ni, S.H. (1985), "Effects of Stress State and Strain Amplitude on Shear Modulus of Dry Sand," Proceedings, Second Symposium on the Interaction of Non-nuclear Munition with Structures, Panama City Beach, Florida, April, pp. 407-412.

Stokoe, K.H., II, Lee, S.H.H., and Chu, H.Y.F. (1985), "Effect of Stress State on Velocities of Low-Amplitude Compression and Shear Waves in Dry Sand," Proceedings, the Second Symposium on the Interaction of Non-nuclear Munition with Structures, Panama City Beach, Florida, April, pp. 358-363.

Stokoe, K.H., II, Lee, S.H.H., and Knox, D.P. (1985), "Shear Moduli Measurement Under True Triaxial Stresses," Proceedings Advances in the Art of Testing Soils Under Cyclic Conditions, Geotechnical Engineering Division, ASCE, Detroit, Michigan, pp. 166-185.

Stokoe, K.H., II, Roesset, J.M., Knox, D.P., Kopperman, S.E., and Suddhiprakarn C. (1980), "Development of a Large-Scale Triaxial Testing Device for Wave Propagation Studies," Report GR80-10, Civil Engineering Department, University of Texas at Austin, 182 pp.

Stokoe, K.H., II, and Kim, D. (1989), "Preliminary Evaluation of Shear Modulus and Material Damping of Soft Specimen (TU-700), Civil Engineering Department, University of Texas at Austin, May 15, 1989, 15 pages.

Stokoe, K.H., Kim, D., and Andrus, R.D. (1990), "Development of Reference Specimens for Calibration and Evaluation of Resilient Modulus Equipment," Paper presented at the 1990 Annual Meeting of the Transportation Research Board.

Strachan, P. (1985), "Alternative Test Method for Ensuring Full Saturation in Triaxial Samples," Geotechnical Testing Journal, GTJODJ, Vol. 8, No. 1, March 1985, pp. 43-46.

Tawfiq, K.S., Aggour, M.S., and Al-Sanad, H.A. (1988), "Dynamic Properties of Cohesive Soils from Impulse Testing," Proceedings of Ninth World Conference on Earthquake Engineering, August 2-9, 1988, (Vol. III), Tokyo-Kyoto, Japan.

Tatsuoka, F., Iwasaki, T., Yoshida, S., Fukushima, K., and Sudo, H. (1979), "Shear Modulus and Damping by Drained Tests on Clean Sand Specimens Reconstituted by Various Methods," Soils and Foundations, International Society of Soil Mechanics and Foundation Engineering, Vol. 19, No. 1, March, pp. 39-54.

Taylor, P.W., and Huges, J.M.O. (1965), "Dynamic Properties of Foundation Subsoils as Determined from Laboratory Tests," Proceedings, the Third World Conference on Earthquake Engineering, New Zealand, Vol. 1, pp. 196-209.

Timoshenko, S.P., and Goodier, J.N. (1951), Theory of Elasticity. McGraw-Hill Book Co., New York, 506 pages.

Vaid, Y.P., and Chern, J.C. (1985), "Cyclic and Monotonic Undrained Response of Saturated Sands," Advances in Soils Testing, 1985, pp. 120-147.

Wilson, S.D., and Dietrich, R.J. (1960), "Effect of Consolidation Pressure on Elastic and Strength Properties of Clay," Research Conference on Shear Strength of Cohesive Soils, ASCE, pp. 419-435.

Wilson, S.D., and Miller, R.P. (1962), Discussion of "Foundation Vibrations," Transactions, ASCE, Vol. 127, Part 1, pp. 913-917.

Woods, R.D. (1978), "Measurement of Dynamic Soil Properties," Proceedings of the Earthquake Engineering and Soil Dynamics Conference, ASCE, Pasadena, CA, June 19-21, 1978, Vol. I, pp. 91-178.

Yu, P., and Richart, F.E., Jr. (1984), "Stress Ratio Effects on Shear Modulus of Dry Sands," Journal of Geotechnical Engineering, ASCE, Vol. 110, No. 3, pp. 331-345.

## VITA

Major Martin David Lewis [REDACTED]

[REDACTED] the son of Marcus Carter Lewis and Alice Barbara Ruth Lewis, U.S. Citizens. After graduating valedictorian of the class of 1973 from Corvallis High School, Corvallis, Oregon, he entered Oregon State University. Upon graduation in March 1978 with a degree of Bachelor of Science in Civil Engineering, he was commissioned a 2nd Lieutenant in the United States Air Force. Assignments in Spain and the United Kingdom followed, where he worked as an engineering planner and design manager. He entered the graduate school of the University of Illinois at Urbana-Champaign in August 1983 under the sponsorship of the U.S. Air Force Institute of Technology (AFIT). After graduating in August 1984 with a degree of Master of Science in Civil Engineering, Captain Lewis worked as a Research Civil Engineer at the Air Force Engineering and Services Laboratory, Tyndall AFB, Florida. There he supervised and conducted research in new civil engineering and pavement technology. In August 1987, again under the sponsorship of the AFIT, Major Lewis entered the Graduate School of the University of Texas at Austin.

[REDACTED]

This dissertation was typed by the author and his wife, Teresa D. Lewis.